Nonlinear Optical Probes for Measuring Membrane Potential in Neurons

Anjul Khadria

2014 – 2017

DPhil in Systems Biology (Organic Chemistry)

St Catherine's College

University of Oxford

Supervisor: Professor Harry Laurence Anderson FRS

A thesis submitted to the board of the faculty of Mathematical, Physical & Life sciences in partial fulfilment of the requirements for the degree of *Doctor of Philosophy* of the University of Oxford.

–To my Mummy (Saroj Khadria), my Papa (Basant Khadria), *Guru-Ma* Mahamandleshwar Sadhvi Karunagiri Mataji, Rani Sati Dadi, Hanumanji, Maa Kamakhya and KotiLing Shivji!

गुरुर ब्रह्मा गुरुर विष्णु, गुरुर देवो महेश्वरा ।
गुरुर साद्वात् परम ब्रह्मा, तस्मै श्री गुरवे नमः ॥

–Ancient Sanskrit Verse

Acknowledgement

First and foremost, I would like to thank my supervisor Prof. Harry L. Anderson for his constant guidance in this challenging project. Since I was the only student in his group working on this project, Harry showed infinite patience with me and was always available to guide me whenever, I faced any difficulty in this project. Harry allowed me to use the multiphoton microscope on my own and let me develop a set of interdisciplinary skills. I always felt inspired by his passion towards his work, which motivated me to push myself beyond the limits to match his level of hard work and dedication.

I would like to extend my thanks to the Clarendon Scholarships Fund, Hilla Ginwala Fund, and Radhakrishnan Memorial fund of the University of Oxford for funding my DPhil. I would also like to thank St Catherine's College Graduate Scholarships for awarding me a scholarship in the final year of my DPhil. I am very thankful to Systems Approaches to Biomedical Sciences and Systems Biology Doctoral Training Centers (DTC) of the University of Oxford. I would also like to thank the EPSRC and The John Fell Fund, University of Oxford for funding of the DTC and the multiphoton microscope.

I would like to thank Dr. Cécile Roche, a former postdoctoral researcher in our group for guiding in organic synthesis during initial days of my DPhil and proof reading numerous reports including this DPhil thesis. I would also like to thank Dr. Przemek Gawel, a current postdoctoral researcher in our group for motivating me to evolve into a better scientist. I would like to thank him for teaching me DFT computational theory, and proof reading each chapter of this thesis carefully. I am also thankful to Andy Hill, the salesman of Olympus for teaching me the controls of multiphoton microscope, and Dr. Robert Jacobs of Oxford Chemistry for helping me with maintenance of the multiphoton microscope.

I would also like to thank Dr. Sarah Wilkins, a former postdoctoral researcher in the Chemistry Department of Oxford University for teaching me immortal cell culture experiments. I am deeply grateful to Dr. Conor McClenaghan, a former DPhil student in the research group of Prof. Stephen Tucker for teaching me patch-clamp experiments, and Nils Rorsman, a DPhil student in the research group of Dr. Paolo Tammaro for teaching to patch-clamping the HEK 293T cells in his lab. I am also very thankful to Dr. Firdus Abd Wahab for connecting me to Dr. McClenaghan.

I would like to extend my thanks to Dr. Michael Kohl and Zoe Curtis (a Part II student in the Kohl group) for giving me mice brain slices for my experiments. I would also like to thank Prof. Nigel Emptage and three members of his group, Henry Taylor, Fran van Heusden, and Dr. Alexander Jeans for providing me 18 coverslips of primary rat hippocampal neurons for testing my dyes. I would also thank Pantelis Antonoudiou and Seher Kosar, two members of Dr. Ed Mann group for providing me few mice brain slices for my experiments. I am very thankful to Chela Nunez Alonso, a research assistant in the research group of Dr. Pawel Sweitach, Oxford University for providing me few coverslips of primary rat heart cells. I would also like to thank Dr. Nobina Mukherjee for collaborating with me in the work of Chapter 6 of this DPhil thesis. I would like to thank Prof. Koen Clays, Katholieke Universiteit de Leuven, Belgium for measuring the first-order hyperpolarizability of the pyropheophorbides that I synthesized and discussed in Chapter 2. I would also like to thank few members of the research group of Prof. Haygan Bayley, Oxford Chemistry for letting me use the glass pipette puller in their lab.

I am very thankful to Prof. Timothy Claridge, the entire NMR spectroscopy team, the entire mass spectrometry team for maintaining an excellent characterization service at the Department of Chemistry of the Oxford University. I would also like to thank Shifali Sisodia, a DPhil student at the Chemistry Department for useful discussion.

I would like to thank most of the previous and current members of Harry Anderson group for making this DPhil journey memorable. They are: Przemek, Cécile, Takayuki, Huawei, Julien, Pablo, Yaoyao, Reneé, Jonathan, Dan, Nuntaporn, Bart, Michel, Michael, Lara, Andreas, Levon, Pengpeng, Steffen, Dmitry, William, Isabell, Wenjun, Pernille, and James.

I would like to thank my friend, Prateek Raj for being like a brother and supporting me throughout my personal and professional life. I would also like to thank Priyanka Raj being a great sister. I would like to express my gratitude and bow my head towards my teacher, Ramakantji Mishra sir for being my *Guru*. Without the guidance of Ramakantji Sir since my childhood, I would have never been able to reach Oxford. I would also like to bow my head in front of Prithvi Giriji Maharaj of Juna Akhada for his blessings.

I would like to thank most of the members of my paternal (Khadria) and maternal (Maskara) families for constantly supporting me.

Five people, whose names I would like to mention are beyond thankfulness and I would not like to mention any adjective with their names. They are my Mummy, my Papa, my *Guru-Ma* Mataji, *Pittarji* Dadaji and my fiancé, Minu.

Abstract

Chapter 1: In Chapter 1, I discuss the design and mechanisms of existing optical techniques to measure membrane potential of live cells. I compare the different fluorescence and second harmonic generation- based methodologies developed over the years to test voltage sensitivity of dyes.

Chapter 2: I discuss the design, synthesis, and characterization of pyropheophorbide-based push-pull dyes as nonlinear optical probes. I show that the pyropheophorbides have different transition dipole moment for two-photon fluorescence and second harmonic generation in both 2D and 3D.

Chapter 3: In this chapter, I investigate the cellular localization of different donor-acceptor porphyrin-based dyes in a multiphoton microscope. The dyes possess the same hydrophobic electron-donor group and porphyrin group but different hydrophilic electron-acceptor groups. The dyes stain different types of cellular organelles depending on the type of hydrophilic head-groups.

Chapter 4: Here, I discuss the existing techniques to test voltage-sensitivity of organic dyes. I also discuss the design of a patch-clamp–based setup that I installed in the multiphoton microscope. I test the efficacy of the setup by testing the voltage sensitivity of commercial dyes. I also investigate the voltage sensing efficacy of plasma membrane bound porphyrin-based dyes.

Chapter 5: In this chapter, I discuss the design, synthesis, and characterization of a new tricationic porphyrin-based dye, **AK-1**. I also investigate the plasma membrane localization of **AK-1** in HEK 293T cells, U-87 MG cells, HeLa cells, rat hippocampal neurons, mice brain slices, contracting neonatal myocytes, gram negative bacteria *E.Coli*, and giant unilamellar vesicles. I demonstrate the voltage sensitivity of the dye in contracting neonatal myocytes. I also demonstrate multimodal imaging efficacy of **AK-1**.

Chapter 6: In this chapter, I study the spatial characteristics of monocellular and multicellular spheroidal tumor models through two-photon microscopy. The spheroids display similar characteristics to real tumors.

Publications

1. *Push-pull pyropheophorbides for nonlinear optical imaging*; Anjul Khadria, Yovan de Coene, Przemyslaw Gawel, Cécile Roche, Koen Clays, Harry L. Anderson; *Org. Biomol. Chem.* 2017, 15, 947-956

   Designated as a 'hot article'. Featured in RSC blogs (OBC blog).
   Author contributions: A.K. carried out all the organic synthesis, characterization, spectroscopy, electrochemistry, microscopy, and image analysis. Y.C. performed the hyper-Rayleigh scattering (HRS) experiments. P.G. performed the DFT modelling. C.R. supervised A.K. for the first six months during organic synthesis and assisted in characterization of the organic molecules. K.C. was involved in HRS experiments. H.L.A devised the project. A.K., P.G., C.R, and H.L.A wrote the paper.

2. *Nonlinear optical dyes for targeting different cellular organelles;* Anjul Khadria, Jan Fleischhauer, James Wilkinson, Igor Boczarow, Michael Kohl, Harry L. Anderson, *In preparation;*

   My work: I performed organic synthesis, characterization, spectroscopy, all the microscopy and image analysis.

3. *Droplet microfluidics based tumour spheroid model for drug screening;* Nobina Mukherjee*, Shaohua Ma*, Anjul Khadria, Linna Zhou, Harry L. Anderson, Hagan Bayley, *In preparation; Authors list and positions not final*

   My work: I performed the two-photon imaging and image analysis of the tumor models, *Co-first authors.

Talks

1. Delivered a talk at 2017 DTC DPhil symposium, Oxford, UK.
2. Invited to give a talk at the St Catherine's College, Oxford Graduate Scholars' Symposium.

Posters

1. 2017 Oxford Biomedical Imaging Festival.
2. 2017 19th IUPAB congress and 11th EBSA congress, Edinburgh, UK.
3. 2016 DTC DPhil symposium, Oxford, UK.
4. 2016 Chemistry Department DPhil symposium, Oxford, UK.

Awards

1. Awarded fully funded Clarendon Scholarship to pursue DPhil at the University of Oxford (*141 students awarded out of more than 20,000 graduate applications to the Oxford University*); awarded Radhakrishnan Memorial Fund scholarship and Hilla Ginwala Scholarship along with the Clarendon Scholarship.
2. Awarded St Catherine's College Graduate Scholarship (*awarded on basis of ongoing DPhil research*).
3. Awarded the competitive European Biophysical Societies' Association bursary to attend the 19th IUPAB congress and 11th EBSA congress at Edinburgh, Scotland.

List of abbreviations

2PA	Two-Photon Absorption	**DIPEA**	*N,N*-Diisopropylethylamine
2PF	Two-Photon Fluorescence	**DMEM**	Dulbecco's Modified Eagle's Medium
AK-1	Anjul Khadria 1	**DMF**	Dimethylformamide
aq.	Aqueous	**DMSO**	Dimethylsulfoxide
Ar	Aryl	**DPhPC**	1,2-Diphytanoyl-sn-glycero-3-phosphocholine
B3LYP	Becke 3-Parameter, Lee,Yang and Parr (exchange-correlation potential)	**EFISHG**	Electric Field Induced Second Harmonic Generation
COSY	Correlation Spectroscopy	**ESI**	Electrospray Ionization
COMU	(1-Cyano-2-ethoxy-2-oxoethylidenaminooxy) dimethylamino-morpholino-carbenium hexafluorophosphate	**GM**	Göeppert Mayer
ChR2	Channelrhodopsin 2	**GUV**	Giant Unilamellar Vesicle
d	Doublet (in NMR)	**HEG**	Hexaethylene glycol
Da	Dalton	**h**	Hours
dba	Dibenzylideneacetone	**HeLa**	Henrietta Lacks
dc-SHG	Direct Current-Second Harmonic Generation	**HEK**	Human Embryonic Kidney
DCM	Dichloromethane	**HLB**	Hemispherical Lipid Bilayer
DDQ	2,3-Dichloro-5,6-dicyano-*para* benzoquinone	**HOMO**	Highest Occupied Molecular Orbital
DFT	Density Functional Theory	**JR1**	James Reeve 1
DIB	Droplet Interfacial Bilayer	**IR**	Infrared
DIPA	Diisopropylamine	***J***	Coupling constant
LUMO	Lowest Unoccupied Molecular Orbital	**SNR**	Signal to Noise Ratio

MALDI - ToF	Matrix-Assisted Laser Desorption Ionization – Time of Flight
m	Multiplet (in NMR)
Me	Methyl
MeOH	Methanol
min	Minutes
ms	Milliseconds
M_W	Molecular weight
NA	Numerical Aperture
NBS	*N-Bromosuccinimide*
NIR	Near-infrared
o	Ortho
p	Para
PCM	Polarizable Continuum Model
PEG	Polyethylene glycol
PMT	Photo Multiplier Tube
PPa	Pyropheophorbide *a*
PPa-OMe	Pyropheophorbide *a* methyl ester
RH123	Rhodamine 123
RH237	Rina Hildesheim 237
RT	Room Temperature
s	Seconds
SHG	Second Harmonic Generation
TEG	Triethylene glycol
TDM	Transition Dipole Moment
TPEF	Two-Photon Excited Fluorescence
TLC	Thin Layer Chromatography
THF	Tetrahydrofuran

Table of Contents

Chapter 5 182

Chapter 1

Introduction: Voltage-Sensitive Dyes

Summary: *In this chapter, I give a brief introduction about membrane potential of cells and various non-optical and optical methods used to measure them. I briefly introduce non-optical techniques, while I discuss the optical techniques in detail. I discuss the advantages and disadvantages of various mechanisms, such as electrochromism, Förster resonance energy transfer, photo-induced electron transfer, and second harmonic generation (SHG). I also discuss about various organic chromophores that employ these mechanisms. In the end, I enlist the advantages of nonlinear optical technique, SHG over other mechanisms to measure membrane potential of cells.*

1.00 Optical dyes for membrane potential

It is estimated that the human brain contains approx. 100 billion neurons.[1] Since the time of neuron doctrine at the end of the nineteenth century,[2–4] we have been exploring the brain and trying to understand how neurons communicate with each other. Study of communication between neurons will give information about the underlying causes of brain communication, as well as help elucidate the nature of various diseases, such as Alzheimer's and Parkinson's.

Neurons communicate through electrical signals *via* potential difference (membrane potential) developed across their plasma membranes,[5–7] which is generated because of concentration gradient-based movement of sodium, potassium, and chloride ions between the nerve cell and the environment, through the various ion-specific channels located in the plasma membrane.[6] Over the last five decades, several non-optical and optical techniques have been developed to measure the membrane potential in neurons.[7–13] In this chapter, I review some of those techniques which are directly related to this thesis. The primary focus of this chapter is on the optical voltage-sensitive dyes, which can measure membrane potential at multiple sites of a neuron and of multiple neurons simultaneously, with high spatial and temporal resolution.

1.10 Membrane potential

A neuron is said to be at rest when the potential difference across its plasma membrane is −70 mV, known as the resting potential. At resting potential, there are more positively charged sodium ions outside the cells than inside and more potassium ions inside the cells than outside leading to a concentration gradient. At the start of an action potential (initiated by a stimulus), the sodium gated ion-based channels open, leading to passive transport of positively charged sodium ions from outside the cells to inside, thus shifting the transmembrane potential towards a positive value. As soon as the voltage reaches a threshold value of −55 mV, more sodium gated ion channels open, which depolarizes the neuron to a transmembrane potential of 30 mV. Once the cell is depolarized, the sodium gated channels close and the potassium gated ion channels open causing the potassium ions to move from inside of the cells to the outside, following which the cell repolarizes to resting potential (Figure 1). During the process of repolarization, the potassium gated ion channels remain open for a longer duration causing hyper-repolarization leading to further decrease of transmembrane potential below −70 mV. Gradually, the potassium gated ion channels close, and an ATP driven sodium and potassium –based pump opens to reinstate the cell at resting potential of −70 mV (Figure 1).

The whole cycle of depolarization and repolarization takes place in a time scale of about 2 ms and is called ‘action potential’.[14] In 1963, the Nobel Prize for Physiology or Medicine was awarded to John Eccles, Alan Lloyd Hodgkin and Andrew Fielding Huxley for their work on transmission of nerve impulse in terms of action potential.[15]

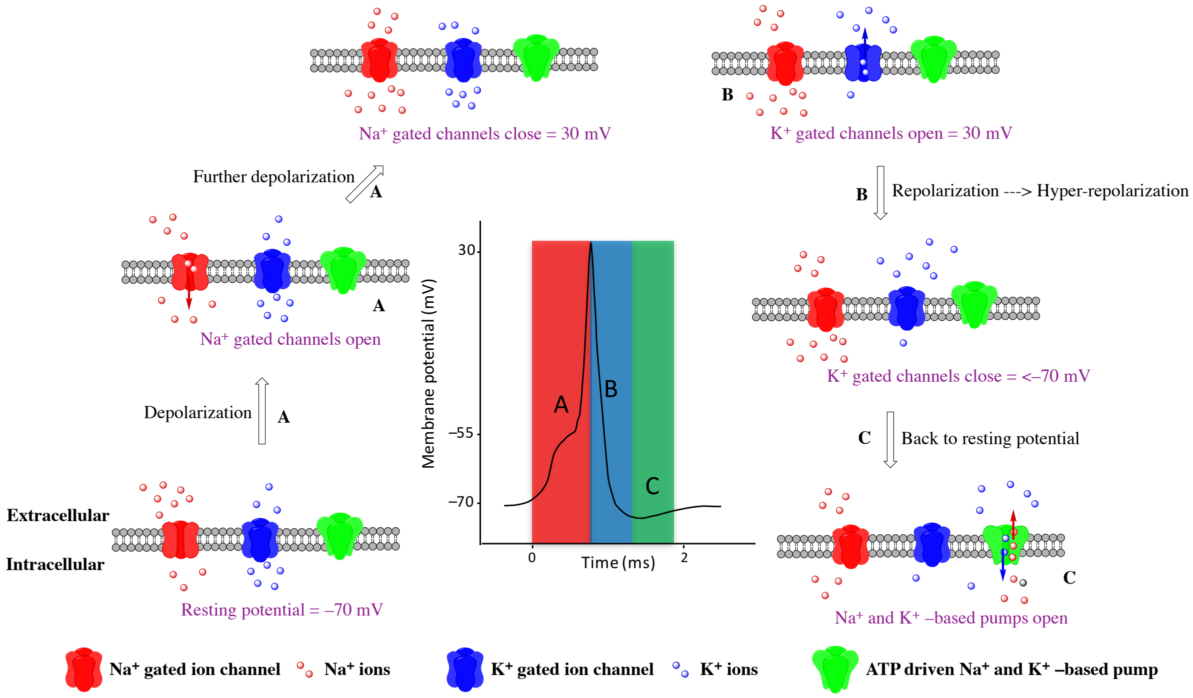

Figure 1: Depiction of activity of the ion channels in plasma membrane on generation of an action potential.

1.20 Measurement of membrane potential

Several non-optical and optical –based techniques have been developed over last few decades to measure the membrane potential of neurons. Although, the techniques have pushed the boundaries in the field of neuroscience and elucidated more information than ever before, they have not yet been able to study the neuronal network in entirety. Here, I discuss the techniques that have been developed over the years to study the membrane potential of neurons. The work described in my DPhil thesis deals with the design, synthesis, and testing of various second harmonic generation-based porphyrin voltage-sensitive dyes in live cells. The goal of this chapter is to discuss the advantages and disadvantages of the existing techniques that are used to measure membrane potential of neurons. In the end of this chapter, I discuss the advantages that the porphyrin-based dyes offer in contrast to the existing techniques.

1.21 Non-optical technique

Non-optical techniques such as patch-clamp,[16,17] intracellular recording,[18] microelectrode arrays,[19] and brain mesh electronics[20,21] have emerged as powerful tools to study the membrane potential/current of excitable cells.

Patch-clamp technique: In patch-clamp technique, a low resistance (2–10 MΩ) glass microelectrode is attached to the cellular plasma membrane, and then the required voltage or current is measured. The attachment is carried out by forming a tight seal such that the electrical resistance of the seal is in the order of giga-ohms. A tight seal of giga-ohmic resistance prevents unwanted leakage of the current, that is flowing between the cell membrane and the microelectrode. Patch-clamp–based techniques are further divided into several subtypes, such as whole-cell patch-clamp, inside out patch-clamp, outside-out patch-clamp, cell-attached patch-clamp, and perforated patch-clamp.[22] All the patch-clamp–based techniques are used for various types of recordings depending on the requirement of the experiment. Currently, patch-clamp is regarded as the most powerful technique to measure membrane potential of neurons both *in vitro* and *in vivo*. I designed and used a whole-cell–based patch-clamp technique to study the voltage sensitivity of organic dyes that I discuss in detail in Chapter 4.

Intracellular recording: In intracellular recording, high resistance (20–40 MΩ) glass microelectrodes are filled with 1–3 M KCl solution, and inserted into the cells to measure the membrane current. The total osmolarity of buffer in which cells are incubated is around 310 mOsm. The mouth of the pipette used in intracellular recording is very small (in the order of nanometers), which does not allow flow of KCl solution from the pipette to the cells and hence there is no osmotic shock. Intracellular recordings are useful to measure the synaptic signals of cells with high signal-to-noise ratio. It cannot be used to excite cells in a controlled manner as in whole-cell patch-clamp technique and often leads to current leaks from the membrane because this technique does not involve formation of any giga-ohmic seals.[23] Intracellular recording is used for both *in vitro* and *in vivo* recordings.

Microelectrode arrays: Microelectrode arrays allow simultaneous detection of hundreds of sites in a neural network.[24] Microelectrode arrays need to be implanted into the brain for *in vivo* experiments and involve a complex electronic set up. Wise and coworkers used microelectrode arrays to record signals from 421 neurons at a resolution in the order of microvolt in live monkey brains after 3–4 weeks of implantation.[25] One of the major disadvantages of microelectrode-based arrays is that they require complicated surgery procedures, and the implanted arrays can lead to unwanted immune response from the body.

Although, microelectrode-based techniques remain among the most reliable methods for measuring the membrane potential, they have several disadvantages.

1. They are not easy to use as they require state-of-the-art facilities and include complex experimental procedures.[26]
2. Microelectrodes are invasive, require advanced experimental skills, and they provide low spatial resolution.[27,28]
3. One of the biggest disadvantages of electrode recording is that it is not high-throughput and hence, signals from large number of neurons (in terms of thousands to millions) cannot be recorded at once. Microelectrode arrays have been demonstrated to record signals only from a few hundred neurons and they are still far behind from recording signals from millions of neurons simultaneously.

However, microelectrode-based techniques are widely used because they have been thoroughly optimized, and so, they provide accurate values of action potential, and give a high temporal resolution. Microelectrodes are not toxic and they do not change the intrinsic characteristics of cells.

Brain mesh electronics: Recently, Lieber and coworkers demonstrated a new technique called ‘Brain Mesh Electronics’, to record signals *in vivo* in mice brain with a resolution in the order of microvolts.[20,21] The nanoscale silicon-based flexible mesh electronics system can be injected into the brain without any complicated surgical procedures. The injectable mesh electronics system can record signals at a single neuron level, recordings can be performed for at least 8 months, and it does not elicit any chronic immune response.[20,29] The technique is still in its nascent stage and needs to be optimized and thoroughly tested, before being regarded as one of the best techniques to measure membrane potential of neurons.

1.22 Optical techniques

Optical-based molecular dyes offer a wide range of advantages over microelectrodes to measure the membrane potential of excitable cells, such as

(1) Optical dyes can measure membrane potential simultaneously from multiple sites of a cell and also of multiple cells simultaneously.[30]

(2) Use of optical dyes does not require complicated surgical procedures.

(3) Optical dyes are not invasive.

(4) They provide high spatial resolution in comparison to the microelectrode-based techniques.

Optical dyes are normally used through two different modes of applications, (a) fluorescence, (b) second harmonic generation (SHG). The voltage sensing efficiency of an optical probe can be assessed by two metrics, which are: (a) signal-to-noise ratio (SNR) and (b) fractional (emitted light) intensity change, $\Delta F/F$ per 100 mV of voltage change, where F is the baseline intensity. The signal in signal-to-noise ratio denotes the change in optical signal generated due to the change in membrane potential. The two metrics are related through the equation:

$$SNR \propto \left(\frac{\Delta F}{F}\right)\sqrt{N}, \qquad \text{Eq. 1}$$

where, N denotes the number of emitted photons.[31] The SNR of a dye can be increased by increasing either the sensitivity of the dye ($\Delta F/F$), or the number of emitted photons (N). The sensitivity, ($\Delta F/F$) can be modulated by engineering of the molecular structures of dyes, while number of emitted photons can be increased by increasing the power of the light source used to illuminate the dye, or by increasing the dye concentration. The approach of increasing the dye concentration or the power of the light source often leads to phototoxicity and photodamage. By engineering the molecular structures of the dyes, the $\Delta F/F$ (and hence, the SNR) can be increased without significant phototoxicity or photodamage. In the bid to measure voltage changes across the plasma membrane of the cell with high SNR, a range of optical dyes have been designed over last few decades. Apart from a high SNR, an ideal voltage-sensitive dye must also give high spatial and temporal resolution, should not show dark toxicity, and must not interfere with the inherent biological characteristics of the cells.[32]

Majority of the optical dyes are fluorescence-based; however, the use of SHG has recently emerged as an alternative approach.[33–42] Here, first I discuss the different classes of fluorescent-based dyes and then I discuss the SHG technique and the dyes that have been so far shown to measure membrane potential of cells through SHG.

1.30 Fluorescent-based dyes

Fluorescent-based optical voltage-sensitive dyes can be classified into two types: (a) Indirect dyes and (b) Direct dyes. Indirect dyes measure the membrane potential by measuring the change of concentration ions, such as Ca^{2+} or Na^{+} that takes place as a result of an action potential. Direct dyes are plasma membrane bound dyes, which directly respond to the change in membrane potential by various mechanisms, such as electrochromism, Förster resonant energy transfer, and photo-induced electron transfer.[35,38,43–45] Here, I briefly describe the indirect and direct dyes, which have been used to measure the membrane potential of cells.

1.31 Indirect dyes

Calcium-sensitive fluorescent dyes have been the most successful indirect dyes used to measure action potential of neurons. Calcium-sensitive probes respond to the change in calcium concentration that takes place due to an action potential. Tsien and coworkers developed a range of highly successful fluorescent-based calcium dyes, such as **Quin-2**, **Fura-2**, **Fluo-3**, and **Fluo-4**, which are a combination of a fluorescent chromophore and a calcium binding chelator, **BAPTA** (Figure 2).[9,46–48]

The dyes developed by Tsien and coworkers (Figure 2) offer high voltage sensitivity with $\Delta F/F$ reaching up to the value of 50% per 100 mV; however, they exhibit poor temporal resolution.[49,50] Since the dyes were designed to measure the change in calcium concentrations, which occur as a result of an action potential, there is always a delay. The temporal resolutions of the calcium-based dyes are dependent on the rate of diffusion of calcium ions through the cell body. Action potentials in neurons occur in a timescale of approx. 2 ms but these dyes respond in the timescale of up to few seconds. Moreover, small molecule-based calcium dyes could not be easily used for *in vivo* experiments due to delivery and toxicity issues.

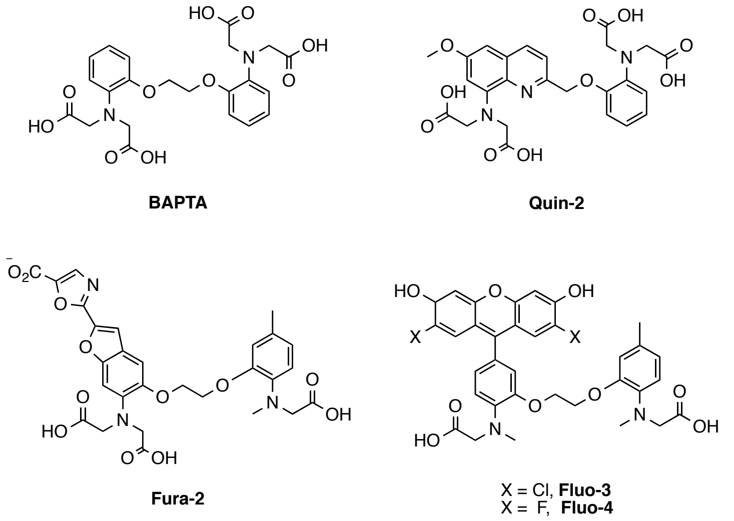

BAPTA

Quin-2

Fura-2

X = Cl, **Fluo-3**
X = F, **Fluo-4**

Figure 2: Chemical structures of a calcium chelator, **BAPTA** and the calcium sensitive fluorescent probes, **Quin-2, Fura-2**, **Fluo-3**, and **Fluo-4**.

To overcome the issues of low temporal resolution and inefficient *in vivo* delivery, Tsien and coworkers designed a new generation of protein-based calcium dyes widely known as genetically encoded calcium indicators (GECIs).[51] The GECIs are classified into two distinct types: FRET (Förster resonance energy transfer)-based and single-fluorophore–based. These dyes give high spatial and temporal resolution and are compatible with different types of cells both *in vitro* and *in vivo*. The working principle of various calcium-based fluorescent indicators are briefly described in Figure 3.[52]

In spite of major developments, calcium-based dyes have several disadvantages. In several cases, the calcium binding chelators were found to perturb calcium homeostasis, thus affecting the cellular electrical activity.[49,53] Many calcium-based dyes cannot retain their efficiency over time due to saturation effect. The GECIs have been found to exhibit better temporal resolution than small molecule-based calcium dyes, but often they do not reflect reliable calcium signals associated with single action potential.[54] Moreover, GECIs cannot measure subthreshold repolarization and depolarization events and are restricted to measuring only spikes of an action potential.[55]

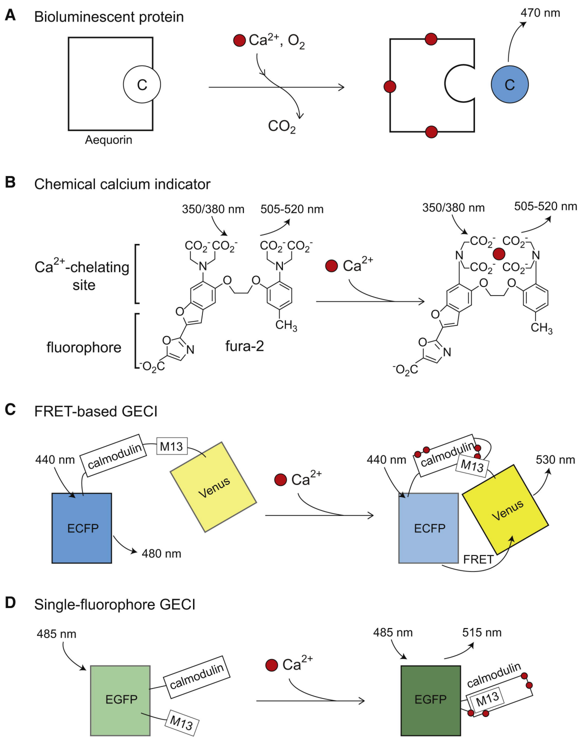

Figure 3: Working mechanism of different calcium-based fluorescent dyes. (A) **Bioluminescent protein:** Calcium ions bind to photoprotein, aequorin thus oxidizing, coelenterazine (C, left side) to colenteramide (C, right side). Colenteramide relaxes to the ground state emitting a photon at 470 nm. (B) **Organic calcium indicator:** Fura-2 is a UV light based dye which absorbs at 350 nm and 380 nm. It emits light between 505 and 520 nm regardless of the excitation wavelength. The ratio of the fluorescence emission of **Fura-2** at 350 nm 380 nm is dependent on the concentration of the calcium ions. (C) **FRET-based calcium indicator (GECI):** After binding of calcium ions, two fluorescent proteins, ECFP (donor) and Venus (acceptor), approach towards each other leading to FRET mechanism thus changing the emission of the whole molecule. (D) **Single-fluorophore-based GECI:** The GCaMP protein molecule undergoes conformational intramolecular changes due to binding of calcium ions. The conformational changes lead an increase in the emitted fluorescence at 515 nm. Image adapted with permission from *Neuron*, 2012, **73**, 862–885. Copyright 2012 Elsevier.

1.32 Direct Dyes

The plasma membrane bound amphiphilic direct dyes were designed to directly sense the change in membrane potential. Majority of the small molecule-based fluorescent direct dyes are divided into three types: (i) Electrochromic dyes, (ii) Förster resonance energy transfer (FRET)-based dyes, and (iii) Photo induced electron transfer (PeT)-based dyes.

Apart from the three classes of fluorescent direct dyes as mentioned above, there also exist a range of dyes that work by rotation and reorientation mechanisms as a result of an action potential, such as 8-anilinonaphthalene-1-sulfonic acid (**ANS**), **Merocyanine 540**, and **DiS-C$_2$-(5)** (Figure 4). These dyes undergo macromolecular changes such as rotation, dimerization, and reorientation in the cell membrane due to an action potential. Such types of dyes were one of the earliest fluorescence-based voltage-sensitive dyes (developed in 1960s and 1970s). Although these dyes report the change in membrane potential, they either give very poor sensitivity ($\Delta F/F \approx 10^{-5} - 10^{-3}$) or poor temporal resolution (seconds to minutes).[10,42,56–59]

Due to the low sensitivity, these types of dyes give very poor signal-to-noise ratio. Moreover, the results from these dyes have reproducibility issues and they behave differently in different environments. To address these issues, new classes of fluorescence-based direct dyes were designed, which are discussed below.

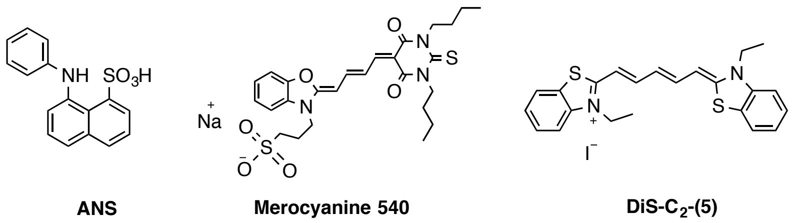

Figure 4: Molecular structure of 8-anilinonaphthalene-1-sulfonic acid (**ANS**), **Merocyanine-540**, and **DiS-C$_2$-(5)** dyes.

Electrochromic dyes: Electrochromic dyes are based on the molecular Stark effect to give direct electro-optic response to an applied electric field.[60–64] By the effect of electrochromism, the absorption and emission wavelengths of a chromophore change (i.e. change in electronic energy levels) when placed in a local electric field. The shift in the energy levels is expressed as:

$$\Delta\nu = -\frac{\Delta\mu}{h}\boldsymbol{E} - \frac{\Delta\alpha}{2h}\boldsymbol{E}^2 \qquad \text{Eq. 2}$$

where, $\Delta\nu$ is the shift in the frequency of the electronic transition (absorption and fluorescence spectra) on application of an electric field $\boldsymbol{E}$, $\Delta\mu$ and $\Delta\alpha$ are the changes in the static dipole moment and polarizability between the ground state and the electronic excited state of the molecule, and h is the Plank's constant. The second term, $\frac{\Delta\alpha}{2h}\boldsymbol{E}^2$ in the above equation is relatively insignificant in comparison to the first term for cell membrane potential measurements. Therefore, the change in energy levels primarily depends on $\Delta\mu$ in the presence of a static electric field $\boldsymbol{E}$. For a chromophore to respond to the changing electric field, it must follow two primary requirements: (a) The chromophore dipole must be rigidly and anisotropically oriented with respect to the electric field,[65] and (b) the chromophore should exhibit large shift in the electron density distribution ($\Delta\mu$) upon excitation by light.

Loew and coworkers designed a amphiphilic donor-acceptor–based rod shaped dye, **di-5-ASP**-based on the structure of 4-aminostyryl-1-methylpyridinium iodide (**ASP**, Figure 5).[66,67]

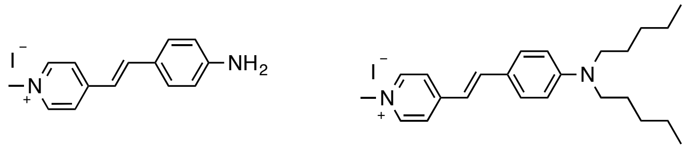
ASP **di-5-ASP**

Figure 5: Molecular structures of **ASP** and **di-5-ASP**.

The alkyl chains of **di-5-ASP** fit the hydrophobic core of the membrane while the charged part at the other end of the dye strongly interacts with the hydrophilic part of the membrane, thus satisfying the first criterion of rigid and anisotropic orientation. The compound is strongly polar (μ_g = 11.1 Debye in $CHCl_3$[68]). In the ground state, the electron density is localized in the aniline ring while in the first excited state, it is localized in the pyridinium ring (Figure 6) thus exhibiting significant shift in the electron density on photoexcitation, which is the second criterion for an electrochromic chromophore. This dye gives sensitivity $\Delta F/F$ as large as 5% per 100 mV in a hemispherical lipid bilayer, which was significantly higher than the previous dyes.[39]

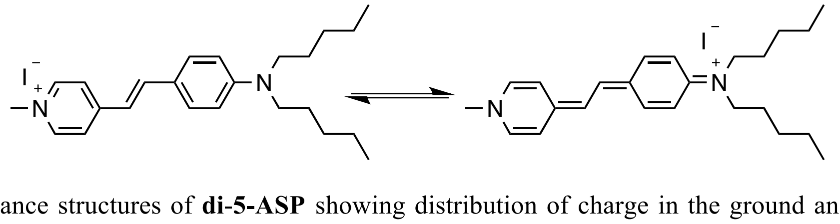

Figure 6: Resonance structures of **di-5-ASP** showing distribution of charge in the ground and first electronic excited states.

Since electrochromism is based on the shift in the emission spectrum, the voltage sensitivities, $\Delta F/F$ of the electrochromic dyes depend on the wavelengths of the spectra at which the photons are collected. An electrochromic dye gives higher voltage sensitivity at the tail region (region 2, Figure 7), than the regions at the middle of the spectrum (e.g. region 1, Figure 7). Hence, to give high *SNR* along with high voltage sensitivity, an electrochromic dye must have high quantum yield (Eq. 1).

The microscope also plays an important role in deciding the voltage sensitivity of electrochromic dyes because the range of wavelengths at which the photons are collected are dependent on the configuration of the microscope in use. In a multiphoton microscope (used in this DPhil study), limited collection of photons (i.e. photons only from an area of the fluorescence spectrum) is ensured by using cutoff filters, which collect light only from above or below a specified wavelength. Usually, different dyes have different emission spectra and hence it is not always possible to install a separate filter for a specific dye.

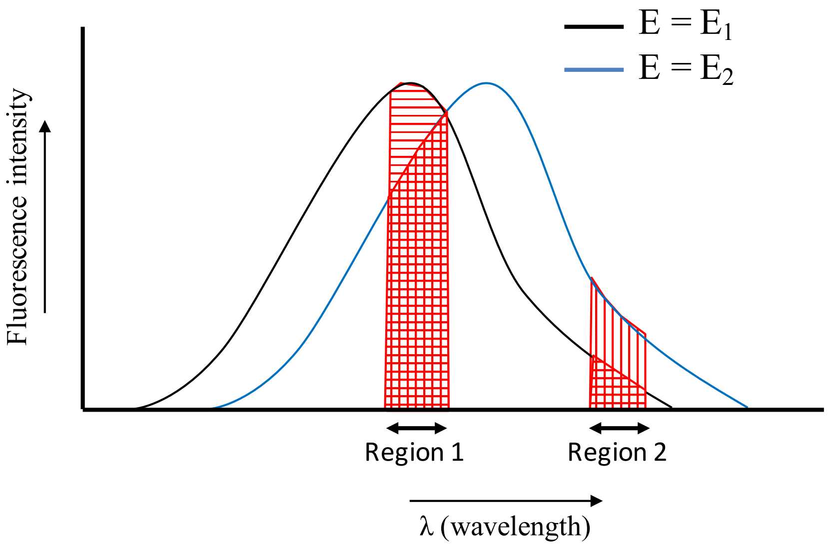

Figure 7: False emission spectra to demonstrate electrochromism. Due to the shift of the emission spectrum towards the right side at electric field, $E = E_2$ from E_1, higher voltage-sensitivity (change in spectrum) can be recorded by collecting photons from the tail (region 2) than in the middle (region 1). The collection of photons depends on the configuration of the microscope in use.

The dipole moment of a dye becomes stronger, when the length of electronic conjugation between its electron donor and acceptor moieties increases.[69,70] Hence, dyes with longer electronic conjugation should have greater electrochromic shifts when placed in an applied electric field (due to increased $\Delta\mu$). Additionally, in a plasma membrane, the maximum change in the transmembrane potential takes place at the middle of the bilayer across the fully dehydrated region.[32,70–72] Since the typical thickness of the lipid bilayer in a plasma membrane is 4–5 nm, by increasing the overall size of the dye molecule (size of **di-5-ASP** ≈ 1.7 nm) a greater electrochromic change can be achieved. Hildesheim and coworkers developed a new class of RH-based (Rina Hildesheim) dyes by extending the conjugation of **ASP** dye by adding extra ethene linkers and modifying the polar headgroups.[73,74] Loew and coworkers designed a new class of naphthalene-based amphiphilic ANEP (amino naphthenyl-pyridinium) dyes with extended conjugations, and studied their voltage sensitivity in artificial lipid bilayers and live cells.[75–77] **Di-4-ANEPPS** (Figure 8) emerged as the most successful dye of the ANEP family. It has a sensitivity of $\Delta F/F$ = 8% / 100 mV in hemispherical lipid bilayers (HLBs).[76] Preuss *et al.* compared voltage sensing efficiency of **di-4-ANEPPS** with an RH-based dye, **RH795** based on their toxicity profiles.[78] The *SNR* of **RH795** (Figure 8) was found to be almost half than that of **di-4-ANEPPS**; however, **di-4-ANEPPS** photobleached faster than **RH795** under the same imaging conditions. They proposed that **di-4-ANEPPS** is suitable for short-term experiments, while **RH795** is apt for long-term experiments. Loew and coworkers showed that excitation and emission spectra of the hemicyanine dyes could be finely tuned by fluorination.[79] The authors synthesized a series of dyes and fluorinated them to show that fluorination at specific positions can alter the spectra of the dye. Fluorination was found to increase the photostability of the dye and improved the *SNR* as compared to non-fluorinated dyes. They found that the fluorinated dye, **di-4-AN(F)EP(F)PTEA** (Figure 8C) photobleaches almost two times slower than **di-4-ANEPPS** in a guinea pig heart. Apart from improved *SNR* and photostability, the fluorinated dye washes out twice slower than **di-4-ANEPPS** from the cellular membranes and hence is also suitable for longtime measurements. The reason for the slow washout could also be the dicationic character of the fluorinated dye, while **di-4-ANEPPS** is zwitterionic. A detailed study of different dyes with different solubilizing polar head groups is discussed in Chapter 3. Despite having similar molecular structures, the two dyes behaved notably different, which means that the photobleaching and washout issues of the existing organic voltage-sensitive electrochromic dyes can be successfully addressed by fluorination.

One of the major issues with the styryl-based dyes is that they undergo *cis-trans* photoisomerism which also contributes to shifts in the absorption and emission spectra, thus the voltage sensitivity is not relaiable.[80,81] Fromherz and coworkers synthesized a range of rigid dyes, **ANNINE-5**, **ANNINE-6**, **ANNINE-6plus** (Figure 8) that do not undergo photoisomerism.[70,82] The ANNINE-based dyes gave very high voltage sensitivity with $\Delta F/F$ as high as 50% per 100 mV.[80,82] Although, highly voltage sensitive, the toxicity of ANNINE-based dyes has not been thoroughly studied and these dyes are not commercially available.

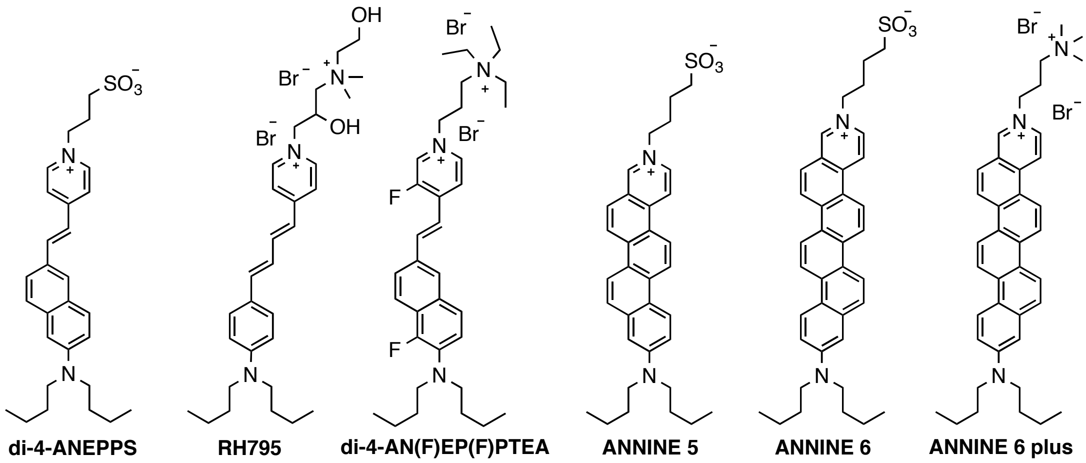

Figure 8: Molecular structures of (A) **di-4-ANEPPS**, (B) **RH795**, (C) **di-4-AN(F)EP(F)ETEA**, (D) **ANNINE-5**, (E) **ANNINE-6**, and (F) **ANNINE-6plus**.

Although, electrochromic dyes have emerged as powerful tools to measure voltage changes in cellular plasma membranes, they have a general disadvantage that the maximum voltage sensitivity is observed only at the tails of the emission spectra where the number of emitted photons is low leading to poor *SNR*. Moreover, electrochromic dyes are polarity-sensitive and thus give different fluorescence emission in media of different polarities. Lipids in the plasma membrane undergo polarity changes due to biological events because of which they become tightly packed or loosely packed. Tightly packed lipids are less polar than loosely packed lipids due to presence of less amount of water molecules. The electrochromic dyes are widely used to study polarity changes in lipid bilayers.[83–85] When an electrochromic dye is used for membrane potential measurements, the contribution of changes in lipid order to the fluorescence emission of the dye cannot be segregated and so the dyes do not necessarily reflect true changes in the membrane potential.

Förster Resonance Energy Transfer (FRET):[86] FRET-based voltage-sensitive dyes were first designed by Tsien and coworkers.[87] Since then, FRET-based dyes have received significant attention as membrane potential sensing tools because they have been found to be highly voltage-sensitive and to provide good *SNR*. FRET-based dyes use a pair of chromophores where one chromophore is a membrane bound energy-donor while the other chromophore is a membrane bound mobile voltage-sensitive energy-acceptor. When the cell is at resting membrane potential (outer membrane is positively changed and the inner membrane is negatively charged), both the donor and acceptor chromophores are bound to the outer leaflet of the plasma membrane. This is because generally, the amphiphilic donor chromophore is designed to bind permanently to the extracellular leaflet of the dye while, the anionic acceptor chromophore bind to the extracellular leaflet due to electrostatic interaction (Figure 9). At this state, Förster resonant energy transfer takes place from the donor chromophore to the acceptor chromophore, which results into the quenching of fluorescence emission of the donor chromophore, and enhancement of fluorescence emission of the acceptor chromophore. As the membrane potential changes, the cell becomes depolarized (outer membrane becomes negative and the inner membrane becomes positive) because of which the anionic mobile acceptor travels towards the intracellular leaflet of the plasma membrane due to electrostatic interaction. As the mobile acceptor travels, quenching of FRET takes place resulting in a change in the fluorescence. The ratio of change in fluorescence emissions of the donor and acceptor chromophore denotes the change in membrane potential (Figure 9). For FRET to take place, the acceptor chromophore must be in the vicinity of the donor chromophore because the efficiency of FRET probes is proportional to $\frac{R_0}{r^6}$, where r is the distance between the two chromophores and R_0 is Förster radius (distance between the donor and the acceptor at which 50% of the energy is transferred).[88] In conventional donor-acceptor pairs of FRET-based dyes, the R_0 value lie in the range of 2–8 nm, which is similar to the thickness of cellular plasma membrane and hence it is possible to use these dyes for measuring membrane potential of cells.[89]

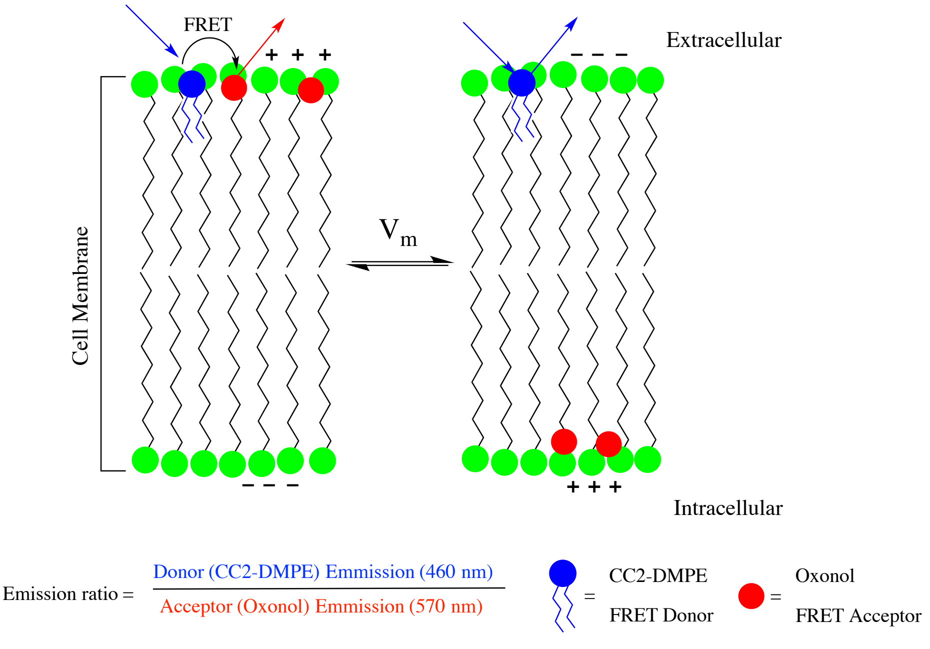

Figure 9: Depiction of FRET mechanism. In resting membrane potential (intracellular is negative), both molecules of the FRET pair bind to the extracellular leaflet of the cell membrane leading to efficient FRET. After depolarization (intracellular is positive), the anionic mobile acceptor (oxonol) shifts to the intracellular leaflet of the cell membrane while the donor remains bound the outer surface thus quenching the FRET. The fluorescence intensity ratio of the donor to acceptor molecules denotes the changes in membrane potential.

Anionic oxonol-based dyes such as **DiSBAC$_2$(3)** and **DiSBAC$_4$(3)** (Figure 10) are widely used as FRET acceptor chromophores in combination with coumarin phospholipid, **CC2-DMPE** as the donor chromophore (Figure 10).[90] Pair of **CC2-DMPE** and **DiSBAC$_2$(3)** as a FRET-based system has been shown to give voltage sensitivity, $\Delta F/F$ up to 300% in live cells.[91]

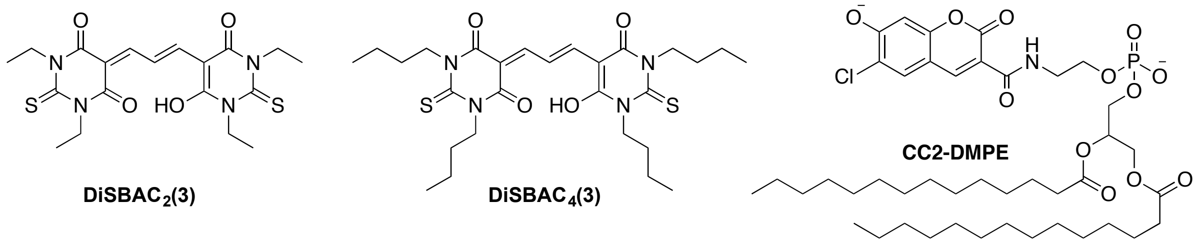

Figure 10: Molecular structures of oxonol FRET-based acceptor dyes **DiSBAC$_2$(3)** and **DiSBAC$_4$(3)**, and the donor dye, **CC2-DMPE**.

FRET-based dyes have several disadvantages that have hindered their widespread use as a voltage-sensitive tool. The donor and acceptor chromophores of FRET-based dyes require precise stoichiometry, which is difficult to achieve in most of the cases due to low aqueous solubility of the hydrophobic mobile acceptors. For example, **DiSBAC$_4$(3)** requires the use of pluronic F-127 surfactant for staining. Other chromophores such as **DiSBAC$_2$(3)** do not require pluronic F-127 as they are more polar but they need to be loaded in high concentrations up to 20 mM. Such high concentration of chromophores can affect the resting potential of the cells, as they tend to increase the cell capacitance and hence perturb the inherent synaptic properties.[92] Moreover, the temporal resolution of FRET mechanism is dependent on the translocation of the mobile acceptor inside the cell membrane and hence it is not a purely electro-optic response.

Dyes based on photo-induced electron transfer (PeT) through molecular wires:[93] Tsien and coworkers were the first to design and demonstrate the use of PeT-based dyes to measure membrane potential of live cells.[94] The recent voltage-sensitive PeT-based dyes are composed of three different parts, an electron-rich donor moiety known as the fluorescence quencher, a fluorophore moiety, and a molecular wire connecting the electron-rich quencher and the fluorophore. In PeT, when the molecule is in an electronic excited state (when irradiated by light), electron transfer takes place from the electron-rich quencher to the fluorophore *via* the molecular wire, to quench the fluorescence of the fluorophore (Figure 11). The dye is designed to be amphiphilic so that it remains bound to the plasma membrane such that the fluorophore is bound to the extracellular leaflet, and the electron rich quencher moiety is bound towards the intracellular leaflet of the plasma membrane (Figure 11).

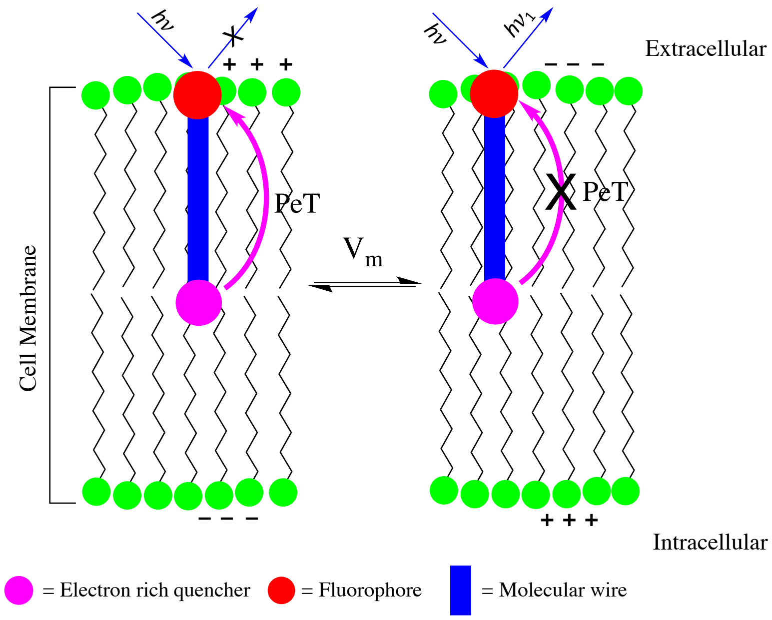

Figure 11: Depiction of photo induced electron transfer (PeT) mechanism. When the cell is at resting potential, PeT takes place from the electron rich quencher to the fluorophore *via* the molecular wire. As the cell depolarizes, the PeT becomes less prominent and hence the fluorophore emits light. The change in fluorescence intensity represents the change in membrane potential.

When the cell is at resting potential (inner leaflet of the cell membrane is negatively charged and the outer leaflet is positively charged) and the molecule is electronically excited by light, then the PeT transfer efficiency is highest. As the voltage across the cell membrane changes and the plasma membrane depolarizes (inner leaflet becomes positively charged and outer leaflet becomes negatively charged), the efficiency of the PeT is affected and hence, there is a change in fluorescence intensity of the fluorophore. The change in the fluorescence denotes the change in membrane potential. It must be noted that the electron transfer is not between an 'electron-rich donor group' and an 'electron-deficient acceptor group' as the fluorophore is not an electron-deficient moiety; therefore, it is different from electrochromic dyes. An advantage of PeT-based dyes over FRET-based dyes is that the temporal resolution is dependent on the intramolecular electron transfer which takes place in a time range of femtoseconds to picoseconds and hence, the dyes could be used to resolve fast action potential spikes in neurons.[94]

The initial PeT-based dyes synthesized by Tsien and coworkers incorporated dichlorosulfofluorescein as the membrane bound fluorophore, *N,N*-dimethyl- or *N,N*-dibutylaniline as the electron-rich quencher moiety, and *p*-phenylenevinylene (PPV) as the molecular wire to synthesize three dyes, **VF1.4.Cl**, **VF2.1.Cl** and **VF2.4.Cl** (Figure 12).[94]

These dyes did not show any capacitive loading when tested in leech neurons, which make them favorable over FRET-based dyes. The dyes exhibited fast kinetics and reported voltage sensitivity $\Delta F/F$ of approx. 20–27% per 100 mV. Tsien and coworkers improved the design to synthesize **VF2.1(OMe).H** (Figure 12) which gave voltage sensitivity, $\Delta F/F$ as high as 48% per 100 mV, which is twice the sensitivity of the previous PeT-based dyes.[38] Apart from these dyes, several other similar PeT-based dyes have been synthesized to increase the voltage-sensitivity, plasma membrane binding efficiency, and photostability.[95–99]

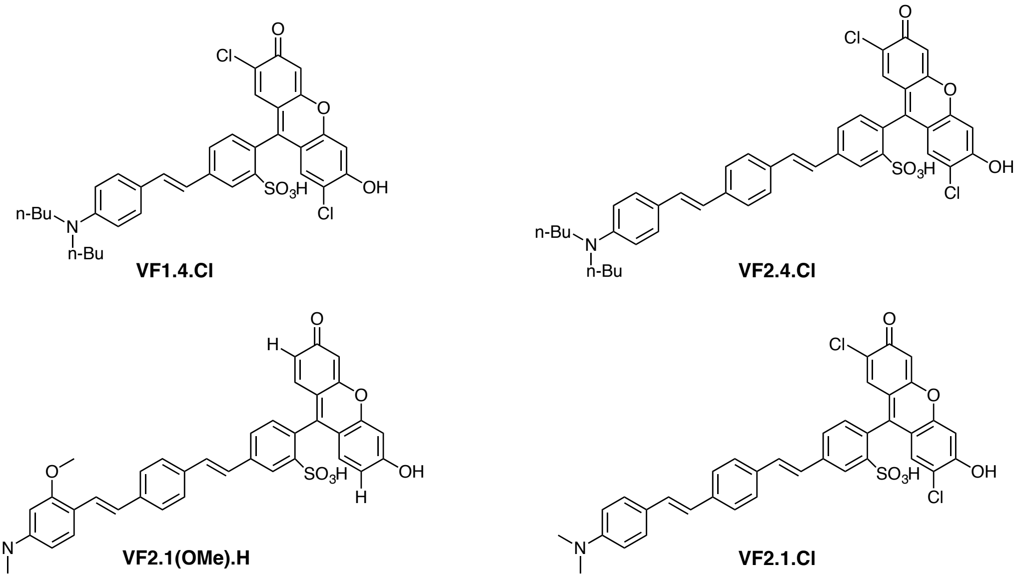

VF1.4.Cl **VF2.4.Cl** **VF2.1(OMe).H** **VF2.1.Cl**

Figure 12: Molecular structures of PeT-based dyes.

Although, PeT-based voltage-sensitive dyes have given promising results with good voltage sensitivity and temporal resolution (in the order of milliseconds), there are a few challenges that remain associated with them. PeT-based dyes are easily taken up by the cells resulting in background fluorescence from the intracellular area. For an efficient PeT, all the dye molecules must be aligned in a similar orientation in the cellular membranes; however, such an orientation does not always take place. A major problem associated with PeT is that its efficiency decreases exponentially with the increase in the length of molecular wires.[100] To sense the change of voltage across the plasma membrane efficiently, a PeT-based dye should span across the whole plasma membrane. However, the longer the dye the lower the PeT efficiency and thus a compromise must be made between efficient PeT and efficient voltage sensing. Moreover, the existing PeT-based dyes are styryl-based dyes because of which they undergo photoisomerism that contributes to fluorescence change as discussed above for electrochromic styryl-based dyes.

As described above through three different mechanisms, electrochromism, FRET, and PeT, the small molecule-based voltage-sensitive dyes offer good voltage sensitivity and temporal resolution and are easy to deliver in cells; however, there are certain limitations associated with them. Such dyes cannot be easily used for *in vivo* voltage sensing in live mammals due to toxicity issues. Moreover, there are issues related to background fluorescence, single cell imaging from a bulk of cells, and dark toxicity. To overcome these challenges, genetically encoded protein-based dyes were designed as briefly discussed below.

1.33 Genetically encoded voltage indicators (GEVIs)

The first genetically encoded voltage sensor was reported by Isacoff and coworkers in 1997;[11] however, it was only after 2005 that the research in the field of GEVIs gained pace when Okamura and coworkers discovered a single protein-based voltage-sensitive phosphatase.[101] Since then, different types of GEVIs have been demonstrated that work by use of voltage sensing domains,[102] electrochromic rhodopsins,[103,104] and dual opsin-based FRET mechanism.[44,105] GEVIs offer the advantage of being targeted to specific cell types in an ensemble of cells, which is not a trivial task in case of small molecules.[106] The brain consists of different types of neurons and each type has its own inherent firing characteristic accounting for different functions of our body. Simultaneous and specific targeting of different cell types is important to study the neuronal communication. Unlike small molecule-based voltage indicators, GEVIs do not require invasive craniotomy to be delivered *in vivo* and they can also be used for long term (days to months) experiments.[107] GEVIs have also been shown to record spikes in neurons of awake mouse.[105] In the last few years, GEVIs have pushed the boundaries in the research of voltage sensing tools to study the neuronal communication; however, there are certain challenges associated with them. Sometimes these indicators cross the plasma membrane (due to cellular trafficking) and accumulate inside the cells; such incidences can be fatal for live *in vivo* imaging as they can alter the dynamics of the brain.[108] Expression of GEVIs in neurons is not trivial and requires advanced experimental skills to avoid any unwanted mutations. Due to these challenges, many researchers still pursue conventional techniques like patch-clamp and small molecule voltage-indicators to study membrane potential of neurons.

1.34 Challenges with fluorescence-based techniques

Fluorescent-based voltage-sensitive dyes have revolutionized the field of neurobiology because of their ability to test membrane potential from multiple neurons simultaneously.

Fluorescent-based dyes offer the advantage of being used at a range of wavelengths from visible to infrared. With the use of easily accessible epifluorescence and confocal microscopes, fluorescence based-dyes have pushed the frontiers of biological imaging. However, there are certain issues associated with the principle of fluorescence microscopy which have posed significant challenges in bioimaging.

1. **Phototoxicity and photobleaching**: Fluorescence works by the principle of photoexcitation of a fluorophore from the electronic ground state to an excited state resulting in radiative decay (fluorescence) back to the ground state.[109] Due to involvement of excited states, molecular oxygen present in the medium can be transformed to toxic reactive oxygen species that are harmful for both the biological species (phototoxicity) and the molecular dyes (photobleaching).[110,111] Photobleaching has been a major concern for voltage sensitive dyes leading to generation of new types of photostable dyes or use of oxygen scavengers.[75,95,99,112]
2. **Photodamage**: Many fluorophores absorb light in the blue and green regions of the visible light spectrum. Use of blue and green light can lead to photodamage of cells for example, blue light is has been linked to mitochondrial DNA damage.[113,114] Long term imaging is not possible with the use of blue and green dyes.
3. **Deep imaging**: Short wavelength light (350 nm–700 nm) cannot penetrate in deep tissues beyond 100–300 μm because low wavelength light get either absorbed or scattered by the tissues.[115] Due to light penetration issues it has not been possible to image thick biological tissues (>300 μm) and record signals from thick brain slices with epifluorescence or one-photon–based confocal microscopies. Two-photon microscopy which utilizes longer wavelength light (>700 nm) is used for imaging deep tissues. Chapter 6 of this DPhil thesis involves study of two-photon microscopy on millimeter sized thick tumor models.
4. **Background signal**: During fluorescence imaging, unwanted background fluorescence causes decrease of *SNR*.[35,116] For membrane potential experiments, the dyes must localize at the plasma membrane of the cells; however, it has been a challenge to stop the dyes from being internalized in to the cells due to cellular trafficking. Since most of the conventional dyes are gradually taken up by the cells, they result in background fluorescence which interfere with the fluorescence signal of interest.

Due to the concurrent issues (as discussed above) that remain associated with the conventional fluorescence-based techniques, second harmonic generation, a nonlinear optical technique has emerged as an alternative method for measuring membrane potential of cells.

1.40 Second harmonic generation (SHG)

Second harmonic generation (SHG) is a nonlinear optical process that occurs when a medium of high quadratic hyperpolarizability encounters an intense, focused, and coherent laser light to generate light of exactly twice the frequency.[117] In simple terms, it can be stated that when a non-centrosymmetric molecule in a non-centrosymmetric medium is irradiated with two photons of equal wavelength, it generates (scatters) light of exactly half the wavelength, which is known as SHG (Figure 13). SHG is a single wavelength phenomenon and does not include a range of wavelengths as it is in the case of fluorescence (Figure 13). SHG occurs only at the interfaces that are populated with an ensemble of non-centrosymmetric molecules with ordered first-order hyperpolarizabilities.[117] Since SHG is not observed in isotropic media,[118] it is useful for measuring plasma membrane potential of cells without any background signals.[119,120] SHG is a scattering technique and does not involve population of excited states because of which there is no phototoxicity or photobleaching. It must be noted that since SHG is a scattering technique, the SHG light is scattered only in the forward direction i.e. towards the direction at which the incident light travels. Unlike fluorescence, SHG light is very weak in the reflected direction and hence it cannot be used for brain related *in vivo* experiments, which is a major disadvantage of SHG-based imaging.

Optical SHG was first observed by Franken *et al.* in 1961[121] and since then the development and application of SHG-based techniques have received significant attention.[122–129] SHG has been used in producing continuous-wave green light laser of 532 nm by doubling the frequency of a pumped ytterbium fiber crystal laser at 1064 nm[130,131] and has found application in surface studies too.[132] Biological imaging through SHG was first reported by Sprecher and coworkers in 1986 to study the polarity of collagen fibers in rat tail tendons,[133] and since then it has been used in number of biological imaging applications, such as disease imaging,[127] imaging collagen fibrils,[134] imaging biomolecular arrays in cells,[135] and measurement of membrane potential of excitable cells.[36,117]

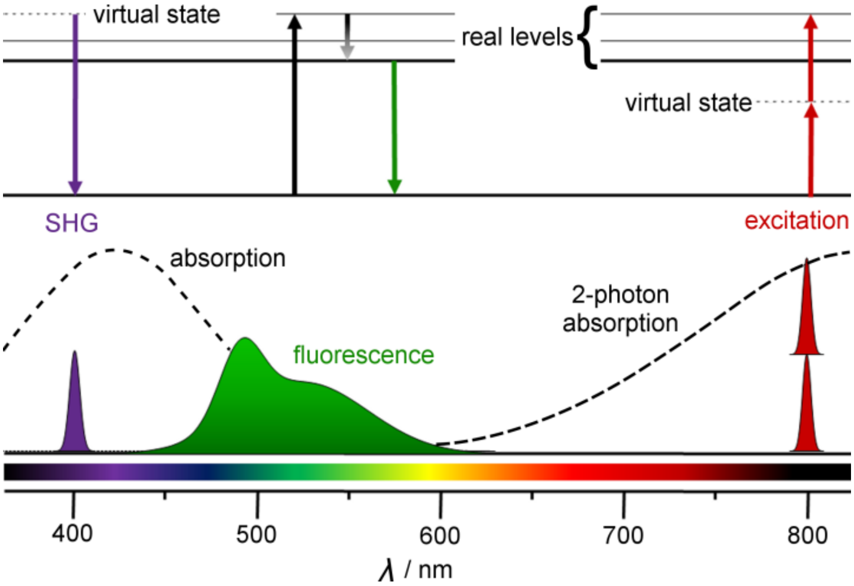

Figure 13: Representation of energy level of real states (solid) and virtual states (dashed) and the transitions between them. If a molecule is excited at 800 nm (red) by two photons simultaneously, it gives SHG (blue) at 400 nm, and fluorescence at wavelengths greater than 400 nm (green). Image adapted with permission from *Phys. Chem. Chem. Phys.*, 2010, **12**, 13484–13498. Copyright 2010 Royal Society of Chemistry.

1.41 Theory of SHG

If a molecule with a dipole moment is placed in a strong oscillating electric field, $\boldsymbol{E}$ (e.g. a laser beam), then an oscillating dipole moment, μ is induced, which can be represented in the form of Taylor series as,

$$\mu = \alpha \boldsymbol{E} + \beta \boldsymbol{E}^2 + \gamma \boldsymbol{E}^3 \dots\dots \qquad \text{Eq. 3}$$

where, α is the linear polarizability, responsible for one photon absorption and linear Rayleigh scattering, β is the first-order hyperpolarizability, responsible for SHG (determined through hyper-Rayleigh scattering)[116,136,137], and γ is the second-order hyperpolarizability, responsible for factors, such as two-photon absorption and SHG-based voltage sensivity.[33,117]

To show that SHG is not displayed by centrosymmetric molecules, the induced dipole moment, μ of Eq. 1 can be expressed in terms in polarization density $\boldsymbol{P}$ as,

$$\boldsymbol{P} = \epsilon_0(\chi^{(1)}\boldsymbol{E} + \chi^{(2)}\boldsymbol{E}^2 + \chi^{(3)}\boldsymbol{E}^3 \dots\dots) \qquad \text{Eq. 4}$$

where, ϵ_0 is the permittivity of space, $\chi^{(n)}$ is the n-ordered susceptibility ($\chi^{(2)}$ is responsible for SHG) and $\boldsymbol{E}$ is the electric field. The SHG is denoted by the second term, which can be written as,

$$\boldsymbol{P}^{(2)} = \epsilon_0\chi^{(2)}\boldsymbol{E}^2 \qquad \text{Eq. 5}$$

$\boldsymbol{E}$ *and* $\boldsymbol{P}$ are vector quantities. Let's consider a scenario of isotropic media where $\boldsymbol{E}$ exists in all the directions. For a horizontal x-direction, Eq. 5 remains as it is while in the horizontal –x-direction, Eq. 5 becomes,

$$-\boldsymbol{P}^{(2)} = \epsilon_0 \chi^{(2)} (-\boldsymbol{E})^2 \qquad \text{Eq. 6}$$

Eq. 5 and Eq. 6 can only be equal when $\chi^{(2)} = 0$, which means that there will be no SHG in isotropic media.[118] It must be noted that since SHG is a vector quantity and comes from an ensemble of molecules, in scenarios where any two molecules are in opposite directions, there will be overall zero SHG signal. Figure 14 shows orientation of an amphiphilic SHG-based dye around monolayer of lipid-based water droplets suspended in oil (dodecane). The dye was dissolved in oil before imaging and naturally oriented around the lipid-based interface of water and oil. Fluorescence (red) is visible from isotropic oil media while, SHG is visible only from the monolayer interface of water and oil.

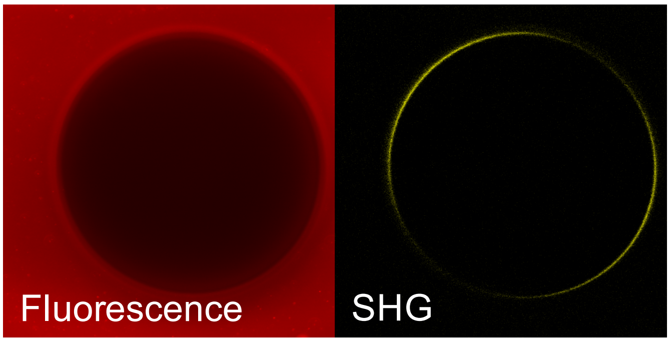

Figure 14: Two-photon excited fluorescence and SHG images of an amphiphilic dye oriented around lipid-based monolayer water droplet (diameter ≈ 150 µm) suspended in oil. Fluorescence (red) is visible from isotropic media of oil (dodecane) while, SHG (yellow) is visible only from the monolayer interface of water and oil. The amphiphilic dye was dissolved in oil so that it naturally orients at the interface of the water and oil. λ_{ext} = 840 nm. The images are taken by me using a pyropheophorbide dye (explained in detail in Chapter 2).

The SHG intensity, $\boldsymbol{I}_{SHG}$ given by a molecule when shone by intense light is expressed as,[117]

$$\boldsymbol{I}_{SHG} = G(\chi^{(2)}_{zzz})^2 \boldsymbol{I}_o{}^2 \qquad \text{Eq. 7}$$

where, G is a constant depending on various experimental factors, $\boldsymbol{I}_o$ is the intensity of incident light, and $\chi^{(2)}_{zzz}$ is the second-order susceptibility in z-axis.[117] The term $\chi^{(2)}_{zzz}$ can be further expressed as,

$$\chi^{(2)}_{zzz} = N f \beta_{zzz} < \cos^3 \alpha > \qquad \text{Eq. 8}$$

where, N is the number density of the molecules, f is the global local field factor related to the refractive index of the media, n, represented by $f = (n^2 + 2)/3$, β_{zzz} is the major hyperpolarizability tensor which is parallel with the polarization of the incident laser light. $< \cos^3 \alpha >$ is an orientation factor of the molecule, α is the orientation angle between the major transition dipole moment of the molecule and the normal of the cell membrane axis (orientation angle of pyropheophorbide-based molecules in cell membrane is studied in detail in Chapter 2).[117,138] By substituting Eq. 8 in Eq. 7, $\boldsymbol{I}_{SHG}$ becomes,

$$\boldsymbol{I}_{SHG} = GN^2 f^2 {\beta_{zzz}}^2 < \cos^3 \alpha >^2 {\boldsymbol{I}_o}^2 \qquad \text{Eq. 9}$$

Eq. 9 shows that SHG intensity of a molecule in non-centrosymmetric media depends on the squared of number density of the molecules and on the squared of second-order hyperpolarizability. Eq. 9 also shows that in media with higher refractive index more intense SHG signals will be seen.

1.4.1 Theory of SHG-based voltage sensitivity

According to Eq. 1, the voltage sensitivity of a dye is described as $\Delta F/F$; however, in case of SHG, let the voltage sensitivity be described as $\Delta S/S$, which can be expressed as,

$$\frac{\Delta S}{S} = \frac{S(E_2) - S(E_1)}{S(E_1)} \qquad \text{Eq. 10}$$

where, S is the SHG intensity in electric fields E_1 and E_2. By substituting Eq. 9 in Eq. 10, $\Delta S/S$ can be rewritten as,

$$\frac{\Delta S}{S} = \frac{\beta_{eff}^2(E_2) - \beta_{eff}^2(E_1)}{\beta_{eff}^2(E_1)} \qquad \text{Eq. 11}$$

where, $\beta_{eff}(E)$ is related to both first-order hyperpolarizability (Eq. 3) and second-order hyperpolarizability. In presence of a membrane electric field E_m, an SHG is induced, known as electric field induced second harmonic generation (EFISHG),[35,139] which involves the third-order term of polarization density $\boldsymbol{P}$ of Eq. 4 and expressed as, $\chi^{(3)}\boldsymbol{E}^2 E_m$. Considering the effect of EFISHG, $\beta_{eff}(E)$ is expressed as,[33,35]

$$\beta_{eff}(E) = \beta^{(0)} + \gamma E_m \qquad \text{Eq. 12}$$

where, $\beta^{(0)}$ is the first-order hyperpolarizability in the absence of a static electric field (i.e. β only due to laser beam) and γ is the second-order hyperpolarizability. For simplicity, let $E_1 = 0$ and by substituting Eq. 12 in Eq. 11, $\Delta S/S$ is represented as,[33]

$$\frac{\Delta S}{S} = 2\frac{\gamma E_2}{\beta^{(0)}} + \left(\frac{\gamma E_2}{\beta^{(0)}}\right)^2 \qquad \text{Eq. 13}$$

Eq. 13 shows that SHG-based voltage sensitivity is proportional to the second-order hyperpolarizability γ.[33]

It must be noted that a good SHG signal can be observed only if the SHG response of the dye is significantly higher than the background SHG response of the tissues (intracellular or extracellular regions of the specimen under study), which can themselves have significant bulk hyperpolarizabilities.[36,122]

1.4.1 SHG-based voltage-sensitive dyes

Loew and coworkers first reported (in the year 1993) that SHG can be used to measure membrane potential by testing the SHG-based voltage sensitivities of styryl-based dyes, such as **di-4-ANEPPS** and **JPW1290** (Figure 15) in hemispherical bilayers.[140] They further extended the use of **JPW1290** to probe membrane potential of photoreceptor cells (photoreceptor cells develop self-membrane potential on excitation with light) of white eyed Musca flies.[120] They recorded SHG-based voltage sensitivity, $\Delta S/S$ up to 30%.

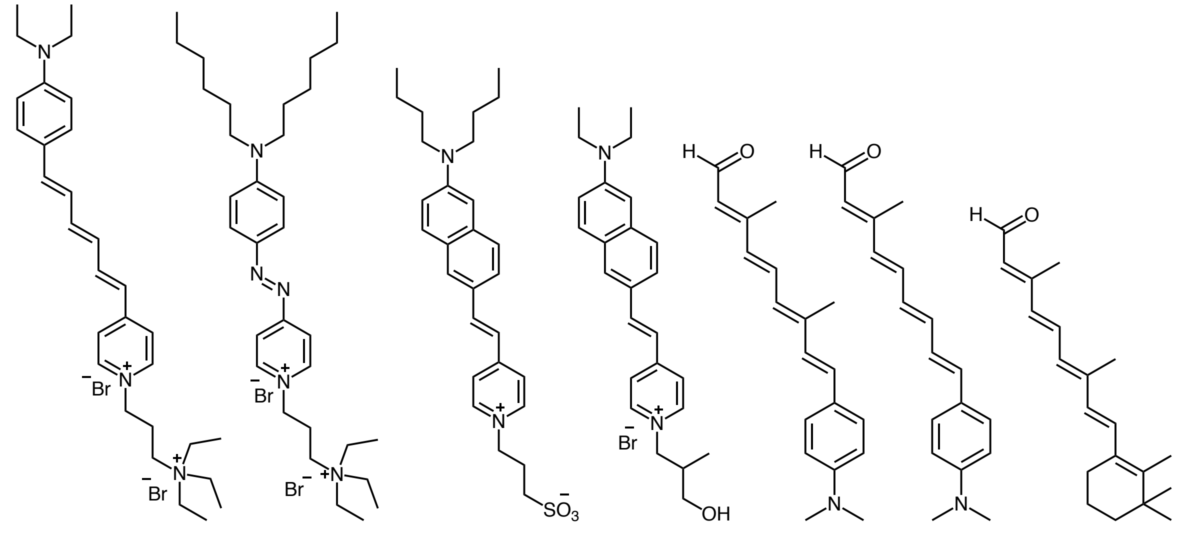

Figure 15: Chemical structures of SHG-based voltage sensitive dyes, **FM4-64**, **Ap3**, **di-4-ANEPPS**, **JPW1290**, **AR4**, **AR3**, and **ATR**.

Since the work of Loew and coworkers, a number of styryl-based dyes have been shown to record membrane potential in lipid bilayers and live cells by SHG.[13,33,34,36,112,141–144] Loew and coworkers further studied the SHG-based voltage sensitivity of **di-4-ANEPPS** in live cells by patch clamping the cells.[13] Whole-cell patch-clamp is a reliable technique to test voltage sensitivity of a dye in live cells because the input voltage in the cell membrane can be controlled and thus can be mapped against the optical readout of the dye. I used the whole-cell patch-clamp technique to test voltage sensitivities of **di-4-ANEPPS** and a styryl-based dye, **FM4-64** in live HEK 293T cells as discussed in Chapter 4. Dombeck *et al.* tested the voltage sensitivity **FM4-64** (Figure 15) in both cultured neuronal cells and neurons in rat brain slices by using patch-clamp technique.[36,112] They compared both fluorescence and SHG –based voltage sensitivities of **FM4-64** with **ANNINE-6**, an electrochromic voltage-sensitive dye (Figure 8) in cultured neurons. As expected, the fluorescence-based voltage sensitivity of **ANNINE-6** was 40 times higher than that of **FM4-64**; however, the SHG-based voltage sensitivities of both the dyes were found to be similar. Moreover, in neurons of rat brain slices, **FM4-64** gave very low fluorescence-based voltage sensitivity with $\Delta F/F$ less than 0.5% per 100 mV but decent SHG-based voltage sensitivity, $\Delta S/S$ at 7.5% per 100 mV with sub-millisecond temporal resolution. Although, **ANNINE-6** gave good SHG-based voltage sensitivity in cultured neurons; surprisingly, in neurons of brain slices, **ANNINE-6** did not localize in the plasma membrane, for which no explanation was given by the authors. It must be noted that **FM4-64** is a dicationic dye while, **ANNINE-6** is a sulfonate-based zwitterionic dye. In Chapter 3 of this DPhil thesis, I describe the effects of various hydrophilic head-groups in plasma membrane localization of live cells and reach a conclusion that sulfonate-based dyes are not very effective in plasma membrane localization as are the dicationic dyes. Theer *et al.* compared the SHG-based voltage sensitivity of **FM4-64** with retinal dyes and found that the retinal dyes (Figure 15) exhibit better voltage sensitivity than **FM4-64**.[35] The retinal dyes, all-*trans* retinal (**ATR**), 3-methyl-7-(4′-dimethylamino-phenyl)-2,4,6-heptatrienal (**AR3**), and 3,7-dimethyl-9-(4′-dimethylamino-phenyl)-2,4,6,8-nonatetraenal (**AR4**) (Figure 15) reported almost two times better voltage sensitivity than **FM4-64** along with better temporal resolution (~20 μs for **AR3** and **AR4**, 1 ms for **ATR** and 1.6 ms for **FM4-64**).[35] Although the retinal dyes have higher voltage sensitivity than **FM4-64**, the *SNR* of **FM4-64** was found to be higher (~2 for **ATR** and **AR3**, ~4 for **AR4** and ~5 for **FM4-64**) because the retinal dyes do not generate as much SHG light as **FM4-64** (Eq. 1). Jiang *et al.* reported a temporal resolution of sub-millisecond timescale for **FM4-64** in mice brain slices with a voltage sensitivity of 10.3% per 100 mV.[142] The voltage sensitivity and temporal resolution data reported by the different authors vary among themselves due to several factors. Apart from giving SHG, **FM4-64** is also a non-photostable fluorescent dye (fluorescence quantum yield in chloroform is 35%)[145] that photobleaches when excited by intense light from a femtosecond pulsed-laser. Photobleaching causes the dye to degrade and hence, the overall $\beta_{eff}(E)$ of the dye changes causing inconsistencies in the reported voltage sensitivity data. Nuriya *et al.* developed a photostable azo-based dye, **Ap3** (Figure 15), which has a negligible fluorescence quantum yield and works as an SHG only dye.[34] They recorded voltage sensitivity of 4% per 100 mV for **Ap3**, and 8% per 100 mV for **FM4-64** in mice neurons. It is shown in Eq. 13, that the SHG-based voltage-sensitivity depends on first-order and second-order hyperpolarizabilities of a dye, β and γ respectively, apart from the strength of electric field applied. Both the first-order and second-order hyperpolarizabilities are wavelength and media dependent. The imaging conditions and wavelength of the excitation light were different in the studies discussed above and hence, it is not surprising that they get different values for voltage sensitivity and temporal resolution. Apart from the experimental conditions, the signal-to-noise ratio, voltage sensitivity, and temporal resolution of the dye are also dependent on the experimental procedures. Dombeck *et al.* found that from a single imaging trial, the *SNR* of **FM4-64** is 1. They averaged signals from as many as 50 imaging trials to achieve higher signal-to-noise ratio.[12] Similarly, all the other studies reported the voltage sensitivity and *SNR* data after averaging the signals from at least 30 imaging trials. Different studies use different imaging methods, such as line scan, full-frame scan of the cell, and point scan at different conditions, which give different values for *SNR*, voltage sensitivity, and temporal resolution.

Anderson and coworkers synthesized a new donor-acceptor–based voltage-sensitive dye, **JR1** with increased π-conjugation compared to the existing styryl-based SHG dyes.[33,116] Molecules with enhanced π-conjugation have high second-order hyperpolarizability, γ and thus they should give better SHG-based voltage sensitivity (Eq. 13).[33,146,147] A porphyrin molecule was used as the π-conjugated linker between the donor and acceptor moieties because of its inherent enhanced first-order and second-order hyperpolarizabilities.[148,149] The new donor-acceptor–based porphyrin dye, **JR1** gave 5–10 times higher electro-optic SHG response than styryl-based SHG dyes, such as **FM4-64**, **di-4-ANEPPS**, and **RH237** (Figure 16) in hemispherical lipid bilayers.[33]

Molecular design of JR1

Electron-donor moiety

Dioctyl aniline is used as the electron-donor group for two major reasons: (1) Aniline acts as a strong electron-donor group and has been used to design various voltage-sensitive dyes as discussed in this chapter, and (2) The long octyl chains provide robust binding at the lipids bilayer of the plasma membrane and will cause a reduced tendency to be washed out.[150,151] However, the drawback of long alkyl chains is that they decrease the solubility of dyes in aqueous solutions, and make staining much slower. Molecules such as pluronic F-127 and cyclodextrin can be used to enhance the aqueous solubility of the dye; however, there have also been reports suggesting that these surfactants interfere with the intrinsic properties of cells.[152–155]

Electron-acceptor group

Pyridinium is used as the electron-acceptor moiety because it has been one of the most favored electron-acceptor groups to design voltage-sensitive dyes due to two main reasons: (1) It can act as both electron-acceptor and water-solubilizing group because of which the transition dipole moment (TDM) of the dye will be coaxial with its amphiphilic orientation axis. Collinearity of the TDM and the orientation axis will ensure brighter optical response,[137,138] (2) A wide range of solubilizing groups such as monocations, dications, and sulfonates can be attached to the dye *via* the pyridinium moiety.

Porphyrin group

A porphyrin molecule is used as the π-conjugated linker between the electron-donor and the acceptor moieties. Donor-porphyrin-acceptor dyes possess higher second-order hyperpolarizability (γ) than styryl-based dyes, such as **FM4-64** and **di-4-ANEPPS** and hence, they exhibit higher voltage sensitivity. Moreover, these dyes generate brighter SHG signals due to their high first-order hyperpolarizability, β because of which they give increased *SNR*.[116,148]

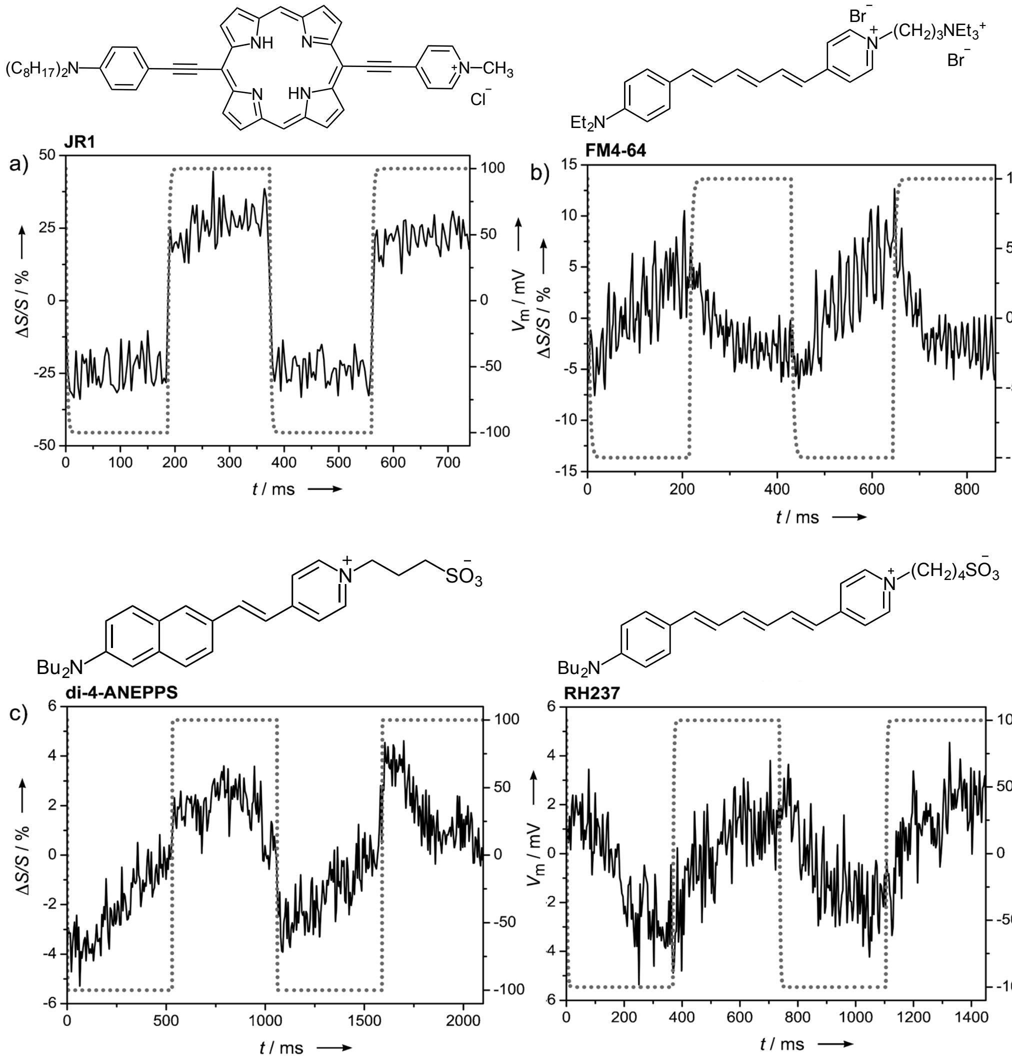

Figure 16: Change in SHG intensity caused by an alternating transmembrane potential of V_m = ±100 mV (dotted curve) for a) **JR1**, b) **FM4-64**, c) **di-4-ANEPPS**, and d) **RH237** in hemispherical bilayers. Traces (b)–(d) are averages over 4, 3, and 4 experiments, respectively.[33] It can be seen that **JR1** gives better sensitivity on application of ±100 mV voltage than the other three dyes. *ΔS/S* represents the SHG-based voltage sensitivity of the dye; V_m represents the applied voltage and *t* represents time in milliseconds. λ_{ext} = 850 nm at 90 mW laser power. Image adapted with permission from *Angew. Chem. Int. Ed.*, 2013, **52**, 9044–9048. Copyright 2013 The Authors. Published by Wiley-VCH Verlag GmbH & Co. KGaA.

The small molecule-based dyes, as discussed above give good SHG-based voltage sensitivity and temporal resolution. Although these dyes cannot be used for *in vivo* experiments (because SHG is detected mostly only in forward direction), they could be useful for neurobiological studies in cells *in vitro* and *ex vivo*. *In vitro* delivery of the dyes in cells can be achieved by direct staining i.e. by dissolving the dye in the cell media; however, the delivery in cells *ex vivo* remains a challenge. Dissolving the dye in media for *ex vivo* delivery has not been able to generate SHG signals because in *ex vivo* tissue slices, there exist multiple blood vessels, tissue structures, dead cellular structures, lipid-based water bubbles etc. along with the cells. Apart from staining the cells, the dyes also stain all the non-cellular structures and hence it generates a lot of background signal or no SHG signal at all (causing an effect of centrosymmetric arrangement). Dombeck *et al.* delivered **FM4-64** in neurons in rat brain slices by intracellular injection i.e. delivering dye to one cell at a time.[36] Such a delivery method does not serve any purpose because the whole point of using optical techniques over the patch-clamp technique is to be able to study multiple neurons simultaneously, for which the dye must stain multiple neurons simultaneously. Genetically encoded SHG-based voltage sensors could be useful for *ex vivo* studies; however, to date no such voltage-sensitive sensor has been reported. Jinno *et al.* developed a genetically encoded SHG-based chromophore, **mVe9Knus-CVIM**, which could be targeted to specific cells anisotropically.[156] The chromophore exhibited SHG in HEK293 cells, however, the authors concluded that the dye does not give voltage dependent signals. Clays and coworkers have previously determined the values of first-order hyperpolarizability β, for light-sensitive protein, bacteriorhodopsin through hyper-Rayleigh scattering technique; however, they have not reported SHG or SHG-based voltage sensitivity results for these proteins.[136,157,158]

The good voltage sensitivity and temporal resolution of **JR1** in comparison to other styryl-based dyes, make porphyrin-based dyes promising candidates for measuring membrane potential of neurons. A highly sensitive and fast SHG-based dye will help elucidate information about neuronal communication, which have not been possible with the existing fluorescent dyes. Although, **JR1** gives good voltage sensitivity in hemispherical lipid bilayers, it does not localize in the plasma membrane of live cells. Plasma membrane localization of porphyrin-based dyes has been a major issue for testing the dyes in live cells and for further research.

Table 1 gives an overview about the prospects and consequences of the different types of voltage-sensitive dyes discussed above. Barring *in vivo* imaging, SHG-based dyes addresses all the challenges faced by the different classes of fluorescence-based dyes.

Table 1: Overview of different classes of optical voltage-sensitive dyes.

	Voltage sensitivity	**Temporal resolution**	**Background signal**	**Phototoxicity**
Calcium indicators	Good	Poor	High	High
Electrochromic dyes	Good	Very good	Moderate/High	Moderate/High
FRET dyes	Good	Moderate	Moderate/High	Moderate/High
PeT dyes	Good	Very good	Moderate/High	Moderate/High
SHG dyes	Very good	Very good	None	Moderate/Low

1.50 Multiphoton microscope

Advances in microscopy techniques have enabled the efficient use of SHG technique. SHG is considered analogous to two-photon excited fluorescence (TPEF) because both the techniques involve the use of intense laser light from a femtosecond-pulsed laser. Both TPEF and SHG techniques can be used for deep imaging of tissues (up to several millimeters depending on the focusing objective) and cause less photodamage than one-photon microscopy because they employ longer wavelength light (>700 nm). Since, both the techniques require the sample under study to be irradiated with two photons of same energy almost simultaneously, the probability of such an event is so low that it occurs only at the focal point because of which these techniques do not give out of focus background signal and do not cause out of focus photobleaching.[149,159] Figure 17 represents the schematic of the microscope that I used during my DPhil research to study TPEF and SHG efficiency of various porphyrin-based dyes in lipid-based systems and live cells. Inspired from the highly voltage-sensitive porphyrin-based dye, **JR1**, in my DPhil thesis, I embarked on designing, synthesizing, and testing other porphyrin-based dyes that will be able to measure membrane potential of neurons.

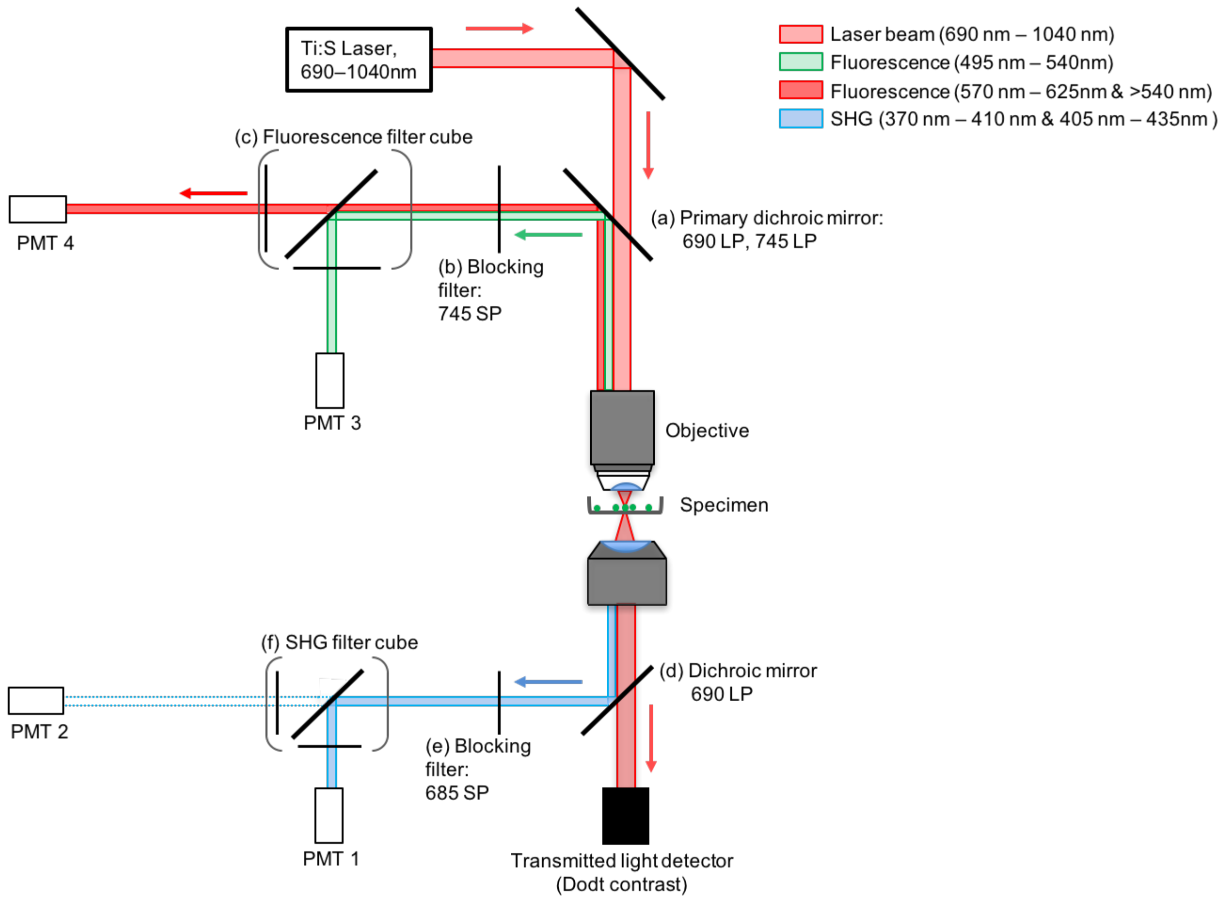

Figure 17: Schematic of laser, fluorescence, and SHG light paths of the multiphoton microscope used in my DPhil study.

1.51 Summary of my work

In Chapter 2, I discuss the synthesis and study of linear and nonlinear photophysical properties of a new class of donor-acceptor–based pyropheophorbide dyes. In Chapter 3, I discuss the plasma membrane localization of more than ten types of porphyrin-based dyes (synthesized by previous students in the Anderson group) in three different types of live cells and comment on their plasma membrane localization efficiency. In Chapter 4, I demonstrate the design and testing of a whole-cell patch-clamp system integrated with the multiphoton microscope to test the fluorescence and SHG –based voltage sensitivities of the dyes. In Chapter 5, I discuss the design, synthesis, and characterization of a new porphyrin-based dye that efficiently localizes at the plasma membrane of live cells. I also tested the SHG-based voltage-sensitivity of the dye in contracting neonatal myocytes. Finally, in Chapter 6, I present the two-photon microscopy of 3D tumor models to visualize their structure. The work on 3D tumor models is performed in collaboration with the Haygen Bayley group at the Department of Chemistry, University of Oxford.

1.60 References

1 S. Herculano-Houzel, *Front. Hum. Neurosci.*, 2009, **3**.
2 R. Yuste, *Nat. Rev. Neurosci.*, 2015, **16**, 487–497.
3 S. R. y Cajal, *Rev. Trim. Hist. Norm. Pat.*, 1888, **1**, 1–10.
4 C. S. Sherrington, *J. Physiol.*, 1906, **34**, 1–50.
5 C. Matteucci, *Ann. Chim. Phys. III*, 1842, **6**, 301–339.
6 B. P. Bean, *Nat. Rev. Neurosci.*, 2007, **8**, 451–465.
7 E. Neher and B. Sakmann, *Nature*, 1976, **260**, 799–802.
8 O. Shimomura, F. H. Johnson and Y. Saiga, *Science*, 1963, **140**, 1339–1340.
9 R. Y. Tsien, *Biochemistry*, 1980, **19**, 2396–2404.
10 F. Conti, *Annu. Rev. Biophys. Bioeng.*, 1975, **4**, 287–310.
11 M. S. Siegel and E. Y. Isacoff, *Neuron*, 1997, **19**, 735–741.
12 D. A. Dombeck, M. Blanchard-Desce and W. W. Webb, *J. Neurosci.*, 2004, **24**, 999–1003.
13 A. C. Millard, L. Jin, A. Lewis and L. M. Loew, *Opt. Lett.*, 2003, **28**, 1221–1223.
14 A. L. Hodgkin, *J. Physiol.*, 1976, **263**, 1–21.
15 G. T. Dickinson, *Can. Med. Assoc. J.*, 1963, **89**, 998–999.
16 A. Molleman, *Patch Clamping: An Introductory Guide to Patch Clamp Electrophysiology. 2003*, John Wiley & Sons, Ltd, 2003.
17 T. W. Margrie, A. H. Meyer, A. Caputi, H. Monyer, M. T. Hasan, A. T. Schaefer, W. Denk and M. Brecht, *Neuron*, 2003, **39**, 911–918.
18 J. V. Halliwell, M. J. Whitaker and D. Ogden, *Microelectrode Techniques - The Plymouth Workshop Handbook*, The Company of Biologists Limited, Cambridge, 2nd edn., 1994.
19 M. M. Churchland, B. M. Yu, M. Sahani and K. V. Shenoy, *Curr. Opin. Neurobiol.*, 2007, **17**, 609–618.
20 T.-M. Fu, G. Hong, T. Zhou, T. G. Schuhmann, R. D. Viveros and C. M. Lieber, *Nat. Methods*, 2016, **13**, 875–882.
21 X. Dai, W. Zhou, T. Gao, J. Liu and C. M. Lieber, *Nat. Nanotechnol.*, 2016, **11**, 776–782.
22 D. Ogden and P. Stanfield, *Microelectrode Techniques - The Plymouth Workshop Handbook*, The Company of Biologists Limited, Cambridge, 2nd edn., 1994.
23 W.-C. Li, S. R. Soffe and A. Roberts, *J. Neurophysiol.*, 2004, **92**, 380–386.
24 M. Meister, J. Pine and D. A. Baylor, *J. Neurosci. Methods*, 1994, **51**, 95–106.
25 M. A. L. Nicolelis, D. Dimitrov, J. M. Carmena, R. Crist, G. Lehew, J. D. Kralik and S. P. Wise, *Proc. Natl. Acad. Sci.*, 2003, **100**, 11041–11046.
26 E V Mosharov and D. Sulzer, *Nat Meth*, 2005, **2**, 651–658.
27 J. L. Peters, L. H. Miner, A. C. Michael and S. R. Sesack, *J. Neurosci. Methods*, 2004, **137**, 9–23.
28 D. J. Bakkum, U. Frey, M. Radivojevic, T. L. Russell, J. Müller, M. Fiscella, H. Takahashi and A. Hierlemann, *Nat. Commun.*, 2013, **4**, 2181.
29 T. Zhou, G. Hong, T.-M. Fu, X. Yang, T. G. Schuhmann, R. D. Viveros and C. M. Lieber, *Proc. Natl. Acad. Sci.*, 2017, **114**, 5894–5899.
30 M. Zochowski, M. Wachowiak, C. X. Falk, L. B. Cohen, Y. W. Lam, S. Antic and D. Zecevic, *Biol. Bull.*, 2000, **198**, 1–21.
31 L. B. Cohen, in *Membrane Potential Imaging in the Nervous System Methods and Applications*, eds. M. Canepari and D. Zecevic, Springer, 2010, pp. 1–12.
32 D. S. Peterka, H. Takahashi and R. Yuste, *Neuron*, 2011, **69**, 9–21.
33 J. E. Reeve, A. D. Corbett, I. Boczarow, W. Kaluza, W. Barford, H. Bayley, T. Wilson

and H. L. Anderson, *Angew. Chem. Int. Ed.*, 2013, **52**, 9044–9048.
34 M. Nuriya, S. Fukushima, A. Momotake, T. Shinotsuka, M. Yasui and T. Arai, *Nat. Commun.*, 2016, **7**.
35 P. Theer, W. Denk, M. Sheves, A. Lewis and P. B. Detwiler, *Biophys. J.*, 2011, **100**, 232–242.
36 D. A. Dombeck, L. Sacconi, M. Blanchard-Desce and W. W. Webb, *J. Neurophysiol.*, 2005, **94**, 3628–3636.
37 M. Canepari, D. Zecevic and O. Bernus, *Membrane potential imaging in the nervous system and heart*, Springer, 2015.
38 C. R. Woodford, E. P. Frady, R. S. Smith, B. Morey, G. Canzi, S. F. Palida, R. C. Araneda, W. B. Kristan, C. P. Kubiak, E. W. Miller and R. Y. Tsien, *J. Am. Chem. Soc.*, 2015, **137**, 1817–1824.
39 L. M. Loew, S. Scully, L. Simpson and A. S. Waggoner, *Nature*, 1979, **281**, 497–499.
40 A. Waggoner, *J. Membr. Biol.*, 1976, **27**, 317–334.
41 D. R. Hochbaum, Y. Zhao, S. L. Farhi, N. Klapoetke, C. A. Werley, V. Kapoor, P. Zou, J. M. Kralj, D. Maclaurin, N. Smedemark-Margulies, J. L. Saulnier, G. L. Boulting, C. Straub, Y. K. Cho, M. Melkonian, G. K.-S. Wong, D. J. Harrison, V. N. Murthy, B. L. Sabatini, E. S. Boyden, R. E. Campbell and A. E. Cohen, *Nat. Methods*, 2014, **11**, 825–833.
42 L. B. Cohen, B. M. Salzberg, H. V Davila, W. N. Ross, D. Landowne, A. S. Waggoner and C. H. Wang, *J. Membr. Biol.*, 1974, **19**, 1–36.
43 S. M. Baylor, in *Comprehensive Physiology*, John Wiley & Sons, Inc., 2010.
44 Y. Gong, M. J. Wagner, J. Zhong Li and M. J. Schnitzer, *Nat. Commun.*, 2014, **5**.
45 L. M. Loew, *J. Biochem. Biophys. Methods*, 1982, **6**, 243–260.
46 R. Y. Tsien, T. Pozzan and T. J. Rink, *J. Cell Biol.*, 1982, **94**, 325–334.
47 A. Minta, J. P. Y. Kao and R. Y. Tsien, *J. Biol. Chem.*, 1989, **264**, 8171–8178.
48 R. Rudolf, M. Mongillo, R. Rizzuto and T. Pozzan, *Nat. Rev. Mol. Cell Biol.*, 2003, **4**, 579–586.
49 D. Smetters, A. Majewska and R. Yuste, *Methods*, 1999, **18**, 215–221.
50 R. Yuste and W. Denk, *Nature*, 1995, **375**, 682–684.
51 A. Miyawaki, J. Llopis, R. Heim, J. M. McCaffery, J. A. Adams, M. Ikura and R. Y. Tsien, *Nature*, 1997, **388**, 882–887.
52 C. Grienberger and A. Konnerth, *Neuron*, 2012, **73**, 862–885.
53 T. D. Plant, N. B. Standen and T. A. Ward, *J. Physiol.*, 1983, **334**, 189–212.
54 Y. Yamada, T. Michikawa, M. Hashimoto, K. Horikawa, T. Nagai, A. Miyawaki, M. Häusser and K. Mikoshiba, *Front. Cell. Neurosci.*, 2011, **5**, 18.
55 H. H. Yang and F. St-Pierre, *J. Neurosci.*, 2016, **36**, 9977–9989.
56 I. Tasaki, A. Watanabe, R. Sandlin and L. Carnay, *Proc. Natl. Acad. Sci. U. S. A.*, 1968, **61**, 883–888.
57 P. Wahl, M. Kasai and J. Changeux, *Eur. J. Biochem.*, 1971, **18**, 332–341.
58 W. N. Ross, B. M. Salzberg, L. B. Cohen and H. V Davila, *Biophys. J.*, 1974, **14**, 983–986.
59 H. V Davila, L. B. Cohen, B. M. Salzberg and B. B. Shrivastav, *J. Membr. Biol.*, 1974, **15**, 29–46.
60 J. R. Platt, *J. Chem. Phys.*, 1956, **25**, 80–105.
61 J. R. Platt, *J. Chem. Phys.*, 1961, **34**, 862–863.
62 W. Liptay, *Angew. Chem. Int. Ed. Eng.*, 1969, **8**, 177–188.
63 H. Bücher, J. Wiegand, B. B. Snavely, K. H. Beck and H. Kuhn, *Chem. Phys. Lett.*, 1969, **3**, 508–511.
64 B. Chance, M. Baltscheffksy, J. Vanderkooi and W. Cheng, in *Perspectives in*

Membrane Biology, Elsevier, 1974, pp. 329–369.
65 R. Reich and S. Schmidt, *Berichte der Bunsengesellschaft für Phys. Chemie*, 1972, **76**, 589–598.
66 L. M. Loew and L. L. Simpson, *Biophys. J.*, 1981, **34**, 353–365.
67 L. M. Loew, G. W. Bonneville and J. Surow, *Biochemistry*, 1978, **17**, 4065–4071.
68 T. M. Inerbaev, S. Saito, R. V. Belosludov, H. Mizuseki, M. Takahashi and Y. Kawazoe, *J. Chem. Phys.*, 2006, **125**, 234702–234709.
69 W. Liptay, *Zeitschrift für Naturforsch. A*, 1956, **20**, 1441–1471.
70 G. Hübener, A. Lambacher and P. Fromherz, *J. Phys. Chem. B*, 2003, **107**, 7896–7902.
71 C. Xu and L. M. Loew, *Biophys. J.*, 2003, **84**, 2768–2780.
72 M. Przybylo, T. Borowik and M. Langner, *J. Fluoresc.*, 2010, **20**, 1139–1157.
73 A. Grinvald, A. Fine, I. C. Farber and R. Hildesheim, *Biophys. J.*, 1983, **42**, 195–198.
74 A. Grinvald, R. Hildesheim, I. C. Farber and L. Anglister, *Biophys. J.*, 1982, **39**, 301–308.
75 A. Hassner, D. Birnbaum and L. M. Loew, *J. Org. Chem.*, 1984, **49**, 2546–2551.
76 E. Fluhler, V. G. Burnham and L. M. Loew, *Biochemistry*, 1985, **24**, 5749–5755.
77 L. M. Loew, L. B. Cohen, J. Dix, E. N. Fluhler, V. Montana, G. Salama and W. Jianyoung, *J. Membr. Biol.*, 1992, **130**, 1–10.
78 S. Preuss and W. Stein, *PLoS One*, 2013, **8**, e75678.
79 P. Yan, C. D. Acker, W.-L. Zhou, P. Lee, C. Bollensdorff, A. Negrean, J. Lotti, L. Sacconi, S. D. Antic, P. Kohl, H. D. Mansvelder, F. S. Pavone and L. M. Loew, *Proc. Natl. Acad. Sci.*, 2012, **109**, 20443–20448.
80 B. Kuhn and P. Fromherz, *J. Phys. Chem. B*, 2003, **107**, 7903–7913.
81 G. Hübener, A. Lambacher and P. Fromherz, *J. Phys. Chem. B*, 2003, **107**, 7896–7902.
82 P. Fromherz, G. Hübener, B. Kuhn and M. J. Hinner, *Eur. Biophys. J.*, 2008, **37**, 509–514.
83 L. Jin, A. C. Millard, J. P. Wuskell, X. Dong, D. Wu, H. A. Clark and L. M. Loew, *Biophys. J.*, 2006, **90**, 2563–2575.
84 G. Parisio, A. Marini, A. Biancardi, A. Ferrarini and B. Mennucci, *J. Phys. Chem. B*, 2011, **115**, 9980–9989.
85 E. Sezgin, F. Schneider, V. Zilles, I. Urbančič, E. Garcia, D. Waithe, A. S. Klymchenko and C. Eggeling, *Biophys. J.*, 2017, **7**, 24–35.
86 T. Förster, *Ann. Phys.*, 1948, **437**, 55–75.
87 J. E. González and R. Y. Tsien, *Biophys. J.*, 1995, **69**, 1272–1280.
88 K. F. Wong, B. Bagchi and P. J. Rossky, *J. Phys. Chem. A*, 2004, **108**, 5752–5763.
89 P. G. Wu and L. Brand, *Anal. Biochem.*, 1994, **218**, 1–13.
90 J. E. González, K. Oades, Y. Leychkis, A. Harootunian and P. A. Negulescu, *Drug Discov. Today*, 1999, **4**, 431–439.
91 J. E. González and M. P. Maher, *Recept. Channels*, 2002, **8**, 283–295.
92 B. Chanda, R. Blunck, L. C. Faria, F. E. Schweizer, I. Mody and F. Bezanilla, *Nat. Neurosci.*, 2005, **8**, 1619–1626.
93 L. Li, *Nano Lett.*, 2007, **7**, 2981–2986.
94 E. W. Miller, J. Y. Lin, E. P. Frady, P. A. Steinbach, W. B. Kristan and R. Y. Tsien, *Proc. Natl. Acad. Sci.*, 2012, **109**, 2114–2119.
95 Y. L. Huang, A. S. Walker and E. W. Miller, *J. Am. Chem. Soc.*, 2015, **137**, 10767–10776.
96 V. Grenier, A. S. Walker and E. W. Miller, *J. Am. Chem. Soc.*, 2015, **137**, 10894–10897.
97 P. E. Deal, R. U. Kulkarni, S. H. Al-Abdullatif and E. W. Miller, *J. Am. Chem. Soc.*, 2016, **138**, 9085–9088.

98 R. U. Kulkarni, H. Yin, N. Pourmandi, F. James, M. M. Adil, D. V Schaffer, Y. Wang and E. W. Miller, *ACS Chem. Biol.*, 2017, **12**, 407–413.
99 R. U. Kulkarni, D. J. Kramer, N. Pourmandi, K. Karbasi, H. S. Bateup and E. W. Miller, *Proc. Natl. Acad. Sci. U. S. A.*, 2017, **114**, 2813–2818.
100 W. B. Davis, W. A. Svec, M. A. Ratner and M. R. Wasielewski, *Nature*, 1998, **396**, 60–63.
101 Y. Murata, H. Iwasaki, M. Sasaki, K. Inaba and Y. Okamura, *Nature*, 2005, **435**, 1239–43.
102 M. S. Siegel and E. Y. Isacoff, *Neuron*, 1997, **19**, 735–741.
103 J. M. Kralj, A. D. Douglass, D. R. Hochbaum, D. Maclaurin and A. E. Cohen, *Nat Meth*, 2012, **9**, 90–95.
104 J. M. Kralj, D. R. Hochbaum, A. D. Douglass and A. E. Cohen, *Science.*, 2011, **333**, 345–348.
105 Y. Gong, C. Huang, J. Z. Li, B. F. Grewe, Y. Zhang, S. Eismann and M. J. Schnitzer, *Science.*, 2015, **350**, 1361–1366.
106 T. Knöpfel, J. Díez-García and W. Akemann, *Trends Neurosci.*, 2015, **29**, 160–166.
107 H. Mutoh, W. Akemann and T. Knöpfel, *ACS Chem. Neurosci.*, 2012, **3**, 585–592.
108 F. St-Pierre, M. Chavarha and M. Z. Lin, *Curr. Opin. Chem. Biol.*, 2015, **27**, 31–38.
109 J. R. Lakowicz, *Principles of Fluorescence Spectroscopy*, Springer, 3rd edn., 2007.
110 D. R. Kearns, *Chem. Rev.*, 1971, **71**, 395–427.
111 A. Diaspro, G. Chirico, C. Usai, P. Ramoino and J. Dobrucki, in *Handbook of Biological Confocal Microscopy*, 2006, pp. 690–702.
112 L. Sacconi, D. A. Dombeck and W. W. Webb, *Proc. Natl. Acad. Sci.*, 2006, **103**, 3124–3129.
113 B. F. Godley, F. a Shamsi, F.-Q. Q. Liang, S. G. Jarrett, S. Davies and M. Boulton, *J. Biol. Chem.*, 2005, **280**, 21061–21066.
114 J. Liebmann, M. Born and V. Kolb-Bachofen, *J. Invest. Dermatol.*, 2010, **130**, 259–269.
115 K. R. Byrnes, R. W. Waynant, I. K. Ilev, X. Wu, L. Barna, K. Smith, R. Heckert, H. Gerst and J. J. Anders, *Lasers Surg. Med.*, 2005, **36**, 171–185.
116 J. E. Reeve, H. A. Collins, K. De Mey, M. M. Kohl, K. J. Thorley, O. Paulsen, K. Clays and H. L. Anderson, *J. Am. Chem. Soc.*, 2009, **131**, 2758–2759.
117 J. E. Reeve, H. L. Anderson and K. Clays, *Phys. Chem. Chem. Phys.*, 2010, **12**, 13484–13498.
118 Y. R. Shen, *Nature*, 1989, **337**, 519–525.
119 J. Y. Huang, A. Lewis and L. Loew, *Biophys. J.*, 1988, **53**, 665–670.
120 I. Benoren, G. Peleg, A. Lewis, B. Minke and L. Loew, *Biophys. J.*, 1996, **71**, 1616–1620.
121 P. A. Franken, A. E. Hill, C. W. Peters and G. Weinreich, *Phys. Rev. Lett.*, 1961, **7**, 118–119.
122 P. J. Campagnola, M. D. Wei, A. Lewis and L. M. Loew, *Biophys. J.*, 1999, **77**, 3341–3349.
123 L. Sacconi, M. D'Amico, F. Vanzi, T. Biagiotti, R. Antolini, M. Olivotto and F. S. Pavone, *J. Biomed. Opt.*, 2005, **10**, 024014–024021.
124 J. Zeng, M. Yuan, W. Yuan, Q. Dai, H. Fan, S. Lan and S. Tie, *Nanoscale*, 2015, **7**, 13547–13553.
125 A. Khadria, Y. de Coene, P. Gawel, C. Roche, K. Clays and H. L. Anderson, *Org. Biomol. Chem.*, 2017, **15**, 947–956.
126 T. F. Heinz and G. A. Reider, *Trends Anal. Chem.*, 1989, **8**, 235–242.
127 P. J. Campagnola and C.-Y. Dong, *Laser Photon. Rev.*, 2011, **5**, 13–26.

128 S. Awasthi, L. T. Izu, Z. Mao, Z. Jian, T. Landas, A. Lerner, R. Shimkunas, R. Woldeyesus, J. Bossuyt, B. Wood, Y. J. Chen, D. L. Matthews, D. K. Lieu, N. Chiamvimonvat, K. S. Lam, Y. Chen-Izu and J. W. Chan, *Circ. Res.*, 2016, **118**, e19–e28.

129 H. Linnenbank, Y. Grynko, J. Forstner and S. Linden, *Light Sci Appl*, 2016, 5, e16013–e16019.

130 S. C. Kumar, G. K. Samanta and M. Ebrahim-Zadeh, *Opt. Express*, 2009, **17**, 13711–13726.

131 G. K. Samanta, S. C. Kumar and M. Ebrahim-Zadeh, *Opt. Lett.*, 2009, **34**, 1561–1563.

132 I. Arfaoui, V. Bermúdez, G. Bottari, C. De Nadai, J. P. Jalkanen, F. Kajzar, D. A. Leigh, M. Lubomska, S. M. Mendoza, J. Niziol, P. Rudolf and F. Zerbetto, *J. Phys. Chem. B*, 2006, **110**, 7648–7652.

133 I. Freund, M. Deutsch and A. Sprecher, *Biophys. J.*, 1986, **50**, 693–712.

134 X. Chen, O. Nadiarynkh, S. Plotnikov and P. J. Campagnola, *Nat. Protoc.*, 2012, **7**, 654–669.

135 P. J. Campagnola and L. M. Loew, *Nat. Biotechnol.*, 2003, **21**, 1356–1360.

136 K. Clays and A. Persoons, *Phys. Rev. Lett.*, 1991, **66**, 2980–2983.

137 A. Khadria, Y. De Coene, P. Gawel, C. Roche, K. Clays and H. L. Anderson, *Org. Biomol. Chem.*, 2017, **15**, 947–956.

138 J. E. Reeve, A. D. Corbett, I. Boczarow, T. Wilson, H. Bayley and H. L. Anderson, *Biophys. J.*, 2012, **103**, 907–917.

139 B. F. Levine and C. G. Bethea, *Appl. Phys. Lett.*, 1974, **24**, 445–447.

140 O. Bouevitch, A. Lewis, I. Pinevsky, J. P. Wuskell and L. M. Loew, *Biophys. J.*, 1993, **65**, 672–679.

141 A. C. Millard, L. Jin, M. Wei, J. P. Wuskell, A. Lewis and L. M. Loew, *Biophys. J.*, 2004, **86**, 1169–1176.

142 J. Jiang, K. B. Eisenthal and R. Yuste, *Biophys. J.*, 2007, **93**, L26–L28.

143 M. Nuriya, J. Jiang, B. Nemet, K. B. Eisenthal and R. Yuste, *Proc. Natl. Acad. Sci.*, 2005, **103**, 786–790.

144 J. Jiang and R. Yuste, *Microsc. Microanal.*, 2008, **14**, 526–531.

145 I. López-Duarte, P. Chairatana, Y. Wu, J. Pérez-Moreno, P. M. Bennett, J. E. Reeve, I. Boczarow, W. Kaluza, N. A. Hosny, S. D. Stranks, R. J. Nicholas, K. Clays, M. K. Kuimova and H. L. Anderson, *Org. Biomol. Chem.*, 2015, **13**, 3792–3802.

146 S. R. Marder, *Science.*, 1997, **276**, 1233–1236.

147 J. L. Bredas, C. Adant, P. Tackx, A. Persoons and B. M. Pierce, *Chem. Rev.*, 1994, **94**, 243–278.

148 S. M. LeCours, H.-W. Guan, S. G. DiMagno, C. H. Wang and M. J. Therien, *J. Am. Chem. Soc.*, 1996, **118**, 1497–1503.

149 M. Pawlicki, H. A. Collins, R. G. Denning and H. L. Anderson, *Angew. Chem. Int. Ed.*, 2009, **48**, 3244–3266.

150 W. J. Betz, F. Mao and C. B. Smith, *Curr. Opin. Neurobiol.*, 1996, **6**, 365–371.

151 L. M. Loew, in *Membrane Potential Imaging in the Nervous System and Heart*, eds. M. Canepari, D. Zecevic and O. Bernus, Springer, 2015.

152 Z. Lojewska and L. M. Loew, *BBA - Biomembr.*, 1987, **899**, 104–112.

153 J. P. Wuskell, D. Boudreau, M. De Wei, L. Jin, R. Engl, R. Chebolu, A. Bullen, K. D. Hoffacker, J. Kerimo, L. B. Cohen, M. R. Zochowski and L. M. Loew, *J. Neurosci. Methods*, 2006, **151**, 200–215.

154 J. J. Sutachan, J. V. Montoya G, F. Xu, D. Chen, T. J. J. Blanck and E. Recio-Pinto, *Brain Res.*, 2006, **1068**, 131–137.

155 M. Pytel, K. Mercik and J. W. Mozrzymas, *Br. J. Pharmacol.*, 2006, **148**, 413–422.

156 Y. Jinno, K. Shoda, E. Rial-Verde, R. Yuste, M. Atsushi and H. Tsutsui, *Front. Mol. Neurosci.*, 2014, **7**, 93.

157 K. Clays, E. Hendrickx, M. Triest, T. Verbiest, A. Persoons, C. Dehu and J. L. Brédas, *Science.*, 1993, **262**, 1419–1422.

158 Y. De Coene, S. Van Cleuvenbergen, N. Van Steerteghem, V. Baekelandt, T. Verbiest, C. Bartic and K. Clays, *J. Phys. Chem. C*, 2017, **121**, 6909–6915.

159 F. Helmchen and W. Denk, *Nat. Methods*, 2006, **2**, 932–940.

Chapter 2

Push-pull Pyropheophorbides for Nonlinear Optical Imaging[*]

---

[*] The work presented in this chapter has been published as a journal article: "Khadria *et al. Org. Biomol. Chem.*, 2017, **15**, 947-956". The article was designated as a *Hot article* by the reviewers and editors, and featured in the RSC blogs.

Summary: *Pyropheophorbide-a methyl ester (PPa-OMe) has been modified by attaching electron-donor and -acceptor groups to alter its linear and nonlinear optical properties. Regioselective bromination of the terminal vinyl position and Suzuki coupling were used to attach a 4-(N,N-diethylaminophenyl) electron-donor group. The electron-acceptor dicyanomethylene was attached at the cyclic ketone position through a Knoevenagel condensation. Four different derivatives of PPa-OMe, containing either electron-donor or electron-acceptor groups, or both, were converted to hydrophilic bis-TEG amides to generate a series of amphiphilic dyes. The absorption and emission properties of all the dyes were compared to a previously reported push-pull porphyrin-based dye and a commercial push-pull styryl dye, FM4-64. Electrochemical measurements reveal that the electron donor group causes a greater decrease in HOMO-LUMO gap than the electron-acceptor. TD-DFT calculations on optimized geometries (DFT) of all four dyes show that the HOMO is mostly localized on the donor, 4-(N,N-diethylaminophenyl), while the LUMO is distributed around the chlorin ring and the electron-acceptor. Hyper-Rayleigh scattering experiments show that the first-order hyperpolarizabilities of the dyes increase on attaching either electron-donor or -acceptor groups, having the highest value when both the donor and acceptor groups are attached. Two-photon excited fluorescence (TPEF) and second harmonic generation (SHG) images of the bis-TEG amide attached dyes in lipid monolayer-coated droplets of water-in-oil reveal that the TPEF and SHG involve transition dipole moments in different orientations.*

2.00 Introduction

Cellular imaging techniques based on nonlinear optical processes, such as two-photon excited fluorescence (TPEF) and second harmonic generation (SHG), are gaining prominence because they can probe deeper into the biological tissues, exhibit reduced out of focus fluorophore bleaching and generate less out of focus emitted and scattered light, compared to other optical microscopy techniques.[1–4] Both TPEF and SHG involve simultaneous interaction of two photons with the chromophore; hence, they require a high density of photons delivered by pulsed (typically sub-picosecond) focused laser beams. While TPEF is detected in all directions around the sample, SHG is mostly detected in the forward direction of the incident light. TPEF signals from individual dye molecules placed in any orientation add up, while the overall SHG signal from anti-parallel dyes cancels. The intensity of an SHG signal is dependent on the second-order polar tensor, χ^2 induced when a non-centrosymmetric molecule is placed in a non-centrosymmetric medium.[5–10] SHG is an ideal technique to image interfaces while avoiding background signals from isotropic regions. TPEF takes place *via* two-photon absorption (TPA) and requires population of real excited states, while SHG is a scattering effect that generates light of twice the incident frequency, only involving virtual states. Both TPA and SHG are enhanced when the electric field of the light is polarized in the direction of the transition dipole moment (TDM) of the molecule.[5,11] TPA and SHG have both been used to probe the electric potentials across cellular membranes.[12–17]

Porphyrins and related porphyrinoid chromophores, such as chlorins and bacteriochlorins find applications in various fields, such as photodynamic therapy (PDT), fluorescence microscopy, chemical sensing, and photovoltaics because they have excellent linear and nonlinear optical properties due to their large π-system, which can be engineered by various structural modifications.[3,18–23] TPA in porphyrin-related compounds has already been applied in PDT.[24,25] Previously, the Anderson group demonstrated that the TPA efficiency of porphyrin dimers could be significantly increased by attaching electron-donor and -acceptor groups.[26] The Anderson group found that apart from increased TPA cross-section, donor-acceptor–based porphyrins give a high SHG response.[4] One of the donor-acceptor free-base porphyrins, **JR1**, is highly voltage-sensitive in comparison to commercial dyes, such as **FM4-64**, **Di-4-ANEPPS**, and **RH237** (Figure 1), which makes it a good candidate to probe electrical potential differences across cellular membranes.[4,14] The Anderson group studied the effect of individual electron-donating and -accepting groups attached to porphyrin systems on SHG efficiency, and found that the free-base porphyrin core is substantially electron-deficient, making the electron-withdrawing group redundant.[8]

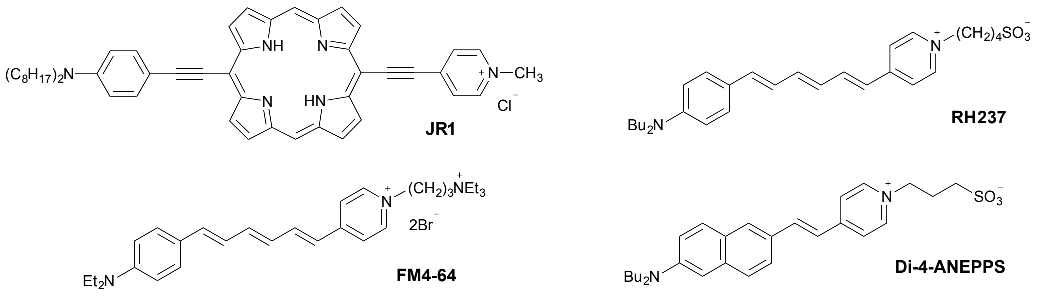

Figure 1: Molecular structures of voltage-sensitive dyes.[14]

It has been previously suggested that porphyrins substituted with phenyl rings at opposite *meso*-positions have ambivalent nature, i.e. they can behave both as an electron donor and an acceptor to create a push-pull effect when connected with either an acceptor or a donor group at *meso* or β-positions.[27,28] The orientations of SHG-based probes within biological membranes play crucial roles for an effective SHG response. For any dye to give maximum SHG or TPEF signal, its transition dipole moment (TDM) must be parallel to the polarization of the laser light exciting the dye. Various studies demonstrate different methods to determine the orientation of molecular probes, such as TPEF-based microscopy, solid-state NMR, fluorescence anisotropy, and SHG-based microscopy,[29–33] while the Anderson group utilized the optical anisotropy of dyes in lipid-based water-in-oil monolayers and bilayers.[11] In this study, I modified the structure of a chlorin molecule, pyropheophorbide-a methyl ester to enhance its linear and nonlinear optical properties.

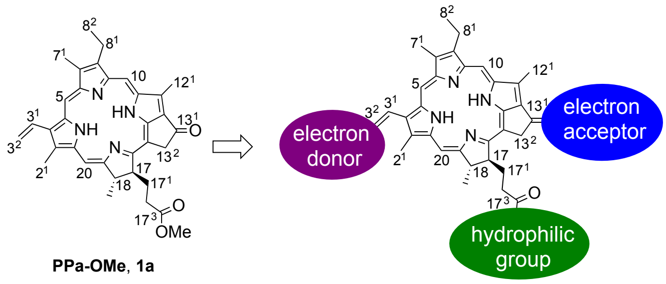

Figure 2: Modification of pyropheophorbide-a methyl ester (PPa-OMe) for enhanced nonlinear optical properties. Electron-donor, -acceptor, and hydrophilic groups are attached at various positions of PPa-OMe.

Pyropheophorbide-a methyl ester (PPa-OMe, **1a**, Figure 2) is a photosynthetic chlorin obtained by decarboxylation of methyl pheophorbide-a, which is commonly obtained from *Spirulina maxima* algae.[34] Being a non-centrosymmetric π-system, **1a** is expected to give a SHG response when located in a non-centrosymmetric environment. Since it consists of a conjugated macrocycle with several positions available for chemical modifications and creates singlet oxygen with high quantum yield, **1a** and its derivatives have been extensively studied for *in vitro* and *in vivo* imaging, as well as photodynamic therapy.[35–38] The effects of chemical modification of the π-system of **1a** on its optical properties have been explored in several studies.[39–46] The electronic absorption spectrum of **1a** is characteristic of chlorins, and is dominated by two absorption bands, one in the high-energy region at the border of the UV (Soret band) and one in the far-red visible region (Q band). Absorption in the far-red region is useful for one-photon techniques because photo-damage is reduced at these energies compared to shorter wavelengths. Although the linear optical properties of **1a** and its various derivatives have been widely studied, there are few reports on its nonlinear optical properties.[47,48] The TPA cross-section, σ of **1a** at 800 nm in methanol is only 3.5 GM, which is low compared to many other dyes (porphyrin monomers and dimers have GM values ranging from hundreds to thousands).[3,24,48,49] It has recently been shown that aggregates of pyropheophorbide-a (**1b**, the acid form of **1a**) give an SHG response.[47] Cui *et al.* formed aggregates of **1b** ($\approx$ 100 nm), organized non-centrosymmetrically in liposomes and studied its optoelectronic properties. They investigated the uptake of **1b**-containing liposomes by live cells and imaged the interior of the cells through SHG and third harmonic generation microscopy.[47]

In order to explore the potential of **1a** as a structural framework for the linear and nonlinear optical imaging of membrane potentials of excitable cells[14,15,50,51] and for imaging biological structures through TPEF and SHG-based microscopy,[2–4,47] I describe the design, synthesis, and properties of a new group of chromophores based on **1a** (Scheme 1). The parent structure of **1a** was modified by attaching electron-donating and -accepting groups to form compounds **2a**, **3a**, and **4a**. I aimed to increase the non-centrosymmetry and alter the electronic structure of the parent molecule, to tune its linear and nonlinear optical properties. To increase the amphiphilicity of the compound, I also attached a hydrophilic group. Yovan de Coene, (a PhD student in the group of Prof. Koen Clays, Katholieke Universiteit Leuven, Belgium) investigated the first-order hyperpolarizability β of the chromophores to study the effect of individual electron donor and acceptor groups on their SHG efficacies. Dr. Przemyslaw Gawel (a postdoctoral researcher in the Anderson group) performed TD-DFT (time dependent-density functional theory) computations. While studying the orientation of the compounds in lipid-based water-in-oil monolayer droplets, I found that TPA and SHG in these set of molecules occur through different transition dipole moments (TDMs), which was supported by the TD-DFT calculations.

2.10 Materials and Methods

2.11 Reverse-phase (RP) HPLC used for monitoring reactions i, ii, iii, and iv (Scheme 1).

Table 1: Triple eluent gradient system for monitoring reactions through RP-HPLC

Time (minutes)	H_2O (%)+ 0.1% TFA	Acetonitrile (%)	Methanol (%)
0	30	70	0
2	10	60	30
10	0	50	50
25	0	75	25
26	95	5	0

The solvent flow rate was set to 1 mL/min and the oven temperature to 40 °C. A Zorbax Eclipse XDB C18 column (4.6 x 150 mm, 5 µM) was used to analyze the reaction mixtures and purity of compounds.

2.12 Determination of molar absorptivity

For all the compounds, the absorption spectra were measured at five or six different concentrations to calculate the molar absorptivity, ε.

General protocol: The compound was weighed (~1–2 mg, weighed with 0.01 mg precision) and dissolved in CH_2Cl_2 (1.00 mL) to prepare the stock solution. A blank measurement of pure CH_2Cl_2 (450 µL) was taken before taking the absorbance measurements. The absorption spectra of the dyes were measured for five or six different concentrations (by incrementally adding 1 µL of stock solution using a 5 µL Hamilton glass syringe to the sample before taking the absorbance measurements). An absorbance vs. concentration graph was drawn to calculate the extinction coefficient. According to Beer-Lambert law:

$$A = \varepsilon CL,$$

where A is the absorbance, ε is the molar absorptivity in $M^{-1}cm^{-1}$, C is the concentration in M (molar) and L is the length of the light path (1.00 cm in all cases).

2.13 Measurement of fluorescence quantum yields

The quantum yield of a compound is given by the equation:

$$\phi_C = \phi_R \, \frac{I_c * A_R}{I_R * A_C}$$

where ϕ_C is the quantum yield of the compound, ϕ_R is the quantum yield of the reference compound, I_c is the fluorescence intensity of the compound, I_R is the fluorescence intensity of the reference compound, A_c is the absorbance of the compound (<0.1) and A_R is the absorbance of the reference compound (<0.1). The absorbance values, A_c and A_R were measured at fluorescence excitation wavelengths. To quantify the fluorescence intensities, I_c and I_R, the emission spectra of the compounds were integrated over the whole region. The reference and the unknown compound were analyzed in the same solvent (CH_2Cl_2).

The quantum yields of the dyes were calculated by measuring their absorbances and fluorescence intensities and then comparing them with the absorbance and fluorescence intensity of the reference compound, **1a** according to the above equation. For each compound, five measurements were done at different absorbances (<0.1). The reported quantum yield of **1a** ($\phi = 0.22$ in CH_2Cl_2) was used as a reference.[39]

2.14 Electrochemistry

The square-wave voltammograms of **1a**, **2a**, **3a** and **4a** measured in THF with 0.1 M NBu_4PF_6 as electrolyte (Figure 5). The scan rate of each measurement was 0.05 V/s at 10 Hz with voltage step of 0.005 V. In all the voltammograms, ferrocene (Fc/Fc^+ 0 V) was used as an internal reference.

2.15 Microscopy

Droplet experiments

The dye (20 μM) was added to a mixture of 1,2-diphytanoyl-*sn*-glycero-3-phosphocholine (DPhPC, Avanti lipids) (0.5 mg/mL) and phosphate buffer (1 mL, 50 mM H_2KPO_4, 50 mM NaCl, pH 7.0) and sonicated until the dye was fully dissolved. The phosphate buffer (10 μL) solution was then added to a solution of DPhPC lipid (5 mg/mL) in dodecane (0.5 mL) and gently shaken. The droplets are then imaged in a 35 mm glass bottom well dish (MatTek®).

Microscope

The microscopy experiments were done using an Olympus FV1200MPE-BX61WI microscope equipped with Mai Tai® eHP DeepSee™ Ti:Sapphire laser (70 fs pulse width, 80 MHz repetition rate, continuously tunable between 690–1040 nm) from Spectra-Physics. The light was focused using a 2 mm working distance 25X multiphoton objective (XLPLN25XWMP2). For TPEF, the reflected light was passed through a 750 nm short pass filter before being passed through a 540 nm long pass (LP) filter or a dichroic mirror separating the light to pass through green (495 nm–540 nm) and red (570 nm–625 nm) band pass filters and then was detected by PMT detectors (Hamamatsu R3896 for green and Hamamatsu IR sensitive PMT-R10699 for red). For SHG, the light in the transmitted direction was collected through a 0.9 NA air-based condenser and then passed through a band-pass filter (420±15 nm) before being detected through a PMT detector (Hamamatsu R3896). All the images were acquired in analog-integration mode unless otherwise specified. The images were processed using Olympus Fluoview software and Imaris x64 7.7 software.

The light pulses were passed through a long pass 690 nm dichroic mirror. For TPEF, the reflected light was passed through a 750 nm short pass filter before passing through a 540 nm long pass (LP) filter and then detected by a PMT detector (Hamamatsu IR sensitive PMT-R10699). For SHG, the light in the transmitted direction was passed through a band-pass filter (420±15 nm) before being detected through a PMT detector (Hamamatsu R3896). All the dyes were excited at 840 nm.

Tilt angle experiments

Two-photon excited fluorescence and second harmonic generation images of one droplet of each of the dye **1c**, **2c**, and **4c** are shown in Figure 10.

2.16 Presence of different transition dipole moments at different wavelengths

Compound **3c** was dissolved in deionized water and then mixed with glycerol in such a way that the concentration of water is 10% v/v. The compound was added in such a way that the total absorbance of the glycerol-water mixture is less than 0.1. The excitation spectrum (λ_{em} = 730 nm) of the sample is measured by placing it between two polarization filters at parallel directions to each other. After the first measurement, the polarization filter placed between the sample and the detector is rotated by 90° angle and the spectrum was measured again. Both spectra are plotted and then normalized at 707 nm for better comparison (Figure 13).

2.20 Results and Discussion

2.21 Synthesis

I modified the structure of **1a** (Scheme 1) by attaching electron-donor (4-(*N,N*-diethylaminophenyl)) and -acceptor (dicyanomethylene) groups to increase the polarization of its π-system, with the objective of increasing its SHG intensity. I attached a hydrophilic group, bis-triethylene glycol (TEG) amide, at the carboxylic positions of derivatives of **1a** to make it more amphiphilic and to favor incorporation into lipid membranes.

In an attempt to attach the donor group at the 3^2-vinyl position; initially, I used Heck olefination, but I was unsuccessful despite several attempts. I also tested metathesis reaction as previously described by Liu *et al.* who used Grubbs catalyst second generation to attach 1-hexene at the 3^2-vinyl position of a porphyrin-based molecule.[52] I was successful in applying these conditions on pyropheophorbide-a methyl ester; however, the reaction did not work for attaching the 4-vinyl-diethylaniline at the 3^2-vinyl position of pyropheophorbide-a methyl ester. Following several unsuccessful attempts to attach the donor group by Heck olefination and metathesis reactions, I developed a new strategy to selectively brominate at the 3^2-vinyl position of **1a** and then perform Suzuki coupling. Functionalization at the 3^2-position of **1a** is often carried out by oxidation of the vinyl group to an aldehyde using OsO_4.[43,53] Lonin *et al.* achieved bromination at the 3^2-vinyl position of **1a** by reacting it with Br_2 at –90 °C. The resulting dibromoolefin was heated to eliminate HBr.[54] In my attempts, this procedure was low yielding and gave inconsistent results. Vincente *et al.* used two molar equivalents of *N*-bromosuccinimide (NBS) in the presence of azobisisobutyronitrile (AIBN) on octaethylporphyrin to form *trans*-(2-bromovinyl)-heptaethylporphyrin.[55] Based on this method, I used NBS in the absence of radical initiator to brominate the 3^2-vinyl position of **1a** (Scheme 1), and monitored the reaction by reverse-phase HPLC (RP-HPLC, Figure 3). Bromination occurs selectively at the 3^2-vinyl position giving **5** in 78% yield. The reaction is stereoselective giving the *E*-product, as evident from the HPLC trace (Figure 3) and ^{1}H-NMR spectrum (J = 14.0 Hz, ^{1}H-NMR spectrum at Figure 14). Suzuki coupling was successfully applied (step (ii) in Scheme 1) to attach 4-*(N,N*-diethylaminophenyl) to **5** to give compound **2a**.

I synthesized compounds **3a**, **3b**, and **4a** by attaching malononitrile at the 13^1-carbonyl positions of chlorins **1a**, **1b**, and **2a** respectively, by Knoevenagel condensation.[39,41] This method affords derivatives functionalized with electron-acceptor groups in good yields.

I attached the polar TEG groups by first hydrolyzing the methyl esters **2a**, **3a**, and **4a** to carboxylic acids **2b**, **3b**, and **4b** (step (iv), Scheme 1), respectively. Compound **3b** can be formed with higher yield by first performing the Knoevenagel reaction on **1a** to form **3a** and then hydrolyzing the ester rather than directly attaching malononitrile on the carboxylic acid derivative **1b**. The higher isolated yield may be the result of easier purification of the methyl ester derivatives compared to the corresponding carboxylic acids. Compounds **1b**, **2b**, **3b**, and **4b** were reacted with bis-TEG amine in the presence of the amide coupling reagent, COMU[56] to form the amphiphilic compounds **1c**, **2c**, **3c**, and **4c** (step (v), Scheme 1), respectively.

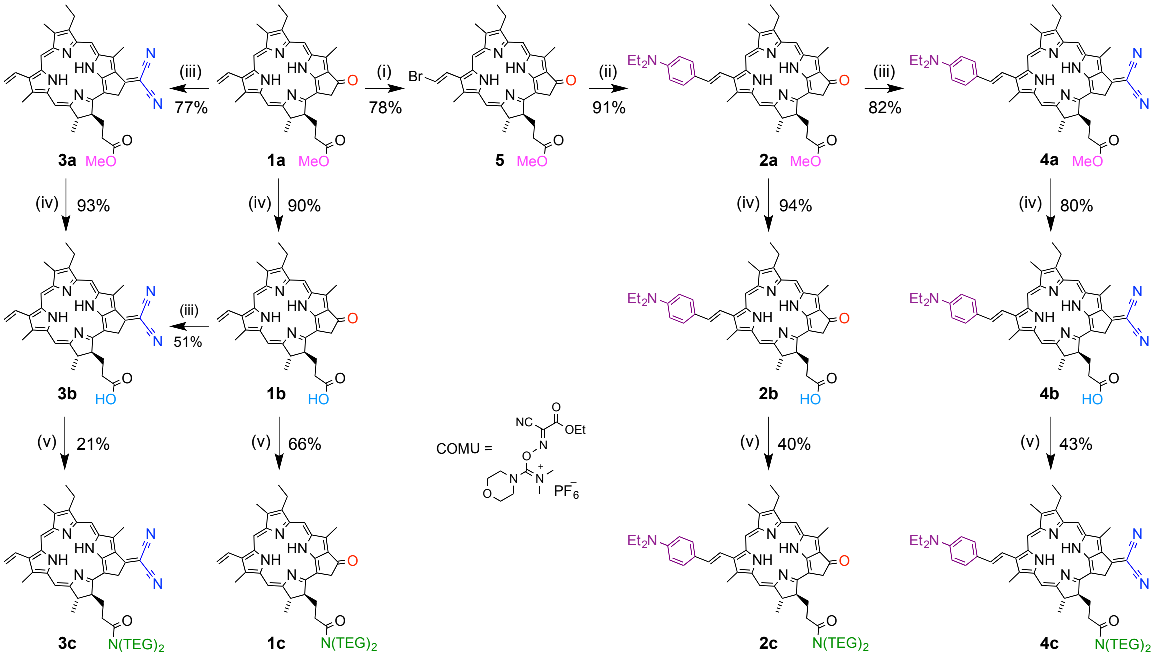

Scheme 1 Synthesis of derivatives of pyropheophorbide-a methyl ester **1a**. Reagents and conditions: (i) *N*-bromosuccinimide (NBS), 1,2-dichloroethane, reflux; (ii) 4-*N,N*-diethylaminophenyl boronic acid, $Pd(PPh_3)_4$, Bu_4NBr, toluene, NaOH (0.2 M aq.), 80 °C; (iii) $CH_2(CN)_2$, Et_3N, reflux; (iv) HCl (aq.), 20 °C; (v) $HN(TEG)_2$, COMU, DMF, $i$$Pr_2NEt$, 0 °C (TEG: triethyleneglycol).

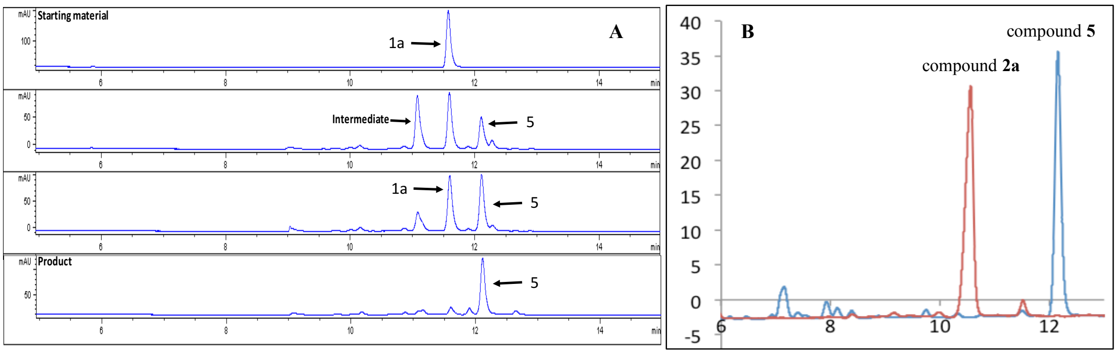

Figure 3: Reaction monitoring by RP-HPLC: **(A)** HPLC traces of Reaction (i) in Scheme 1 to form compound **5** from **1a**. The top chromatogram shows **1a** at a retention time of around 11.5 min. The second chromatogram shows formation of an intermediate at around 11 min and product **5** at 12.2 min. The peaks in third chromatogram show the depletion of the intermediate and starting material, **1a** along with the formation of product **5** while the fourth row shows only the peak of the product **5** at 12.2 min. **(B)** Reaction (ii) in Scheme 1 to form compound **2a** from 5. The retention time of compound **2a** is 10.5 min while that of compound **5** is 12.2 min. Peaks were detected at 665 nm.

2.22 Linear Optical Properties

The electronic absorption and emission spectra of all the compounds were measured in dichloromethane solution at 25 °C. The absorption spectra are characteristic of chlorins with Soret bands in the blue region and intense Q bands in the far-red region. The absorption and emission spectra of **1a**, **2a**, **3a**, and **4a** (Figure 4) show a clear effect of functionalization with electron-donating and -accepting groups. The presence of the strongly electron-withdrawing dicyanomethylene group in **3a** causes a greater bathochromic-shift than the electron-donating 4-(*N,N*-diethylaminophenyl) in **2a**. On attaching either electron-donating or accepting groups, the intensity of the Soret band decreases, and absorption in this region becomes structured into a complex pattern of bands. The presence of various transitions within the Soret region is supported by TD-DFT calculations (*vide infra*). The multiple transition bands in the Soret region of **3a** are of similar intensities unlike the bands of **1a**, **2a**, and **4a**. I observe a nearly two-fold increase in intensity of the Q band on attachment of the only acceptor group in **3a**. This effect is not observed on attachment of the donor group (compound **2a**), or of both the donor and acceptor groups (compound **4a**). Similarly, in the emission spectra, a greater bathochromic shift was observed for compound **3a** (with electron-acceptor) than for compound **2a** (with electron-donor), compared to the parent compound **1a**. The emission maximum is further shifted towards a longer wavelength when both the electron-donating and -accepting groups are attached in compound **4a**.

The attachment of electron-donor and -acceptor groups did not substantially affect the Stokes shift, which is approx. 0.025 eV for all compounds. In the PPa-OMe family of dyes (**1a**, **2a**, **3a** and **4a**), the fluorescence quantum yield decreases slightly while substituting with the electron-donating group; however, it increases while attaching the electron-accepting group (Table 2). In the push–pull derivative **4a** the quantum yield decreases by more than 99% (Table 2), which is beneficial for SHG imaging as there is less collateral TPEF. Tamiaki and co-workers have studied the properties of derivatives of **1a** constructed by various functionalizations at its 3^1 and 3^2 positions and attaching malononitrile at its 13^2 position.[39,43] However, none of those compounds exhibited quantum yields as low as **4a**. It appears that the 4-(*N,N*-diethylaminophenyl) moiety plays a critical role in fluorescence quenching, probably via intramolecular charge transfer.[57–59] I also measured the absorption and emission spectra of **1b**, **2b**, **3b**, and **4b** to investigate the effect of the hydrolysis of ester to carboxylic group on the optical properties. This change does not alter the optical properties significantly (Figure 4).

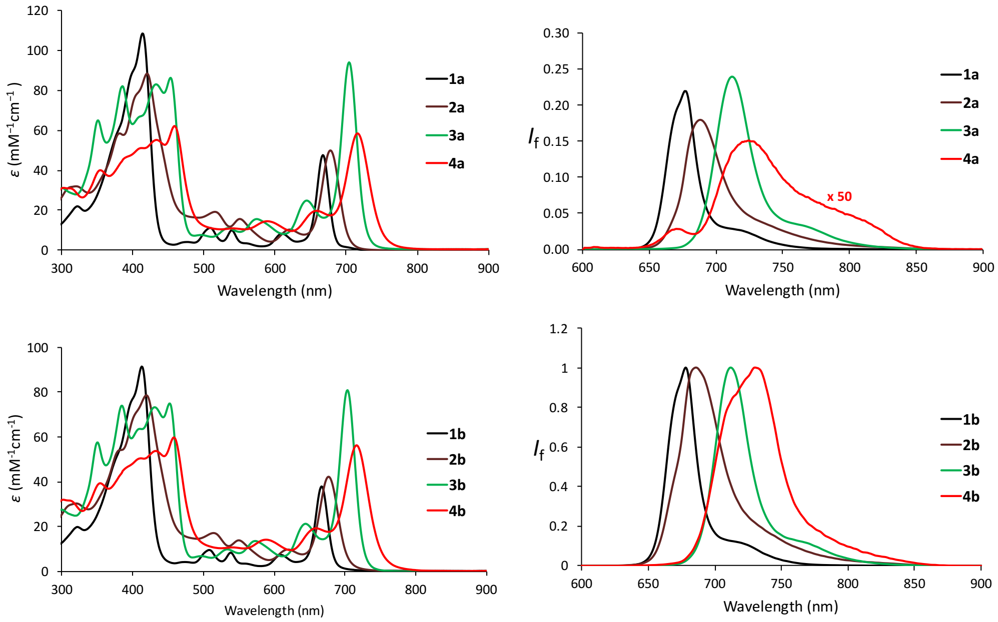

Figure 4: Absorption and emission spectra of dyes, **1a**–**4a** and **1b**–**4b**. Attaching the electron donor and acceptor groups causes a red shift in the absorption and emission bands, indicating a decrease in the HOMO-LUMO band gap. Measurements were performed in CH_2Cl_2 at 25 °C. For fluorescence measurements, the compounds were excited at their respective Soret bands. The fluorescence intensity of **1a**–**4a** are normalized such that the areas of the peaks are proportional to their fluorescence quantum yields. The fluorescence intensity for **4a** is multiplied by a factor of 50 for visible comparison. The fluorescence intensities of **1b**–**4b** are normalized to unity.

Table 2: Linear and nonlinear optical properties of **1a**–**4a** and other dyes

Dye	**λ_{max}^{abs} (log ε) / nm**	**λ_{max}^{em}/nm**	**ϕ_F**	**$\Delta\tilde{\nu}$ /eV**	**β_{zzz} (λ)/10^{-30} esu (nm)**	**β_{HRS} (λ)/10^{-30} esu (nm)**
1a	413 (5.0), 667 (4.7)	678	0.22[39]	0.030	350 ± 50 (800), 1760 ± 340 (840)	140 ± 30 (800), 730 ± 140 (840)
2a	420 (4.9), 678 (4.7)	689	0.18	0.029	790 ± 150 (800), 2700 ± 500 (840)	330 ± 60 (800), 1100 ± 200 (840)
3a	453 (4.9), 704 (5.0)	713	0.24	0.022	800 ± 150 (800), 3200 ± 560 (840)	330 ± 60 (800), 1300 ± 200 (840)
4a	458 (4.8), 716 (4.8)	726	0.003	0.023	1330 ± 240 (800), 4700 ± 800 (840)	550 ± 100 (800), 2000 ± 340 (840)
JR1[4]	448 (5.0), 723 (4.9)	803	0.13	0.1708	2300 ± 150 (800), 5800 ± 200 (840)	970 ± 50 (800), 2440 ± 70 (840)
FM4-64[6]	564 (4.7)	761	0.35	0.5690	1150 ± 220 (800)	470 ± 90 (800)

The absorption and emission spectra of pyropheophorbides are measured in CH_2Cl_2 and that of **JR1** and **FM4-64** in in $CHCl_3$. The β values of all the compounds are measured in $CHCl_3$. $\Delta\tilde{\nu}$ is the Stokes shift; **1a** was used as reference for calculating the fluorescence quantum yields, ϕ_F of all pyropheophorbide-based compounds.[39] ε is the molar absorption coefficient in $M^{-1}cm^{-1}$.

2.23 Electrochemical properties

I performed electrochemical measurements (square wave voltammetry) on the chromophores to determine the energies of their frontier orbitals (Table 3, Figure 5). As expected, the electrochemical HOMO–LUMO gap (E_{ox}^{1} − E_{red}^{1}) decreases on attaching electron-donor and -acceptor groups. However, in contrast to the UV-Vis spectra, attachment of the donor group in **2a** decreases the HOMO-LUMO gap more than the acceptor group in **3a**. On attaching the donor group, both the first oxidation and first reduction potentials decrease, while on attaching the acceptor group, they both increase. Tamiaki and coworkers found that on attaching only electron-withdrawing groups (carbonyl and dicyanomethylene) at the 13^{1} and 3^{2} positions of **1a**, the potentials of oxidation and reduction increase, in agreement with these results.[39]

Table 3: Oxidation and reduction potentials of **1a**–**4a**[a]

Dye	E^{1}_{ox} (V)	E^{1}_{red} (V)	E_{ox}^{1}–E_{red}^{1} (V)
1a	0.43	–1.62	2.05
2a	0.17	–1.63	1.80
3a	0.52	–1.38	1.90
4a	0.20	–1.40	1.60

[a] All potentials were measured in THF with 0.1 M NBu_4PF_6, relative to internal ferrocene, Fc/Fc^{+} at 0 V.

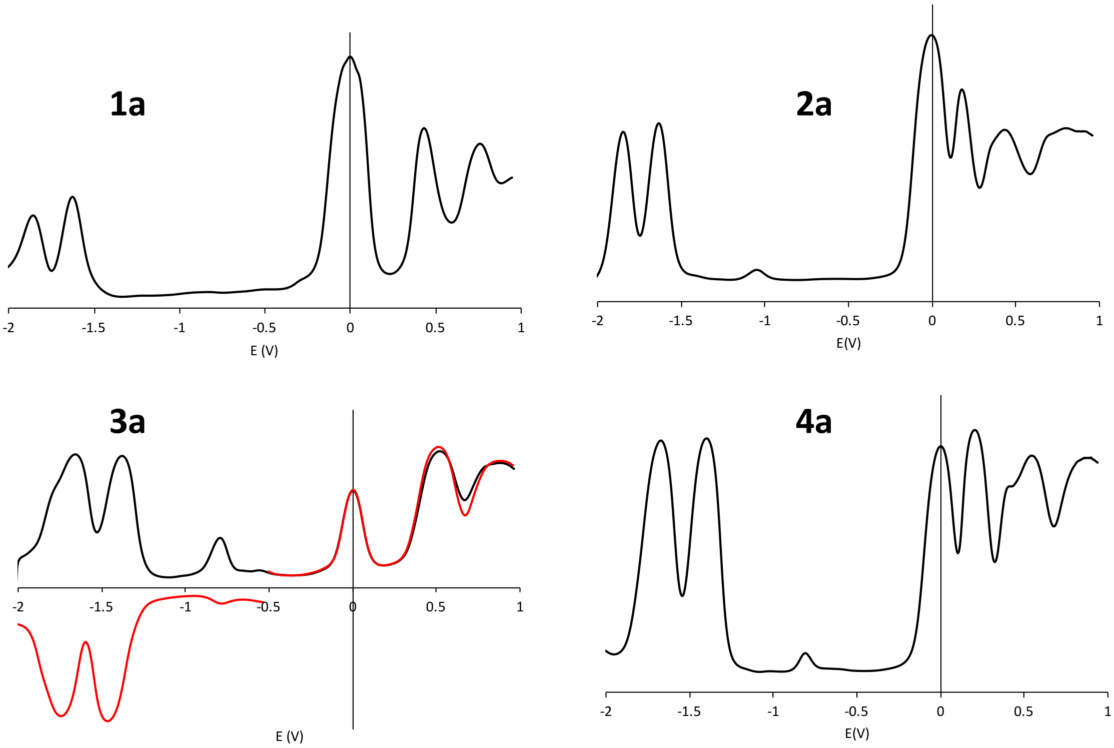

Figure 5: Square-wave voltammogramms of **1a**, **2a**, **3a**, and **4a**. In **3a**, a bump or a small peak is visible at around 0.75 V. The bump is visible when the measurement is done from –1.5 V to 1.5 V; however, its size reduces significantly, when the measurements are performed from 0 V to –1.5 V and 0 V to 1.5 V. The bump is also present in **2a** and **4a** but their sizes are negligible in comparison to the oxidation and reduction peaks.

2.24 Electronic Structure Calculations

The ground-state geometries of **1a**, **2a**, **3a**, and **4a** were optimized by density functional theory (DFT) at the B3LYP/6-31G(d) level of theory with solvation in CH_2Cl_2 using the polarizable continuum model (PCM) implemented in the Gaussian09 package by Dr. Przemyslaw Gawel.[60]

The calculated frontier molecular orbitals show a significant difference in the localization of the HOMO and LUMO in **2a** and **4a** (Figure 6). This suggests that the HOMO-to-LUMO transitions in these derivatives have intramolecular charge-transfer (ICT) character. In the case of **1a** and **3a**, which do not contain the 4-(*N,N*-diethylaminophenyl) group, both the HOMO and LUMO are located on the central chlorin ring. The fact that the LUMO is localized on the chlorin in **2a**, while the HOMO is localized on the 4-(*N,N*-diethylaminophenyl) group, implies that the chlorin ring can act as an electron-acceptor. The calculated ground-state dipole moments show a strong increase in the order: **1a** (7.6 D), **2a** (12.5 D), **3a** (14.6 D) to **4a** (20.7 D).

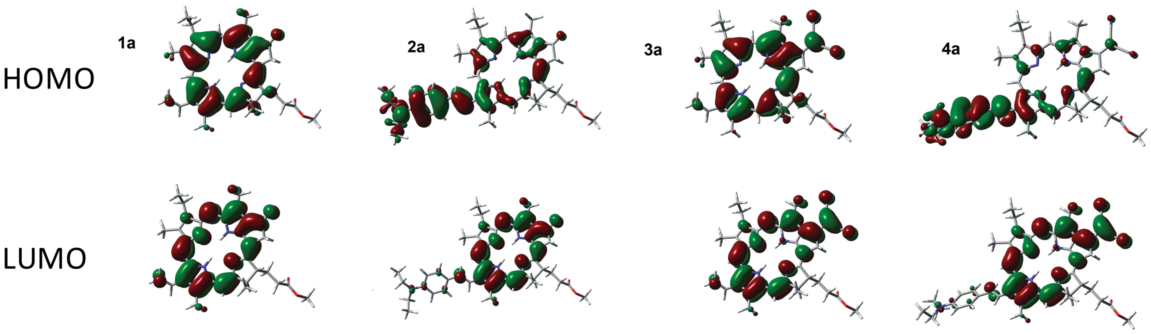

Figure 6: Frontier molecular orbitals of **1a**, **2a**, **3a**, and **4a** at the B3LYPP-31G(d) level of theory. 0.02 is isovalue.

On these geometries, vertical optical transitions were calculated by TD-DFT at the B3LYP/LANL2DZ level of theory.[61–63] In the case of **2a** and **4a**, the lowest energy transition (Q band) is found with high precision (difference of 0.06 eV and 0.07 eV, respectively, compared with experiment; Figure 7). On the contrary, the Q band transition energy of **1a** and **3a** is underestimated by 0.31 eV and 0.30 eV, respectively. The splitting of the Soret band into multiple transitions in the higher energy region was predicted with variable precision and the general shape of the spectra could be reproduced (Figure 7). In case of **3a**, there are two transitions (S5 and S8 in Figure 7) within the Soret region whose TDMs are almost perpendicular to each other. This result explains different directoin of TPEF and SHG signals, *vide infra*. I presume that each of these signals is activated by one of these TDMs.

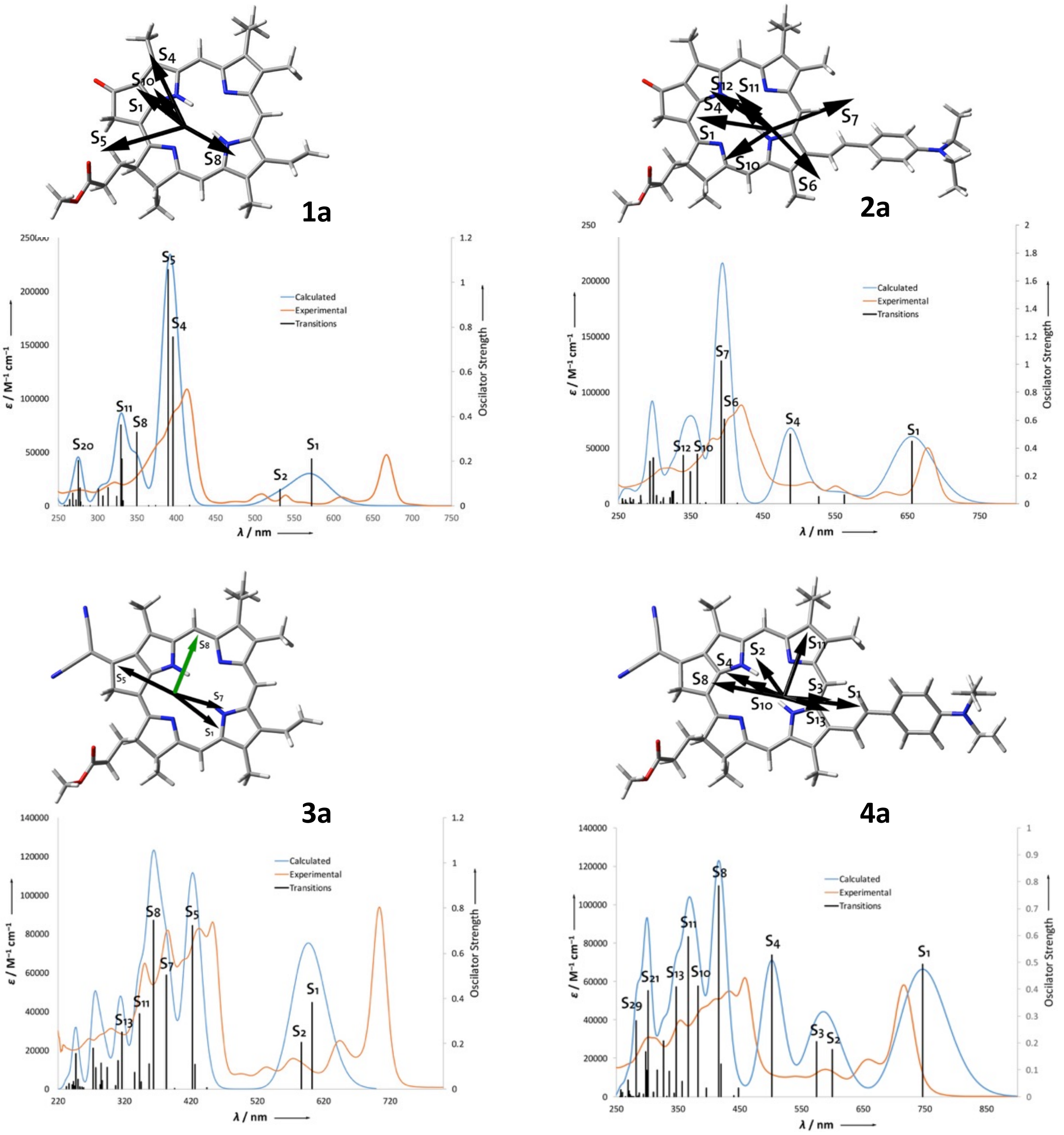

Figure 7: Overlay of the measured absorption spectra of **1a**, **2a**, **3a**, and **4a** (CH_2Cl_2) and their calculated electronic transitions (TD-DFT B3LYP/LANL2DZ, PCM solvation in CH_2Cl_2). The vertical bars represent oscillator strength of the transitions. The calculated electric transition dipole moments for the main electronic transitions are visualized on the geometrically optimized structures of the compounds (TD-DFT B3LYP/LANL2DZ level of theory).

2.25 Hyper-Rayleigh Scattering

The second-order polarizabilities (β_{HRS}) and the component of β along the molecular-axis (β_{zzz}) were measured for the series of PPa-OMe derivatives **1a**–**4a** in chloroform at 800 nm and 840 nm by hyper-Rayleigh scattering (Table 2).[64,65] The contribution to the β_{zzz} values of both the donor and acceptor at 800 nm are similar. This contrasts with previously reported porphyrin-based dyes studied by Anderson and coworkers, where an acceptor does not contribute to the

β value.[8] The observed difference between the series of dyes may result from the nature of the conjugated core (porphyrin *vs.* chlorin). A free-base porphyrin, when substituted with a strong donor group can itself act as an electron acceptor, making the need of an additional acceptor redundant. However, chlorins exhibit higher electron density than porphyrins, which makes them weaker electron acceptors. The β values increase on attaching either the donor in **2a** or the acceptor in **3a**, which means that the chlorin moiety can act as both the acceptor (for compound **2a**) and the donor (for compound **3a**). The β_{zzz} value of **4a** at 800 nm is about half that of the previously studied porphyrin-based SHG voltage sensitive dye, **JR1**.[4,14] However, it is more than the value that is measured in the same conditions for the commercial SHG dye, **FM4-64** (Table 2). The electron donor and acceptor groups in **JR1** are attached at *meso*-positions, whereas, in **4c** they are attached to the chlorin ring at the *beta*-positions. This change of conjugation path undoubtedly contributes towards the difference in HRS behavior.

2.26 Multiphoton Microscopy

Anderson and coworkers reported a polarization-based methodology to study the probability distribution of the angular orientations of amphiphilic dyes in lipid-based monolayers and bilayers.[11] Studying the orientation (tilt angle, φ in Figure 8) of amphiphilic dyes in lipid membrane is important because the dye gives maximum TPEF or SHG signal when its TDM is parallel to the polarization of the laser light.

This methodology employs optical anisotropy data from three polarization-based imaging techniques which are, one-photon microscopy (confocal microscopy), two-photon microscopy, and second harmonic generation microscopy. It requires at least two of the three microscopy data (TPEF and SHG used here) to study the angular distribution of the orientation of an amphiphilic molecule. The method requires data from at least two microscopy methodologies because the probability distribution function is based on two different order parameters which are, (1) μ, the most preferred orientation of the molecule around lipid monolayer/bilayer and (2) γ, the range of the orientations that the molecule can adopt. Figure 8 describes the angular orientation of a dye (φ and Ψ) in a lipid-based monolayer water droplet. The model determines the probability distribution of the average orientation (tilt angle, φ in Figure 8) and gives information about the most preferred orientation of the dye (the angle of highest probability at which the orientation of the dye is preferred).

The model is based on photoselection rules, which have the primary requirement that the molecule must have a single active transition dipole moment (TDM) at the excitation wavelength. It most cases, the TDM of an amphiphilic dye is assumed to be coincident with the long axis, i.e. hydrophobic-hydrophilic axis. I used this methodology to study the angular orientation of **1c**–**4c** in lipid-based monolayer water droplets suspended in oil. The complete theoretical explanation of the model and its execution involves complex mathematical solutions[11] and is beyond the scope of this DPhil thesis. I also attempted to study the orientation of **1a**–**4a** but the compounds do not orient at the water-oil interphase and stay in the oil part. Compounds **1b**–**4b** tend to aggregate in the water droplets proving that **1c**–**4c** are more amphiphilic in nature.

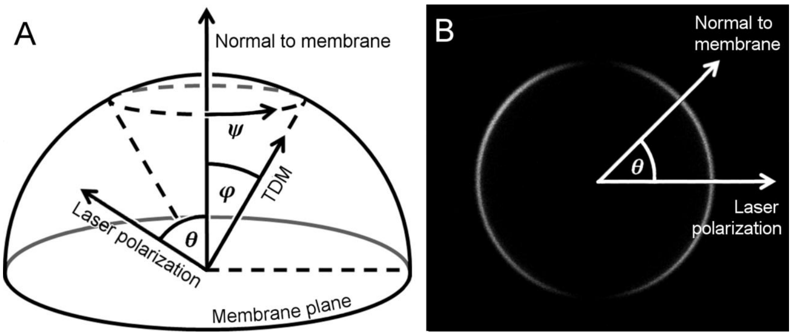

Figure 8: Depiction of orientation of dye molecule in a lipid-based monolayer water droplet suspended in oil. (A) The transition dipole moment (TDM) of a dye tilted at an angle of φ from normal to the membrane and an angle Ψ around it. The extent of SHG or TPEF signal from an ensemble of dyes depends on the angle $\varphi + \Theta$. Small the summation of φ and Θ, more intense with will be SHG and TPEF. (B) Variation of SHG of an amphiphilic dye oriented in a lipid-based model membrane. The SHG varies periodically with θ around the equator of the model membrane. The shape of this angular intensity function, when fit to a model, allows extraction of trigonometric moments of the tilt distribution. The direction of laser excitation is collinear with the direction of signal detection and perpendicular to the plane of the image in (B). Image adapted with permission from *Biophys. J.,* 2012, **103**, 907, 917. Copyright 2012 Elsevier.

I imaged the TEG-substituted amphiphilic dyes, **1c**–**4c**, in droplets of water in oil encapsulated by a lipid monolayer oil (depicting a simple model for a cell membrane) using a multiphoton microscope, to test their suitability for SHG and TPEF imaging, and to study their average tilt angle and probability distribution of the orientations (Figures 9 and 10). Droplets of phosphate buffer (aqueous phase) were mixed with lipids (DPhPC) and dye, and suspended in dodecane (oil phase) already mixed with DPhPC lipids. The amphiphilic dyes locate at the water-oil interface of the spherical droplets. All four compounds give clear SHG images, and the SHG signal is brightest for the push–pull dye **4c**. Upon imaging under the multiphoton microscope, two distinct dark regions are observed around the edge of the droplets where the TDM of the dye is perpendicular to the direction of the polarization of the excitation light, and two bright regions where the TDM is parallel to the polarization of the excitation light (Figures

8, 9 and 10). To calculate the average tilt angle and their distribution in monolayers, I used the same MATLAB-based image-processing software designed by Anderson and coworkers.[11]

Aiming to obtain average tilt angles and probability distribution of **1c**, **2c**, **3c**, and **4c** in water-in-oil based lipid monolayers, through their TPEF and SHG images, I attempted to fit the images using the MATLAB-based image processing software (Figures 9 and 10).[11] Particularly in **3c**, I found that the intensity maxima (bright regions) and minima (dark regions) of SHG are shifted compared to their counterparts in TPEF (Figure 9). These results suggest that at the wavelength of excitation (840 nm), **3c** has different TDMs active for TPA and SHG. I compared the change of phase angles (angle around the droplet at which the intensity is at maximum or minimum) for TPA and SHG of **3c** with that of **di-8-ANEPPS**, an SHG-based dye previously used to demonstrate the same model (Figure 9). **Di-8-ANEPPS** is a linear molecule with a single dominant TDM and hence no shift in the phase angles was observed in the droplets monolayers coated with **di-8-ANEPPS**.

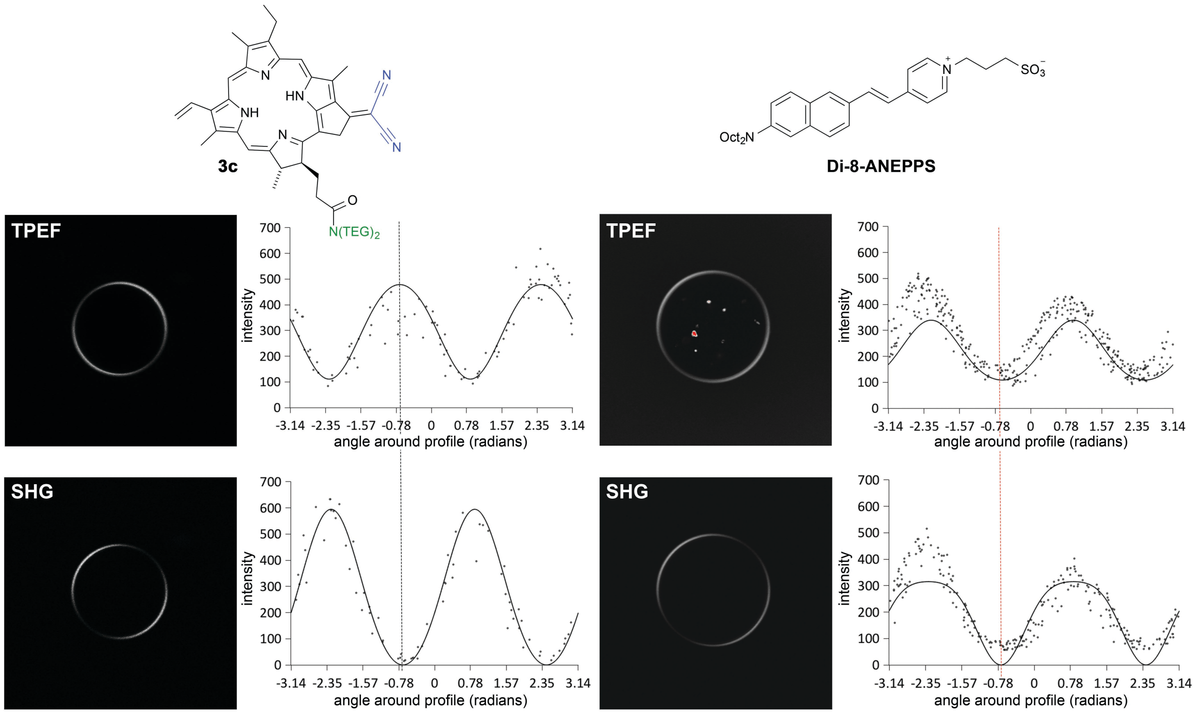

Figure 9: Two-photon excited fluorescence (TPEF) second harmonic generation (SHG) images of **3c** and **di-8-ANEPPS**. The cusp shape of TPEF and SHG are in different directions for **3c**, while they are in the same direction for **di-8-ANEPPS**. The angular based intensity plots describe the change of intensity as a function of the phase angle (angle around the droplet). The black dotted line shows the angle at which the TPEF intensity for compound **3c** is at maximum, but SHG is at minimum. The intensities maxima and minima of TPEF and SHG for **di-8-ANEPPS** are the same at the same angle (red dotted line). Droplet diameter: 70 µm (**3c**), 150 µm (**di-8-ANEPPS**). λ_{ext} = 840 nm (**3c**), 850 nm (**di-8-ANEPPS**).

The phase angles of **1c**, **2c**, and **4c** in SHG and TPEF were also slightly shifted from each other when processed in the MATLAB-based software (Figure 10). Hence, I presume that these chromophores also have different TDMs active for TPEF and SHG. TD-DFT calculations predicted that all the four compounds **1a**, **2a**, **3a**, and **4a** have several TDMs in various directions (Figure 6). This circumstance makes the model unsuitable to measure the probability distribution of tilt angles because the model assumes that both TPEF and SHG are occurring through the same TDM and requires the use of both techniques. Nonetheless, the individual TPEF and SHG images can be used to determine their individual average tilt angles (angle between the active TDM and the normal to the membrane plane), assuming that all the molecules in the droplet orient at the same tilt angle.[11]

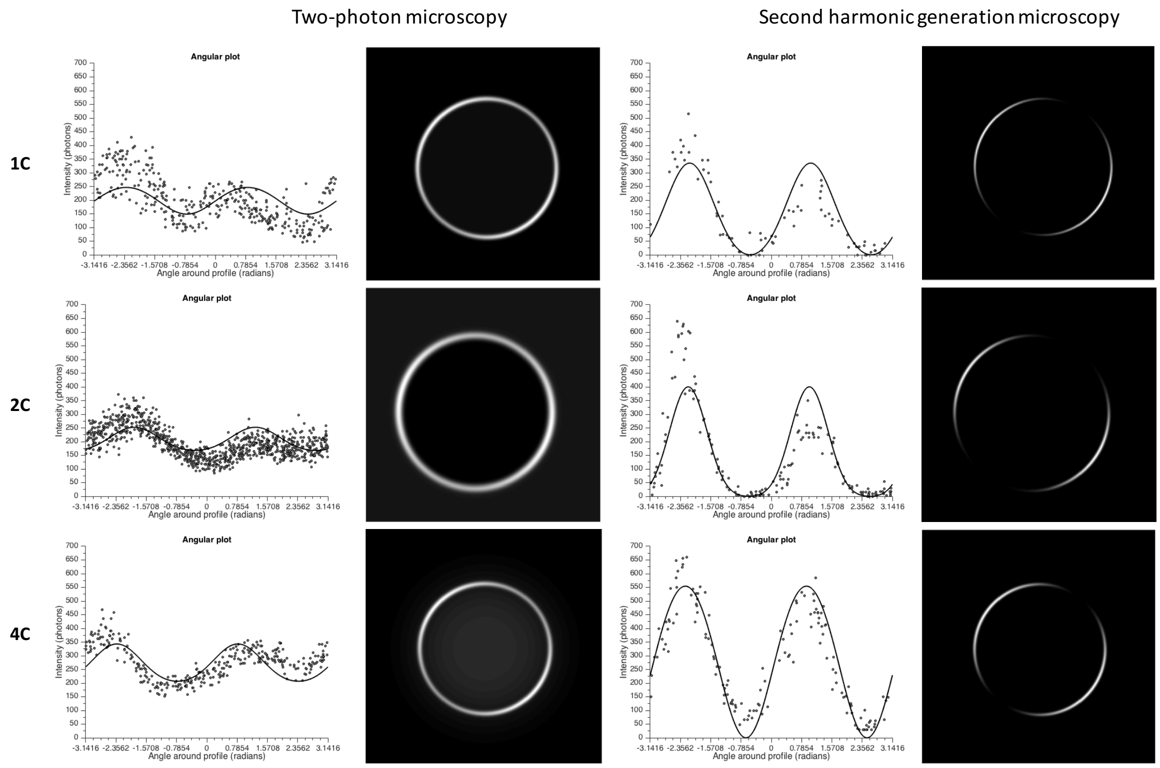

Figure 10: Analysis of physical orientation of **1c**, **2c**, and **4c** in monolayer droplet by two-photon and second harmonic generation –based microscopy. λ_{ext} = 840 nm, Droplet diameter: 250 µm (**1c**), 130 µm (**2c**), 225 µm (**4c**).

I processed the TPEF and SHG images of **1c**, **2c**, **3c**, and **4c** and fitted the model to calculate their respective average tilt angles (Figure 11). These average tilt angles obtained by their individual TPEF and SHG images differ by more than 20% for all the dyes. The value of tilt does not change substantially on attaching the donor group (**1c** to **2c**) but decreases on attaching the acceptor group (**1c** to **3c**) and remains similar on attaching both the donor and acceptor groups (**1c** to **4c**). The average tilt angle from SHG for all the compounds vary between 30° to 40°, while that of TPEF varies between 40° to 50° (Figure 11). As a control experiment, I also processed the TPEF and SHG images of **di-8-ANEPPS**, for which the average tilt angles for both TPEF and SHG were found to be the same (the difference of around 5% lies within experimental error). In the PPa-OMe family dyes, SHG is most likely to be resonance enhanced by the TDM lying in the donor-acceptor axis (long axis of the molecule) as evident from the change of β_{zzz} value on attaching individual donor and acceptor groups. This means that the information about the orientation of the whole molecule can be predicted from the average tilt angle values of SHG for **1c**, **2c**, **3c**, and **4c** (Figure 12).

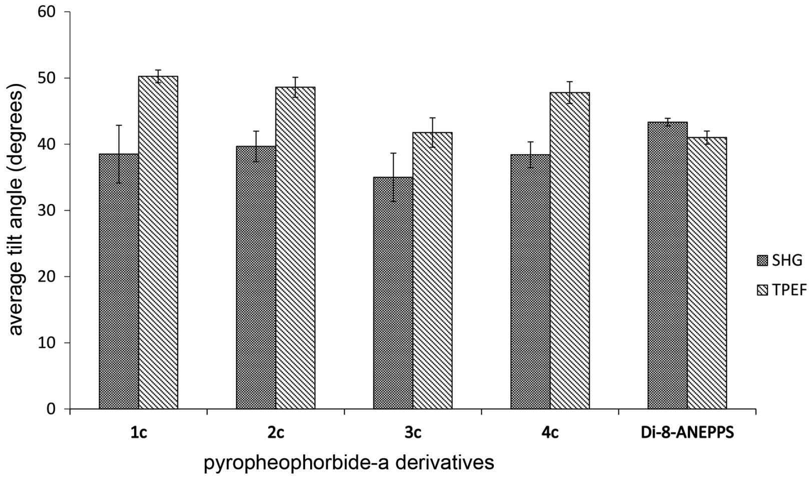

Figure 11: Comparison of average tilt angles obtained from TPEF and SHG images. The average tilt angle obtained from the TPEF and SHG images for **1c**, **2c**, **3c**, and **4c** differ by more than 20%, while the difference for **Di-8-ANEPPS** is approx. 5%. This means that there are different TDMs active for TPA and SHG for **1c**, **2c**, **3c**, and **4c** but same TDM for **Di-8-ANEPPS**. The angles decrease on attaching the electron-acceptor group, while they increase on attaching the electron donor group. Error bars represent standard deviation ($n \geq 4$; $n_{\text{Di-8-ANEPPS}} = 3$; n = number of samples).

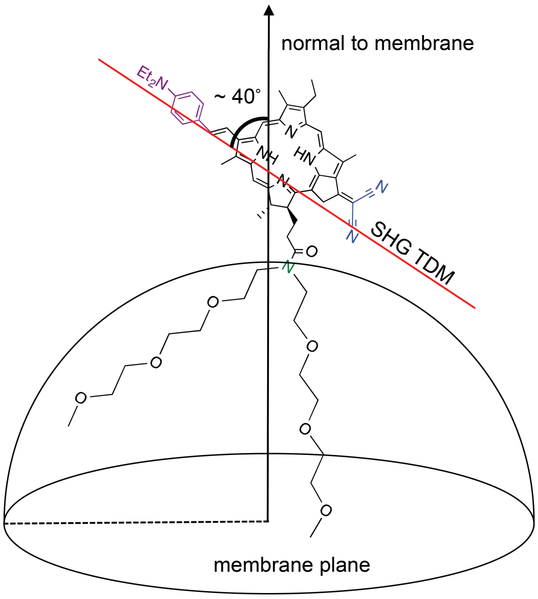

Figure 12: Physical interpretation of orientation of **4c**, based on the assumption that the average tilt angle of the dye is the angle derived from SHG image.

Since these molecules contain a non-centrosymmetric core macrocycle, they have TDMs pointing at various directions, as shown by TD-DFT calculations (Figure 6). To experimentally confirm the existence of various TDM directions at different wavelengths, I measured the polarized fluorescence excitation spectra of **3c** (Figure 13). This experiment was performed in glycerol-water mixture (9:1) as a solvent, to minimize diffusional reorientation of molecules. The orientation of the polarization filter placed between the sample and the light source was kept constant, while the polarization filter (analyzer) placed between the sample and the detector was rotated by 0° or 90° and the excitation spectrum was measured. The difference in the intensity for these two spectra varies across the UV and visible range, indicating that the direction of TDMs responsible for the absorption varies at different wavelengths (Figure 13). This observation is supported by TD-DFT calculations, which show that the TDMs within the Soret band of **3a** are situated at approx. 90°. In contrast to other derivatives, in **3a** the three strong perpendicular transitions dominate the Soret band (Figure 6).

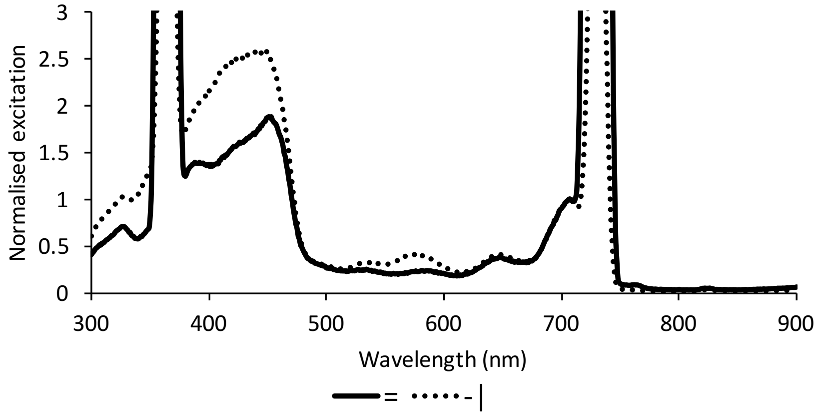

Figure 13: Excitation spectra comparison of **3c** (in glycerol mixed with 10% v/v water) at different orientations of the polarization filters. The solid curve depicts the spectrum when both the filters placed at either side of the sample are in same orientation (=). The dotted curve depicts the spectrum when the orientation of only the filter placed between the sample and the detector is rotated by 90° angle. The difference in the change in intensities is not constant, when the curves are normalized at 707 nm. The peaks at 730 nm and 365 nm are scattering peaks. λ_{em} = 730 nm.

Study of transition dipole moments in 3D

I performed 3D imaging of the droplets to study the orientation of the TDM of the dyes in 3D around a full droplet. The imaging was performed using a 25X water immersion multiphoton focusing objective with high numerical aperture 1.05. For imaging, the lipid-water mixture was suspended in oil-lipid mixture to form water-in-oil droplets in a glass-bottom dish. The oil-lipid mixture was pre-dissolved with the dye. The glass-bottom dish was covered with a coverslip and then a pellet drop of water was suspended on top of the coverslip for imaging using the water immersion lens.

In **3c**, due to background fluorescence, the TPEF signal was not visible clearly, while SHG was visible (yellow box, Figure 14). In 2D measurements, the dye was dissolved in the water droplet because of which there was no background fluoresce then; however, those experiments were performed using an air-based 0.4 NA focusing objective. It is not trivial to perform these experiments with a water immersion focusing objective because when the glass bottom dish is covered with a coverslip, it introduces a pocket of air which leads to coalescence of the lipid-based water droplets in the oil. A high numerical aperture water immersion objective is necessary for full 3D imaging because the low numerical aperture lens was unable to take images of a full droplet with high resolution.

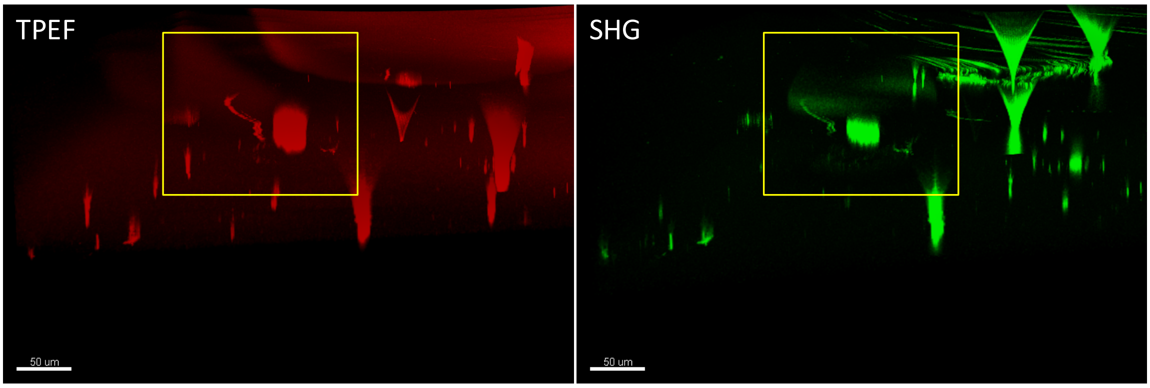

Figure 14: TPEF and SHG images of **3c** oriented around a full water droplet (yellow box). In TPEF, due to background signal, the droplet could not be visualized while, it is clearly visualized in the SHG image. Scale bar = 50 μm.

The images were processed using Imaris x64 8.0.2 software to remove the background signals. The pixels were converted into voxels such that a collection of adjoining pixels form one voxel without distorting the shape of the image. The intensities of the voxels were normalized for clarity (Figure 15). The fluorescence and SHG signals were visible only from the area around equator and near the bottom region (Figure 15) and the image of full droplet could not be achieved. Signals from the full droplet could not be achieved because of the lensing effect that is caused because of the differences between refractive indices of the water (1.33) and oil (dodecane = 1.42). Due to the difference between the refractive indices of water and dodecane, the water droplets themselves act as lenses. Due to lensing effect, all the emitted light is not collected by the optics system of the microscope and light from certain area are only collected. Nonetheless, the acquired images gave useful information about the orientation of the dyes. As expected and seen in 2D images, the TDMs of **3c** for TPEF and SHG are orthogonal to each other at the equatorial region (Figure 15). At the bottom regions, a bowl shape was assumed by the dyes with the TPEF and SHG overlapping on each other. No dark regions were observed because the TDM of the dye is in slanted direction in the vertical plane and hence it is not orthogonal to the polarization of the laser light in any direction.

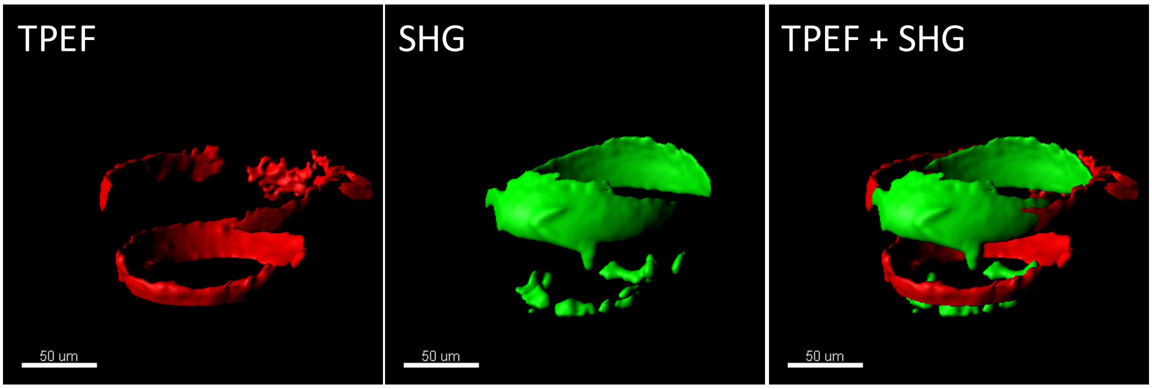

Figure 15: Voxel-based images of **3c**. The TDMs of TPEF and SHG are orthogonal to each other. Scale bar = 50 µm.

For other dyes too, similar observations were made. A clear pixel-based overlap of TPEF and SHG image of **1c** is shown in Figure 16. Due to high background fluorescence, the intensity of TPEF is reduced manually.

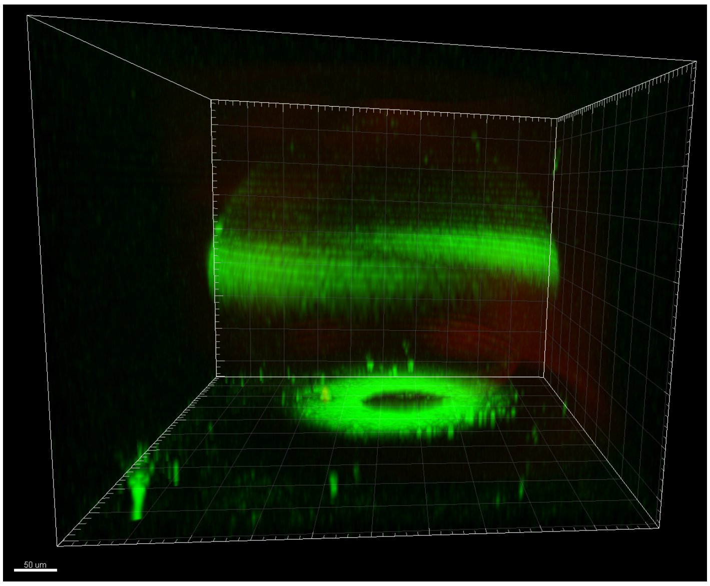

Figure 16: Pixel-based image of overlap of fluorescence and SHG of **1c**. Scale bar = 50 µm.

2.30 Conclusions

I have synthesized donor-acceptor functionalized amphiphilic derivatives of pyropheophorbide-a methyl ester and studied their linear and nonlinear optical properties in organic solutions and at water-in-oil droplet interfaces. I demonstrated a new approach to functionalize the 3^2-vinyl position of pyropheophorbide-a methyl ester **1a** *via* a stereoselective bromination. This approach gives high yields, and could prove useful for the introduction of a wide range of functional groups. The electronic absorption and emission spectra of all the derivatives are characteristic for chlorins. The push-pull substitution pattern results in a strong red-shift in the absorption and fluorescence spectra, with a corresponding reduction in the electrochemical HOMO-LUMO gap and an increase in the hyperpolarizability, β measured by hyper-Rayleigh scattering. The fluorescence quantum yield of the push-pull derivative **4a** is drastically reduced, possibly due to photoinduced charge-separation. Analysis of the TPEF and SHG images of lipid-monolayer coated droplets containing these dyes shows that the TDMs dominating the SHG are sometimes orthogonal to those responsible for two-photon absorption, depending on the wavelength of excitation. The presence of several TDMs in various directions was confirmed by TD-DFT calculations and by polarized fluorescence excitation spectra. Since the SHG of a dye depends on the orientation of its dominant TDM, control of the orientation of the TDMs is crucial in the design of a SHG dye. Amphiphilic chromophores based on **4c** are promising prototypes for voltage-sensitive dyes for monitoring membrane potential in excitable cells, such as neurons through TPEF and SHG. To work as voltage-sensitive probes to measure the membrane potential, the dyes must localize in the plasma membrane of live cells.

2.40 Outlook

As mentioned in the introduction section of this chapter, the pyropheophorbides have found extensive use in the field of biological research. The new TEG-substituted pyropheophorbides, **1c**–**4c** with enhanced polarity could be very useful for biological experiments due to enhanced aqueous solubility. Moreover, the red-shifted molecules will ensure deeper penetration of light for imaging in thick (>100 µm) biological specimens for various studies, such as imaging cellular structures, PDT, and membrane potential experiments. The electron-donor group attached dyes could be further investigated to be used as molecular rotors to study intracellular viscosities.[66,67] The electron-acceptor group attached molecule, **3c** possessing orthogonal TDMs for TPEF and SHG could be further used to study different planes of lipid-based 3D structures. These molecules (**1c**–**3c**) with better aqueous solubility, enhanced linear and nonlinear optical properties, and decoupled orthogonal TDMs offer several research possibilities, such as designing new dyes with different functional groups at the 3^2 and 17^3 positions of PPa-OMe, designing molecules with decoupled TDMs, and studying the effect of different functional groups on PDT efficiency.

In the next chapter, I study the cellular localization of the amphiphilic pyropheophorbides, **1c**–**4c** along with other amphiphilic donor-acceptor–based porphyrin dyes synthesized in the Anderson group.

2.50 Synthetic experimental procedures

General Procedure: Pyropheophorbide-a methyl ester (**1a**) was purchased from Chemieliva (China). All other chemicals were purchased from Sigma Aldrich and used without further purification; only *N*-bromosuccinimide, malononitrile and [Pd(PPh_3)$_4$] were purified before use. The chemical reactions were performed under inert an atmosphere (Ar gas) unless otherwise stated. HPLC was performed on an Agilent 1100 instrument (Zorbax Eclipse XDB C18 column (4.6 x 150 mm, 5 μM). NMR spectra were acquired on 400 MHz (Bruker AVIIIHD 400), 500 MHz (Bruker AVII 500, Bruker AVIIIHD 500), 600 MHz (Bruker AVIIIHD 600), and 700 MHz (Bruker AVIII 700) spectrometers. Chemical shifts are reported in ppm relative to TMS and with the solvent ($CDCl_3$ unless otherwise stated) resonance as internal standard. The ^{1}H-NMR spectra of all the compounds were assigned using the spectrum of **1a** as reference, and also using COSY for some compounds. The ^{13}C-NMR spectra of the compounds were assigned using their HSQC and HMBC spectra. MALDI-ToF (Waters MALDI micro) spectrometer was used for mass analysis. The UV-Vis (Perkin Elmer Lambda 20) and fluorescence (ISA instruments SA Inc., FluoroMax-2) measurements were performed in CH_2Cl_2 at 25 °C. The units of molar absorptivity are M^{-1} cm^{-1}, and their logarithmic values are reported.

2.51 Synthesis

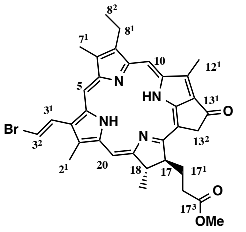

(*E*)-3^2-Bromopyropheophorbide-a methyl ester 5: Pyropheophorbide-a methyl ester **1a** (25.0 mg, 45 μmol) was dissolved in 1,2-dichloroethane (15 mL) in a round bottom two-neck flask. *N*-Bromosuccinimide (8.2 mg, 45 μmol) was dissolved in 1,2-dichloroethane (1 mL) and added to the first solution. The reaction mixture was then heated to reflux under Ar at 84 °C. The reaction was monitored throughout using reverse phase HPLC (Table 1). After 3 h, an additional portion of *N*-bromosuccinimide (4.1 mg, 22 μmol) was added to the reaction mixture followed by the addition of another batch of *N*-bromosuccinimide (4.1 mg, 22 μmol) after 6.5 h. The heating was stopped after 9 h, and the reaction mixture was brought to room temperature. Two reactions were performed in parallel at 25 mg scale and then both mixtures were combined after the reaction was completed. The resultant mixture was passed through a plug of SiO_2 using 5% MeOH in CH_2Cl_2 as eluent, followed by purification through flash column chromatography using 5% EtOAc in CH_2Cl_2 as eluent to give **5**. **Yield:** 44.4 mg, 78 %. **^{1}H-NMR** (400 MHz, $CDCl_3$) δ/ppm: 9.17 (s, 1H; 10-H), 8.65 (s, 1H; 5-H), 8.44 (s, 1H; 20-

H), 7.84 (d, ^{3}J = 14.0 Hz, 1H; 3^1-H), 6.90 (d, ^{3}J = 14.0 Hz, 1H; 3^2-H), 5.23 (d, ^{2}J = 19.6 Hz, 1H; 13^2-$\mathbf{CH_2}$), 5.08 (d, ^{2}J = 19.6 Hz, 1H; 13^2-$\mathbf{CH_2}$), 4.47 (q, *J* = 7.3 Hz, 1H; 18-H), 4.27 (m, 1H; 17-H), 3.69 (q, ^{3}J = 9.9 Hz, 2H; 8^2-$\mathbf{CH_2}$), 3.67 (s, 3H; 12-CH_3), 3.52 (s, 3H; 17^3-$CO_2\mathbf{CH_3}$), 3.11 (s, 3H; 2^1-CH_3), 2.90 (s, 3H; 7^1-CH_3), 2.76-2.20 (several m, 4H; 17-$\mathbf{CH_2CH_2}$COOMe), 1.84 (d, ^{3}J = 7.3 Hz, 3H; 18^1-$\mathbf{CH_3}$), 1.57 (t, ^{3}J = 7.6 Hz; 8^2-$\mathbf{CH_3}$), –0.08 (br s, 1H; NH) and –2.26 (br s, 1H; NH). **^{13}C-NMR** (100 MHz, $CDCl_3$) δ/ppm: 196.4 ($C13^1$), 172.5 ($C17^3$), 171.2 (C19), 160.8 (C16), 154.7 (C6), 150.8 (C9), 149.0 (C14), 144.9 (C8), 140.9 (C1), 138.1 (C12), 136.0 (C7), 134.9 (C4), 133.0 (C3), 131.3 (C11), 130.8 (C2), 129.5 ($C3^1$), 128.8 (C13), 112.1 ($C3^2$), 106.4 (C15), 104.0 (C10), 96.7 (C5), 93.3 (C20), 52.0 (C17), 52.0 ($C17^5$), 50.1 (C18), 48.3 ($C13^2$), 31.3 ($C17^2$), 30.1 ($C17^1$), 23.4 ($C18^1$), 19.5 ($C8^1$), 17.6 ($C8^2$), 12.4 ($C2^1$), 12.2($C12^1$), 11.3 ($C7^1$). ***m/z* (MALDI-ToF)** 628.8 ($C_{34}H_{35}N_4O_3{}^{81}Br$: $[M+H]^+$ calculated 628.2).

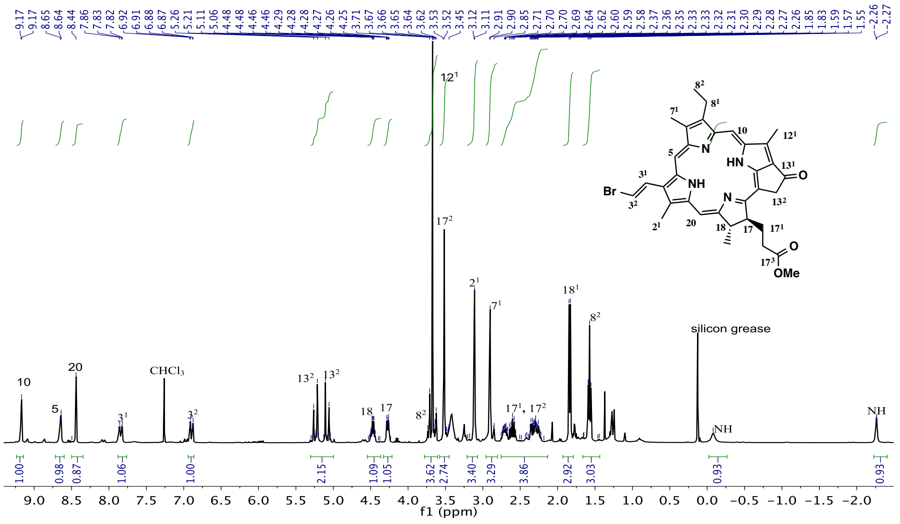

Figure 17: ^{1}H-NMR spectrum of **5** (400 MHz, $CDCl_3$, 298 K).

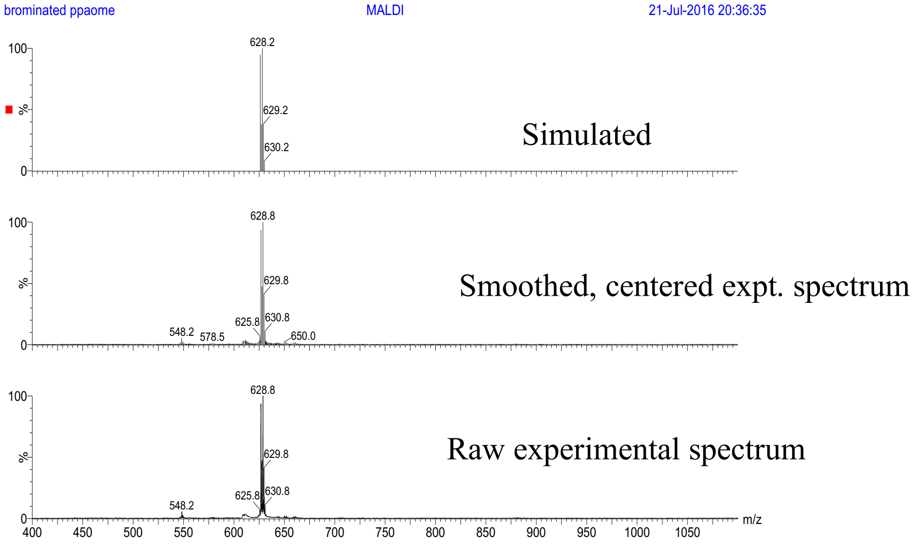

Figure 18: MALDI ToF mass spectrum of **5.**

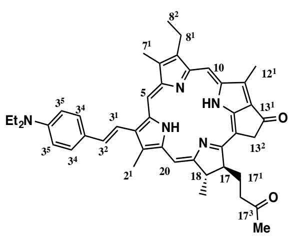

(*E*)-3^2-(*para*-Diethyl amino phenyl) pyropheophorbide-a methyl ester 2a: (*E*)-3^2-Bromopyropheophorbide-a methyl ester **5** (44.0 mg, 67 μmol) was mixed with *para*-(*N,N*-diethylamine)phenyl boronic acid (64.6 mg, 334 μmol), $[Pd(PPh_3)_4]$ (7.8 mg, 6.7 μmol), tetrabutylammonium bromide (21.6 mg, 66.9 μmol), aq. sodium hydroxide (1.00 mL, 200 μmol) and toluene (4 mL) in a Schlenk tube. The mixture was degassed by three freeze-pump-thaw cycles and then stirred at 80 °C for 30 min under Ar atmosphere. The reaction was monitored by reverse-phase HPLC (Table 1, Figure 3). The reaction mixture was then washed with water and extracted with CH_2Cl_2, dried over Na_2SO_4 and concentrated. The crude was purified by flash column chromatography using 5% EtOAc in CH_2Cl_2 as eluent and then recrystallized (CH_2Cl_2/hexane) to give **2a** as a brown solid. **Yield:** 44.5 mg, 91 %. **^{1}H-NMR** (400 MHz, $CDCl_3$) δ/ppm: 9.41 (s, 1H; 10-H), 9.32 (s, 1H; 5-H), 8.49 (s, 1H; 20-H), 8.02 (d, ^3J = 16.3 Hz, 1H; 3^2-H), 7.79 (d, ^3J = 8.4 Hz, 2H; 3^4-H and 3^8-H), 7.48 (d, ^3J = 16.3 Hz, 1H; 3^1-H), 6.84 (d, ^3J = 8.4 Hz, 2H; 3^5-H and 3^7-H), 5.23 (d, ^2J = 19.7 Hz, 1H; 13^2-C**H$_2$**), 5.09 (d, ^2J = 19.7 Hz, 1H; 13^2-C**H$_2$**), 4.47 (q, J = 7.4 Hz, 1H; 18-H), 4.26 (m, 1H; 17-H), 3.63 (m, 2H; 8^1-C**H$_2$**), 3.63 (s, 3H; 12^1-CH_3), 3.62 (s, 3H; 17^2 -CO_2C**H$_3$**), 3.50 (q, ^3J = 7.0 Hz, 4H; N(C**H$_2$**CH_3)$_2$), 3.38 (s, 3H; 2^1-CH_3), 3.17 (s, 3H; 7^1-CH_3), 2.75-2.25 (several m, 4H; 17-C**H$_2$**C**H$_2$**COOMe), 1.82 (d, ^3J = 7.3 Hz, 3H; 18^1-C**H$_3$**), 1.68 (t, ^3J = 7.6 Hz; 8^2-C**H$_3$**), 1.29 (t, ^3J = 7.0 Hz, 6H; N(CH_2C**H$_3$**)$_2$), 0.58 (br s, 1H; NH) and –1.63 (br s, 1H; NH). **^{13}C-NMR** (100 MHz, $CDCl_3$) δ/ppm: 196.5 (C13^1), 173.8 (C17^3), 171.6 (C19), 160.3 (C16), 155.4 (C6), 150.6 (C9), 149.3 (C14), 148.2 (C3^6), 144.9 (C8), 142.3 (C1), 137.8 (C12), 137.3(C3^1), 137.0 (C13), 136.8 (C4), 136.0 (C7), 130.4 (C3), 129.9 (C2), 128.5 (C3^4), 128.0 (C11), 125.2 (C3^3), 115.4 (C3^2), 112.0 (C3^5), 105.9 (C15), 104.1 (C10), 96.9 (C5), 92.8 (C20), 52.0 (C17), 51.8 (C17^5-OCH_3), 50.2 (C18), 48.3 (C13^2), 44.6 (N**C**H$_2$CH$_3$), 31.3 (C17^1), 30.1 (C17^2), 23.4 (C18^1), 19.6 (C8^1), 17.7 (C8^2), 13.0 (NCH$_2$**C**H$_3$), 12.6 (C2^1), 12.2(C12^1), 11.4 (C7^1). ***m/z* (MALDI-ToF)** 696.6 ($C_{44}H_{49}N_5O_3$: $[M+H]^+$ calculated 696.4). **UV-Vis** (CH_2Cl_2, 25 °C) λ_{max} (log ε): 678 nm (4.70), 621 nm (4.02), 550 nm (4.20), 515 nm (4.28) and 420 nm (4.94).

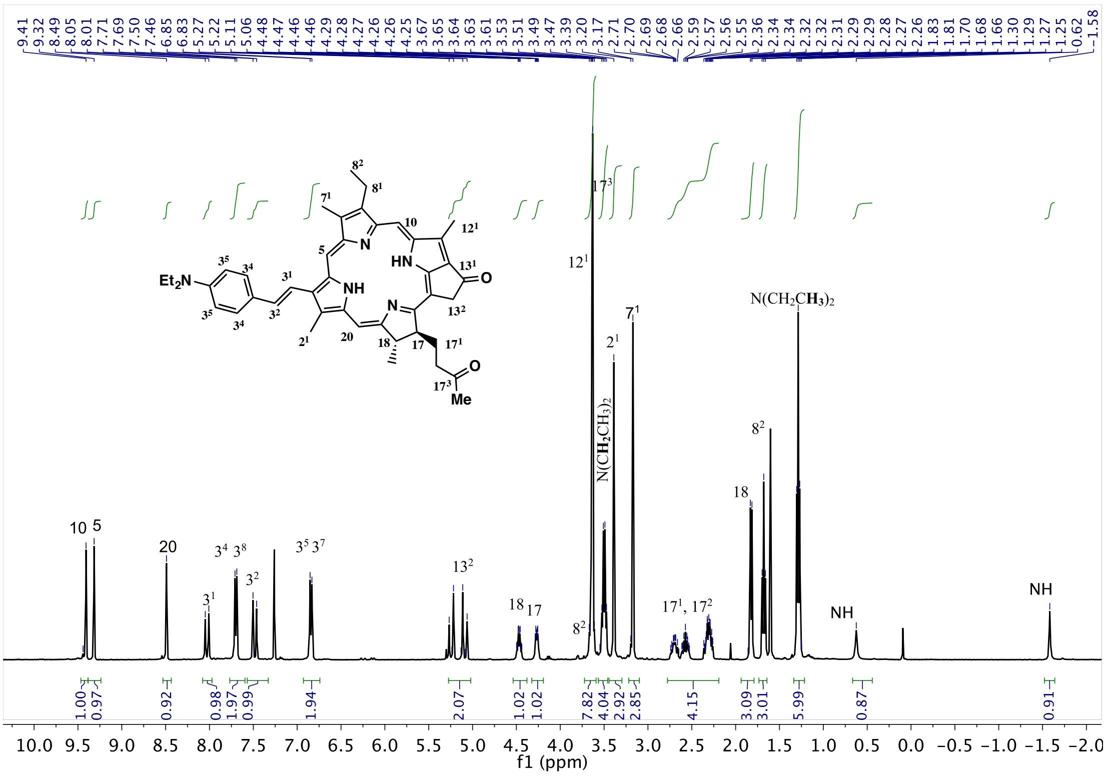

Figure 19: ^{1}H-NMR spectrum of **2a** (400 MHz, $CDCl_3$, 298 K).

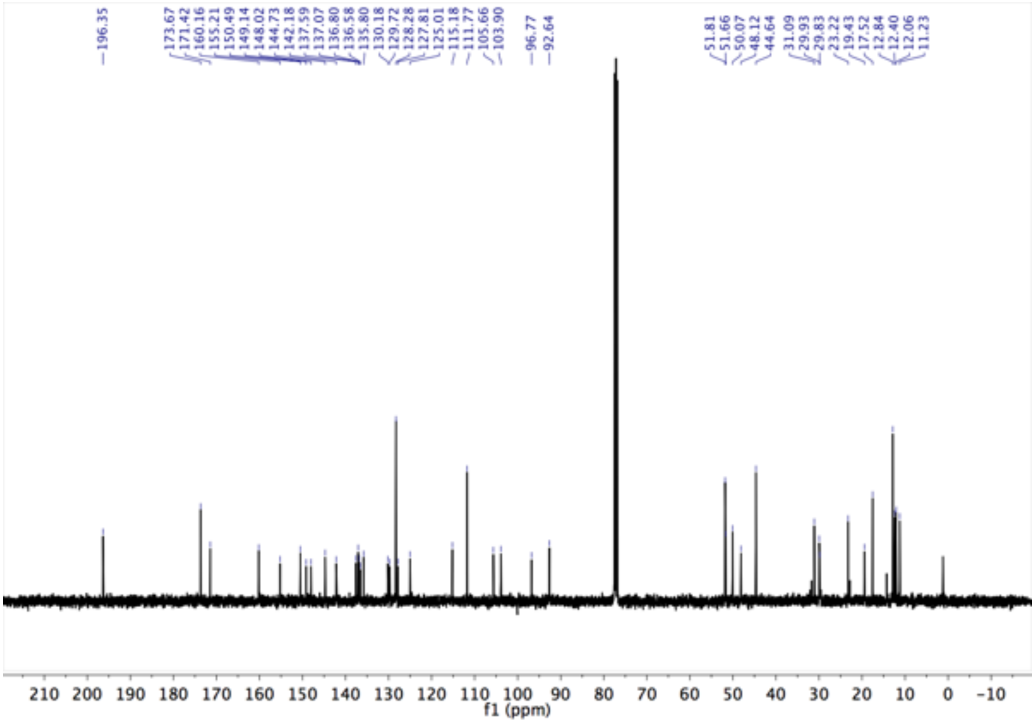

Figure 20: ^{13}C NMR of spectrum of **2a** (100 MHz, CDCl3, 298 K).

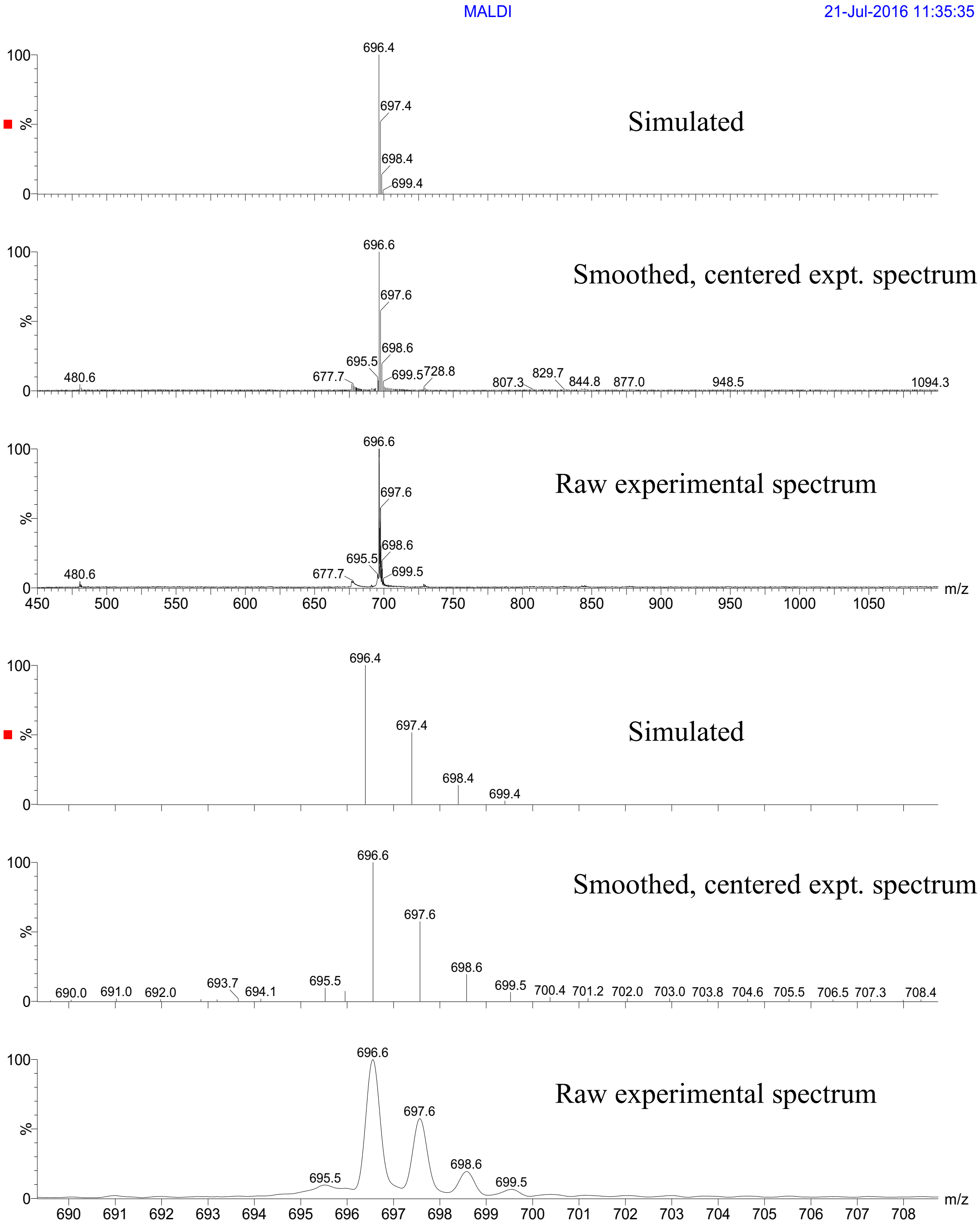

Figure 21: MALDI ToF mass spectrum of **2a.**

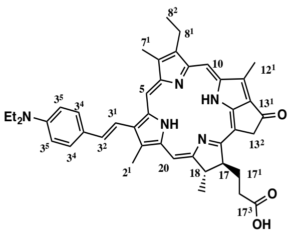

(*E*)-3^{2}-(*para*-Diethyl amino phenyl) pyropheophorbide-a 2b: (*E*)-3^{2}-(*para*-Diethyl amino phenyl) pyropheophorbide-a methyl ester **2a** (30.0 mg, 42.6 µmol) was dissolved in 37% concentrated HCl (18 mL) at 0 °C and stirred at 20 °C under Ar atmosphere for 3 h. After 3 h, the reaction mixture was poured in an ice/water bath and the compound was extracted with chloroform. The organic layer was washed with sat. $NaHCO_3$ (aq) and water. The organic layer was then dried over Na_2SO_4 and the solvent was evaporated under reduced pressure. The solid material was recrystallized (CH_2Cl_2/hexane) to give **2b** as a brown solid. **Yield:** 27.5 mg, 94 %. **^{1}H-NMR** (500 MHz, $CDCl_3$) δ/ppm: 9.35 (s, 1H; 10-H), 9.24 (s, 1H; 5-H), 8.45 (s, 1H; 20-H), 7.97 (d, ^{3}J = 16.3 Hz, 1H; 3^{2}-H), 7.69 (d, ^{3}J = 8.2 Hz, 2H; 3^{4}-H and 3^{8}-H), 7.46 (d, ^{3}J = 16.3 Hz, 1H; 3^{1}-H), 6.83 (d, ^{3}J = 8.2 Hz, 2H; 3^{5}-H and 3^{7}-H), 5.22 (d, ^{2}J = 19.3 Hz, 1H; 13^{2}-C**H**$_2$), 5.03 (d, ^{2}J = 19.3 Hz, 1H; 13^{2}-C**H$_2$**), 4.45 (m, 1H; 18-H), 4.24 (m, 1H; 17-H), 3.58 (m, 5H; 8^{1}-**CH$_2$**; 12^{1}-CH$_3$), 3.49 (q, ^{3}J = 7.0 Hz, 4H; N(C**H$_2$**CH$_3$)$_2$), 3.34 (s, 3H; 2^{1}-CH$_3$), 3.12 (s, 3H; 7^{1}-CH$_3$), 2.72–2.18 (several m, 4H; 17-C**H$_2$**C**H$_2$**COOH), 1.78 (d, ^{3}J = 7.4 Hz, 3H; 18^{1}-C**H$_3$**), 1.65 (t, ^{3}J = 7.7 Hz,3H; 8^{2}-C**H$_3$**), 1.28 (t, ^{3}J = 7.0 Hz, 6H; N(CH$_2$C**H$_3$**)$_2$), –1.61 (br s, 1H; NH). **^{13}C-NMR** (125 MHz, $CDCl_3$) δ/ppm: 196.7 (C13^{1}), 177.8 (C17^{3}), 171.6 (C19), 160.3 (C16), 155.4 (C6), 150.6 (C9), 149.3 (C14), 147.9 (C3^{6}), 144.9 (C8), 142.3 (C1), 137.7 (C12), 137.1 (C3^{1}), 137.0 (C13), 136.7 (C4), 135.9 (C7), 130.1 (C3), 129.9 (C2), 128.3 (C3^{4}), 127.9 (C11), 125.3 (C3^{3}), 115.4 (C3^{2}), 112.0 (C3^{5}), 105.7 (C15), 104.1 (C10), 96.9 (C5), 92.8 (C20), 51.6 (C17), 50.1 (C18), 48.1 (C13^{2}), 44.8 (N**C**H$_2$CH$_3$), 31.0 (C17^{1}), 29.9 (C17^{2}), 23.4 (C18^{1}), 19.5 (C8^{1}), 17.5 (C8^{2}), 12.8 (NCH$_2$**C**H$_3$), 12.4 (C2^{1}), 12.0 (C12^{1}), 11.3 (C7^{1}). ***m/z* (MALDI-ToF):** 682.5 ($C_{43}H_{47}N_5O_3$:$[M+H]^+$ calculated 682.4). **UV-Vis** (CH_2Cl_2, 25 °C) λ_{max} (log ε): 677 nm (4.62), 620 nm (3.98), 550 nm (4.14), 515 nm (4.23) and 420 nm (4.89).

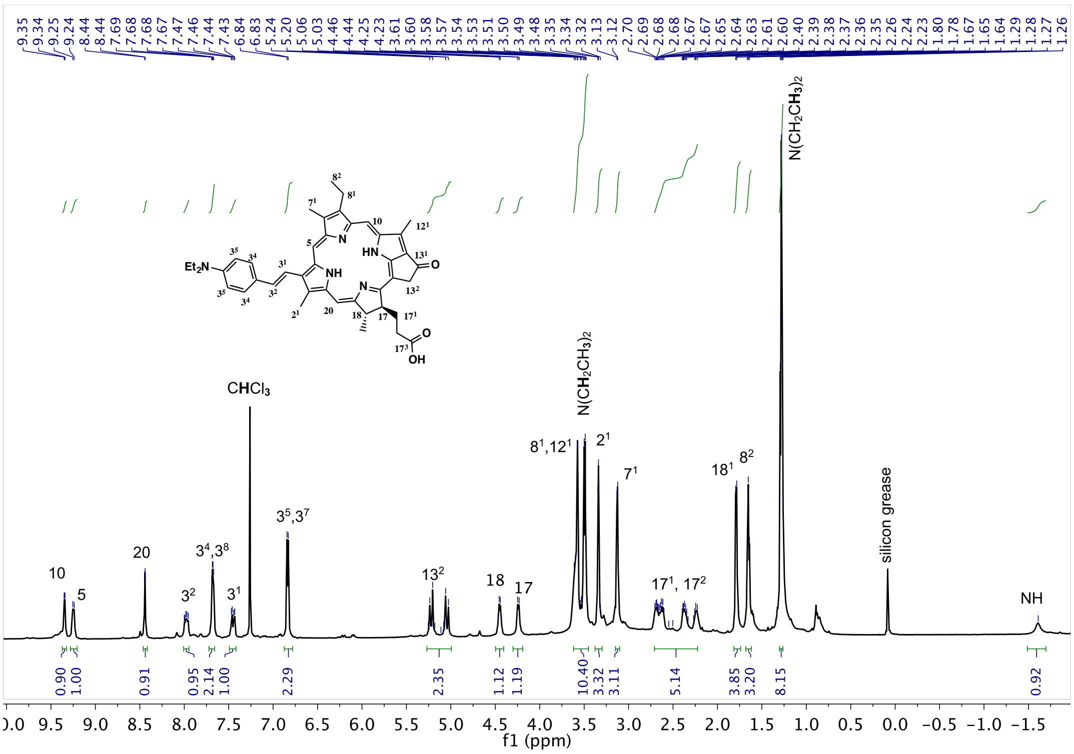

Figure 22: ^{1}H-NMR spectrum of **2b** (500 MHz, $CDCl_3$, 298 K).

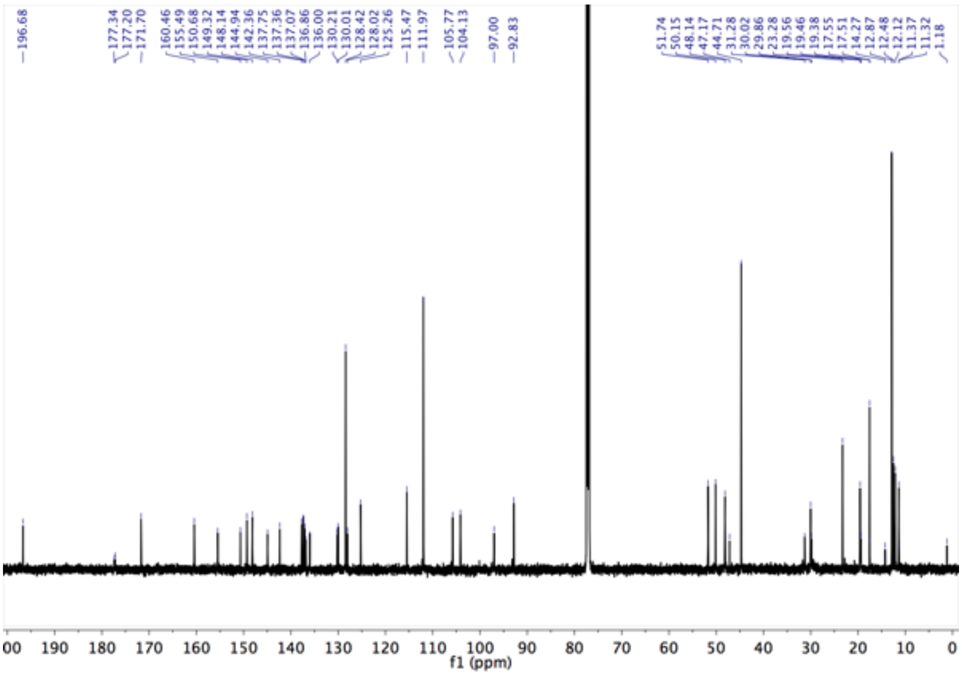

Figure 23: ^{13}C NMR spectrum of **2b** (125 MHz, $CDCl_3$, 298 K).

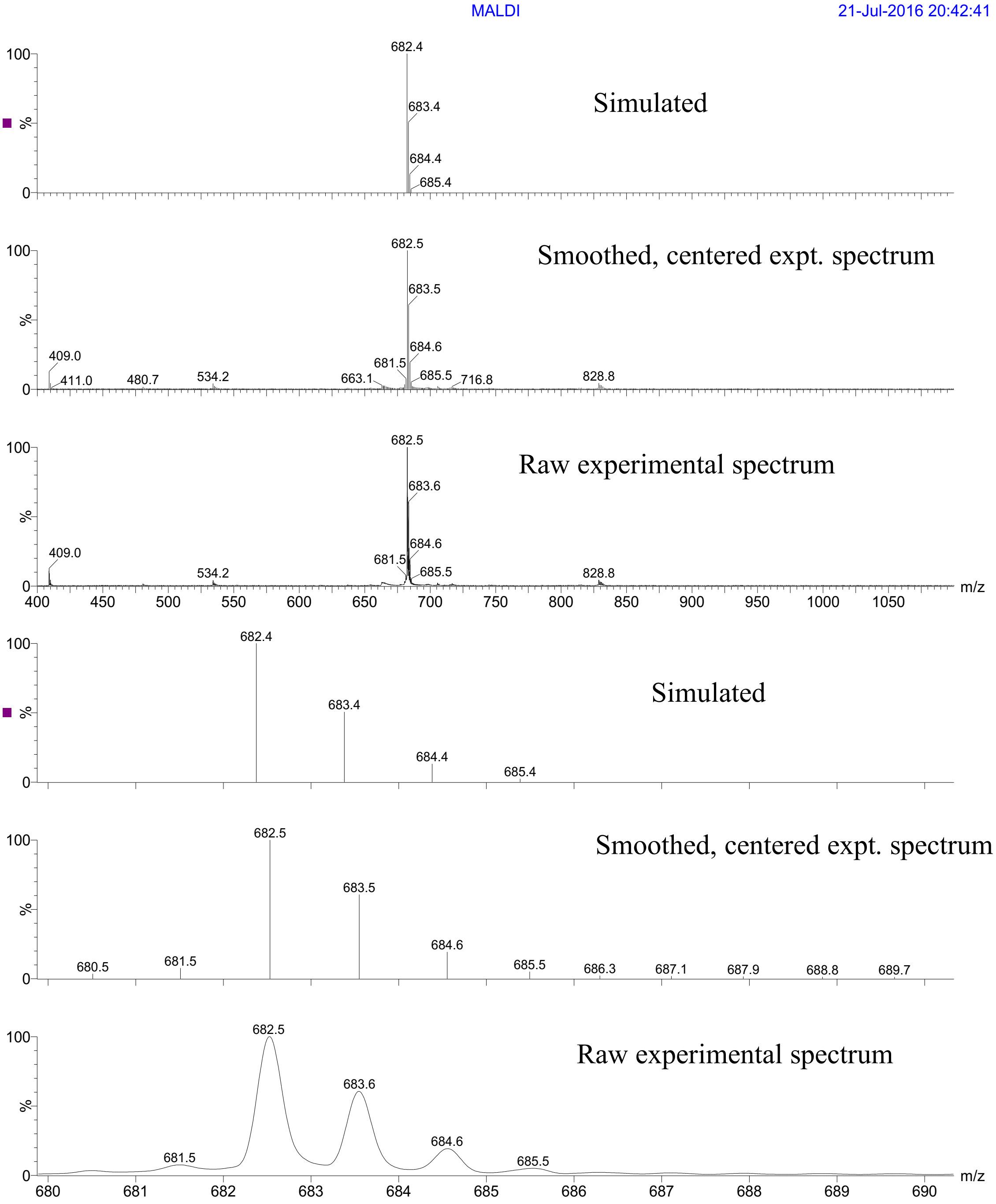

Figure 24: MALDI ToF mass spectrum of **2b**.

Methyl-13^1-Deoxo-13^1-(dicyanomethylene)pyropheophorbide-a 3a:[39]

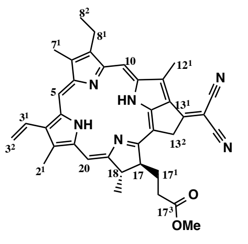

Pyropheophorbide-a methyl ester **1a** (25 mg, 46 µmol), malononitrile (301 mg, 4.5 mmol) and triethylamine (1.4 mL) were dissolved in anhydrous THF (6.9 mL). The reaction mixture was heated to reflux at 67 °C for 1 h under Ar atmosphere. The reaction was monitored through RP-HPLC. When small peaks of byproducts were observed after around 1 h, the heating and stirring was stopped, and the solvent was evaporated at 40 °C at 290 mbar pressure to complete the reaction. The residue obtained was added to an aq. HCl solution (1%) and extracted with CH_2Cl_2. The crude product was washed with water, dried over Na_2SO_4, filtered and the solvent was evaporated. The crude product was then purified by flash column chromatography (0.5–1% Et_2O in CH_2Cl_2) and recrystallized (CH_2Cl_2/hexane) to give **3a** as a dark green solid. **Yield**: 21.0 mg, 77%. **^{1}H-NMR** (400 MHz, $CDCl_3$) δ/ppm: 9.12, 8.82 and 8.37 (each s, 1H; meso H), 7.87 (dd, ^3J = 11.6 Hz, ^3J = 17.9 Hz, 1H; C***H***=CH$_2$), 6.26 (dd, ^3J = 17.9 Hz, ^2J= 1.1 Hz, 1H; CH=C***H***$_2$), 6.17 (dd, ^3J= 11.6 Hz, ^2J= 1.1 Hz, 1H; CH=C***H***$_2$), 5.20 (d, ^2J = 20.7 Hz, 1H; 13^2-C*H*$_2$, exocyclic ring), 5.09 (d, ^2J = 20.7 Hz, 1H; 13^2-C*H*$_2$, exocyclic ring), 4.30 (q, ^3J= 7.2 Hz, 1H; 18-H), 4.02 (d, ^3J= 9.1 Hz, 1H; 17-H), 3.67 (s, 6H; OC*H*$_3$), 3.47 (q, ^3J = 7.6 Hz, 2H; 8^1-C***H***$_2$-CH$_3$), 3.33, 3.14, and 3.09 (each s, 3H; 12^1, 2^1, 7^1-C*H*$_3$), 2.61-1.91 (several m, 4H; C***H***$_2$C***H***$_2$COOMe), 1.75 (d, ^3J= 7.3 Hz, 3H; 18-CH$_3$), 1.55 (t, ^3J= 7.6 Hz, 3H; CH$_2$C***H***$_3$) and 0.89 (br s, 1H; NH) and –1.11 (br s, 1H; NH). **^{13}C-NMR** (100 MHz, $CDCl_3$) δ/ppm: 173.3 (C19), 172.7 (C17^3), 168.0 (C16), 160.9 (C6), 156.5 (C9), 151.3 (C14), 147.2 (C13^1), 145.3 (C8), 143.0 (C1), 138.4 (C12), 137.5 (C3^1), 136.6 (C13), 132.3 (C4), 129.5 (C7), 128.9 (C3), 127.7 (C2), 123.2 (C11), 116.1 (13^1-**C**N), 115.5 (C3^2), 105.0 (C15), 103.4 (C10), 97.6 (C5), 93.4 (C20), 70.2 (**C**CN), 52.0(17^5-OMe), 51.5 (C17), 50.0 (C18), 45.8 (C13^2), 31.2 (C17^1), 30.0 (C17^2), 23.0 (C18^1), 19.4 (C8^1), 17.3 (C8^2), 14.0 (C2^1), 12.2 (C12^1), 11.3 (C7^1). ***m/z*** **(MALDI-ToF)** 596.7 ($C_{37}H_{36}N_6O_2$, $[M]^+$ calculated 596.3). **UV-Vis** (CH_2Cl_2, 25 °C) λ_{max} (log ε): 704 nm (4.97), 645 nm (4.39), 574 nm (4.19), 534 nm (4.05) and 453 nm (4.93), 432 nm (4.91), 385 nm (4.91), 351 nm (4.81).

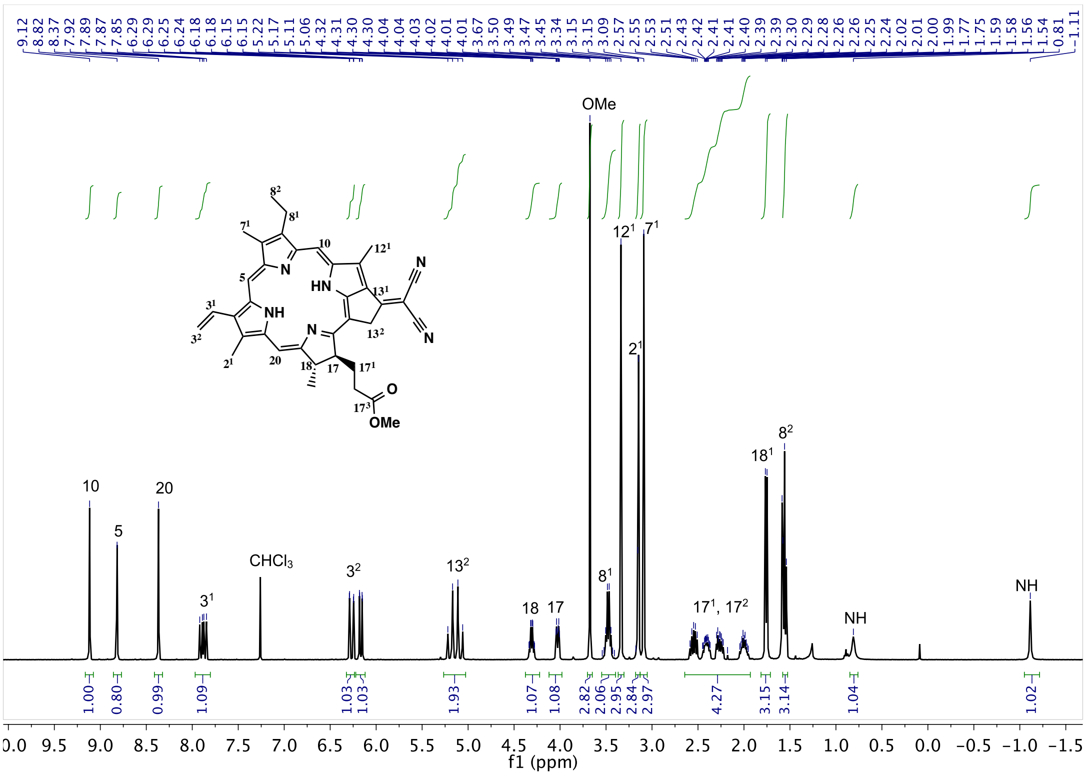

Figure 26: ^{1}H-NMR spectrum of **3a** (500 MHz, $CDCl_3$, 298 K).

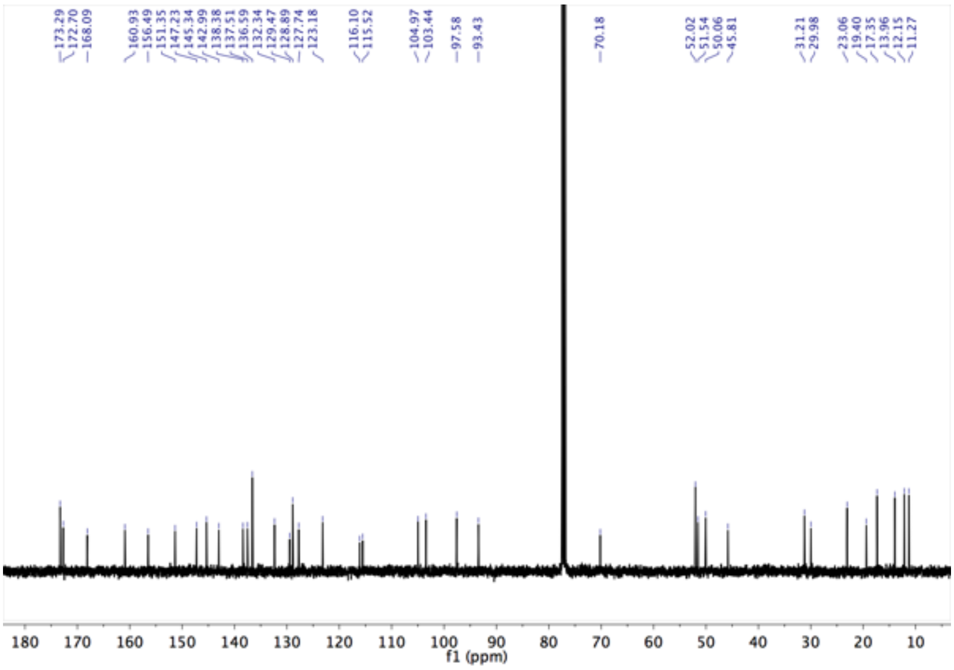

Figure 27: ^{13}C NMR spectrum of **3a** (125 MHz, $CDCl_3$, 298 K).

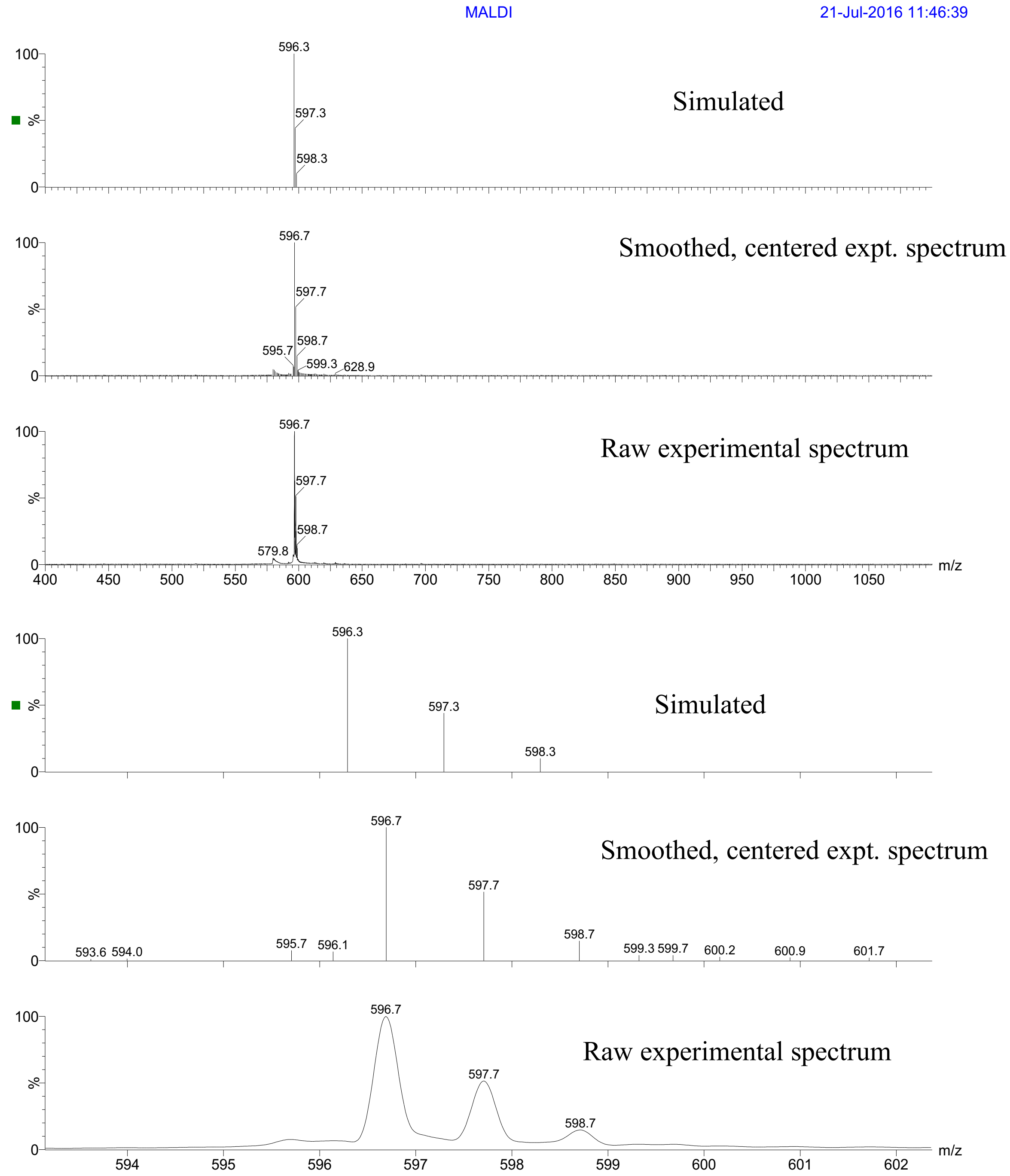

Figure 28: MALDI ToF mass spectrum of **3a**.

13^1-Deoxo-13^1-(dicyanomethylene)pyropheophorbide-a 3b:

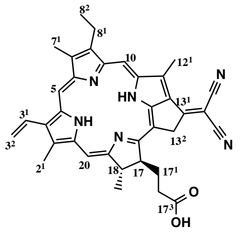

Pyropheophorbide-a **1b** (11 mg, 20 µmol), malononitrile (135 mg, 1.9 mmol) and triethylamine (617 µL, 4.42 mmol) were dissolved anhydrous THF (3 mL). The reaction mixture was degassed by freeze-pump-thaw and then heated to reflux at 67 °C for 1 h under Ar atmosphere. After 1 h, the solvent was evaporated at 40–45 °C at 300 mbar pressure to complete the reaction. TLC (49% $CHCl_3$, 49% EtOAc, 2% MeOH, 0.1% CH_3COOH) and MALDI mass spectrometry of the crude product confirmed the completion of the reaction. The residue obtained was added to an aq. HCl solution (1%) and extracted with CH_2Cl_2. The crude product was washed with water, dried over Na_2SO_4, filtered and the solvent was evaporated. The residue was then purified by flash column chromatography using the same eluent system used for TLC and recrystallized (CH_2Cl_2/hexane) to give **3b** as a green solid. **Yield**: 6.0 mg, 51%.

Alternatively, **3b** was synthesized by hydrolyzing the ester of **3a** (21.0 mg, 35 µmol) by following the protocol used to synthesize **2b** from **2a**. Yield: 19.0 mg, 93%. **^{1}H-NMR** (700 MHz, $CDCl_3$, TFA added) δ/ppm: 10.05, 9.77, and 8.69 (each s, 1H; meso H); 7.76 (dd, ^3J=11.6 Hz, ^3J = 17.7 Hz, 1H; 3^1-H); 6.36 (d, ^3J = 11.6 Hz, 1H; 3^2-H); 6.16 (d, ^3J = 17.7 Hz, 1H; 3^2-H); 5.83 (d, ^2J = 21.0 Hz, 1H; 13^2-H; exocyclic ring); 5.69 (d, ^2J = 21.0 Hz, 1H; 13^2-H; exocyclic ring); 4.68 (m, 2H; 18-H; 17-H); 3.86 (s, 3H; 12^1- CH_3); 3.84 (q, ^3J = 9.7 Hz, 2H; 8^1- $C\boldsymbol{H_2}CH_3$); 3.30 and 3.24 (each s, 3H; 2^1- CH_3, 7^1- CH_3); 2.96-2.49 (several m, 4H; 17^1-CH_2, 17^2-CH_2); 1.87 (d, ^3J = 7.4 Hz, 3H; 18^1-CH_3); 1.63 (t, ^3J = 7.6 Hz, 3H; 8^2-CH_3). **^{13}C-NMR** (175 MHz, $CDCl_3$, TFA added) δ/ppm: 179.7 ($C17^3$), 168.0 (C19), 163.7 (C16), 154.4 (C6), 151.8 (C9), 151.1 (C14), 148.2 ($C13^1$), 144.8 (C8), 142.3 (C1), 141.6 (C12), 141.0 ($C3^1$), 139.7 (C13), 139.0 (C4), 137.5 (C7), 136.3 (C3), 133.8 (C2), 128.8 (C11), 127.0 (13^1-**C**N), 109.5 ($C3^2$), 105.0 (C15), 103.5 (C10), 92.3 (C5), 86.6 (C20), 77.6 (**C**CN), 51.1 (C17), 47.0 (C18), 45.8 ($C13^2$), 30.0 ($C17^1$), 29.9 ($C17^2$), 22.1 ($C18^1$), 20.0 ($C8^1$), 16.1 ($C8^2$), 15.2 ($C2^1$), 11.8 ($C12^1$), 11.1 ($C7^1$). ***m/z*** **(MALDI-ToF)** 582.6 ($C_{36}H_{34}N_6O_2$, $[M]^+$ calculated 582.3). **UV-Vis** (CH_2Cl_2, 25 °C) λ_{max} (log ε): 709 nm (4.90), 644 nm (4.33), 574 nm (4.13), 534 nm (3.99) and 453 nm (4.87), 431 nm (4.86), 385 nm (4.86), 351 nm (4.76).

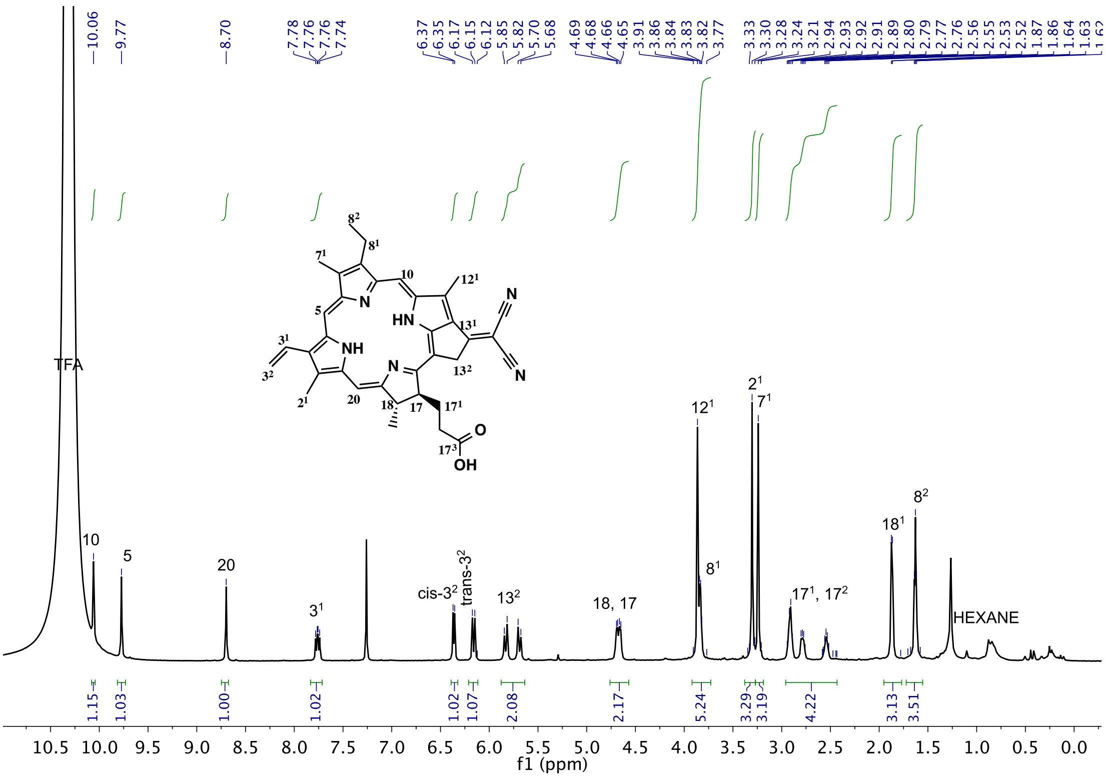

Figure 29: ^{1}H-NMR spectrum of **3b** (700 MHz, $CDCl_3$, TFA, 298 K).

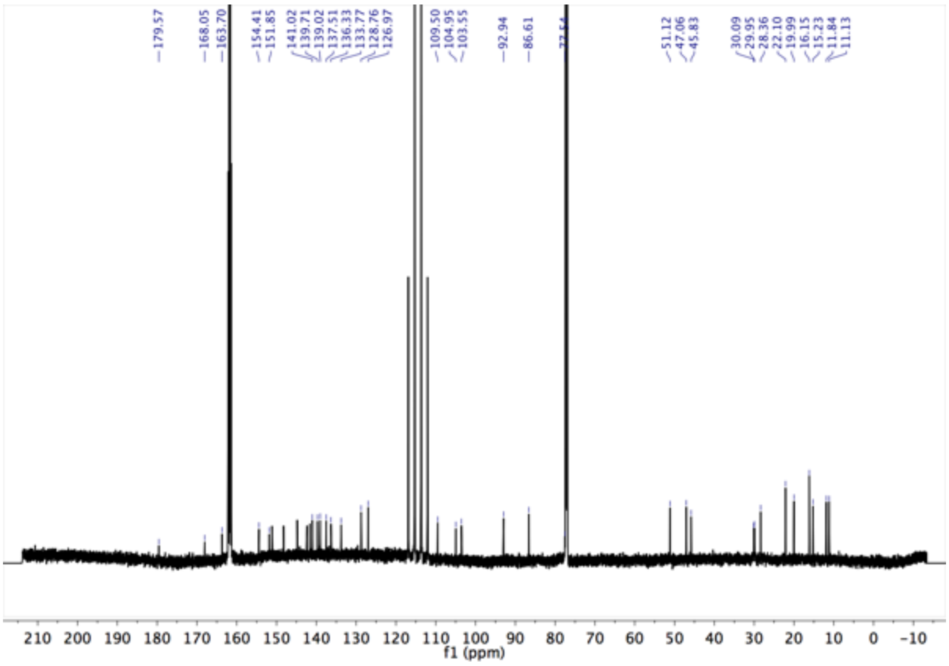

Figure 30: ^{13}C NMR spectrum of **3b** (175 MHz, $CDCl_3$, TFA, 298 K).

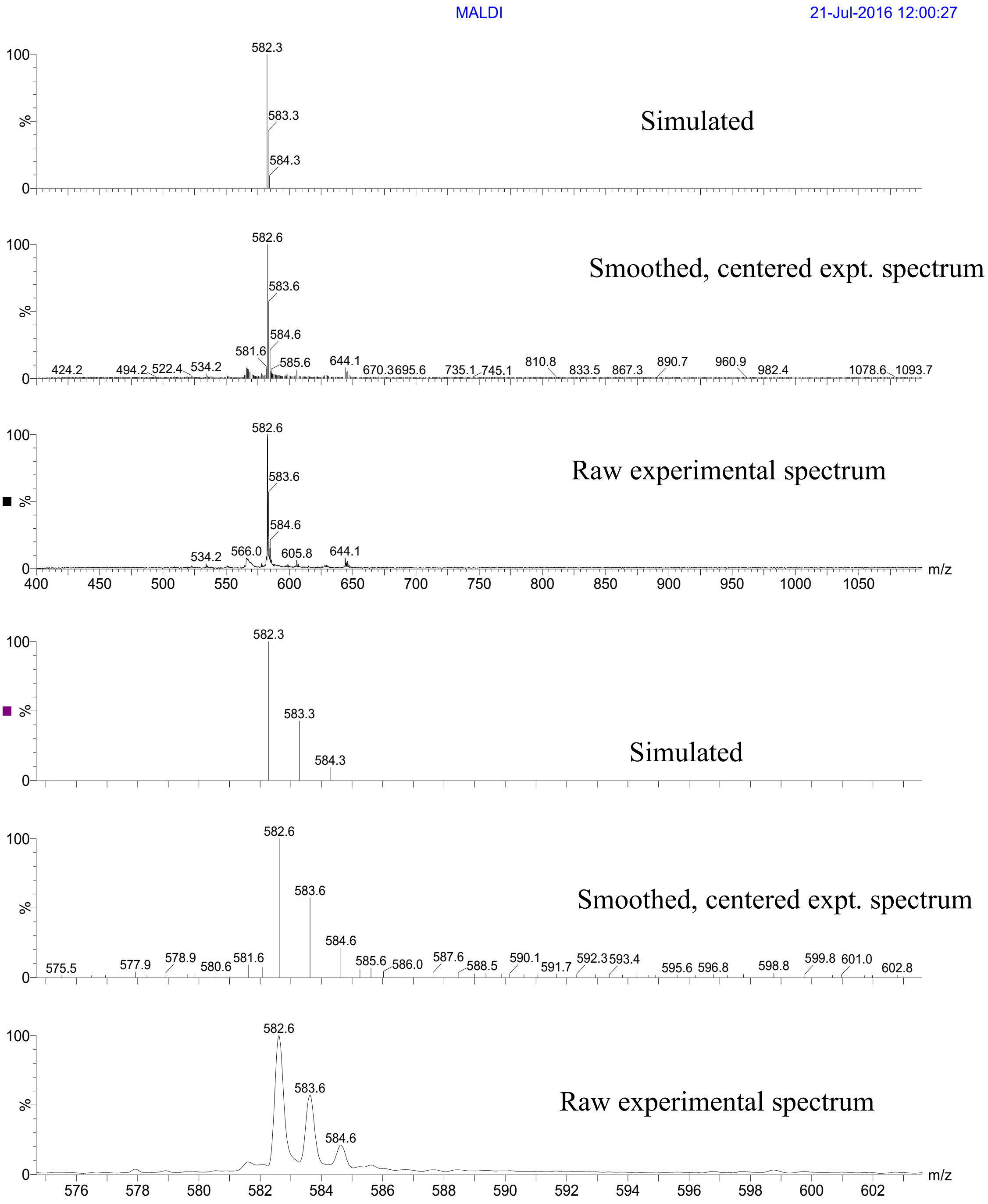

Figure 31: MALDI ToF mass spectrum of **3b**.

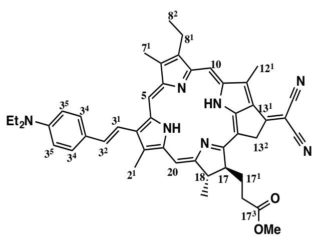

Methyl-13^1-deoxo-13^1-(dicyanomethylene)-(E)-3^2-(*para*-diethyl amino phenyl) pyropheophorbide-a 4a: (*E*)-3^2-(*para*-Diethyl amino phenyl) pyropheophorbide-a methyl ester **2a** (40.0 mg, 57.5 µmol), malononitrile (380 mg, 5.75 mmol) and triethylamine (1.72 mL, 12.3 mmol) were dissolved in anhydrous THF (11 mL). The reaction mixture was degassed by freeze-pump-thaw and then heated to reflux at 67 °C for 1 h under inter atmosphere. After 1 h, the solvent was evaporated at 40 °C at 300 mbar pressure to complete the reaction. The completion of the reaction was confirmed by RP-HPLC using the gradient triple eluent system (Table 1) and TLC (2% Et_2O in CH_2Cl_2). The reaction mixture was added to an aq. HCl solution (1%) and extracted with CH_2Cl_2. The mixture was washed with water, dried over Na_2SO_4, filtered and then the solvent was evaporated. The crude product was then purified by flash column chromatography (1% Et_2O in CH_2Cl_2) and recrystallized (CH_2Cl_2/hexane) to give **4a** as a green solid. **Yield**: 35.3 mg, 82%. **^{1}H-NMR** (400 MHz, $CDCl_3$) δ/ppm: 9.19 (s, 1H; 10-H), 9.12 (s, 1H; 5-H), 8.30 (s, 1H; 20-H), 7.94 (d, ^3J = 16.3 Hz, 1H; 3^2-H), 7.69 (d, ^3J = 8.8 Hz, 2H; 3^4-H and 3^8-H), 7.45 (d, ^3J = 16.3 Hz, 1H; 3^1-H), 6.84 (d, ^3J = 8.8 Hz, 2H; 3^5-H and 3^7-H), 5.58 (d, ^2J = 20.9 Hz, 1H; 13^2-CH_2), 5.46 (d, ^2J = 20.9 Hz, 1H; 13^2-CH_2), 4.34 (m, 1H; 18-H), 4.15 (m, 1H; 17-H), 3.70 (s, 3H; 12^1-CH_3), 3.64 (s, 3H; 17^2-OMe), 3.58 (q, J^3 = 7.6 Hz, 2H; 8^1-CH_2), 3.51 (q, J^3 = 7.1 Hz, 4H; $N(C\mathbf{H_2}CH_3)_2$), 3.30 (s, 3H; 2^1-CH_3), 3.10 (s, 3H; 7^1-CH_3), 2.63-2.09 (several m, 4H; 17-$C\mathbf{H_2}C\mathbf{H_2}COOMe$), 1.76 (d, ^3J = 7.3 Hz, 3H; 18^1-CH_3), 1.64 (t, ^3J = 7.6 Hz, 3H; 8^2-CH_3), 1.29 (t, ^3J = 7.1 Hz, 6H; $N(CH_2C\mathbf{H_3})_2$), –0.76 (br s, 1H; NH). **^{13}C-NMR** (175 MHz, $CDCl_3$) δ/ppm: 173.4 (C17^3), 173.0 (C19), 168.7 (C16), 161.1 (C6), 156.8 (C9), 151.5 (C14), 148.2 (C3^6), 147.8 (C13^1), 145.4 (C8), 143.7 (C1), 138.6 (C12), 138.2 (C3^1), 137.7 (C13), 137.4 (C4), 136.4 (C7), 130.3 (C3), 129.7 (C2), 128.5 (C3^4), 127.8 (C11), 124.8 (13^1-**C**N) 116.5 (C3^3), 115.8 (13^1-**C**N), 114.7 (C3^2), 111.8 (C3^5), 104.9 (C15), 103.7 (C10), 97.2 (C5), 93.1 (C20), 69.9 (**C**CN), 52.0 (C17), 51.5 (C17^5), 50.0 (C18), 46.0 (C13^2), 44.7 ($\mathbf{N}CH_2CH_3$), 31.7 (C17^1), 30.0 (C17^2), 23.0 (C18^1), 19.4 (C8^1), 17.4 (C8^2), 14.4 (C2^1), 12.9 (NCH_2CH_3), 12.4 (C12^1), 11.3 (C7^1). ***m/z* (MALDI-ToF**) 744.9 ($C_{47}H_{49}N_7O_2$, $[M+H]^+$ calculated 744.4). **UV-Vis** (CH_2Cl_2, 25 °C) λ_{max} (log ε): 716 nm (4.76), 658 nm (4.29), 589 nm (4.15), 541 nm (4.02) and 458 nm (4.79), 433 nm (4.74), 354 nm (4.60).

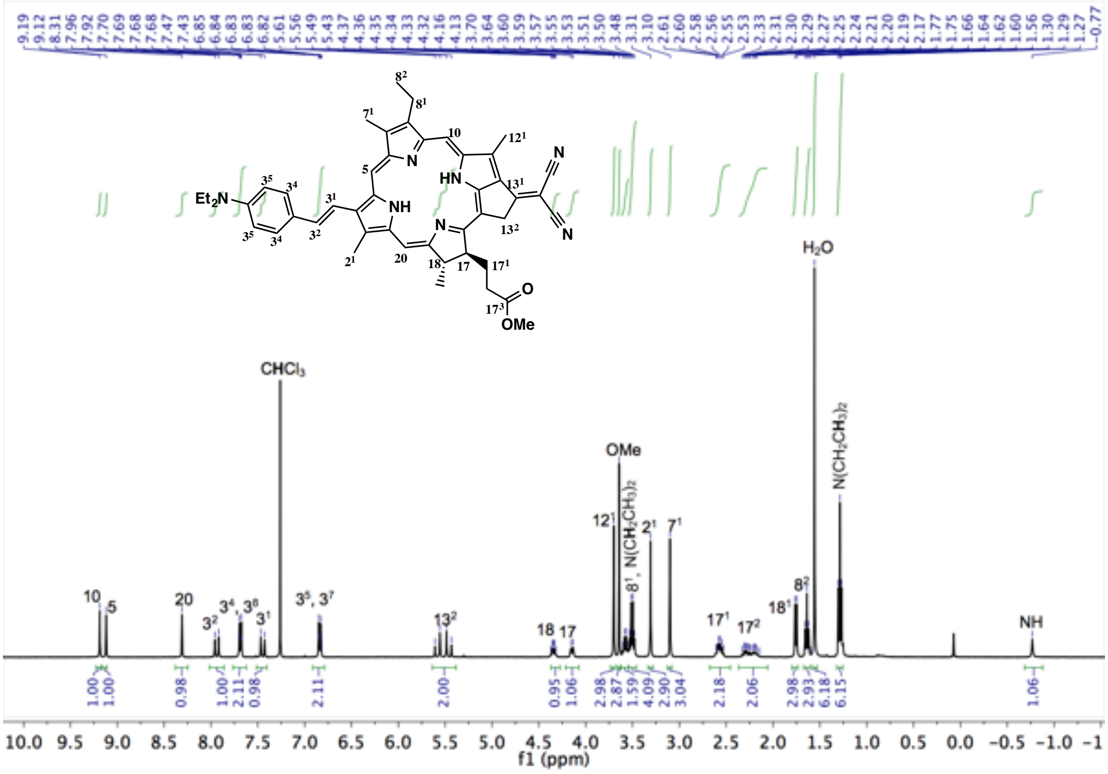

Figure 32: ^{1}H-NMR spectrum of **4a** (400 MHz, CDCl$_3$, 298 K).

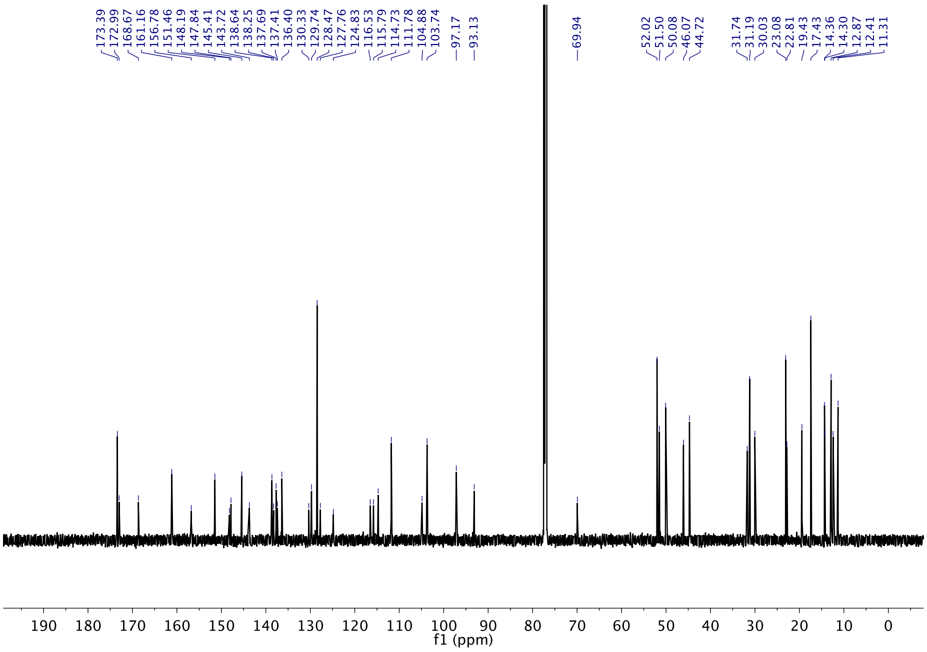

Figure 33: ^{13}C NMR spectrum of **4a** (175 MHz, CDCl$_3$, 298 K).

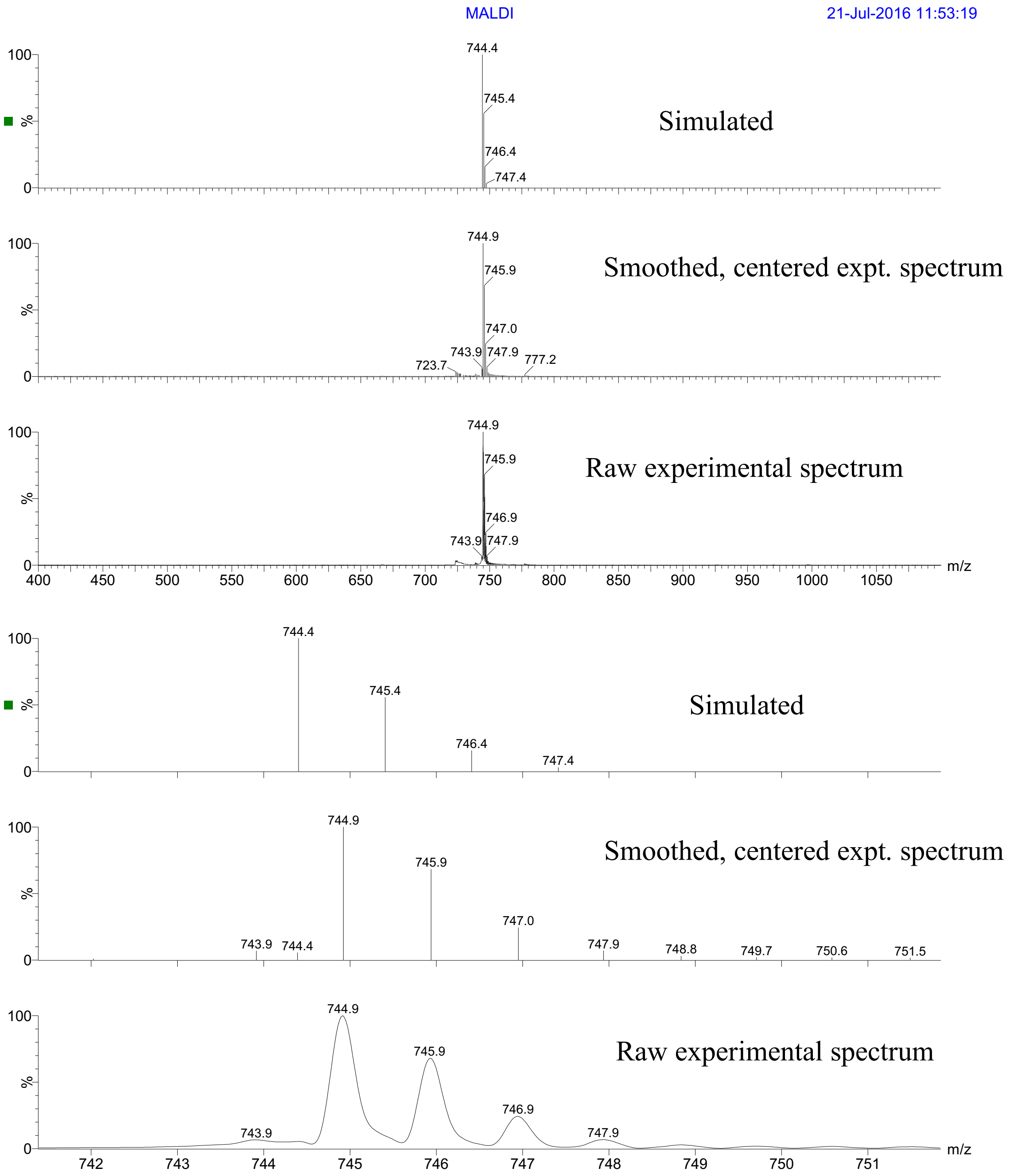

Figure 34: MALDI ToF mass spectrum of **4a**.

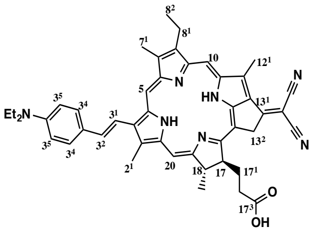

13^1-Deoxo-13^1-(dicyanomethylene)-(*E*)-3^2-(*para*-diethyl amino phenyl) pyropheophorbide-a 4b: Methyl-13^1-deoxo-13^1-(dicyanomethylene)-(*E*)-3^2-(*para*-diethyl amino phenyl) pyropheophorbide-a **4a** (7.0 mg, 9.4 µmol) was dissolved in 37% concentrated HCl (4.5 mL) at 0 °C and stirred at 20 °C under Ar atmosphere for 3 h. After 3 h, the reaction mixture was poured in an ice/water bath and the compound was extracted with chloroform. The organic layer was washed with sat. $NaHCO_3$ (aq.) and water. The organic layer was then dried over Na_2SO_4 and the solvent was evaporated under reduced pressure. The solid material was recrystallized (CH_2Cl_2/hexane) to give **4b** as a dark green solid. **Yield:** 5.5 mg, 80%. **^{1}H-NMR** (600 MHz, $CDCl_3$) δ/ppm: 9.19 (s, 1H; 10-H), 9.11 (s, 1H; 5-H), 8.30 (s, 1H; 20-H), 7.93 (d, ^3J = 16.3 Hz, 1H; 3^2-H), 7.68 (d, ^3J = 8.3 Hz, 2H; 3^4-H and 3^8-H), 7.44 (d, ^3J = 16.3 Hz, 1H; 3^1-H), 6.84 (d, ^3J = 8.3 Hz, 2H; 3^5-H and 3^7-H), 5.59 (d, ^2J = 20.3 Hz, 1H; 13^2-CH_2), 5.45 (d, ^2J = 20.3 Hz, 1H; 13^2-CH_2), 4.35 (q, J^3 = 7.5 Hz, 1H; 18-H), 4.17 (m, 1H; 17-H), 3.71 (s, 3H; 12^1-CH_3), 3.57 (q, ^3J = 7.3 Hz, 2H; 8^1-CH_2), 3.50 (q, ^3J = 7.1 Hz, 4H; $N(C\mathbf{H_2}CH_3)_2$), 3.26 (s, 3H; 2^1-CH_3), 3.03 (s, 3H; 7^1-CH_3), 2.68-2.11 (several m, 4H; 17-$C\mathbf{H_2}C\mathbf{H_2}COOH$), 1.76 (d, ^3J = 7.4 Hz, 3H; 18^1-CH_3), 1.63 (t, ^3J = 7.7 Hz, 3H; 8^2-CH_3), 1.28 (t, ^3J = 7.1 Hz, 6H; $N(CH_2C\mathbf{H_3})_2$), –0.77 (br s, 1H; NH). **^{13}C-NMR** (125 MHz, $CDCl_3$) δ/ppm: 174.6 ($C17^3$), 173.2 (C19), 169.2 (C16), 161.4 (C6), 157.0 (C9), 151.7 (C14), 148.3 ($C3^6$), 148.2 ($C13^1$), 145.6 (C8), 143.9 (C1), 139.0 (C12), 138.4 ($C3^1$), 137.9 (C13), 137.7 (C4), 136.5 (C7), 130.5 (C3), 130.0 (C2), 128.5 ($C3^4$), 128.1 (C11), 125.0 (13^1-**C**N) 116.6 ($C3^3$), 115.9 (13^1-**C**N), 114.9 ($C3^2$), 111.9 ($C3^5$), 105.0 (C15), 104.0 (C10), 97.3 (C5), 93.3 (C20), 70.0 (**C**CN), 51.5 (C17), 50.3 (C18), 46.4 ($C13^2$), 44.7 ($N\mathbf{C}H_2CH_3$), 31.7 ($C17^1$), 30.3 ($C17^2$), 23.1 ($C18^1$), 19.5 ($C8^1$), 17.4 ($C8^2$), 14.6 ($C2^1$), 12.9 ($NCH_2\mathbf{C}H_3$), 12.4 ($C12^1$), 11.4 ($C7^1$). ***m/z* (MALDI-ToF)** 730.9 ($C_{46}H_{47}N_7O_2$, $[M+H]^+$ calculated 730.4). **UV-Vis** (CH_2Cl_2, 25 °C) λ_{max} (log ε): 717 nm (4.75), 659 nm (4.28), 589 nm (4.15), 543 nm (4.02) and 459 nm (4.77), 433 nm (4.73), 412 nm (4.70), 354 nm (4.59).

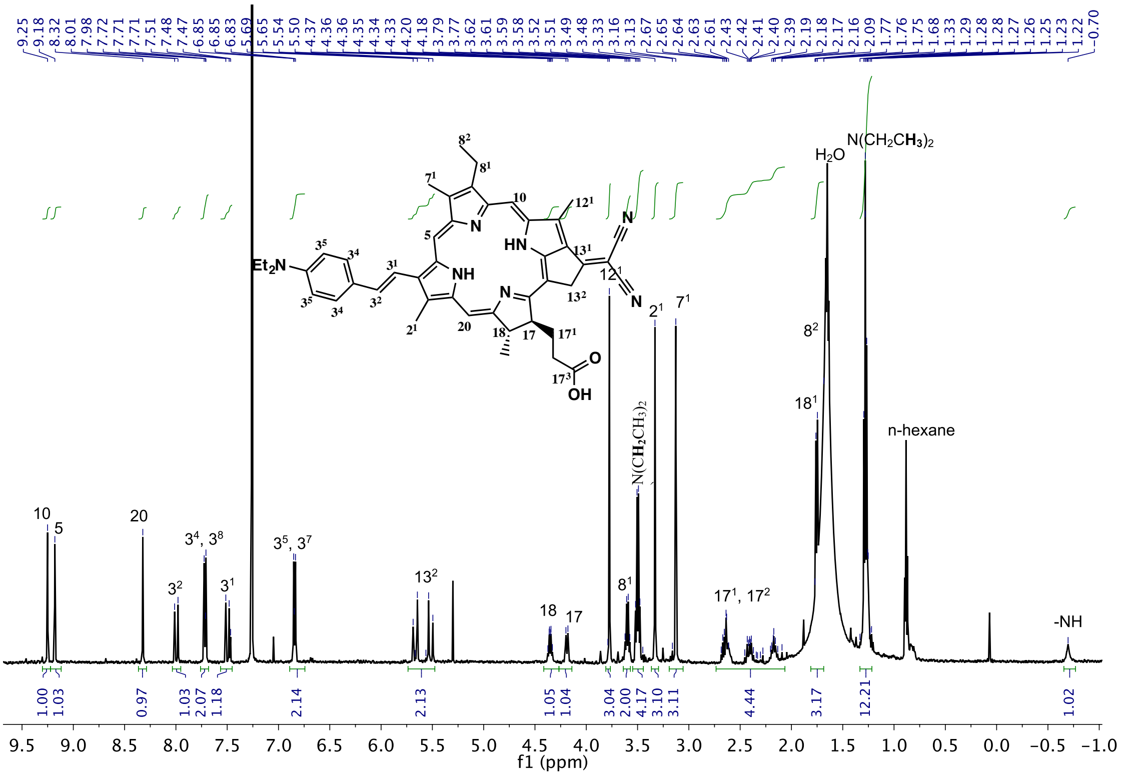

Figure 35: ^{1}H-NMR spectrum of **4b** (700 MHz, $CDCl_3$, 298 K).

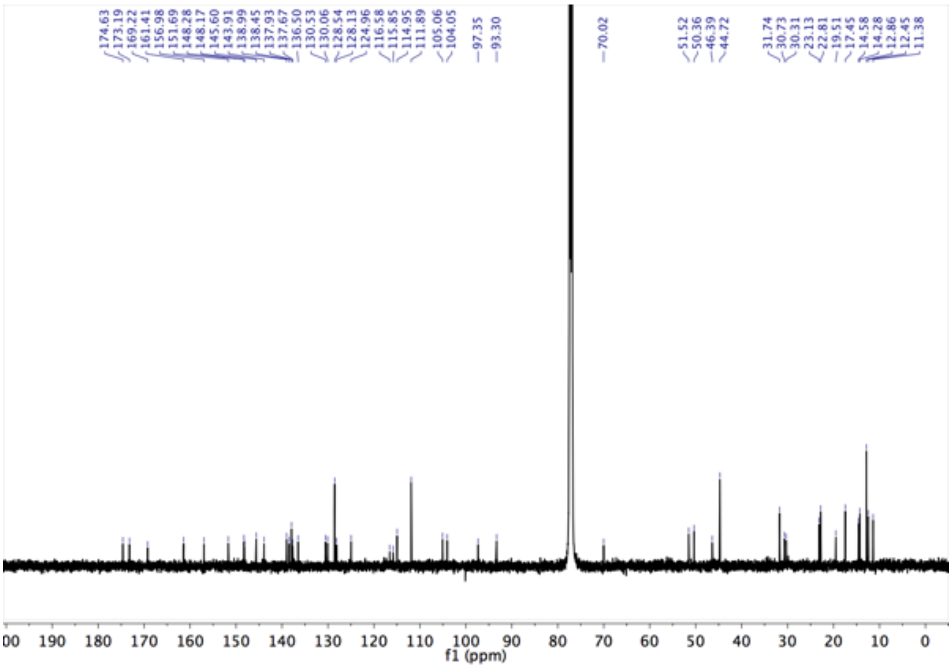

Figure 36: ^{13}C NMR spectrum of **4b** (175 MHz, $CDCl_3$, 298 K).

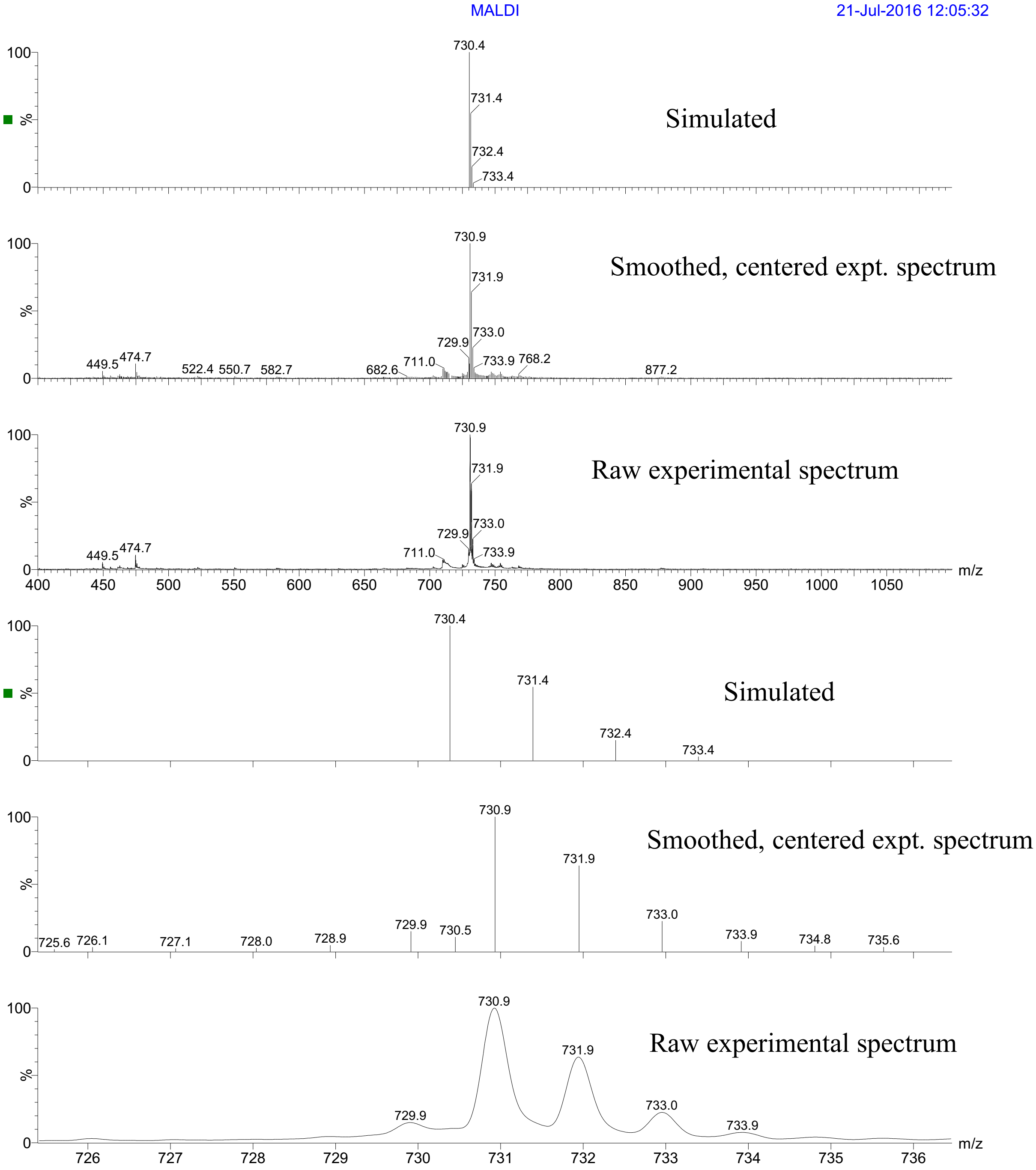

Figure 37: MALDI ToF mass spectrum of **4b**.

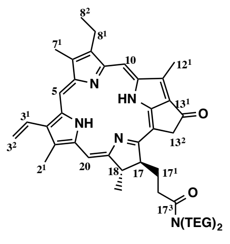

17^3-(bis-(TEG)amide) pyropheophorbide-a 1c:[56] Pyropheophorbide-a **1b** (22.0 mg, 41.1 µmol) was dissolved in a mixture of *N,N*-diisopropylethylamine (15 µL, 82 µmol) in DMF (1.4 mL) followed by addition of (1-cyano-2-ethoxy-2-oxoethylidenaminooxy)dimethylamino-morpholino-carbenium hexafluorophosphate (COMU, 18 mg, 41.1 µmol) at 0 °C under Ar atmosphere. After stirring the reaction mixture for 3 min, bis-TEG amine (13 mg, 41.1 µmol) was added. The mixture was stirred at 0 °C under Ar atmosphere for 2 h. After completion (monitored by RP-HPLC), the reaction mixture was diluted with water and extracted with CH_2Cl_2. The organic phase was dried over Na_2SO_4 and solvent was evaporated. The crude product was purified by flash column chromatography (1% MeOH in CH_2Cl_2). The product was then washed with water to remove ethyl 2-cyano-2-(hydroxyimino)acetate (Oxyma), the leaving group of COMU. The product **1c** was obtained as dark green solid. **Yield:** 22.5 mg, 66%. **^{1}H-NMR** (400 MHz, $CDCl_3$) *δ*/ppm: 9.46, 9.35 and 8.57 (each s, 1H; meso H), 8.00 (dd, ^3J = 11.6 Hz, ^3J = 17.9 Hz, 1H; C***H***=CH_2), 6.29 (dd, ^3J = 17.9 Hz, ^2J= 1.1 Hz, 1H; CH=C***H₂***), 6.17 (dd, ^3J = 11.6 Hz, ^2J= 1.1 Hz, 1H; CH=C***H₂***), 5.29 (d, ^2J = 19.8 Hz, 1H; 13^2-C***H₂***), 5.12 (d, ^2J = 19.8 Hz, 1H; 13^2-C***H₂***), 4.53 (q, ^3J=7.2 Hz, 1H; 18-H), 4.35 (d, ^3J = 6.0 Hz, 1H; 17-H), 3.68 (m, 2H; 8^1-C***H2***-CH_3), 3.66, 3.41 and 3.27 (each s, 3H; 2^1, 7^1, 12^1-CH_3); 3.45–2.94 (several m, 24H; C*H₂* of TEG chains), 3.22 (s, 6H; -OC*H₃* of TEG chains), 2.77–2.24 (several m, 4H; C***H₂***C***H₂***CO-N(TEG)$_2$), 1.81 (d, ^3J = 7.2 Hz, 3H; 18-CH_3), 1.69 (t, ^3J = 7.5 Hz, 3H; CH_2C***H₃***) and –1.71 (br s, 1H; NH). **^{13}C-NMR** (100 MHz, $CDCl_3$) δ/ppm: 196.5 (C13^1), 172.8 (C17^3), 171.9 (C19), 161.1 (C16), 155.2 (C6), 150.8 (C9), 149.0 (C14), 145.0 (C8), 141.5 (C1), 137.9 (C12), 136.2 (C3^1), 136.1 (C13), 135.9 (C4), 131.6 (C7), 130.6 (C3), 129.3 (C2), 128.4 (C11), 122.6 (C3^2), 106.3 (C15), 104.0 (C10), 97.2 (C5), 93.2 (C20), 71.9–68.9 (**C**H$_2$ of bis-TEG), 59.0–59.0 (O**C**H$_3$ of bis-TEG), 52.0 (C17), 50.1 (C18), 48.6–48.3 (N**C**H$_2$ of bis-TEG), 46.2 (C13^2), 30.0 (C17^1), 29.5 (C17^2), 23.3 (C18^1), 19.6 (C8^1), 17.6 (C8^2), 12.3 (C2^1), 12.2 (C12^1), 11.4 (C7^1). ***m/z*** **(MALDI-ToF)** 825.1 ($C_{47}H_{63}N_5O_8$, $[M]^+$ calculated 825.5). **UV-Vis** (solvent: MeOH)**:** λ_{max} = 414 nm (Soret band) and 670 nm (Q band).

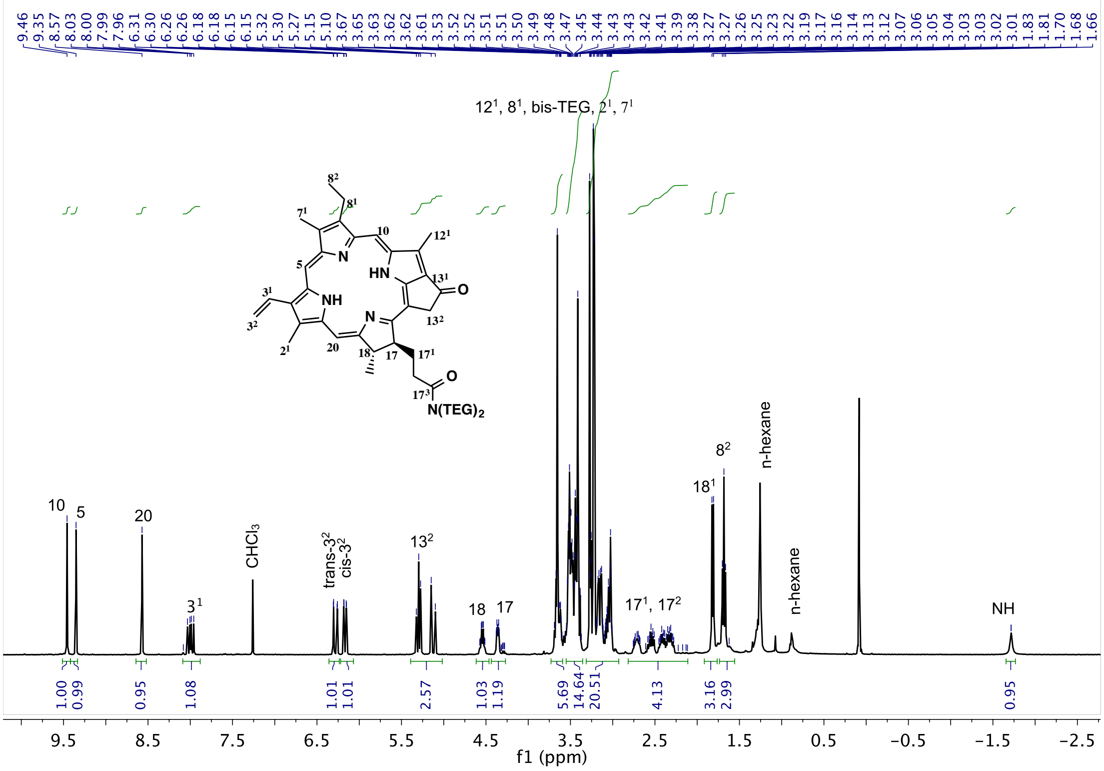

Figure 38: ^{1}H-NMR spectrum of **1c** (400 MHz, $CDCl_3$, 298 K).

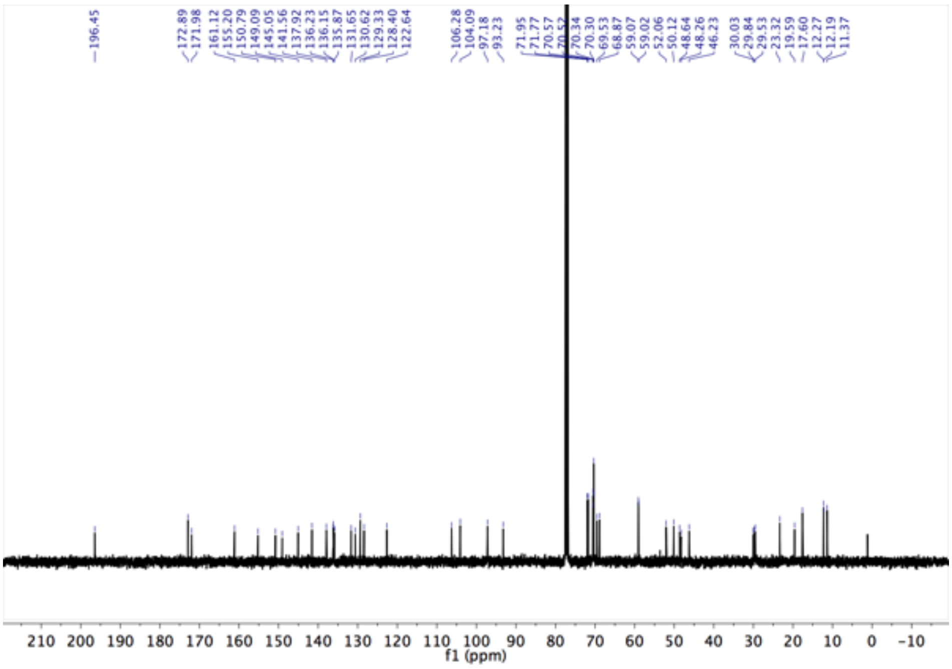

Figure 39: ^{13}C NMR spectrum of **1c** (100 MHz, $CDCl_3$, 298 K).

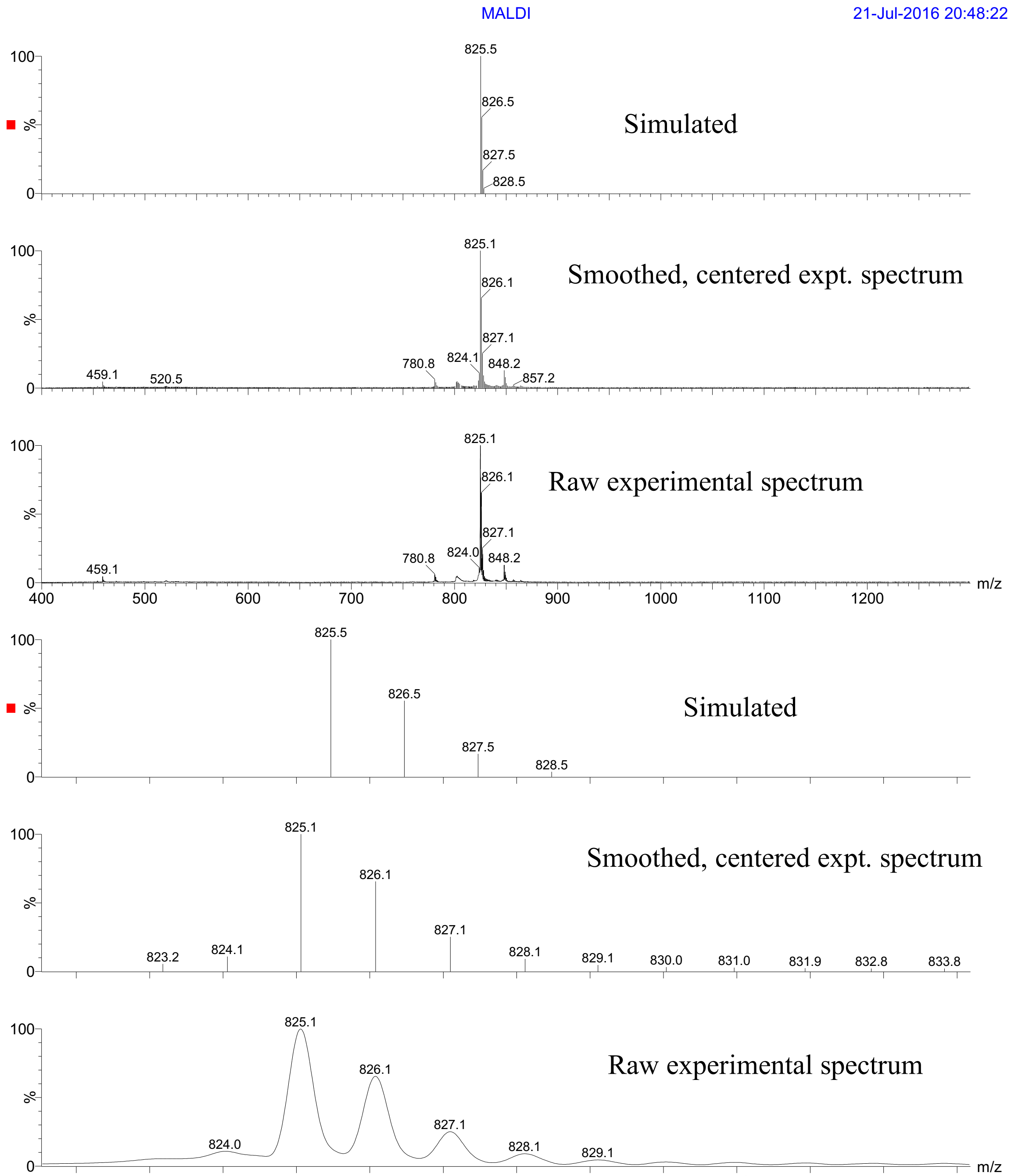

Figure 40: MALDI ToF mass spectrum of **1c**.

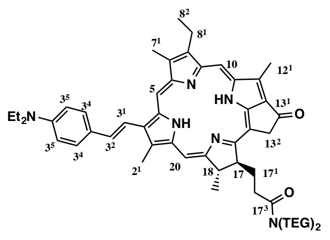

(*E*)-3^2-(*para-D*iethyl amino phenyl)-17^3-(bis-(TEG)amide) pyropheophorbide-a 2c: (*E*)-3^2-(*para*-Diethyl amino phenyl)-pyropheophorbide-a **2b** (9.0 mg, 14 µmol) was dissolved in a mixture of *N,N*-diisopropylethylamine (5 µL, 30 µmol) in DMF (0.1 mL) followed by addition of COMU (6.2 mg, 14 µmol) at 0 °C under Ar atmosphere and stirred for 3 min. Bis-TEG amine (4.5 mg, 14 µmol) was then added to the reaction mixture. The mixture was stirred at 0°C under Ar atmosphere for 2 h followed by stirring at 20 °C for 3 h. After completion (monitored by TLC (47% $CHCl_3$, 47% EtOAc, 5% MeOH and 1% CH_3COOH)), the reaction mixture was diluted with ethyl acetate and extracted successively with 1 N HCl, 1 N $NaHCO_3$ and brine. The mixture was dried over Na_2SO_4 followed by the removal of solvent under reduced pressure. The crude product was purified by flash column chromatography using the same eluent as TLC and recrystallized (CH_2Cl_2/hexane) to give **2c** as a dark brown solid. **Yield:** 5.1 mg, 40%. **^{1}H-NMR** (600 MHz, $CDCl_3$) *δ*/ppm: 9.48 (s, 1H; 10-H), 9.43 (s, 1H; 5-H), 8.53 (s, 1H; 20-H), 8.15 (d, ^3J = 15.8 Hz, 1H; 3^2-H), 7.76 (m, 2H; 3^4-H and 3^8-H), 7.58 (d, ^3J = 15.8 Hz, 1H; 3^1-H), 6.86 (d, 2H; 3^5-H and 3^7-H), 5.28 (d, ^2J = 18.9 Hz, 1H; 13^2-CH_2), 5.11 (d, ^2J = 18.9 Hz, 1H; 13^2-CH_2), 4.53 (m, 1H; 18-H), 4.35 (m, 1H; 17-H), 3.70 (m, 2H; 8^1-$C\mathbf{H_2}$), 3.67 (s, 3H; 12^1-CH_3), 3.58–3.33 (several m, 24H; $C\boldsymbol{H_2}$ of TEG chains), 3.27 (q, ^3J = 7.1 Hz, 4H; $N(C\mathbf{H_2}CH_3)_2$), 3.24 (s, 3H; 2^1-CH_3), 3.22 (s, 3H; 7^1-CH_3), 2.74–2.24 (several m, 4H; 17-$C\mathbf{H_2}C\mathbf{H_2}CON(TEG)_2$), 1.81 (d, ^3J = 7.4 Hz, 3H; 18^1-CH_3), 1.70 (t, ^3J = 7.7 Hz, 8^2-CH_3), 1.60 (t, ^3J = 7.1 Hz, 6H; $N(CH_2C\mathbf{H_3})_2$), –1.54 (br s, 1H; NH). **^{13}C-NMR** (125 MHz, $CDCl_3$) δ/ppm: 196.5 ($C13^1$), 172.8 ($C17^3$), 172.0 (C19), 161.1 (C16), 155.3 (C6), 150.7 (C9), 149.2 (C14), 148.1 ($C3^6$), 145.0 (C8), 142.2 (C1), 137.8 (C12), 137.5 ($C3^1$), 137.0 (C13), 136.1 (C4), 134.5 (C7), 130.5 (C3), 130.0 (C2), 128.5 ($C3^4$), 128.2 (C11), 125.2 ($C3^3$), 115.5 ($C3^2$), 111.9 ($C3^5$), 106.0 (C15), 104.1 (C10), 97.0 (C5), 93.0 (C20), 71.9–68.9 (**C**H_2 of bis-TEG), 59.0–59.0 (O**C**H_3 of bis-TEG), 51.6 (C17), 50.1 (C18), 48.6–48.3 (N**C**H_2 of bis-TEG), 46.2 ($C13^2$), 44.7 ($N\mathbf{C}H_2CH_3)_2$, 30.0 ($C17^1$), 29.5 ($C17^2$), 23.3 ($C18^1$), 19.6 ($C8^1$), 17.6 ($C8^2$), 12.9 ($NCH_2\mathbf{C}H_3)_2$, 12.6 ($C2^1$), 12.2 ($C12^1$), 11.5 ($C7^1$). ***m/z* (MALDI-ToF)** 972.9 ($C_{57}H_{76}N_6O_8$, $[M]^+$ calculated 972.6).

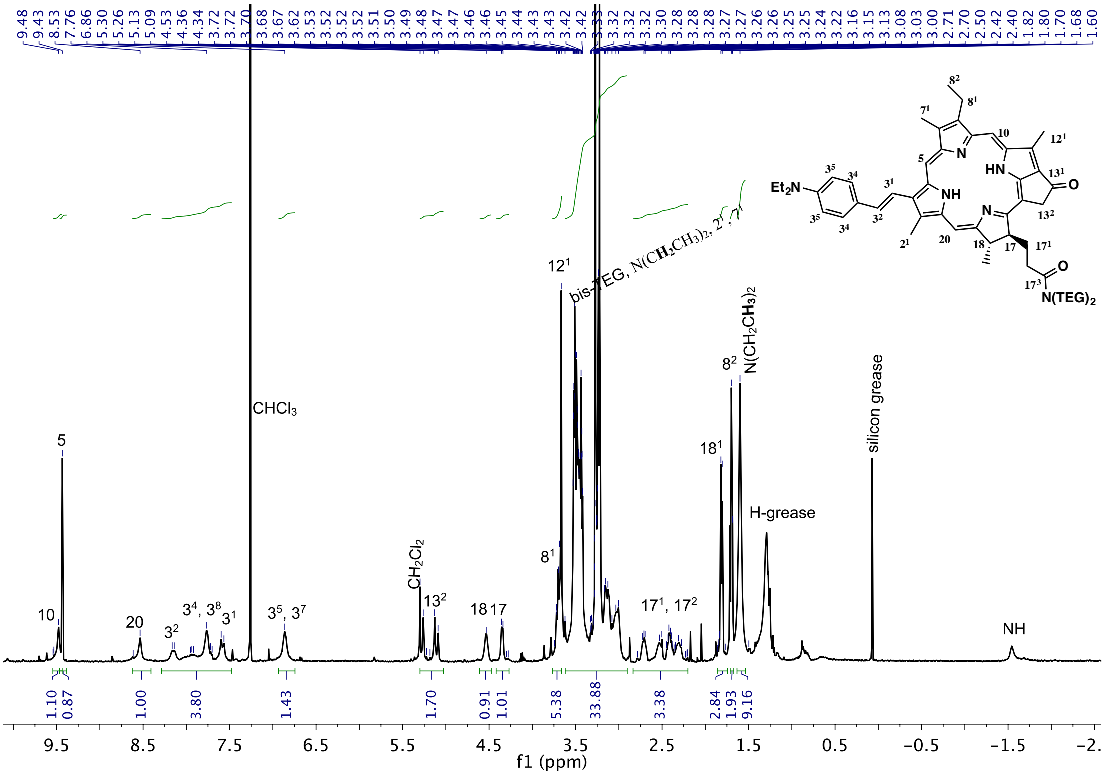

Figure 41: ^{1}H-NMR spectrum of **2c** (600MHz, $CDCl_3$, 298 K).

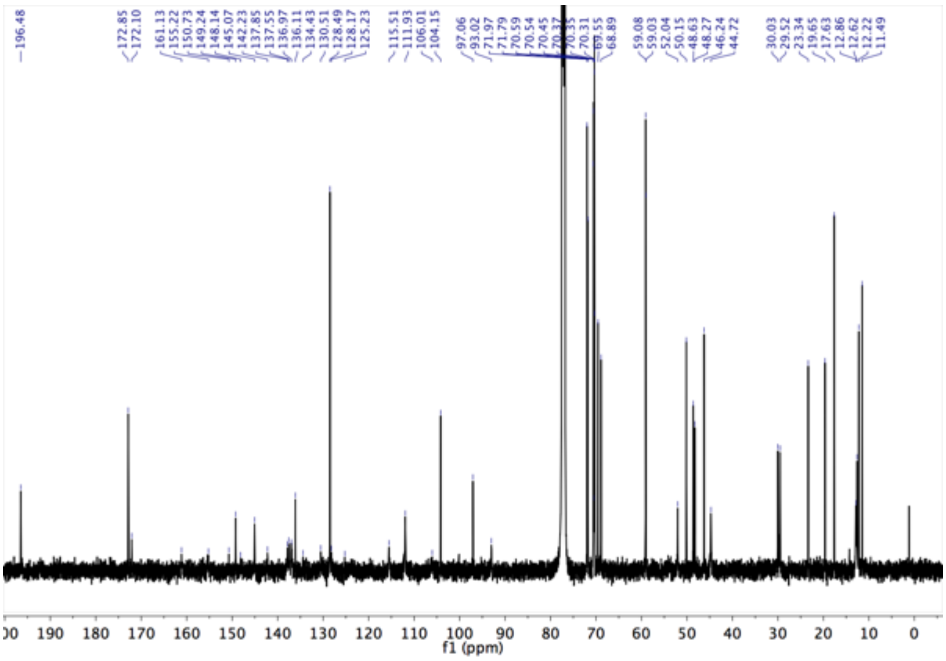

Figure 42: ^{13}C NMR spectrum of **2c** (150 MHz, $CDCl_3$, 298 K).

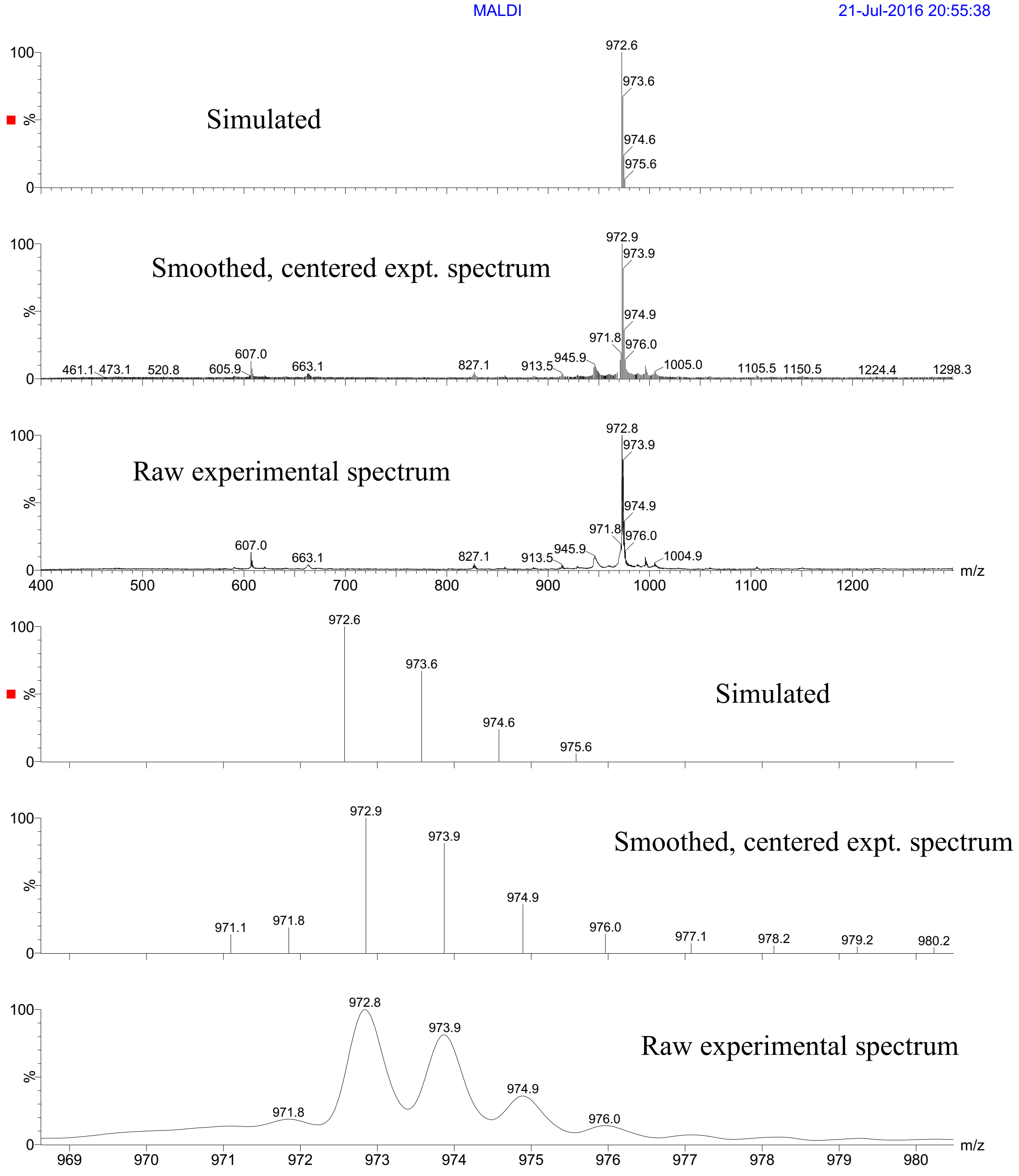

Figure 43: MALDI ToF mass spectrum of **2c**.

13^1-Deoxo-13^1-(dicyanomethylene)-17^3-(bis-(TEG)amide) pyropheophorbide-a 3c:

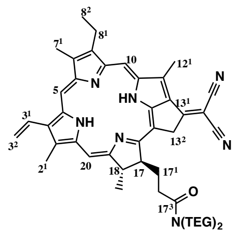

13^1-Deoxo-13^1-(dicyanomethylene)pyropheophorbide-a **3b** (19.0 mg, 32.6 µmol) was dissolved in a mixture of *N,N*-diisopropylethylamine (11.5 µL, 66 µmol) in DMF (1.1 mL) followed by addition of COMU (14 mg, 32 µmol) at 0 °C under Ar atmosphere and stirred for 3 min. Bis-TEG amine (10.2 mg, 32 µmol) was then to the reaction mixture followed by stirring at 0 °C under Ar atmosphere for 2 h. After completion (monitored by RP-HPLC), the reaction mixture was diluted with few drops of water and then extracted using CH_2Cl_2. The organic layer was dried over Na_2SO_4 followed by solvent evaporation. The crude product was purified by flash column chromatography (1% MeOH in CH_2Cl_2) and recrystallized (CH_2Cl_2/hexane) to give **3c** as a dark green solid. **Yield:** 6.0 mg, 21%. **^{1}H-NMR** (400 MHz, $CDCl_3$) *δ*/ppm: 9.19 (s, 1H; 10-H), 9.16 (s, 1H; 5-H), 8.40 (s, 1H; 20-H), 7.91 (dd, $^3J = 11.6$ Hz, $^3J = 17.8$ Hz, 1H; 3^1-H), 6.26 (dd, $^3J = 17.8$ Hz, $^2J = 1.4$ Hz, 1H; *trans* 3^2-H), 6.16 (dd, $^3J = 11.6$ Hz, $^2J = 1.4$ Hz, 1H; cis-3^2-H), 5.67 (d, $^2J = 21.0$ Hz, 1H; 13^2-CH_2), 5.47 (d, $^2J = 21.0$ Hz, 1H; 13^2-CH_2), 4.44 (m, 1H; 18-H), 4.24 (m, 1H; 17-H), 3.70–3.00 (m, 45H; 12^1-CH_3, 8^1-C**H_2,** C***H_2*** of TEG chains, 2^1-CH_3, and 7^1-CH_3), 2.72-2.24 (several m, 4H; 17-C**H_2**C**H_2**CONTEG)$_2$), 1.77 (d, $^3J = 7.3$ Hz, 3H; 18^1-CH_3), 1.63 (t, $^3J = 7.6$ Hz, 3H; 8^2-CH_3), -0.92 (br s, 1H; NH). **^{13}C-NMR** (125 MHz, $CDCl_3$) δ/ppm: 173.5 (C19), 172.6 (C17^3), 168.9 (C16), 162.0 (C6), 156.6 (C9), 151.6 (C14), 147.9 (C13^1), 145.6 (C8), 143.0 (C1), 138.9 (C12), 137.6 (C3^1), 136.5 (C13), 132.4 (C4), 130.1 (C7), 129.0 (C3), 128.4 (C2), 123.1 (C11), 116.5 (13^1-**C**N), 115.7 (C3^2), 105.6 (C15), 103.9 (C10), 97.4 (C5), 93.7 (C20), 71.9–70.4 (bis-TEG), 70.3 (**C**CN), 69.5–68.9 (bis-TEG), 59.1–59.0 (O**C**H_3 of bis-TEG), 52.0 (C17), 50.2 (C18), 48.6–46.4 (bis-TEG), 46.2 (C13^2), 30.2 (C17^1), 29.7 (C17^2), 23.2 (C18^1), 19.5 (C8^1), 17.5 (C8^2), 14.5 (C2^1), 12.2 (C12^1), 11.3 (C7^1). ***m/z*** **(MALDI-ToF**) 873.4 ($C_{50}H_{63}N_7O_7$, $[M]^+$ calculated 873.5)

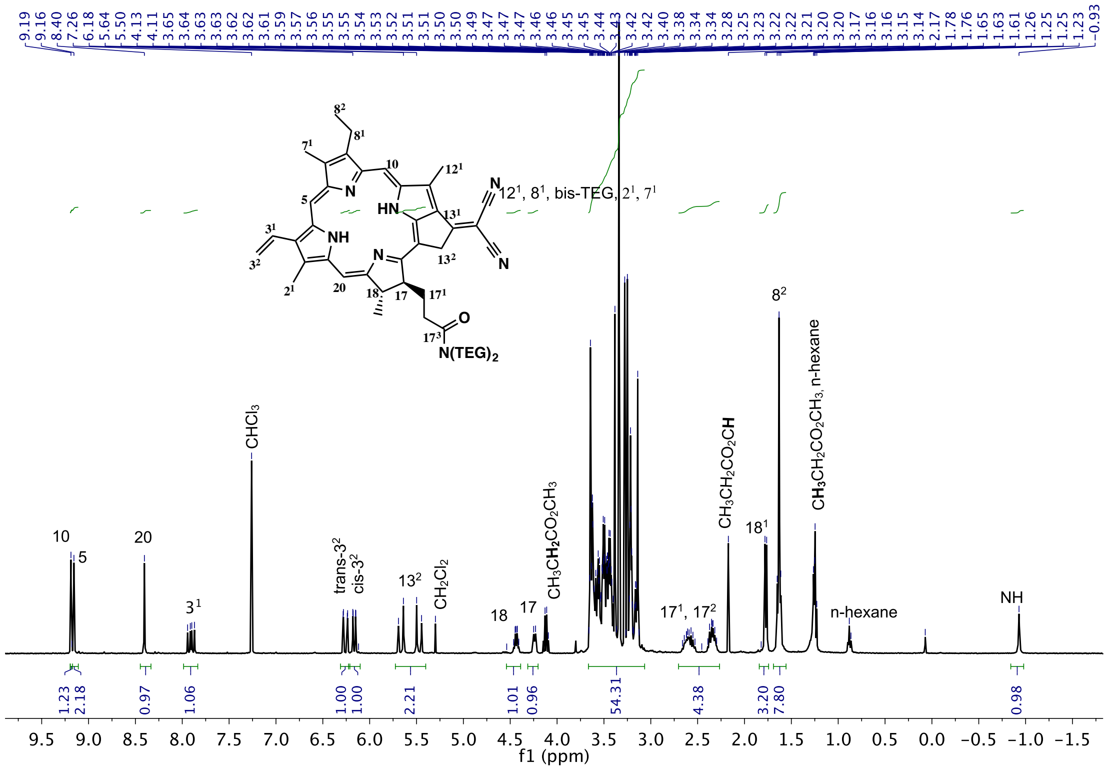

Figure 44: ^{1}H-NMR spectrum of **3c** (400MHz, CDCl$_3$, 298 K).

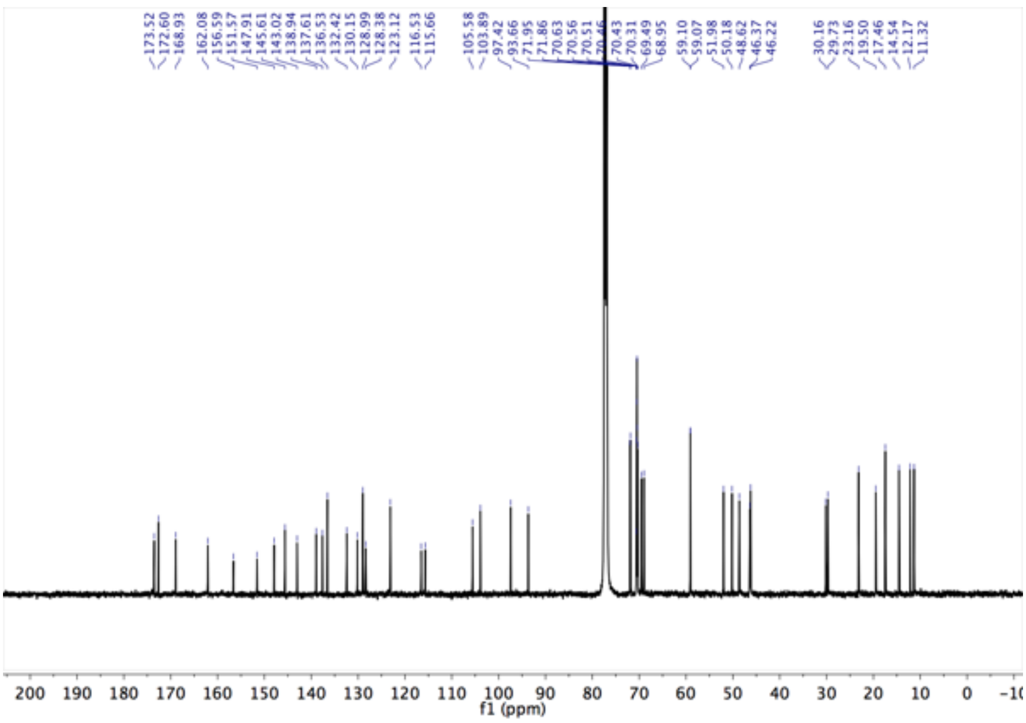

Figure 45: ^{13}C NMR spectrum of **3c** (125 MHz, CDCl$_3$, 298 K).

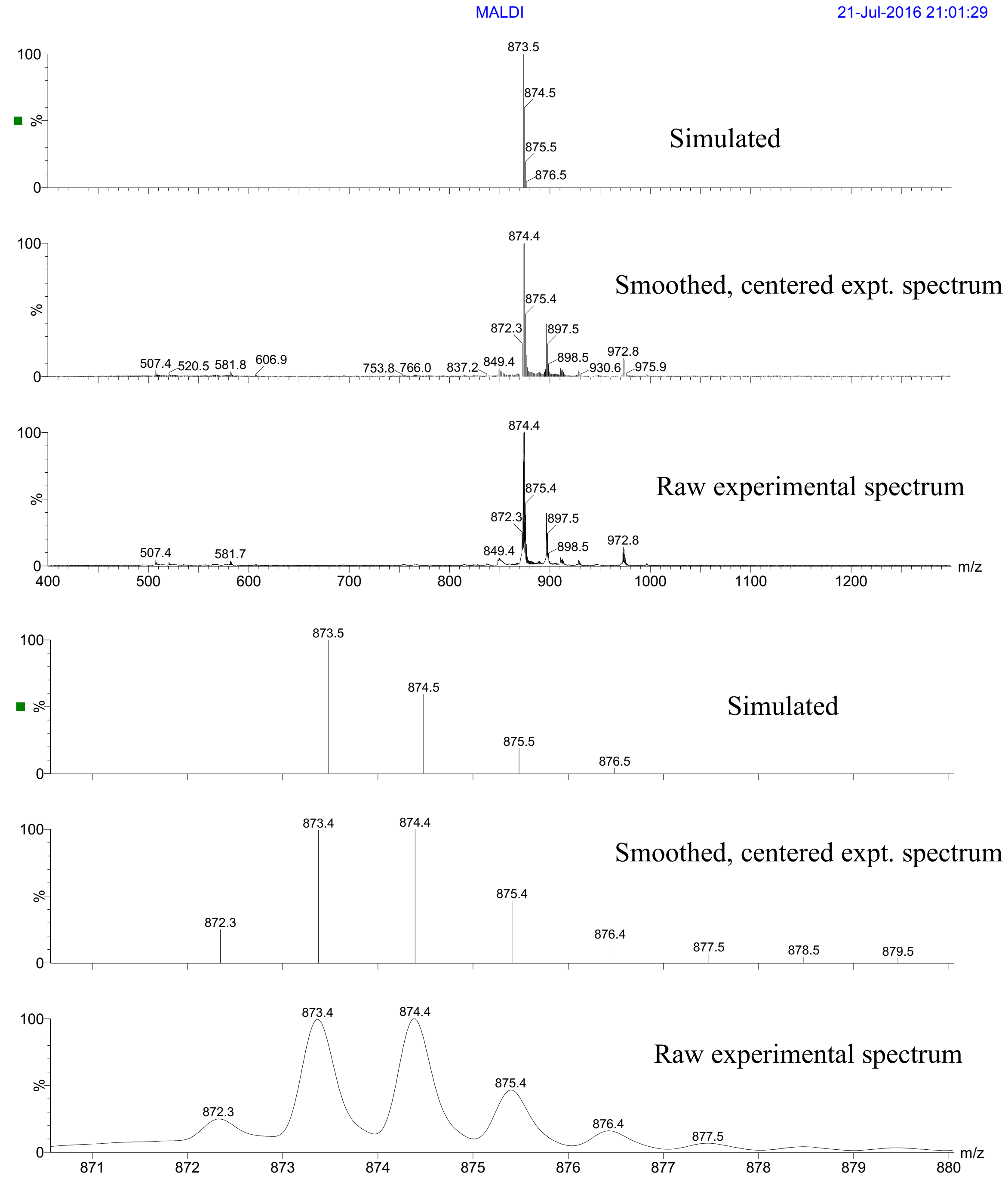

Figure 46: MALDI ToF mass spectrum of **3c**.

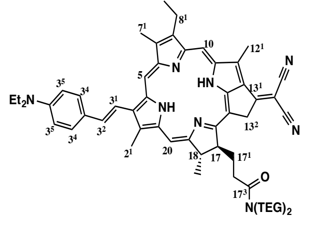

13^1-Deoxo-13^1-(dicyanomethylene)-(E)-3^2-(*para*-diethyl amino phenyl)-17^3-(bis-(TEG)amide)-pyropheophorbide-a 4c: 13^1-Deoxo-13^1-(dicyanomethylene)-(*E*)-3^2-(*para*-diethyl amino phenyl)-pyropheophorbide-a **4b** (15.0 mg, 20 μmol) was dissolved in a mixture of *N,N*-diisopropylethylamine (71.2 μL, 42 μmol) in DMF (0.67 mL) followed by addition of COMU (8.9 mg, 20 μmol) at 0 °C under Ar atmosphere. Bis-TEG amine (6.5 mg, 20 μmol) was then added to the reaction mixture followed by stirring at 0°C under Ar atmosphere for 3 h. After completion, the solvent was evaporated under reduced pressure and the residue was washed with water. The crude product was purified by flash column chromatography. Initially, pure CH_2Cl_2 was used as eluent to remove a light green band and then 1.5% MeOH in CH_2Cl_2 was used as eluent to elute the desired product as dark green band. The starting material was then eluted using a mixture of solvents as eluent (47% CH_2Cl_2, 47% EtOAc, 5% MeOH and 1% CH_3COOH). The product was recrystallized (CH_2Cl_2/hexane) to give **4c** as a dark green solid. **Yield:** 9.0 mg, 43%. **^{1}H-NMR** (500 MHz, $CDCl_3$) *δ*/ppm: 9.22 (s, 1H; 10-H), 9.16 (s, 1H; 5-H), 8.34 (s, 1H; 20-H), 7.98 (d, ^3J = 16.3 Hz, 1H; 3^2-H), 7.71 (d, ^3J = 8.5 Hz, 2H; 3^4-H and 3^8-H), 7.49 (d, ^3J = 16.3 Hz, 1H; 3^1-H), 6.84 (d, ^3J = 8.5 Hz, 2H; 3^5-H; 3^7-H), 5.70 (d, ^2J = 21.1 Hz, 1H; 13^2-CH_2), 5.51 (d, ^2J = 21.1 Hz, 1H; 13^2-CH_2), 4.41 (m, 1H; 18-H), 4.23 (m, 1H; 17-H), 3.74 (s, 3H; 12^1-CH_3), 3.59 (q, ^3J = 7.6 Hz, 2H; 8^1-CH_2), 3.55–3.29 (several m, 22H; C$\boldsymbol{H_2}$ of TEG chains, N(C$\mathbf{H_2}$CH$_3$)$_2$), 3.34 (s, 3H; 2^1-CH_3), 3.33–3.13 (several m, 11H; C$\boldsymbol{H_2}$, C$\boldsymbol{H_3}$ of TEG chains), 3.12 (s, 3H; 7^1-CH_3), 2.69–2.28 (several m, 4H; 17-C$\mathbf{H_2}$C$\mathbf{H_2}$CON(TEG)$_2$), 1.77 (d, ^3J = 7.3 Hz, 3H; 18^1-CH_3), 1.65 (t, ^3J = 7.6 Hz, 8^2-CH_3), 1.28 (t, ^3J = 7.0 Hz, 6H; N(CH$_2$C$\mathbf{H_3}$)$_2$), –0.74 (br s, NH). **^{13}C-NMR** (125 MHz, $CDCl_3$) δ/ppm: 173.6 (C19), 172.6 (C17^3), 169.0 (C16), 162.0 (C6), 156.9 (C9), 151.6 (C14), 148.3 (C3^6), 148.1 (C13^1), 145.5 (C8), 143.7 (C1), 138.9 (C12), 138.4 (C3^1), 137.9 (C13), 137.5 (C4), 136.4 (C7), 130.5 (C3), 130.0 (C2), 128.5 (C3^4), 128.0 (C11), 125.0 (13^1-**C**N), 116.7 (C3^3), 115.8 (13^1-**C**N), 115.0 (C3^2), 111.9 (C3^5), 105.3 (C15), 104.0 (C10), 97.2 (C5), 93.3 (C20), 72.0–70.3 (bis-TEG), 70.2 (**C**CN), 69.5–68.9 (bis-TEG), 59.0 (O**C**H$_3$ of bis-TEG), 51.9 (C17), 50.2 (C18), 48.6–46.4 (bis-TEG), 46.2 (C13^2), 44.7 (N**C**H$_2$CH$_3$)$_2$, 30.1 (C17^1), 29.7 (C17^2), 23.2 (C18^1), 19.5 (C8^1), 17.5 (C8^2), 14.6 (C2^1), 12.9 (NCH$_2$**C**H$_3$)$_2$, 12.5 (C12^1), 11.4 (C7^1). ***m/z* (MALDI-ToF**) 1021.1 ($C_{60}H_{77}N_8O_7$, $[M]^+$ calculated 1020.6).

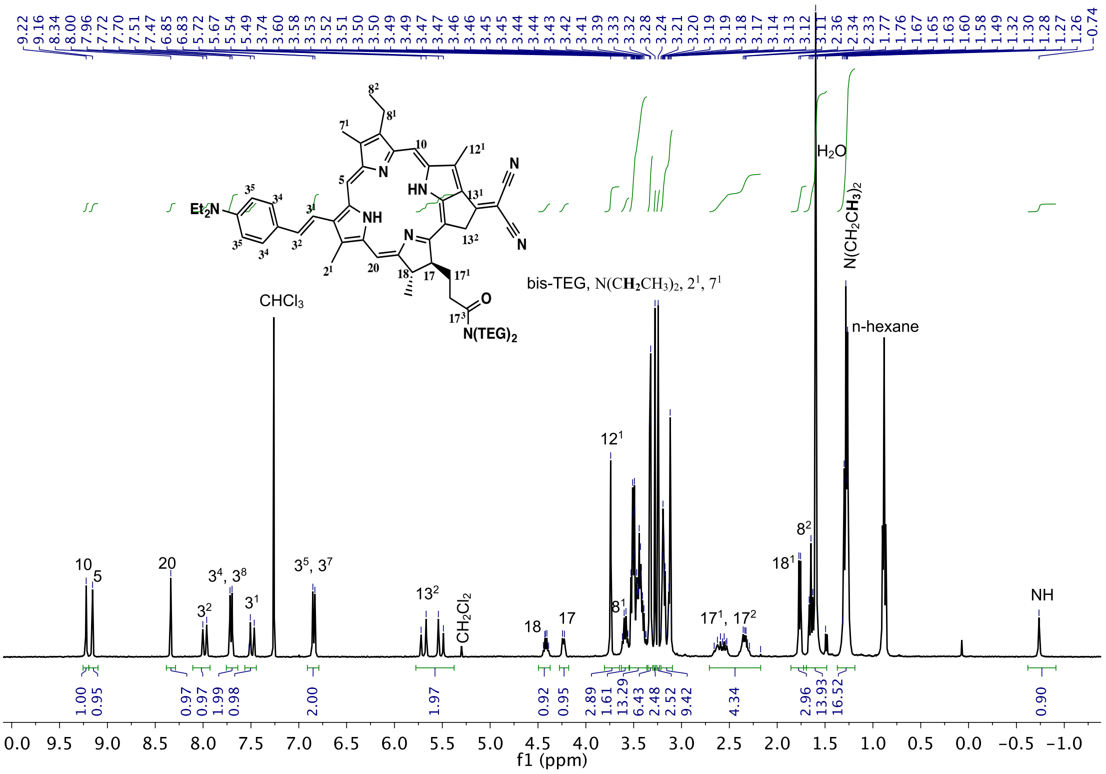

Figure 47: ^{1}H-NMR spectrum of **4c** (500 MHz, $CDCl_3$, 298 K).

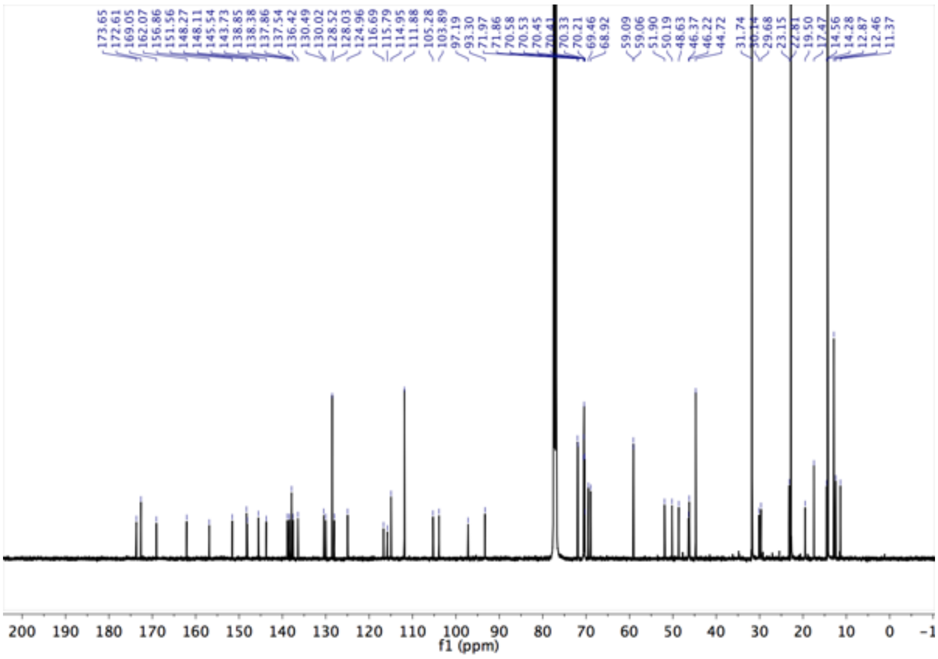

Figure 48: ^{13}C NMR spectrum of **4c** (125 MHz, $CDCl_3$, 298 K).

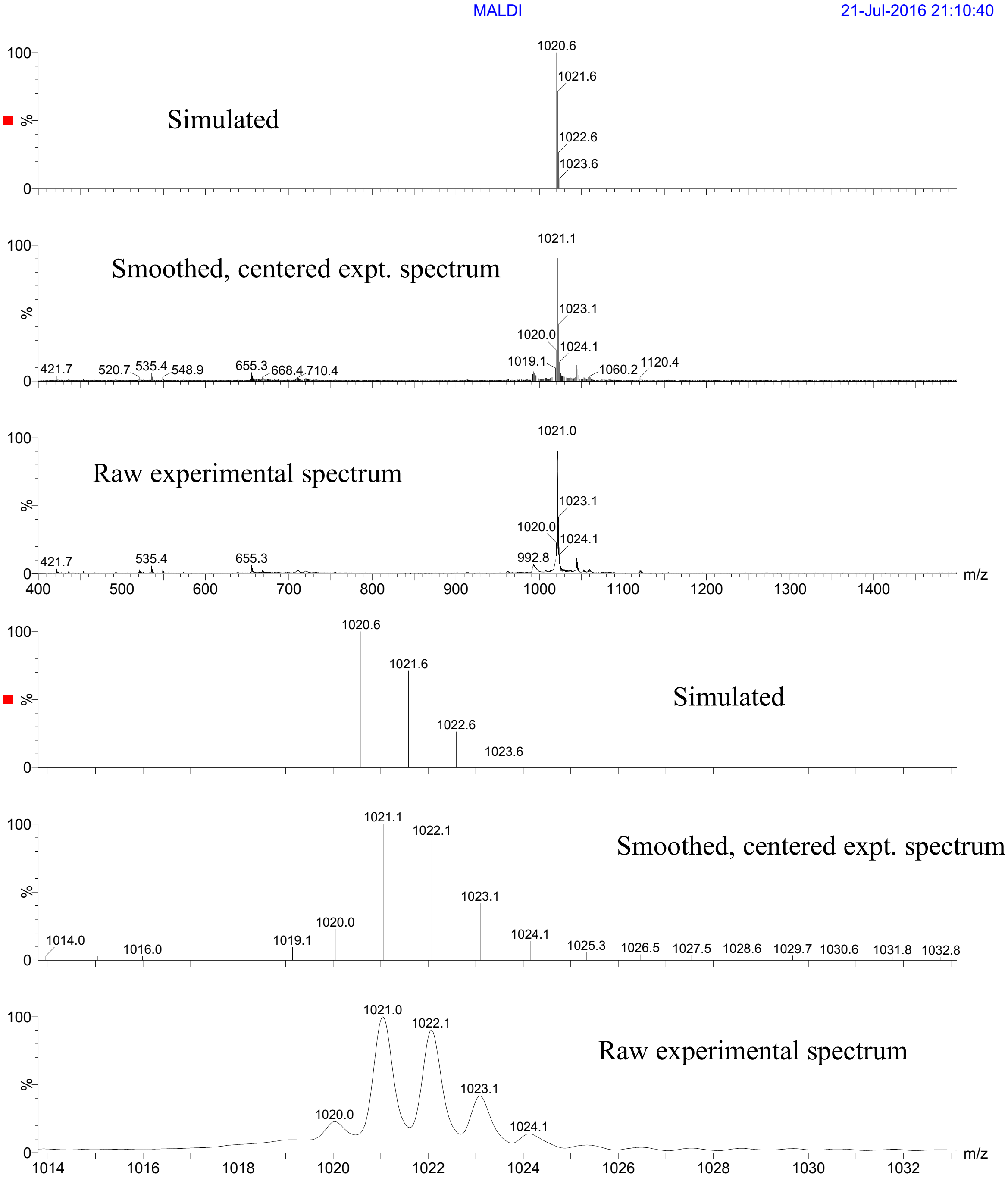

Figure 49: MALDI ToF mass spectrum of **4c**.

Bis-TEG amine:[68]

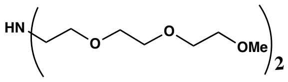

N,*N*-Bis-(2-(2-(2-methoxyethoxy)ethoxy)ethyl)aniline or bis-TEG benzyl amine (1.0 g, 2.6 mmol) was dissolved in ethanol (3 mL; deoxygenated by repeated evacuation), Pd/C (10% w/w Pd; 100 mg) was added, and the mixture placed under Ar atmosphere. H_2 gas (1 atm, approx. 2 L, 89 mmol) was introduced through a balloon and the reaction mixture was stirred at 20 °C for 24 h. The mixture was filtered through Celite®, and the solvent was removed under reduced pressure to isolate bis-TEG amine as yellow liquid. **Yield:** 745.0 mg, 97%. **^{1}H-NMR** (400 MHz, $CDCl_3$) δ/ppm: 3.57 (m, 20H; CH_2), 3.36 (s, 6H; CH_3), 2.80 (t, ^3J = 5.3Hz, 4H; CH_2-NH); 2.10 (br s, 1H; NH), consistent with the literature data.[66]

2.60 References

1 M. Scanziani and M. Hausser, *Nature*, 2009, **461**, 930–939.

2 K. Svoboda and R. Yasuda, *Neuron*, 2006, **50**, 823–839.

3 M. Pawlicki, H. A. Collins, R. G. Denning and H. L. Anderson, *Angew. Chem. Int. Ed.*, 2009, **48**, 3244–3266.

4 J. E. Reeve, H. A. Collins, K. De Mey, M. M. Kohl, K. J. Thorley, O. Paulsen, K. Clays and H. L. Anderson, *J. Am. Chem. Soc.*, 2009, **131**, 2758–2759.

5 T. Verbiest, S. Houbrechts, M. Kauranen, K. Clays and A. Persoons, *J. Mater. Chem.*, 1997, **7**, 2175–2189.

6 I. López-Duarte, P. Chairatana, Y. Wu, J. Pérez-Moreno, P. M. Bennett, J. E. Reeve, I. Boczarow, W. Kaluza, N. A. Hosny, S. D. Stranks, R. J. Nicholas, K. Clays, M. K. Kuimova and H. L. Anderson, *Org. Biomol. Chem.*, 2015, **13**, 3792–3802.

7 T. Cañeque, A. M. Cuadro, J. Alvarez-Builla, J. Pérez-Moreno, K. Clays, O. Castaño, J. L. Andrés and J. J. Vaquero, *Dye. Pigment.*, 2014, **101**, 116–121.

8 I. Lopez-Duarte, J. E. Reeve, J. Perez-Moreno, I. Boczarow, G. Depotter, J. Fleischhauer, K. Clays and H. L. Anderson, *Chem. Sci.*, 2013, **4**, 2024–2027.

9 C. Barsu, R. Cheaib, S. Chambert, Y. Queneau, O. Maury, D. Cottet, H. Wege, J. Douady, Y. Bretonniere and C. Andraud, *Org. Biomol. Chem.*, 2010, **8**, 142–150.

10 V. Parthasarathy, R. Pandey, M. Stolte, S. Ghosh, F. Castet, F. Wurthner, P. K. Das and M. Blanchard-Desce, *Chem. Eur. J.*, 2015, **21**, 14211–14217.

11 J. E. Reeve, A. D. Corbett, I. Boczarow, T. Wilson, H. Bayley and H. L. Anderson, *Biophys. J.*, 2012, **103**, 907–917.

12 P. Theer, W. Denk, M. Sheves, A. Lewis and P. B. Detwiler, *Biophys. J.*, 2011, **100**, 232–242.

13 M. Nuriya, S. Fukushima, A. Momotake, T. Shinotsuka, M. Yasui and T. Arai, *Nat. Commun.*, 2016, **7**.

14 J. E. Reeve, A. D. Corbett, I. Boczarow, W. Kaluza, W. Barford, H. Bayley, T. Wilson and H. L. Anderson, *Angew. Chem. Int. Ed.*, 2013, **52**, 9044–9048.

15 J. Jiang, K. B. Eisenthal and R. Yuste, *Biophys. J.*, 2007, **93**, L26–L28.

16 J. A. N. Fisher and B. M. Salzberg, in *Membrane Potential Imaging in the Nervous System and Heart*, eds. M. Canepari, D. Zecevic and O. Bernus, Springer, 2015, vol. 859, pp. 427–453.

17 D. A. Dombeck, L. Sacconi, M. Blanchard-Desce and W. W. Webb, *J. Neurophysiol.*, 2005, **94**, 3628–3636.

18 T. K. Ahn, K. S. Kim, D. Y. Kim, S. B. Noh, N. Aratani, C. Ikeda, A. Osuka and D. Kim, *J. Am. Chem. Soc.*, 2006, **128**, 1700–1704.

19 K. Kurotobi, K. S. Kim, S. B. Noh, D. Kim and A. Osuka, *Angew. Chem. Int. Ed.*, 2006, **45**, 3944–3947.

20 K. S. Kim, J. M. Lim, A. Osuka and D. Kim, *J. Photochem. Photobiol. C-Photochemistry Rev.*, 2008, **9**, 13–28.

21 E. Secret, M. Maynadier, A. Gallud, A. Chaix, E. Bouffard, M. Gary-Bobo, N. Marcotte, O. Mongin, K. El Cheikh, V. Hugues, M. Auffan, C. Frochot, A. Morere, P. Maillard, M. Blanchard-Desce, M. J. Sailor, M. Garcia, J.-O. Durand and F. Cunin, *Adv. Mater.*, 2014, **26**, 7643–7648.

22 C. M. Lemon, E. Karnas, M. G. Bawendi and D. G. Nocera, *Inorg. Chem.*, 2013, **52**, 10394–10406.

23 Y. Mi, P. Liang, Z. Yang, D. Wang, H. Cao, W. He and H. Yang, *Chem. Res. Chinese Univ.*, 2015, **31**, 992–996.

24 M. Khurana, H. A. Collins, A. Karotki, H. L. Anderson, D. T. Cramb and B. C. Wilson,

Photochem. Photobiol., 2007, **83**, 1441–1448.

25 M. K. Kuimova, H. A. Collins, M. Balaz, E. Dahlstedt, J. A. Levitt, N. Sergent, K. Suhling, M. Drobizhev, N. S. Makarov, A. Rebane, H. L. Anderson and D. Phillips, *Org. Biomol. Chem.*, 2009, **7**, 889–896.

26 J. D. Wilkinson, G. Wicks, A. Nowak-Krol, L. G. Lukasiewicz, C. J. Wilson, M. Drobizhev, A. Rebane, D. T. Gryko and H. L. Anderson, *J. Mater. Chem. C*, 2014, **2**, 6802–6809.

27 E. Annoni, M. Pizzotti, R. Ugo, S. Quici, T. Morotti, M. Bruschi and P. Mussini, *Eur. J. Inorg. Chem.*, 2005, **2005**, 3857–3874.

28 T. Morotti, M. Pizzotti, R. Ugo, S. Quici, M. Bruschi, P. Mussini and S. Righetto, *Eur. J. Inorg. Chem.*, 2006, **2006**, 1743–1757.

29 P. Ferrand, P. Gasecka, A. Kress, X. Wang, F. Z. Bioud, J. Duboisset and S. Brasselet, *Biophys. J.*, 2014, **106**, 2330–2339.

30 R. A. Badley, H. Schneide and W. G. Martin, *Biochem. Biophys. Res. Commun.*, 1971, **45**, 174–183.

31 B. Corry, D. Jayatilaka, B. Martinac and P. Rigby, *Biophys. J.*, 2006, **91**, 1032–1045.

32 R. S. Ries, H. Choi, R. Blunck, F. Bezanilla and J. R. Heath, *J. Phys. Chem. B*, 2004, **108**, 16040–16049.

33 U. A. Vanderheide, B. Orbons, H. C. Gerritsen and Y. K. Levine, *Eur. Biophys. J. with Biophys. Lett.*, 1992, **21**, 263–272.

34 K. M. Smith, D. A. Goff and D. J. Simpson, *J. Am. Chem. Soc.*, 1985, **107**, 4946–4954.

35 J. F. Lovell, C. S. Jin, E. Huynh, H. Jin, C. Kim, J. L. Rubinstein, W. C. W. Chan, W. Cao, L. V Wang and G. Zheng, *Nat. Mater.*, 2011, **10**, 324–332.

36 V. Tassetti, A. Hajri, M. Sowinska, S. Evrard, F. Heisel, L. Q. Cheng, J. A. Miehe, J. Marescaux and M. Aprahamian, *Photochem. Photobiol.*, 1997, **65**, 997–1006.

37 P. Keller, M. Sowinska, V. Tassetti, F. Heisel, A. Hajri, S. Evrard, J. A. Miehe, J. Marescaux and M. Aprahamian, *Photochem. Photobiol.*, 1996, **63**, 860–867.

38 A. P. Castano, P. Mroz and M. R. Hamblin, *Nat. Rev. Cancer*, 2006, **6**, 535–545.

39 S. Sasaki, M. Yoshizato, M. Kunieda and H. Tamiaki, *European J. Org. Chem.*, 2010, **2010**, 5287–5291.

40 G.-F. Han, J.-J. Wang and Y. K. Shim, *J. Photoscience*, **8**, 71–73.

41 J. J. Wang, J. Z. Li, J. Jakus and Y. K. Shim, *J. Porphyr. Phthalocyanines*, 2012, **16**, 122–129.

42 I. Stamati, M. K. Kuimova, M. Lion, G. Yahioglu, D. Phillips and M. P. Deonarain, *Photochem. Photobiol. Sci.*, 2010, **9**, 1033–1041.

43 H. Tamiaki, M. Kuno and M. Ohata, *Photochem. Photobiol.*, 2014, **90**, 1277–1286.

44 H. Tamiaki, K. Fukai, H. Shimazu and S. Shoji, *Photochem. Photobiol.*, 2014, **90**, 121–128.

45 I. Ghosh, N. Saleh and W. M. Nau, *Photochem. Photobiol. Sci.*, 2010, **9**, 649–654.

46 Y. Chen, X. Zheng, M. P. Dobhal, A. Gryshuk, J. Morgan, T. J. Dougherty, A. Oseroff and R. K. Pandey, *J. Med. Chem.*, 2005, **48**, 3692–3695.

47 L. Cui, D. Tokarz, R. Cisek, K. K. Ng, F. Wang, J. Chen, V. Barzda and G. Zheng, *Angew. Chem. Int. Ed.*, 2015, **54**, 13928–13932.

48 T. Luo, B. C. Wilson and Q.-B. Lu, *J. Photochem. Photobiol. B-Biology*, 2014, **132**, 102–110.

49 H. A. Collins, M. Khurana, E. H. Moriyama, A. Mariampillai, E. Dahlstedt, M. Balaz, M. K. Kuimova, M. Drobizhev, V. X. D. Yang, D. Phillips, A. Rebane, B. C. Wilson and H. L. Anderson, *Nat. Photonics*, 2008, **2**, 420–424.

50 D. A. Dombeck, M. Blanchard-Desce and W. W. Webb, *J. Neurosci.*, 2004, **24**, 999–1003.

51 A. C. Millard, L. Jin, A. Lewis and L. M. Loew, *Opt. Lett.*, 2003, **28**, 1221–1223.
52 X. Liu, E. Sternberg and D. Dolphin, *J. Org. Chem.*, 2008, **73**, 6542–6550.
53 H. Tamiaki, S. Miyata, Y. Kureishi and R. Tanikaga, *Tetrahedron*, 1996, **52**, 12421–12432.
54 I. S. Lonin, A. S. Kuzovlev, E. S. Belyaev, G. V Ponomarev, O. I. Koifman and A. Y. Tsivadze, *J. Porphyr. Phthalocyanines*, 2014, **18**, 123–128.
55 M. G. H. Vicente and K. M. Smith, *Tetrahedron*, 1991, **47**, 6887–6894.
56 A. El-Faham and F. Albericio, *J. Pept. Sci.*, 2010, **16**, 6–9.
57 S. Sasaki, G. P. C. Drummen and G. Konishi, *J. Mater. Chem. C*, 2016, **4**, 2731–2743.
58 J. B. Kelber, N. A. Panjwani, D. Wu, R. Gomez-Bombarelli, B. W. Lovett, J. J. L. Morton and H. L. Anderson, *Chem. Sci.*, 2015, **6**, 6468–6481.
59 A. Kahnt, J. Karnbratt, L. J. Esdaile, M. Hutin, K. Sawada, H. L. Anderson and B. Albinsson, *J. Am. Chem. Soc.*, 2011, **133**, 9863–9871.
60 M. J. Frisch, G. W. Trucks, H. B. Schlegel, G. E. Scuseria, M. A. Robb, J. R. Cheeseman, G. Scalmani, V. Barone, B. Mennucci, G. A. Petersson, H. Nakatsuji, M. Caricato, X. Li, H. P. Hratchian, A. F. Izmaylov, J. Bloino, G. Zheng, J. L. Sonnenberg, M. Hada, M. Ehara, K. Toyota, R. Fukuda, J. Hasegawa, M. Ishida, T. Nakajima, Y. Honda, O. Kitao, H. Nakai, T. Vreven, J. A. Montgomery Jr., J. E. Peralta, F. Ogliaro, M. J. Bearpark, J. Heyd, E. N. Brothers, K. N. Kudin, V. N. Staroverov, R. Kobayashi, J. Normand, K. Raghavachari, A. P. Rendell, J. C. Burant, S. S. Iyengar, J. Tomasi, M. Cossi, N. Rega, N. J. Millam, M. Klene, J. E. Knox, J. B. Cross, V. Bakken, C. Adamo, J. Jaramillo, R. Gomperts, R. E. Stratmann, O. Yazyev, A. J. Austin, R. Cammi, C. Pomelli, J. W. Ochterski, R. L. Martin, K. Morokuma, V. G. Zakrzewski, G. A. Voth, P. Salvador, J. J. Dannenberg, S. Dapprich, A. D. Daniels, Ã. Farkas, J. B. Foresman, J. V Ortiz and J. F. Cioslowski Douglas J., 2013.
61 W. R. Wadt and P. J. Hay, *J. Chem. Phys.*, 1985, **82**, 284–298.
62 P. J. Hay and W. R. Wadt, *J. Chem. Phys.*, 1985, **82**, 270–283.
63 P. J. Hay and W. R. Wadt, *J. Chem. Phys.*, 1985, **82**, 299–310.
64 K. Clays and A. Persoons, *Phys. Rev. Lett.*, 1991, **66**, 2980–2983.
65 K. Clays, E. Hendrickx, M. Triest, T. Verbiest, A. Persoons, C. Dehu and J. L. Brédas, *Science.*, 1993, **262**, 1419–1422.
66 I. Lopez-Duarte, T. T. Vu, M. A. Izquierdo, J. A. Bull and M. K. Kuimova, *Chem. Commun.*, 2014, **50**, 5282–5284.
67 M. K. Kuimova, S. W. Botchway, A. W. Parker, M. Balaz, H. A. Collins, H. L. Anderson, K. Suhling and P. R. Ogilby, *Nat. Chem.*, 2009, **1**, 69–73.
68 C. Selve, J.-C. Ravey, M.-J. Stebe, C. El Moudjahid, E. M. Moumni and J.-J. Delpuech, *Tetrahedron*, 1991, **47**, 411–428.

Chapter 3

Nonlinear Optical Imaging of Porphyrin-based Dyes in Live Mammalian Cells

Summary: *One of the primary criteria for SHG-based voltage-sensitive dyes to be able to measure membrane potential of cells, is to localize at the plasma membrane. The dyes must be amphiphilic because of the amphiphilic character of the plasma membrane. Due to the high SHG-based voltage sensitivity of porphyrin-based dyes, Anderson and coworkers developed various kinds of donor-acceptor–based porphyrin dyes to measure membrane potential of live cells. The dyes possessed the same electron-donor moiety, di-alkyl aniline, and the porphyrin linker, while different electron-acceptor–based hydrophilic head-groups, such as, dicationic groups, zwitter ionic groups, and glycol-based neutral groups. I tested the cellular localization of all the porphyrin-based dyes in three different kind of live mammalian cells, which are HEK 293T cells, LN-18 cells, and rat hippocampal neurons under a multiphoton microscope. It was found that the dyes localized in different cellular compartments based on the types of hydrophilic head-groups. The dyes containing dicationic and zwitter ionic groups gave SHG signals from the endoplasmic reticulum of the cells, while the dyes containing hexaethylene-glycol–based neutral group stained the nucleus of the cell. The dye composed of both dicationic and neutral triethylene glycol (TEG) groups localized at the plasma membrane of the cells. This study shows a new structure-property relationship of porphyrin-based dyes to stain various organelles of live cells.*

3.00 Introduction

Second harmonic generation (SHG) –based microscopy offers significant advantages over two-photon excited fluorescence (TPEF) –based microscopy, such as no background signal (signals are generated only at interfaces), low phototoxicity, and low photodamage as discussed in Chapter 1. Anderson and coworkers designed various classes of non-centrosymmetric donor-acceptor–based SHG dyes (Chart 1), as potential candidates to measure membrane potential of neurons. One of the primary requirements for the SHG-based dyes to measure membrane potential, is to localize at the plasma membrane of the cells. Since SHG works only in non-centrosymmetric media, and the plasma membrane of cells are primarily made of amphiphilic lipid bilayers, the dyes must be amphiphilic to localize non-centrosymmetrically in the bilayer.

The basic design of the electrochromic dyes synthesized in the Anderson group was inspired by the existing SHG-based voltage-sensitive dyes, such as **FM4-64** (originally synthesized by Fei-Mao), **di-4-ANEPPS** (originally synthesized by Leslie Loew) and **RH 237** (originally synthesized by Rina Hildesheim) (Figure 1).[1–6]

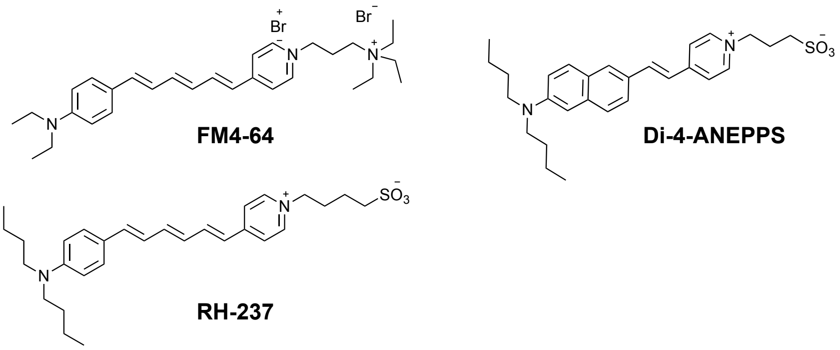

Figure 1: Molecular structures of commercial plasma membrane bound voltage-sensitive dyes.

The scheme generally adopted for designing the plasma membrane bound dyes to measure membrane potential is

Donor (hydrophobic group) − *π-conjugated system* − *Acceptor (hydrophilic group)*

where ‘Donor’ is typically an aniline-based electron-donating group normally bearing alkyl chains (to fit in the hydrophobic tail of lipids) and ‘Acceptor’ is typically a pyridinium ring functionalized with solubilizing charged groups (to interact with the hydrophilic heads of lipids). Additionally, various functional groups, such as ethene or fused benzene rings have been used for the extension of the ‘π-conjugated system’ (Figure 2).[3,7–9] The Anderson group adopted a similar design and used porphyrin molecules as the core of ‘π-conjugated system’ to synthesize new voltage-sensitive dyes (Chart 1).

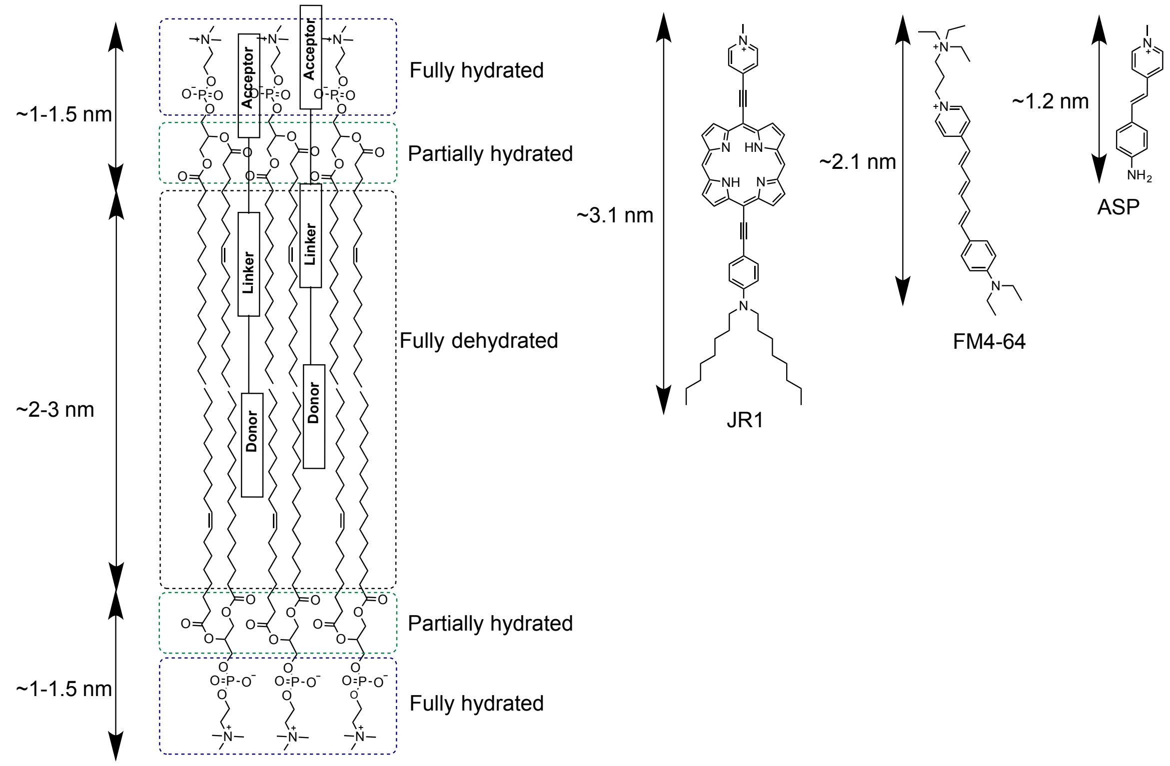

Figure 2: Schematic of a typical lipid bilayer (phosphotidylcholine type) with donor-acceptor based amphiphilic dyes arranged in it. The *donor* group bearing alkyl chains ideally fits among the alkyl chains of the bilayer through hydrophobic interactions, and the *acceptor* group with hydrophilic charged moeties interacts with the hydrated parts of the bilayer. An ideal voltage-sensitive dye will have the *‘π-conjugated system’* or *linker* embedded in between the bilayer, where it has maximum probability to interact with the changing electric field of a cell undergoing depolarization and repolarization during an action potential. For an electrochromic voltage-sensitive dye to give maximum response, ideally it should have a length of ~3–4 nm. The length of porphyrin-based dyes synthesized in the Anderson group is around 3–4 nm and hence they ideally fit this criterion. **FM4-64**, a commercial voltage-sensitive dye has a length of around 2.1 nm, while ASP, one of the fist electrochromic voltage-sensitive dye (no longer in use) has a length of around 1.2 nm.

During the event of an action potential in the plasma membrane of cells, the voltage-drop (maximum electric field) across the lipid bilayer occurs across its fully dehydrated non-polar region,[10] which has a thickness of 2–3 nm (Figure 2). To probe maximum change of the voltage, an ideal voltage-sensitive dye should have a length of around ~3–4 nm so that the ‘π-conjugated system’ spans the center of the bilayer. The porphyrin-based dyes synthesized in the Anderson are longer than 3 nm in length, thus it should experience maximum electric field when localized in a bilayer (Figure 2). The thickness of a bilayer (4–5 nm) should not be confused with the thickness of plasma membrane (7–10 nm) of a cell. Along with a bilayer, the plasma membrane is also composed of membrane proteins, glycoconjugates, and ion channels, which contribute towards the overall thickness of a typical plasma membrane.[11]

Over ten different porphyrin-based dyes were synthesized in the Anderson group (Chart 1). Dialkyl-aniline was used as the electron-donating group in all of them. As an electron-accepting group, various hydrophilic moieties were used, such as cations, zwitterions, and ethylene glycol-based non-charged hydrophilic moieties (Chart 1). Different hydrophilic groups were used to study their effect in plasma membrane localization efficacy and aqueous solubility of the dyes.

At the start of my DPhil work, the plasma membrane localization of only three porphyrin-based dyes, **JR1**, **JR1-plus**, **JR1-minus** (Figure 3) had been studied (at laser powers >20 mW) in SK-OV-3 cells (human ovarian cancer cells). The localization of other porphyrin-based dyes had not been studied and so it was not known which dyes are ideal to be used as cell-based voltage-sensitive dyes. The plasma membrane localizations of **JR1**, **JR1-plus**, **JR1-minus** were not efficient and could not be reproduced.[12] So far, the voltage-sensitivity of only one donor-acceptor–based porphyrin dye, **JR1** (Figure 3) has been studied in synthetic hemispherical lipid bilayer.[2]

In this chapter, I document the investigation that I carried out to study the cellular localization of all the porphyrin-based dyes synthesized in the Anderson group, in human embryonic kidney (HEK) 293T cells, LN-18 cells, and rat hippocampal neurons under the multiphoton microscope. The primary goal of this study was to find the dyes that localizes at the plasma membrane of live mammalian cells at least for 10–15 minutes and give bright SHG signal at low laser powers. Plasma membrane localization for this period is required so that membrane potential of the cells can be measured with high efficiency, and low laser power is important to prevent phototoxicity and photodamage. Three different types of cells are used to study whether the dyes behave uniformly across different cell lines or they display different behavior in different cells. The dye delivery and imaging experiments were designed to study the effect of the various hydrophilic groups on cellular localization.

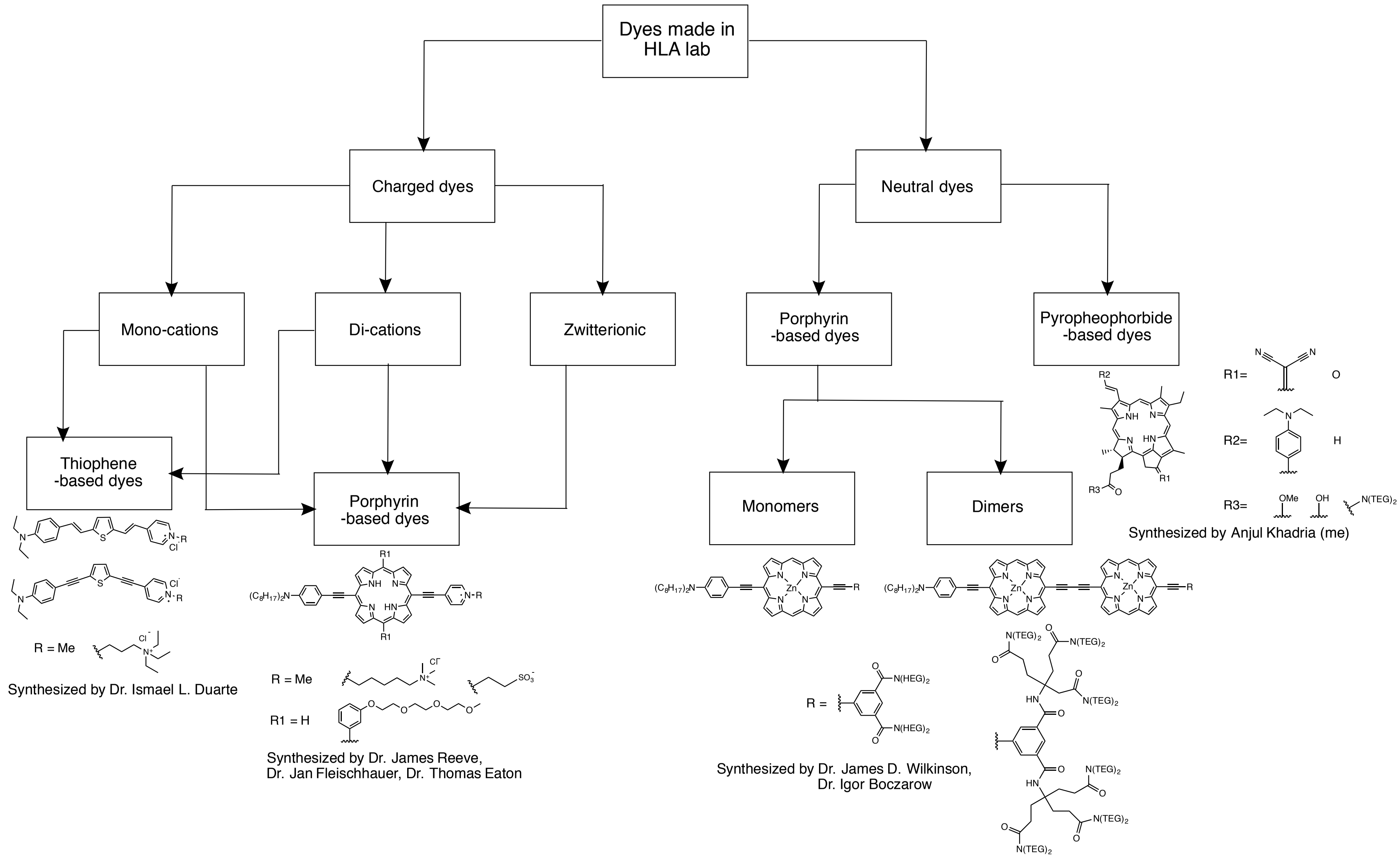

Synthesized by Dr. Ismael L. Duarte

Synthesized by Dr. James Reeve,
Dr. Jan Fleischhauer, Dr. Thomas Eaton

Synthesized by Dr. James D. Wilkinson,
Dr. Igor Boczarow

Synthesized by Anjul Khadria (me)

Chart 1: Molecular prototypes of voltage-sensitive dyes synthesized in the HLA lab

3.10 Materials and Methods

Culturing HEK 293T cells: A stock of human embryonic kidney (HEK) 293T cells was procured from ATCC (American Type Culture Collection) company. All the media and supplements were procured from Sigma Aldrich unless otherwise specified. The cells were suspended in 10 mL of phenol red free DMEM media containing 4.5 g/L glucose supplemented with 10% fetal bovine serum, 2 mM L-glutamine and 1 mM sodium pyruvate. The cell suspension was centrifuged at 200 G for 10 minutes to pellet the cells. The supernatant was discarded and the cell pellet was suspended in 5 mL of supplemented media and then mixed with 10 mL of supplemented media in a T75 flask and incubated at 37 °C in 5% CO_2 for 48 hours. After 48 hours, 1/10th of the cells were passaged to a new T75 flask with 15 mL of fresh phenol red free supplemented media to be incubated at 37 °C in a CO_2 incubator until they are 70% confluent. After the cells became 70% confluent, they were further passaged into six T75 flasks (1/6th of cells in each flask) until they are 70% confluent. Stock solutions were prepared from the six T75 flasks of 1 mL each at a density of 1 million cells/mL in 10% DMSO, 20% FBS supplemented DMEM media (phenol red free) and frozen at −80 °C using Mr. Frosty™ cell freezer.

The cells grown in a T25 or T75 flask were washed with Ca^{2+} and Mg^{2+} free Hank's balance salt solution (HBSS) buffer after decanting the media. The cells were then re-suspended in 5 mL of supplemented media. The cell suspension (500 µL) was then mixed with 6 mL of media in a T25 flask and incubated at 37 °C in a CO_2 incubator until they are about 70% confluent.

Incubation of dye: The cell suspension (200 µL) was incubated with 2 mL of supplemented media in a poly-D-lysine coated 35 mm glass-bottom dish (MatTek®) at 37 °C in a CO_2 incubator until they were 70% confluent. The cells were then washed with Ca^{2+} and Mg^{2+} free HBSS buffer and incubated with the desired concentration of dye in 0.1% DMSO in two different types of HBSS buffers (with Ca^{2+} and Mg^{2+} and without Ca^{2+} and Mg^{2+} ions) for 10 minutes. For co-localization and control experiments, **FM4-64** was procured from Biotium under the tradename SynaptoRed C2. **LysoTracker™ Yellow HCK-123**, rhodamine 123 (**RH123**), **di-4-ANEPPS**, **Hoechst33342**, and **ER-Tracker™ Red (BODIPY™ TR Glibenclamide)** were procured from ThermoFisher Scientific.

LN-18 cells: LN-18 cells are epithelial neuronal glioblastoma cells.[13] The cells were passaged and plated on the glass bottom dishes using the same procedure as for HEK 293T cells. The only difference is that, during passaging, trypsin solution was used to detach the cells from the flasks. For trypsin-based detachment, in a T75 flask, 5 mL of 0.05% trypsin (0.53 mM EDTA) solution was added and the cells were incubated for 1 min at 37 °C in a CO_2 incubator. After 1 min, the trypsin was deactivated by adding the supplemented DMEM media.

Rat hippocampal neurons: Cultured primary rat hippocampal neurons were a kind gift from Prof. Nigel Emptage, Department of Pharmacology at the University of Oxford. All reagents were procured from Invitrogen unless otherwise stated. Hippocampi were dissected from E18 Wistar rat embryos (Charles River Laboratory), dissociated in 0.5 mg/mL trypsin in HBSS for 15 minutes at 37 °C, washed twice in culture medium and gently triturated in culture medium using a briefly fire polished P1000 plastic pipette tip. Dissociated neurons were plated at a density of ~250/mm^2 on alcohol-washed 18 mm glass coverslips (VWR) previously coated with poly-D-lysine (100 µg/mL, Sigma) and fibronectin (50 µg/mL, Sigma). After attachment, coverslips were placed in 12 well plates (Corning) in Neurobasal medium supplemented with 2% fetal calf serum (FCS), 2% B27, 1% Glutamax and 1% penicillin/streptomycin. The day after plating, half the medium was changed for Neurobasal supplemented with 2% B27 and 1% Glutamax only; this medium was used for all further feeds. Cultures were maintained in an incubator at 37 °C perfused with 5% CO_2. Cultures were used for experiments at 14–21 days *in vitro* when synapses are mature.

Imaging: The imaging was performed under an upright multiphoton microscope (Olympus Fluoview FV1200MPE). The microscope is equipped with five PMT detectors (two in the reflected direction and three in the transmitted direction) and a 25X water immersion multiphoton lens objective (XLPLN25XWMP2 from Olympus) with 1.05 numerical aperture (NA) and working distance of 2 mm. The light source of the microscope is a Spectra-Physics MaiTai® eHP DeepSee™ femtosecond pulsed laser (70 fs pulse width, 80 MHz repetition rate, continuously tunable between 690–1040 nm). The dyes were imaged at different wavelengths and up to of 20 mW laser powers to achieve bright images. The femtosecond pulsed-laser light was passed through a 690 nm long pass excitation filter and then focused through the multiphoton focusing objective on the sample. For TPEF, the reflected light emitted from the dyes in the sample was passed through a 750 nm short pass filter before being passed through a 540 nm long pass (LP) filter or a dichroic mirror separating the light to pass through green (495 nm–540 nm) and red (570 nm–625 nm) band pass filters. The light was then detected by PMT detectors (Hamamatsu R3896 for green and Hamamatsu IR sensitive PMT-R10699 for red). For SHG, the light in the transmitted direction was collected through a 0.9 NA air-based condenser and then passed through a band-pass filter (420±15 nm) before being detected through a PMT detector (Hamamatsu R3896). All the imaging was performed at room temperature. The images were processed using Olympus Fluoview 4.2 software. The signal to noise ratio (SNR) of most of the images is digitally enhanced for clarity.

For most of the dyes, I used Hank's balanced salt solution (HBSS) without Ca^{2+} and Mg^{2+} ions to minimize endocytosis; however, some dyes were also imaged in HBSS with Ca^{2+} and Mg^{2+} ions (mentioned in the text) because for membrane potential imaging (discussed in subsequent chapters of this thesis), buffer with Ca^{2+} and Mg^{2+} ions is essential. The images presented here are Kalman frame averaged (5–20 times) and scanned with a pixel dwell time of 4–12.5 µs/pixel at 512 X 512 pixels.

For co-localization experiments, rhodamine123 (**RH123**, see Appendix for structure) (5 µM) and **Hoechst33342** (2 µM, see Appendix for structure) were also added from stock solutions of 10 mM and 1 mM respectively. **RH123** is mitochondria bound dye, while **Hoechst33342** is a nucleus bound dye. Cells were washed with buffer prior to imaging to remove unstained dyes. In all the experiments, **Hoechst33342** was excited at either 720 nm or 740 nm and detected in the transmitted direction through blue filter (390±20 nm). The **RH123** was excited at either 840 nm or 1000 nm and detected through the green filter (495 nm–540 nm). The signals of **RH123** was also detected through the far-red filter (>540 nm), when the porphyrin and pyropheophorbide –based dyes were detected because the emission spectra of all the dyes under investigation starts from 630 nm. Due to overlap of fluorescence signal from **RH123** with the signals of all the dyes under investigation, it could not be deduced if the porphyrin or pyropheophorbides stain mitochondria or not. The dyes were excited at either 840 nm or 870 nm unless otherwise specified.

3.20 Results and discussion

Here, I discuss the study that I performed on both charged and non-charged porphyrin-based dyes in three different types of cells to study if the dyes behave uniformly across all types of cells. HEK 293T cells were chosen because they are robust and easy to handle. Neuronal glioblastoma LN-18 cells were chosen as a control to HEK 293T cells to study if the dyes behave differently in different immortal cell lines. Additionally, since the dyes are designed to study membrane potential of neurons, I used primary rat hippocampal neurons too to study the plasma membrane localization.

3.21 Charged dyes

Anderson and coworkers synthesized charged donor-porphyrin-acceptor compounds, **JR1**, **JR1-plus**, and **JR1-minus** (Figure 3) as the initial porphyrin-based dyes to be used as potential voltage-sensitive probes.[2,12] All the three compounds possess the same electron-donating group (dioctyl aniline), the conjugated π-system (free-base porphyrin), and the electron-accepting group (pyridinium). The difference between the three compounds are the hydrophilic head-groups to form monocationic, dicationic, and zwitterionic character of these compounds. The values of β_{zzz} of porphyrin-based dyes (~ 2500 × 10^{-30} esu)[12] are three times higher than commercial dyes SHG-based voltage-sensitive dyes, such as **FM4-64** (~ 800 × 10^{-30} esu)[14] at 840 nm, thus displaying better second harmonic generation efficiency.

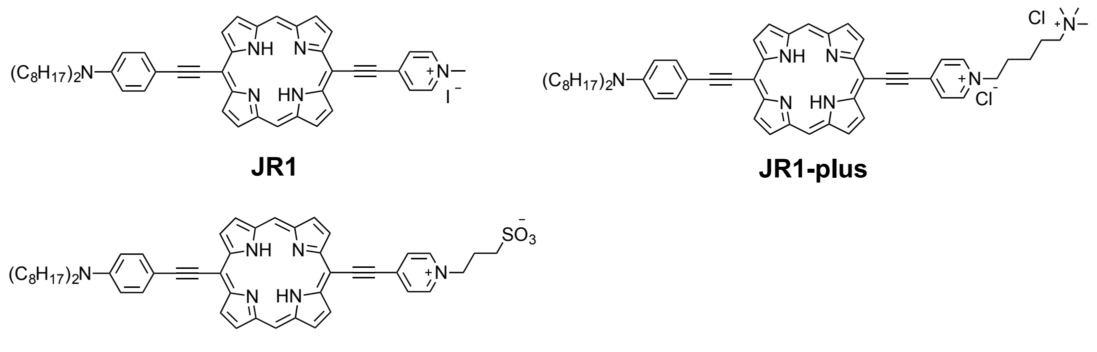

JR1

JR1-plus

JR1-minus

Figure 3: Porphyrin based donor-acceptor compounds developed by Anderson and coworkers.

Reeve *et al.* reported that **JR1-plus** and **JR1-minus** localizes in the plasma membrane of live cells, while **JR1** does not.[12] No time or concentration –based studies were performed on the localization of the dyes and no explanation was presented for different localization patterns. Here, I present a detailed and systematic study of the JR-based dyes and other porphyrin-based dyes synthesized in the Anderson group with different charged hydrophilic head-groups which are, monocationic, dicationic, and zwitterionic (Chart 1), to elucidate their true plasma membrane localization efficiency.

3.21.1 Monocationic dyes

Porphyrin-based dyes: I found that **JR1**, a monocationic dye (Figure 3) stained the interface of a lipid monolayer coated around a water-in-oil droplet, which confirms its amphiphilicity. Bright TPEF and SHG signals were observed (Figure 4; SHG signal not shown) from the dye oriented at the interface of lipid monolayers. Previous results reported by Reeve *et al.* were inconclusive about the localization of **JR1** at the interface of lipid monolayers coated around water-in-oil droplets.[12]

In HEK 293T cells, the dye crossed the plasma membrane and stained the intracellular organelles (Figure 4). **JR1** was incubated with cells through both extracellular and intracellular delivery methods but plasma membrane localization was not achieved. For extracellular delivery, the cells were incubated with the dye (10 µM) in Hank's balance salt solution (HBSS) buffer (without Ca^{2+} and Mg^{2+} ions to minimize endocytosis) for 5–10 minutes at 37 °C in a CO_2 incubator and then washed with HBSS buffer to remove the unstained dyes. For intracellular delivery, the dye was delivered through a glass micropipette by patch-clamp method.

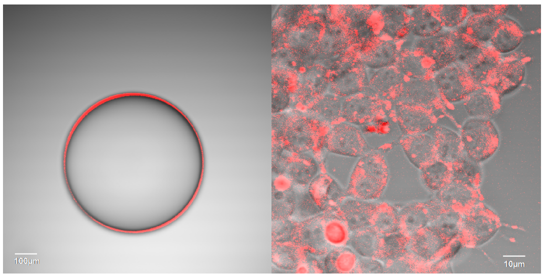

Figure 4: JR1 inside the HEK 293T cells, and at the interface of a water-in-oil drolet coated with lipid monolayer Red color two-photon excited fluorescence (TPEF) is visible from inside the cells and at the interface of the droplet. λ_{ext} = 840 nm. Scale bar = 10 µm (cells), 100 µm (droplet).

Two primary reasons for lack of plasma membrane localization for **JR1** could be:

1. A single positive charge is not sufficient to make the dye amphiphilic enough to localize at the plasma membrane. Monocationic thiophene-based dyes too, **ILD-1a** and **ILD-2a** (Figure 5) have been shown to be rapidly internalized by live SK-OV-3 cells (human ovarian cancer cells) by Anderson and coworkers,[15] which means that monocationic dyes are in general not suitable for plasma membrane localization. Aminostyryl pyridinium (ASP)-based dyes are one of the only few monocationic dyes, which have been previously shown to stain the plasma membrane of the cells (Figure 5).[7]

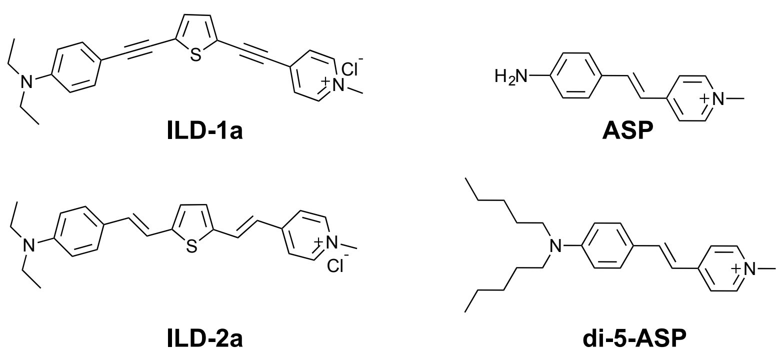

Figure 5: Mono-cationic thiophene and ASP –based dyes.

2. The dyes might be interacting with the negatively charged glycoconjugates on the cells surface or some other receptor proteins on the plasma membrane thus triggering endocytosis.

3.21.2 Dicationic dyes

The rapid uptake of monocationic porphyrin-based dyes by the cells suggested the necessity of synthesizing dicationic dyes with a more hydrophilic head-group. Here, I describe the cellular localization study of porphyrin-based dicationic dyes synthesized in the Anderson group. Four dicationic porphyrin-based dyes, **JR1-plus**, **HLA-1**, **HLA-2**, **HLA2.Cu** were synthesized with structural variations. In the beginning, I discuss the cellular localization of **JR1-plus** dye followed by the study of **HLA1**, **HLA2**, and **HLA2.Cu**.

JR1-plus dye

Reeve *et al.* reported that **JR1-plus** (Figure 3) gives SHG signal from the plasma membrane of SK-OV-3 cells (human ovarian cancer cells), when incubated at a concentration of 10 µM and imaged at 840 nm at a laser power of 21 mW.[12] In these experiments performed by Reeve *et al.*, the imaging was performed immediately after washing the cells, after 10 minutes of dye incubation,[14] and no information was given about the time for which the dye remained localized in the plasma membrane. Typically, 21 mW power from a femtosecond pulsed-laser is catastrophic for live cells because the cells die in 2–4 minutes if continuously exposed to such a high laser power. Here, I report a detailed study of **JR1-plus** in different cell lines at different conditions to elucidate its plasma membrane localization efficiency. Apart from studying the localization in three different types of cells, experiments in HEK 293T cells were performed to track the time-based localization of the dye. A co-localization study with conventional cellular organelle trackers was also performed.

Reeve *et al.* investigated the amphiphilicity of the dye by staining the lipid monolayers coated around water-in-oil droplets, which was also confirmed by me.[12] Although, Reeve *et al.* reported that **JR1-plus** localizes in the plasma membrane of live cells,[12] in my experience, the plasma membrane localization of **JR1-plus** could not be reproduced despite repeated trials using various incubation and imaging conditions in HEK 293T, LN-18, and rat hippocampal neuronal cell lines. Below, I explain the experiments in detail that I carried out to study the cellular localization of **JR1-plus**.

Staining HEK 293T cells

I investigated the cellular localization of **JR1-plus** in HEK 293T cells in both HBSS buffers with and without Ca^{2+} and Mg^{2+} ions. In some studies, it has been reported that the use of Ca^{2+} and Mg^{2+} free HBSS buffer minimizes endocytosis; however, it is not established that such buffer will completely prevent endocytosis. One argument is that calcium has been found to promote endocytosis, so using calcium free buffer could be helpful in suppressing endocytosis.[16–18]

In HBSS without Ca^{2+} and Mg^{2+} ions, I performed a time-based study to track the movement of the dye over 7 hours at 20 °C under air. Dyes were washed with HBSS prior to imaging. The time-based study was repeated in HBSS buffer with Ca^{2+} and Mg^{2+} ions, but the cells were kept at 37 °C in between imaging times to minimize cellular degradation.

In HBSS buffer without Ca^{2+} and Mg^{2+} ions

JR1-plus dye (5 μM) was incubated with the cells extracellularly for 10–15 minutes. The cells were washed to remove the unbound dye molecules following which the cells were imaged. I found that the HEK 293T cells rapidly internalized the **JR1-plus** dye. Images were taken at different time points to study the movement of the dyes inside the cells over time.

Just after incubation (at $t = 0$ min), the dye was found to stain intracellular organelles giving both fluorescence and SHG signals (Figure 6). The organelles which are mostly stained are attached to the nucleus and are structured as concentric semicircles (SHG images in Figure 6), suggesting that it could be endoplasmic reticulum or lipid vesicles.[19] Since the plasma membrane of cells are composed of lipids which are regulated by endoplasmic reticulum,[20] it could be that after attaching to the plasma membrane, the amphiphilic dye molecules could have been taken up by the cells by endocytosis and hence stained the endoplasmic reticulum. No change was observed in the localization of the dyes in the cells after 30 minutes.

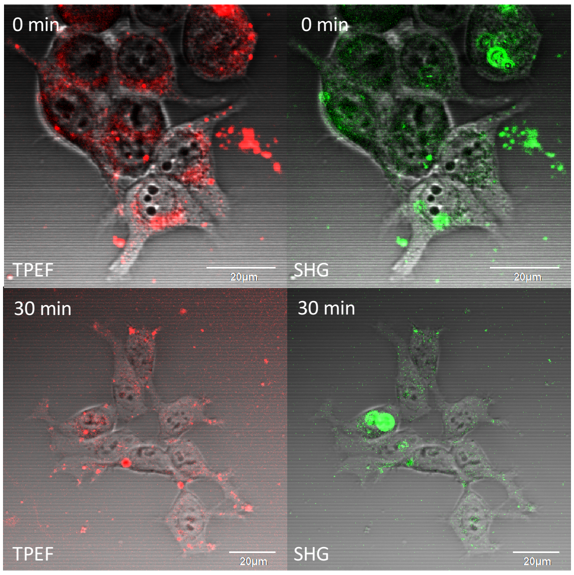

Figure 6: TPEF (left) and SHG (right) images of **JR1-plus** in HEK 293T cells at 0 min and 30 min after incubation. SHG is visible from some of the intracellular organelles in form of concentric circles, which could be endoplasmic reticulum. λ_{ext} = 840 nm. Scale bar = 20 µm.

After two hours of staining, the cell morphology started to change, which is because they were kept at room temperature without supplemented DMEM media (Figure 7). The intracellular organelles were still stained with the dyes, giving bright TPEF and SHG signals. After three hours, strong TPEF and SHG signals were seen from the plasma membrane of the cells. This happened because dyes are pushed out of the cells by exocytosis during which the amphiphilic dyes got trapped in the plasma membrane (Figure 7). It has been previously reported that when the cells become unhealthy they flush out external agents through exocytosis.[21]

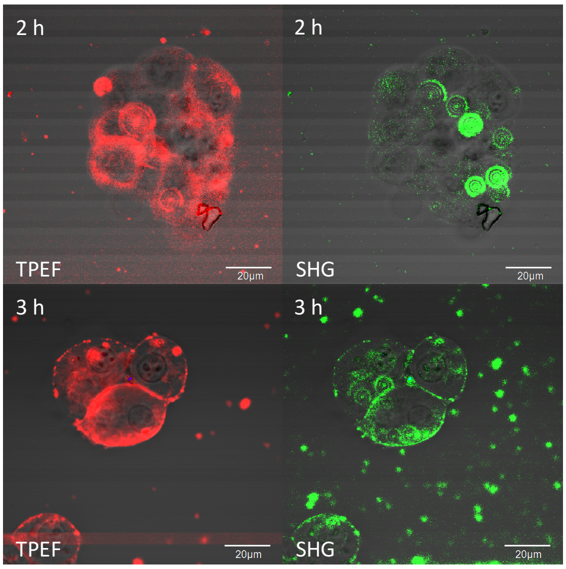

Figure 7: JR1-plus afer two and three hours of staining in HEK 293T cells. The cells have become more rounded as compared to images in Figure 6, which may be due to their storage at room conditions without supplemented media. At 3 h, the dyes stained the plasma membrane, due to exocytosis process of the cells. Strong SHG signals could still be seen from intracellular organelles as well, which could be endoplasmic reticulum. λ_{ext} = 840 nm. Scale bar = 20 µm.

Numerous cellular vesicle-type structures could also be observed outside the cells stained with dyes at 3 h, further confirming that the exocytosis took place. After about 4.5 h, the trend was found to be similar (pictures not shown as they are similar to 3 h in Figure 7). After 6–7 h, most of the cells were found to be completely round (probably dead or very unhealthy) with the dyes inside them.

In HBSS buffer with Ca^{2+} and Mg^{2+} ions

I investigated the cellular localization of **JR1-plus** dye in HBSS buffer with Ca^{2+} and Mg^{2+} ions because Ca^{2+} and Mg^{2+} ions are important for normal biological functions and will be required during the testing of voltage-sensitivity of dyes through patch-clamp method in live cells.[22–27] Since cells do not remain healthy at room conditions for over 7 hours in HBSS buffer, this time I kept the cells at 37 °C in between imaging times. Also, instead of imaging the same sample repeatedly, several samples were prepared for imaging at different times so the incubation conditions are not affected.

After 15 minutes and 1 h of staining at 37 °C, the dyes were found to stain the intracellular organelles, similarly as in the experiment performed in buffer without Ca^{2+} and Mg^{2+} ions. The same trend was observed after 2 h and 4 h of staining at 37 °C (Figure 8). After staining the dyes at 37 °C for 15 h in HBSS buffer, the cells were dead (images not shown). It is not surprising that the cells died because they were stored in HBSS buffer (the dyes are incubated in the buffer) and not in supplemented DMEM media.

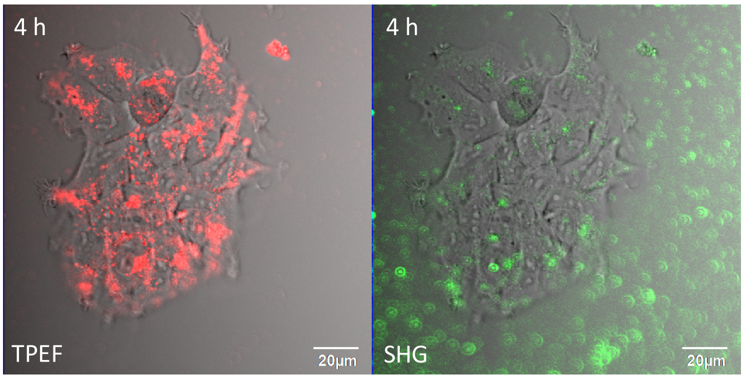

Figure 8: After 4 h of staining at 37 °C in Hank's balanced salt solution (HBSS) with Ca^{2+} and Mg^{2+} ions, the **JR1-plus** dyes stained the intracellular organelles of HEK 293T cells. Flushed out vesicles stained with dyes could be seen in the SHG image. $\lambda_{ext} = 840$ nm. Scale bar = 20 μm.

Since the dyes in TPEF images of Figure 8 could also be seen as small spherical-shaped balls (of sizes around 0.5–1 μm), I performed continuous time-based imaging and found that these spherical balls move inside the cells (Figure 9). These balls appear to be vesicles because the ball movements were also seen in transmitted light images (which are direct images of cells and cellular organelles). The balls cannot be dye precipitates because the movement was more dynamic than it would have been for precipitated particulates and no such precipitates were observed outside cells thus confirming that the cells took up the dye by the process of endocytosis (Figure 9). Dicationic FM (Fei Mao)-based dyes such as **FM4-64** (Figure 1) and **FM1-43** (see Appendix) are widely used to track endocytosis in cells,[28–31] further supporting that **JR1-plus**, a dicationic dye could be taken up by endocytosis. Cationic porphyrin-based dyes have been reported to be taken by the cells *via* endocytosis.[32–34]

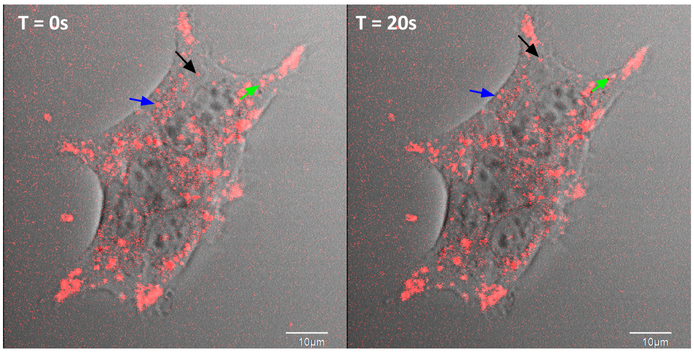

Figure 9: TPEF images of the **JR1-plus** in HEK 293T cells taken at 0 s and 20 s. The arrows in the images show the vesicles whose relative positions are different in the left and right images. λ_{ext} = 840 nm. Scale bar = 10 µm.

I performed a co-localization study of **JR1-plus** in HEK 293T cells with **RH123** (mitochondria bound dye) and **Hoechst33342** (nucleus bound dye) dyes to deduce the organelles inside the cells that **JR1-plus** stains (Figure 10). Due to the absence of relevant fluorescence cut-off filters in our multiphoton microscope, the fluorescence signals of **RH123** could not be separated and hence it was detected in both green and red channels of the microscope because it emits in both green and red regions of visible spectra (Figure 10). **JR1-plus** is a red dye (emission occurs above 630 nm) and is detected only in far-red filter (far-red filter detects all the light above 540 nm). So, the red signals are coming from both **JR1-plus** and **RH123**, while yellow is coming only from **RH123** dye (due to overlap of green and red). I excited the samples at different wavelengths to separate the signals based on excitation wavelength; however, this proved to be futile, since **RH123** has a broad two-photon absorption spectrum (Figure 10). **Hoechst33342** dye stained the nucleus of the cells, which could be clearly distinguished from **RH123** or **JR1-plus** dyes (Figure 10). **JR1-plus** stains several intracellular organelles; however, it is not clear if it stains mitochondria or not, since the signal of **RH123** could not be separated from the red channel. On co-localization with BODIPY™ TR-based **ER-Tracker™ Red** dye, **JR1-plus** was found to give SHG signals from endoplasmic reticulum (Figure 10); however, the staining at the endoplasmic reticulum was not homogeneous suggesting that the dye localized only at the specific parts of the endoplasmic reticulum.

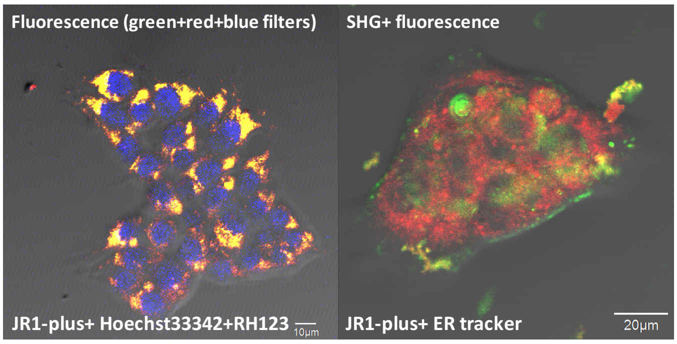

Figure 10: The left image, 'green+red+blue filter' shows nucleus stained with **Hoechst33342** in blue color, the mitochondria stained in yellow color and other intracellular organelles stained with **JR1-plus** dye in red color. The mitochondria stained with **RH123** are yellow because of the mixure of green (green filter) and red (red filter) colors. The right image, SHG+fluorescence shows the colocalization of **JR1-plus** with **ER-Tracker™ Red** dye. The SHG (green) is from the **JR1-plus** dye while, red color fluorescence is from the **ER-Tracker™ Red** dye (detected through 570 nm–625 nm filter). Scale bar = 10 µm and 20 µm.

Staining in LN-18 cells

Since **JR1-plus** does not localize in the plasma membrane of HEK 293T cells, LN-18 cells were used to investigate the plasma membrane localization to check if the lack of plasma membrane localization is restricted only to HEK 293T cells. In LN-18 cells too, the dyes stained the intracellular organelles (probably endoplasmic reticulum and lipid vesicles) like in HEK 293T cells (Figure 11). As expected, after a few hours, the dyes stained the plasma membrane (Figure 11) as previously observed in HEK 293T cells, perhaps because of exocytosis.

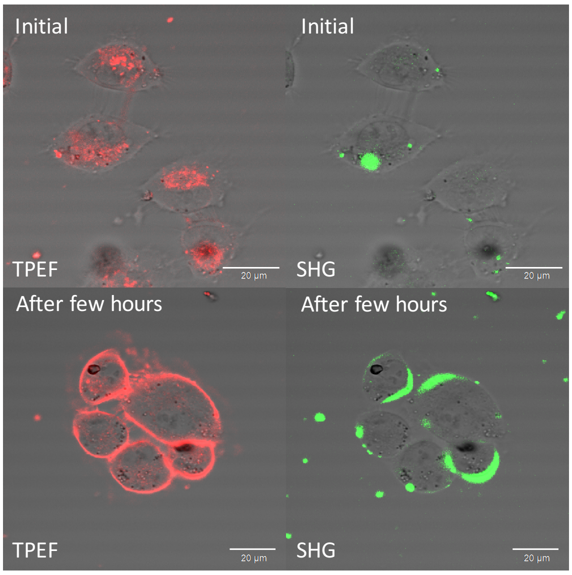

Figure 11: Just after incubating the LN-18 cells with **JR1-plus**, the dyes were found to stain intracellular organelles (upper images); however, after a few hours, the dyes stained the plasma membrane of the cells suggesting that the dyes are flushed out of the cells through exocytosis. SHG and TPEF signals from vesicles flushed out of the cells are visible in the bottom images. λ_{ext} = 840 nm. Scale bar = 20 µm, dye concentraion = 5 µM.

Staining in rat hippocampal neurons

Since porphyrin-based dyes are designed to be used for measuring the membrane potential of neurons, I investigated the localization of **JR1-plus** in rat hippocampal neurons in both

HBSS buffer solutions with and without Ca^{2+} and Mg^{2+} ions. In contrast to HEK 293T cells and LN-18 cells, apart from staining the intracellular area, the dye gave SHG signal from the plasma membrane of a few neurons incubated in HBSS buffer without Ca^{2+} and Mg^{2+} ions. The SHG signal was not observed across all the cells (Figure 12).

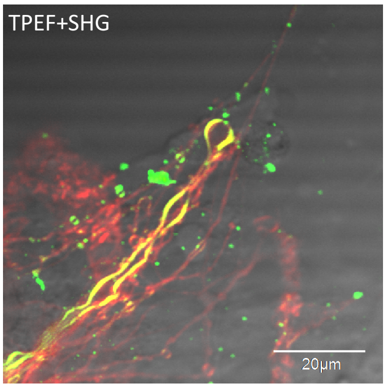

Figure 12: Overlap of TPEF (red and yellow) and SHG (yellow) signals of **JR1-plus** (15 µM) from the plasma membrane of the neurons in Ca^{2+} and Mg^{2+} free HBSS buffer. SHG signal (yellow) is observed only from few cells. Laser power = ~3 mW at 840 nm. Scale bar = 20 µm.

In HBSS buffer with Ca^{2+} and Mg^{2+} ions, plasma membrane localization was not achieved. For clarity, the signal to noise ratio (SNR) of the images are digitally enhanced to observed SHG signals which appear in form of clumps (Figure 13). Most of the dye molecules stained the intracellular organelles like in HEK 293T cells and LN-18 cells.

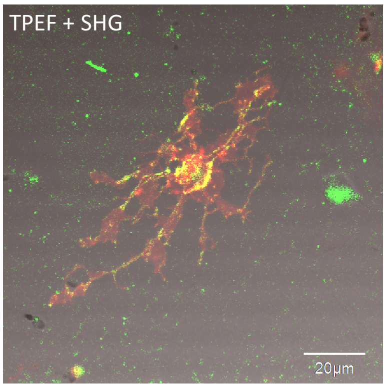

Figure 13: JR1-plus dye molecules internalized by the rat hippocampal neurons. Both TPEF and SHG images show some parts of axons and dendrites, are stained. The SNR of the images are digitallly enhanced for clarity. λ_{ext} = 840 nm. Scale bar = 20 µm.

From the study on all three different cell lines, it is evident that **JR1-plus** dyes enter the cells through endocytosis. It is not understood what triggers the endocytosis of these porphyrin-based dyes, although, it can be speculated that the positive charge interacts with the negatively charged polysachharides and lipids of plasma membrane resulting in endocytosis.[35] HEK 293T and LN-18 cells take up the dyes even in buffer without Ca^{2+} and Mg^{2+} ions; however, plasma membrane localization was sparingly observed in rat hippocampal neurons in buffers without Ca^{2+} and Mg^{2+} ions. Non-uniform plasma membrane localization of **JR1-plus** in three different types of mammalian cells makes it unsuitable to be used as voltage-sensitive dye.

HLA1 and HLA2 dyes

The next types of dicationic dyes whose localization I studied in the three cell lines are **HLA1**, **HLA2**, and **HLA2.Cu** (Figure 14), synthesized by Dr. Jan Fleischhauer, a former postdoctoral researcher in the Anderson group (synthesis and characterization data not yet published).

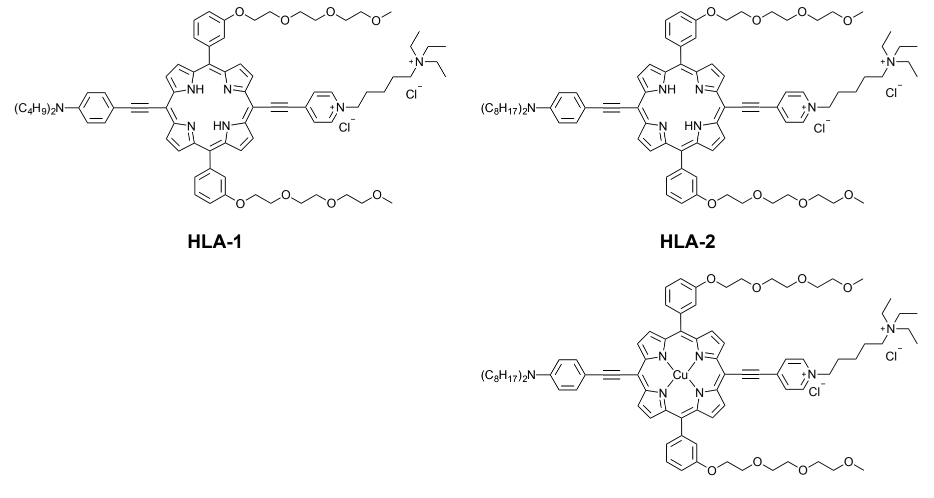

HLA-1 **HLA-2**

HLA2.Cu

Figure 14: Chemical structures of **HLA1**, **HLA2**, and **HLA2.Cu** dicationic dyes.

Dr. James Reeve, who first synthesized the JR-based dyes in the Anderson group speculated that octyl chains make the membranes of neurons very greasy, which hinders their use for patch-clamping experiments.[14] The octyl chains also make staining slower, and might disrupt the lipid packing of the plasma membrane. The solubility of the JR-based dyes in aqueous solutions remained a recurrent problem. To counter these problems, Dr. Jan Fleischhauer synthesized **HLA1**, **HLA2**, and **HLA2.Cu** dyes. All the three dyes are substituted with two triethylene glycol (TEG) substituted aryl groups at the opposite *meso* positions of core porphyrin to enhance the solubility of dyes in aqueous solutions. **HLA1** contains two butyl chains attached to the donor group instead of octyl chains in **HLA2** to address the problems of greasiness and poor solubility. Since both **HLA1** and **HLA2** are structurally similar except the length of alkyl chains, their behavior will be discussed together here. To synthesize

HLA2.Cu, copper was inserted in the porphyrin core of **HLA2** to quench its fluorescence. The study of **HLA2.Cu** is discussed at the end of this section after discussion of plasma membrane localization of **HLA1** and **HLA2**. Attaching TEG-substituted aryl groups at the *meso* porphyrin positions decreases the β_{zzz} of the dyes by one-third (~800 × 10^{-30} esu for **HLA2**) in comparison to **JR1** (~2500 × 10^{-30} esu) at 840 nm, which means that their SHG efficacy also decreases.

I studied the amphiphilicity of **HLA1** in water-in-oil droplets coated with lipid monolayer. The dye was found to orient at the monolayer interface of water-in-oil droplets (Figure 15). No amphiphilicity test was performed for **HLA2** due to the similarity of its hydrophilic head-groups with **HLA1**.

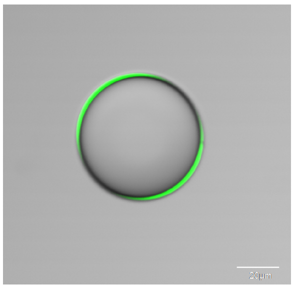

Figure 15: Amphiphilic dye **HLA1** giving SHG signal from the interface of water-in-oil droplet coated with lipid monolayer. Scale bar = 20 μm.

Staining in HEK 293T cells

Pleasingly, both **HLA1** and **HLA2** localized at the plasma membrane of HEK 293T cells (Figure 16) unlike the JR-based dyes. Since **HLA1** and **HLA2** differ from the JR-based dyes only by the presence of hydrophilic TEG-substituted aryl groups, I conclude that these groups play a significant role in the plasma membrane localization of the dyes. The SNR of the images in Figure 16 are digitally enhanced for clarity.

In HBSS buffer without Ca^{2+} and Mg^{2+} ions, the dyes localized at the plasma membrane of the cells. However, the localization was not homogeneous and appeared to form clumps. It is unlikely that the dyes formed precipitated particulates because the aqueous solution saturation concentration of **HLA2** is ~50–60 μM as measured by Dr. James Reeve in pure water.[14] High laser power of 20 mW was required along with digital enhancement of SNR to generate clear TPEF and SHG images.

In HBSS buffer with Ca^{2+} and Mg^{2+} ions too, **HLA1** (30 μM) localized at the plasma membrane of the cells, suggesting that the hydrophilic TEG-substituted aryl groups are indeed preventing the endocytosis of the dyes (Figure 17). The SNR of the images in Figure 17 are digitally enhanced for clarity.

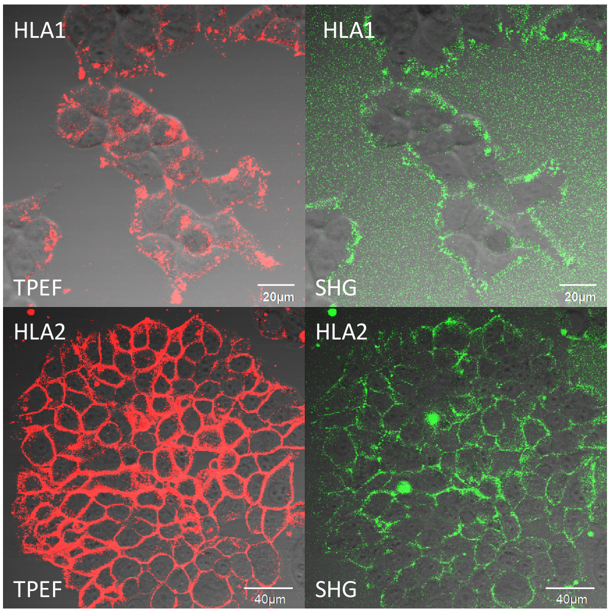

Figure 16: HLA1 (10 µM) and **HLA2** (10 µM) staining the plasma membrane of HEK 293T cells in HBSS buffer without Ca^{2+} and Mg^{2+} ions. Dotty green signals can be seen from the surroundings of cells for both **HLA1** and **HLA2**, whose origin remains unclear. The dyes did not stain the cells homogeneously. The SNR is digitally enhanced for clarity. λ_{ext} = 840 nm at ~20 mW laser power, scale bar = 20 µm (**HLA1**), 40 µm (**HLA2**).

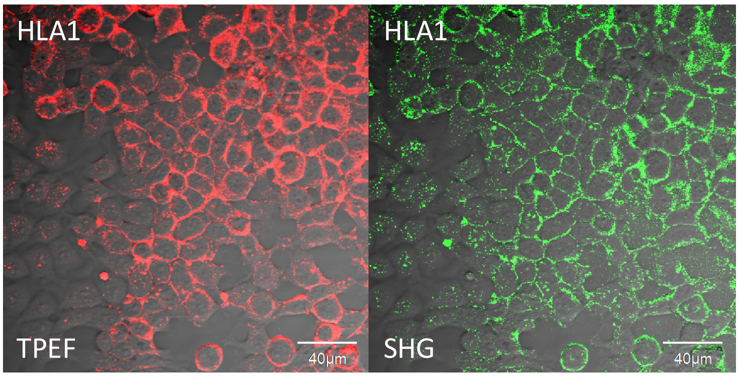

Figure 17: HLA1 (30 µM) localized at the plasma membrane of HEK 293T cells in HBSS buffer with Ca^{2+} and Mg^{2+} ions. This result confirms that TEG-substituted aryl groups attached at the meso positions of the donor-acceptor based amphiphilic porphyrin are playing a crucial role in preventing endocytosis. λ_{ext} = 870 nm, scale bar = 40 µm.

The dyes remain localized at the plasma membrane for more than 2 hours after staining. Co-localization studies with **RH123** and **Hoechst33342** did not give any useful information as **HLA1** stained the plasma membrane, **RH123** stained the mitochondria, and **Hoechst33342** stained the nucleus (images not shown).

Staining in LN-18 cells

In LN-18 cells too, the dyes localized at plasma membranes like in HEK 293T cells (Figure 18). Fluorescence signal was also visible from inside the cells; however, majority of the signal comes from the plasma membrane. High laser power (~20 mW) at 840 nm was required to obtain the signals at a concentration of 10 µM.

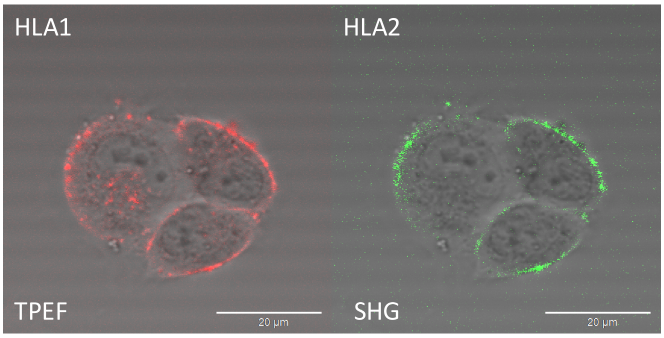

Figure 18: HLA2 (10 µM) staining the plasma membrane of LN-18 cells in HBSS buffer without Ca^{2+} and Mg^{2+} ions. In the TPEF image, some fluorescence signal can also be seen from inside the cells; however, in the SHG image the signal is coming from only the plasma membrane. The SNR is digitally enhanced. λ_{ext} = 840 nm, scale bar = 20 µm.

Staining in rat hippocampal neurons

The plasma membrane localization of **HLA1** and **HLA2** dyes was also achieved in rat hippocampal neurons. TPEF and SHG signals can be seen from the plasma membrane of the soma of the neurons as well as from the branched dendrites and axons (Figure 19). In both the HBSS buffers with and without Ca^{2+} and Mg^{2+} ions, the dyes behaved similarly. Figure 19 depicts the localization of **HLA1** and **HLA2** in neurons in HBSS with Ca^{2+} and Mg^{2+} ions. The SNR in the images are digitally enhanced because the original signal to noise ratio was low.

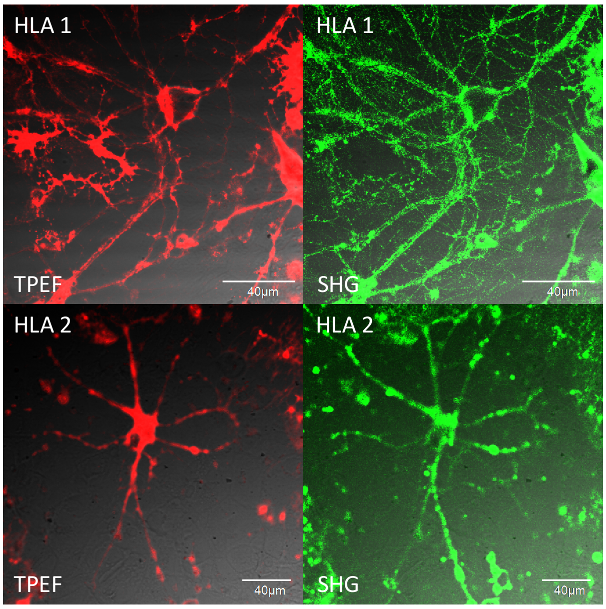

Figure 19: HLA1 (5 µM) and **HLA2** (5 µM) staining the plasma membrane of rat hippocampal neurons (in HBSS with Ca^{2+} and Mg^{2+} ions) with all the dendrites and axons clearly visible in both the TPEF and SHG images. The SNR is digitally enhanced because signal to noise ratio was low. λ_{ext} = 870 nm, Kalman frame averaging = 20, scale bar = 40 µm.

I also tried to label **HLA1** intracellularly staining by dissolving the dyes in aqueous buffer and delivering it through a glass pipette by the patch-clamp technique; however, the dyes did not localize at the plasma membrane and stained the intracellular organelles (Figure 20).

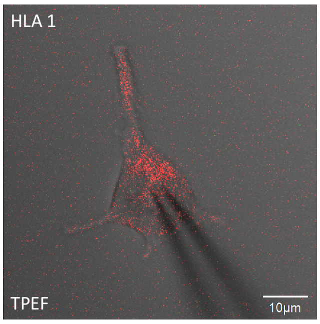

Figure 20: Intracellular delivery of **HLA-1** (15 μM) through patch-clamp technique. The dye molecules stained intracellular organelles but not the plasma membrane. No SHG signal was visible. λ_{ext} = 840 nm, scale bar = 10 μm.

Insertion of metals like copper and nickel in porphyrins is known to quench its fluorescence.[36] **HLA2.Cu**, a copper-based porphyrin dye was synthesized by Dr. Jan Fleischhauer by inserting copper in **HLA2**. On imaging the cells incubated with 10 μM of **HLA2.Cu**, I did not see any fluorescence or SHG signal. On increasing the concentration stepwise to 40 μM (Figure 21), strong SHG signal was seen from the plasma membrane of the cells but no fluorescence was visible as expected (Figure 22).

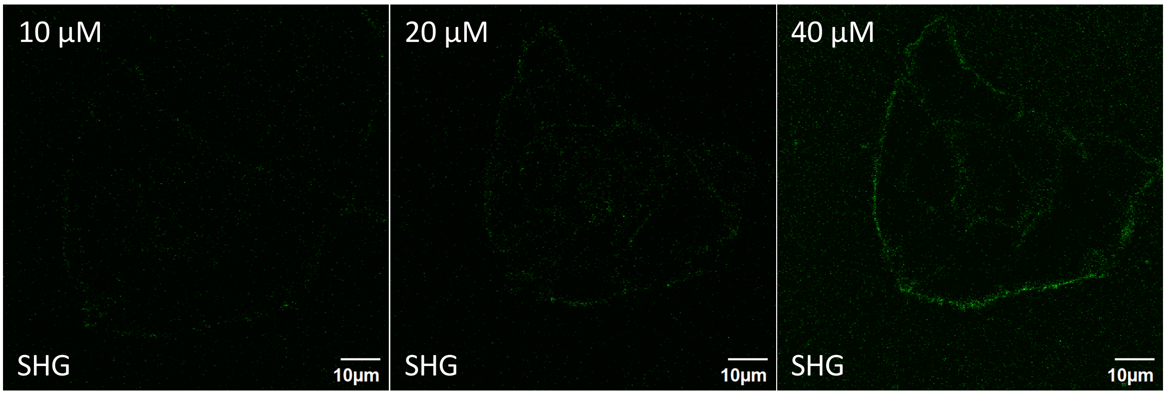

Figure 21: Concentration-based study of **HLA2.Cu** in LN-18 cells in HBSS buffer with Ca^{2+} and Mg^{+2} ions. As the concentration is increased from 10 μM to 40 μM, the SHG intensity increases. Laser power = 1.4 mW, λ_{ext} = 850 nm. Scale bar = 10 μm.

Increasing the concentration to more than 40 μM to get brighter SHG signal, resulted into formation of dye precipitates. Non-fluorescent SHG-based plasma membrane bound dye will provide significant advantages over fluorescent dyes, such as no phototoxicity and no background fluorescence signal. Such a dye will also allow multimodal imaging with other conventional cellular organelle trackers.[37] Until now just one only SHG-based azo-styryl dye has been reported, which does not give any fluorescence signal.[37] **HLA2.Cu** is the first nonlinear optical porphyrin-based dye which gives bright SHG signal but no fluorescence.

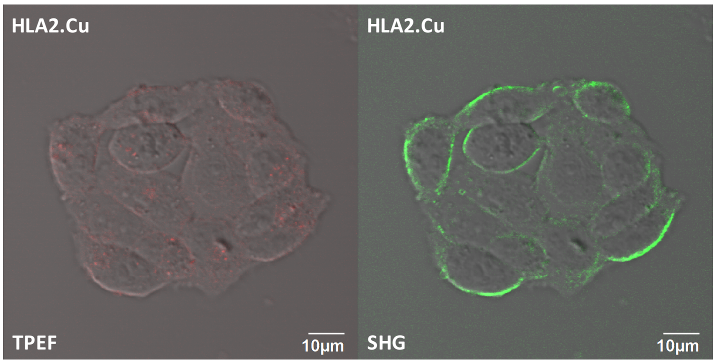

Figure 22: HLA2.Cu staining the plasma membrane of LN-18 cells in HBSS buffer with Ca^{2+} and Mg^{2+} ions. The TPEF signal is reduced in comparison to images in Figure 19; however, the SHG signal is very bright. The dye concentration is 40 μM. Laser power = 4 mW, $\lambda_{ext} = 850$ nm. Scale bar = 10 μm.

It is evident that the TEG-substituted aryl groups play a significant role in preventing endocytosis of the dyes but it comes at the cost of reduced SHG efficiency (in terms of β_{zzz}) and skewed orientation of the dye (the amphiphilic axis and transition dipole moment are not collinear) thus further reducing the SHG efficacy.[38]

I studied the plasma membrane localization of commercial dicationic dye, **FM4-64** in HEK 293T cells (Figure 23) for comparison with porphyrin-based dyes. The value of β_{zzz} of **FM4-64** (~800 × 10^{-30} esu) is less than that of any of the porphyrin dyes (>1000 × 10^{-30} esu) at 840 nm; however, **FM4-64** gave better signal to noise ratio for both TPEF and SHG signals at a low laser power (1.4 mW) at similar concentrations.

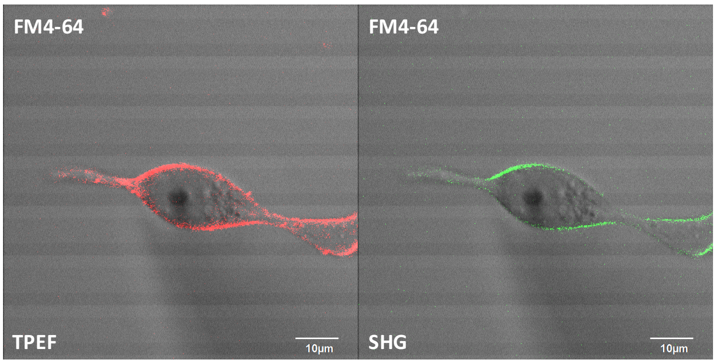

Figure 23: FM4-64 (10 μM) incubated with HEK 293T cells in HBSS with Ca^{2+} and Mg^{2+} ions. Laser power = 1.4 mW, $\lambda_{ext} = 840$ nm. Scale bar = 10 μm.

Better SNR for **FM4-64** could be attributed to three factors: (1) the small size of **FM4-64** makes its density in the plasma membrane larger than **HLA1** and **HLA2** dyes, hence increasing the SHG efficiency of **FM4-64** (refer to Chapter 1 for explanation). (2) Apart from the pyridinium group (acceptor), there is no other hydrophilic group to contribute towards the orientation of the dye in the plasma membrane thus not affecting the direction of its TDM. For a dye to give maximum SHG, the angle between its TDM and the polarization of the excitation laser light shall be minimum (ideally zero) and hence the dye should orient coaxially along the plasma membrane.[38] (3) The TEG-substituted aryl groups might be affecting the overall uptake of the dyes by the plasma membrane.

López-Duarte *et al.* (Anderson group) reported that dicationic thiophene-based dyes **ILD-1b** and **ILB-2b** (Figure 24) localized at the plasma membrane of SK-OV-3 cells just like **FM4-64** and gave SHG signal at a very low laser power.[15] The overall size of thiophene-based dyes is similar to that of **FM4-64**; however, it is significantly smaller than porphyrin-based dyes. This means that the relative sizes and positions of hydrophilic group and the overall dye play a significant role in their plasma membrane uptake and localizations.

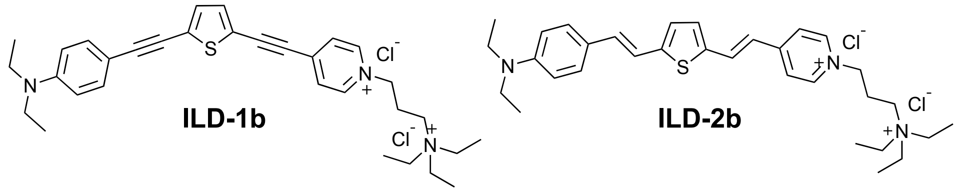

Figure 24: Thiophene-based di-cationic dyes synthesized at Anderson group, which localize at the plasma membrane of the cells to give TPEF and SHG signals.

3.21.3 Zwitterionic dyes

Along with dicationic porphyrin-based dyes, sulfonate-based zwitterionic porphyrin-based dyes, **JR1-minus** and **HLA3** were also synthesized in the Anderson group (Figure 25). Zwitterionic dyes are attractive because of their overall neutral character, which makes them less likely to interact with negatively charged cellular organelles.[7] However, zwitterions are generally less soluble in water than salts (such as dicationic dyes) because there is not the same entropic favorability of forming a solution, this makes zwitterions less hydrophilic than dicationic head-group.

I studied the amphiphilicity of **JR1-minus** in a similar manner as previous dyes, by staining lipid monolayers coated around water-in-oil droplets (Figure 26) and got similar results as reported by Reeve *et al.*[12]

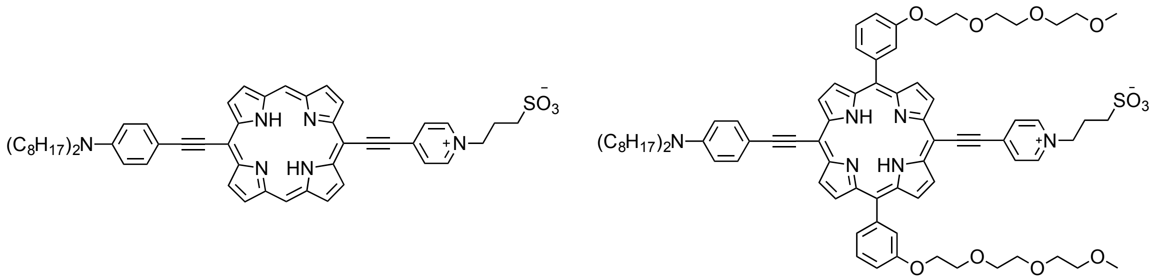

JR1-minus **HLA3**

Figure 25: Molecular structures of **JR1-minus** and **HLA3**.

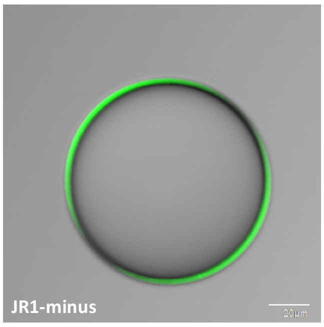

Figure 26: JR1-minus staining the water-oil interface at the lipid monolayer coated around water-in-oil droplets to give SHG signal (green color). $\lambda_{ext} = 850$ nm. Scale bar = 20 µm.

Both the porphyrin-based zwitterionic dyes, **JR1-minus** and **HLA3** rapidly crossed the cell membrane of HEK 293T cells to stain the intracellular area in HBSS buffer without Ca^{2+} and Mg^{2+} ions (Figure 27). Although **JR1-minus** stained the intracellular organelles of HEK 293T cells non-centrosymmetrically to give SHG signals like **JR1-plus**, no SHG signal was detected from intracellular organelles in case of **HLA3**.

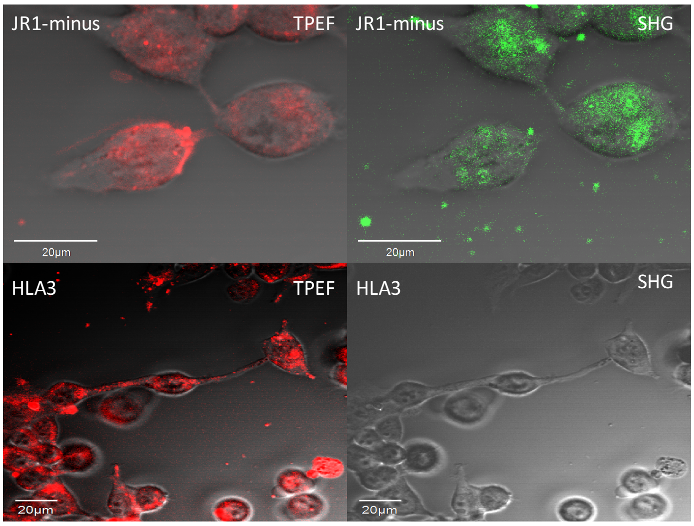

Figure 27: JR1-minus and **HLA3** staining the intracellular organelles of HEK 293T cells. SHG signal of **JR1-minus** could be seen from intracellular organelles but minimal SHG signal from cells incubated with **HLA3** is visible. TPEF from inside the cells is observed for both the dyes. $\lambda_{ext} = 840$ nm. Scale bar = 20 µm

Co-localization studies of **JR1-minus** with **RH123** and **Hoechst33342** confirmed that the dye stains several intracellular organelles (Figure 28) but not the nucleus.

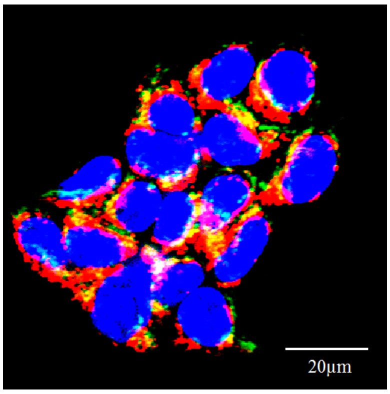

Figure 28: Co-localization of **JR1-minus** (10 µM) with **RH123** (5 µM, mitochondria bound dye) and **Hoechst33342** (2 µM, nucleus bound dye) dyes in HEK 293T cells. The yellow signal (and green) is from the mitochondria stained with **RH123** (and maybe **JR1-minus**); red signals are from the organelles stained with only **JR1-minus** and blue from the nucleus stained with **Hoechst33342**. **Hoechst33342** was excited at 750 nm and **JR1-minus** was excited at 840 nm. **RH123** was excited separately at 1000 nm. Scale bar = 20 µm

Similar results were observed in LN-18 cells. **JR1-minus** entered the cells to stain the intracellular organelles (Figure 29). **HLA3** was not tested in LN-18.

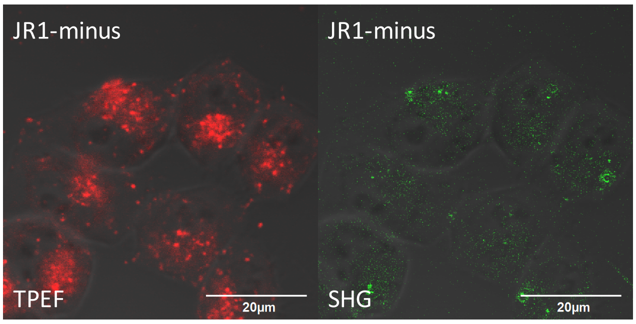

Figure 29: **JR1-minus** staining the intracellular organelles of LN-18 cells. λ_{ext} = 840 nm, Scale bar = 20 µm.

Staining in rat hippocampal neurons

In rat hippocampal neurons too, the **JR1-minus** and **HLA3** dyes stained the intracellular organelles. Imaging was performed in both HBSS buffers with and without Ca^{2+} and Mg^{2+} ions. Imaging results were similar in both the buffers for both the dyes.

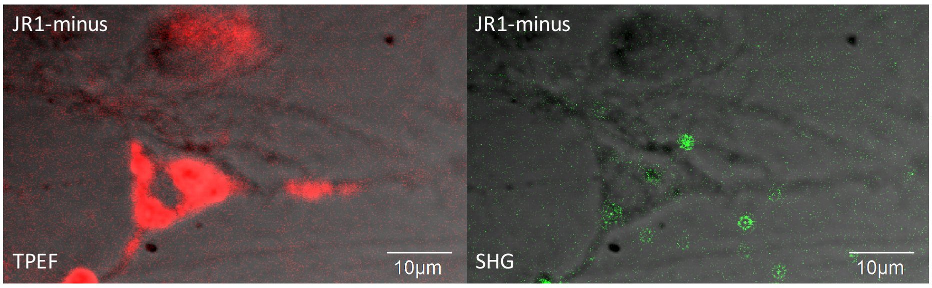

Figure 30: JR1-minus (5 µM) staining the intracellular organelles of rat hippocampal neurons (TPEF and SHG) in HBSS buffer without Ca^{2+} and Mg^{2+} ions. In the SHG image, the signal from cellular organelle(s) what could be endoplasmic reticulum is visible; however, in TPEF image, most of the intracellular organelles are visible to be stained. λ_{ext} = 870 nm, scale bar = 10 µm.

In HBSS buffer without Ca^{2+} and Mg^{2+} ions, the **JR1-minus** dye did not stain the axons and dendritic branches but both TPEF and SHG signals are visible from the intracellular organelles (Figure 30). In HBSS buffer with Ca^{2+} and Mg^{2+} ions, for both **JR1-minus** and **HLA3**, TPEF signals were visible from intracellular organelles but clumps of SHG signals were visible along the dendrites and axons after significant digital enhancement of SNR (Figure 31).

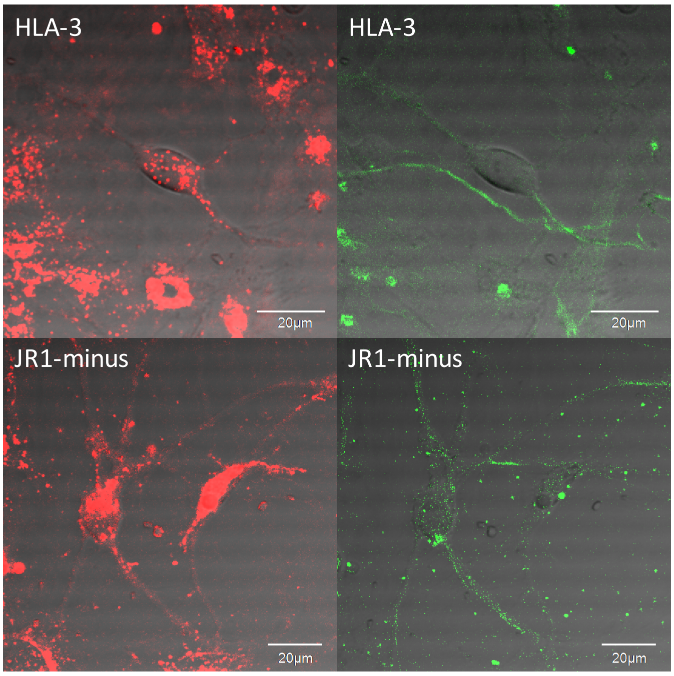

Figure 31: HLA3 (5 µM) and **JR1-minus** (5 µM) staining the rat hippocampal neurons in HBSS buffer with Ca^{2+} and Mg^{2+} ions. In TPEF images, the dyes could be seen from inside the cells along with some signal coming from the dendrites and axons. In SHG images, most of the signal is coming from axons and dendrites. λ_{ext} = 870 nm, Scale bar = 20 µm.

For comparison, I studied the cellular localization of **di-4-ANEPPS**, a commercial zwitterionic dye. The dye gave bright TPEF and SHG signals from the plasma membrane (Figure 32); however, most of the dye molecules crossed the plasma membrane to stain intracellular organelles as seen in TPEF image of Figure 32.

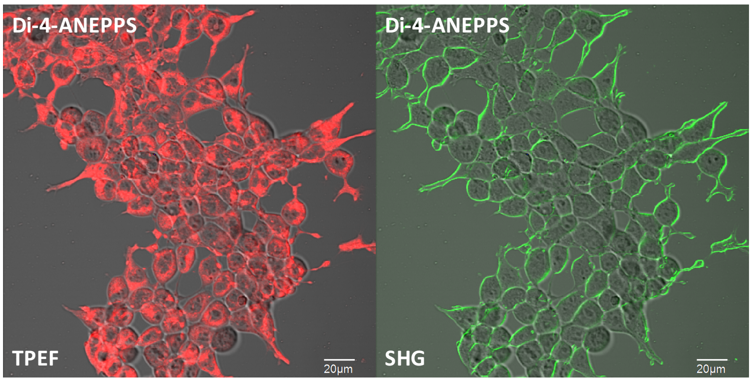

Figure 32: HEK 293T cells stained with **Di-4-ANEPPS** in HBSS with Ca^{2+} and Mg^{+2} ions. The dye is taken up by the cells (TPEF image) as well as localized at the plasma membrane (SHG image). Laser power setting = 1.4 mW, λ_{ext} = 840 nm. Scale bar = 20 µm.

From the above results, it could be concluded that zwitterionic porphyrin-based dyes are unsuitable to be used as electrochromic voltage-sensitive dyes due to their inability to localize at the plasma membrane of cells. The results of zwitterionic porphyrin-based dyes and **di-4-ANEPPS**, suggest that zwitterions although overall non-charged, are less specific than dicationic moieties for plasma membrane localization. It appears that these porphyrin-based dyes are staining the lipid vesicles and endoplasmic reticulum inside the cells like **JR1-plus**. SHG images in the form of concentric circles (like the structure of endoplasmic reticulum) are visible for both **JR1-plus** and **JR1-minus** (Figure 6 and Figure 27). The conventional endoplasmic reticulum bound fluorescent dyes do not give such structural information, which so far could only be obtained *via* electron microscopy (Figure 33) or super-resolution microscopy.[39,40] It is not unusual for charged dyes to end up staining organelles like endoplasmic reticulum and Golgi body. Previously, sulfonate-based zwitterionic dyes have been shown to end up staining the endoplasmic reticulum of live cells.[41] Additionally, genetically encoded plasma membrane bound protein-based voltage-sensitive dyes are encoded with special motifs to prevent localization at endoplasmic reticulum and Golgi body.[42,43] Inclusion of such modification in synthetic organic dyes is not trivial and would require laborious investigation. These results also pave way for research of structure-property relationship of porphyrin-based dyes targeting different cellular organelles.

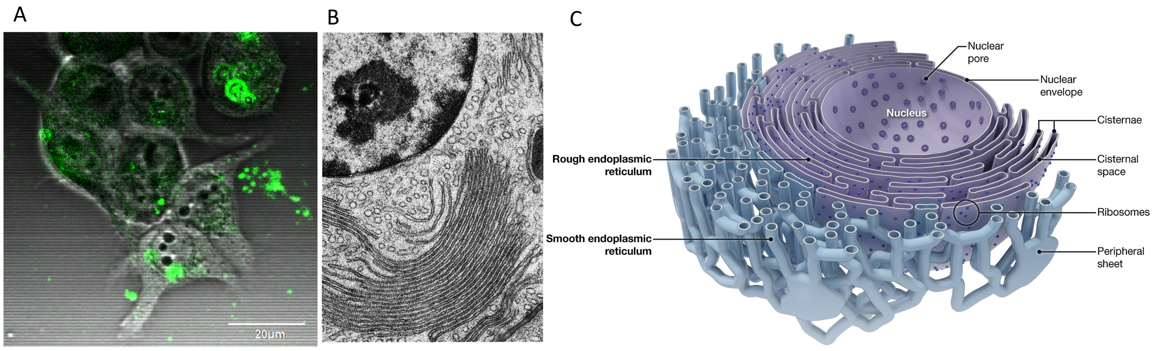

Figure 33: (A) SHG image of **JR1-plus** staining the endoplasmic reticulum in HEK 293T. Concentric semicircles seen attached to the nucleus. (B) Electron micrograph of endoplasmic reticulum from Chapter 5 of 'The Cell, 2nd Ed.' by Don W. Fawcett M.D. Image sourced from The Cell Image Library under Creative Commons Attribution, Non-commercial, No derivatives license. (C) Schematic of cellular organelles including endoplasmic reticulum in a cell. Image adapted from *Biochim. Biophys. Acta - Mol. Cell Res.*, 2013, **1833**, 2492–2498 with permission. Copyright 2013 Elsevier.

In summary, all the JR-based dyes stain the intracellular organelles of neurons; however, the ones which partition at the dendritic branches of neurons could be further investigated to study the synaptic activity at the dendrites and axons.[44] However, characterization of dendritic membrane potential of neurons to test these dyes is not trivial and is beyond the scope of this thesis. Following the above results, the charged dyes **HLA1**, **HLA2**, and **HLA2.Cu** were studied for voltage sensitivity in HEK 293T cells and is discussed in the next chapter (Chapter 4).

3.22 Non-charged dyes

Former students in the Anderson group, Dr. James Wilkinson and Dr. Igor Boczarow, replaced the charged moieties of the JR-based dyes with non-charged oligomeric hydrophilic groups to synthesize a new class of neutral dyes (Figures 34 and 39).[45,46] The dyes synthesized by Dr. Wilkinson and Dr. Boczarow differed from each other by the nature of the hydrophilic groups, which replaced the charged moieties of the JR-based dyes. Dr. Wilkinson used isophthalic acid derivatives functionalized with hexaethylene glycol (HEG) chains while Dr. Boczarow used isophthalic derivatives branched further with triethylene glycol (TEG) chains hoping to provide enhanced solubility and amphiphilicity.

The motivation behind replacing the charged groups with bulky non-charged groups was three-fold:

1. The poor solubility of charged dyes (the dyes aggregate at concentrations above 50 μM) in aqueous solutions hinder their use for optical bioimaging. Although solubilizing agents such as DMSO or pluronic-F127 could be used to enhance the

solubility of the dyes in aqueous solutions, these agents are toxic to the cells. Attachment of large non-charged hydrophilic groups would enhance the solubility of the dyes in aqueous solutions thus removing the need to use solubilizing agents.

2. It has been shown by other groups as well as the Anderson group that an acceptor group (pyridinium in case of JR-based molecules) does not substantially contribute towards the nonlinear optical properties of free-base donor-acceptor based porphyrin molecules.[47–49] The porphyrin core itself is sufficiently electron-deficient and acts as an electron-withdrawing group when decorated with an electron-donating group (dioctyl aniline) thus making the pyridinium group redundant.
3. The binding of charged dyes to the membrane can affect the overall membrane potential of the cells by interfering with the inherent charge (ions) distribution in the lipid bilayer. A neutral dye will make less change to the charge distribution than the charged dyes.

In addition to monomeric non-charged porphyrin-based dyes, dimers of these porphyrin-based dyes were also synthesized by Dr. Wilkinson and Dr. Boczarow. Porphyrin-based dimers possess higher two-photon absorption coefficient, σ_{2PA} than porphyrin monomers.[50] As discussed in Chapter 1, the overall voltage sensitivity of an SHG based dye is dependent on the following equation relating the $\beta_{eff}(E)$ and static molecular polarizabilities.[2]

$$\beta_{eff}(E) = \beta^{(0)} + \gamma_{dc-SHG}\,(E)$$

where, $\beta^{(0)}$ is the first order hyperpolarizability, which is an inherent property of a molecule, while and $\gamma_{dc-SHG}\,(E)$ is the second order hyperpolarizability, which signifies direct current induced SHG in the presence of a static electric field *E*. It has been shown that $\gamma_{dc-SHG}\,(E) \propto \gamma_{2PA}$,[46,51,52] where γ_{2PA} is the second order hyperpolarizability signifying two-photon absorption. Since, $\sigma_{2PA} \propto \gamma_{2PA}$, it can be assumed that a molecule with high two-photon absorption efficiency will have high γ_{dc-SHG} . Porphyrin dimers have σ_{2PA} in the range of thousands of GM (GM is the unit of two-photon absorption cross-section, 1 GM = 10^{-50} cm^4 photon^{-1})[50] and are thus expected to be more voltage sensitive than monomers.

Cellular localization studies of the dyes synthesized by Dr. Wilkinson and Dr. Boczarow were not performed previously, and here I describe the detailed cellular studies of the dyes that I performed. Apart from testing the porphyrin-based non-charged dyes synthesized by Dr. Wilkinson and Dr. Boczarow, I also test the non-charged pyropheophorbide-based dyes that I synthesized, which are discussed in Chapter 2.

Hexaethylene glycol (HEG) chains based dyes synthesized by Dr. James Wilkinson

HEG chains-based dyes, **JDW-M** and **JDW-D** were studied only in HEK 293T cells and LN-18 cells.

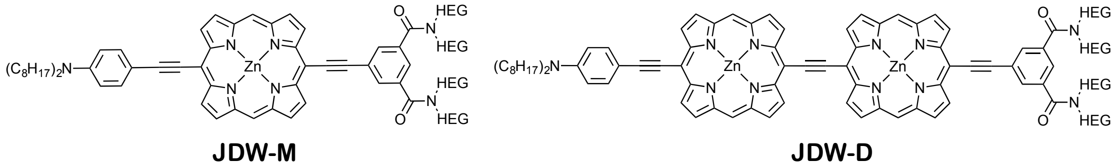

Figure 34: Molecular structures of non-charged dyes synthesized by Dr. James Wilkinson.

I tested the amphiphilicity of **JDW-D** in water-in-oil droplets and it gave similar results to the charged dyes discussed above. The dye stained the lipid monolayer at the interface of water and oil giving a bright SHG signal (Figure 35).

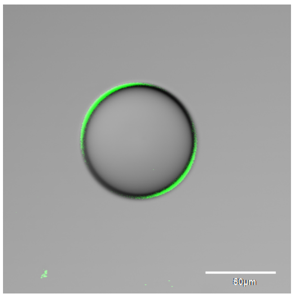

Figure 35: SHG signal from **JDW-D** at the interface of a lipid monolayer coated around water-in-oil droplets. Scale bar = 50 µm.

Staining in HEK 293T cells

On incubation of **JDW-M** (1.25 µM) and **JDW-D** (1.25 µM) dyes with HEK 293T cells in HBSS buffer without Ca^{2+} and Mg^{2+} ions, both dyes crossed the cell membrane to enter the intracellular area. Apart from staining all the cellular organelles, both the dyes seem to enter the nucleus of the cells (Figure 36). TPEF signal was visible from all over the cells but no SHG signal was detected. The nucleus staining was not completely reproducible on repeated experiments. On performing co-localization experiments of **JDW-M** with nucleus bound blue dye, **Hoechst33342**, significant nucleus staining of **JDW-M** was not observed (Figure 37). Dr. Wilkinson also synthesized the free-base monomer version of **JDW-M**, which gave similar results in HEK 293T cells (Figure 37).

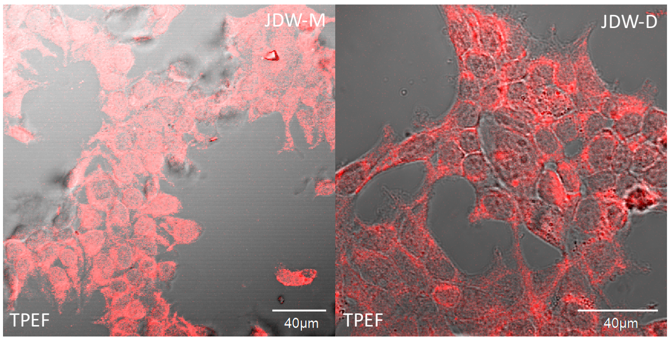

Figure 36: JDW-M (monomer) and **JDW-D** (dimer) staining the intracellular organelles including the nucleus of HEK 293T cells in HBSS buffer without Ca^{2+} and Mg^{2+} ions. $\lambda_{ext} = 800$ nm. Scale bar = 40 µm.

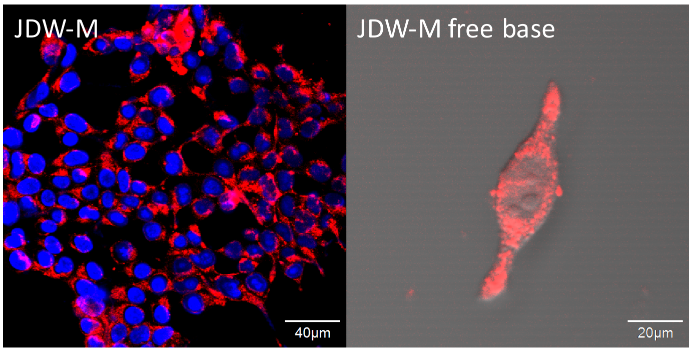

Figure 37: Imaging of **JDW-M** (20 µM) and **JDW-M free base** (20 µM) in HEK 293T cells. Co-localization of **JDW-M** with blue dye, **Hoechst33342** (2 µM) did not show any nucleus staining of **JDW-M**. For co-localization, the cells were first imaged with only **JDW-M** following which **Hoeschst33342** was added and imaged. **JDW-M free base** behaved similar to **JDW-M**. Scale bar = 40 µm (**JDW-M**), 20 µm (**JDW-M free base**).

Staining in LN-18 cells

In LN-18 cells too, similar results were seen for **JDW-D** (10 µM) (Figure 38). The dye stained various intracellular organelles with non-homogeneous staining of nucleus. The dye molecules seem to be internalized by endocytosis. **JDW-M** was not studied in LN-18 cells.

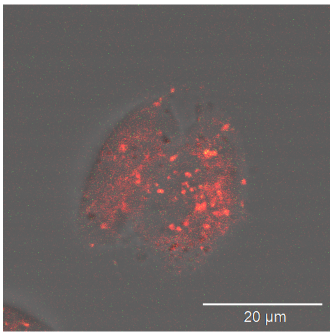

Figure 38: JDW-D dye staining the intracellular organelles including nucleus of LN-18 cells in HBSS buffer without Ca^{2+} and Mg^{2+} ions. $\lambda_{ext} = 840$ nm. Scale bar = 20 µm.

No staining was performed in rat hippocampal neurons due to the limited availability of neurons and the non-plasma membrane localization of these dyes in HEK 293T and LN-18 cells. However, the nucleus localization of the dyes makes them very interesting because they can be further probed to design molecules to measure viscosity of intra-nucleus area. Kuimova and coworkers have pioneered the work on studying the intracellular viscosity using fluorescent molecular rotors including porphyrin-based dimers.[53–56] Molecular rotors can exist in two conformers, twisted and planar due to intramolecular rotations. When the molecule is in ground state, both twisted and planar conformations are equally populated while, in the optically excited state, the molecule prefers to adopt a planar conformation. The two conformations have distinctive emission wavelengths and as the viscosity changes, the intramolecular rotation is affected, and as a result the fluorescence intensities at the distinctive wavelengths change. By ratiometric detection of fluorescence intensities, viscosity-based imaging of intracellular environments is performed. Although, the viscosities of cytosol and plasma membrane of cells are extensively studied and related to different biological events,[53,55,57–60] study of the viscosity of the nucleus remains a challenge due to the lack of an ideal molecular rotor which can stain the nucleus of the cells homogeneously. Although the nucleus staining of the dyes are not consistently reproducible, these results pave way to design future molecular rotors, which might be able to stain nucleus of the cells homogeneously in a reproducible manner.

TEG chains based dyes synthesized by Dr. Igor Boczarow

The dyes synthesized by Dr. Boczarow, **IG-M** (monomer) and **IG-D** (dimer) (Figure 39), were expected to perform better to localize in the plasma membrane than the dyes synthesized by Dr. Wilkinson because of presence of larger hydrophilic groups.

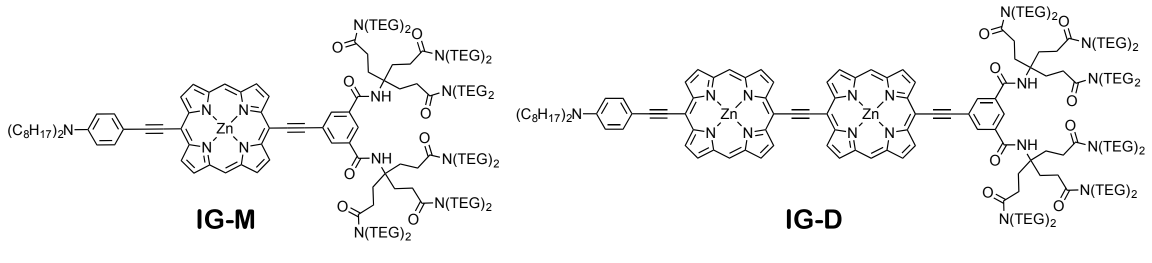

IG-M **IG-D**

Figure 39: Molecular structures of **IG-M** (monomer) and **IG-D** (dimer) dyes synthesized by Dr. Igor Boczarow. The dyes are functionalized with twelve triethylene glycol chains, which are expected to enhance the solubility and amphiphilicity of the dyes.

The **IG-M** and **IG-D** dyes localized at the interface of water in oil droplets coated with lipid monolayer (Figure 40 for **IG-D**). However, these dyes too did not localize at the plasma membrane of live HEK 293T cells (Figures 40 and 41). Dr. Aurimas Vysniauskas and Dr. Maria Izquierdo (two members of Dr. Marina Kuimova's group at Imperial College

London) also confirmed this result SK-OV-3 cells (in HBSS buffer without Ca^{2+} and Mg^{2+} ions) as mentioned in the DPhil thesis of Dr. Igor Boczarow.[46] Here, I performed imaging in three different cell lines under the multiphoton microscope to see if any SHG is visible from intracellular organelles.

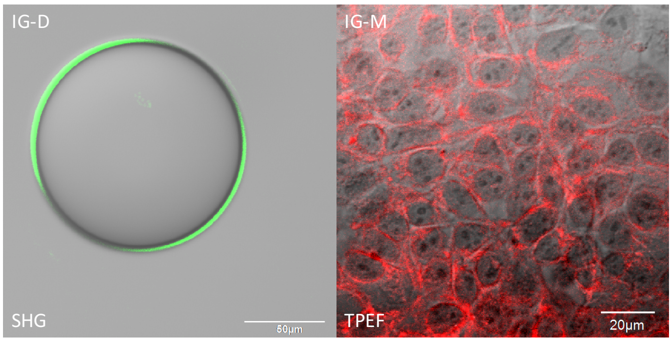

Figure 40: IG-D giving bright SHG response from the interface of water droplets in oil coated with lipid monolayer. **IG-M** (10 µM) giving bright TPEF from the interior of HEK 293T cells in HBSS buffer without Ca^{2+} and Mg^{2+} ions. Scale bar = 50 µm (droplet), 20 µm (cells).

Although **IG-D** (10 µM) is internalized by the HEK 293T cells (Figure 41), at high laser power (25 mW), dim SHG signal was visible from the plasma membrane of the cells. Such high laser power is practically not suitable for imaging live cells. Reeve *et al.* used similar laser power to report SHG from 10 µM of **JR1-plus** in SK-OV-3 cells.[12]

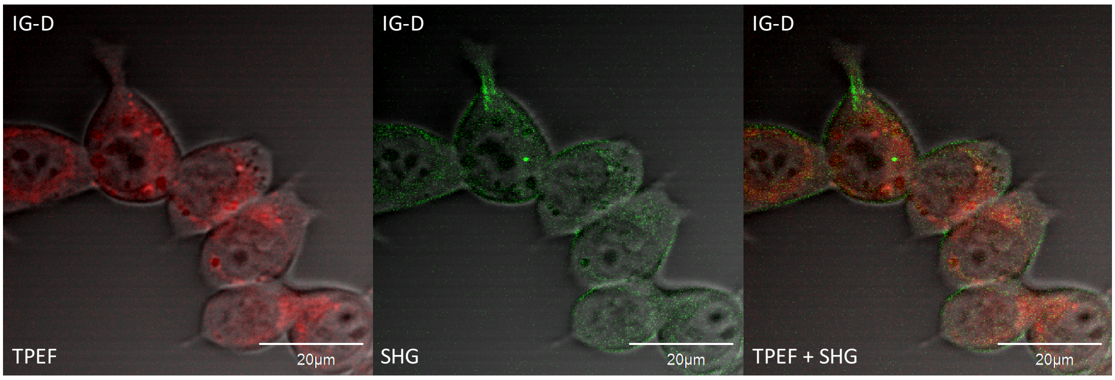

Figure 41: IG-D staining the intracellular organelles of HEK 293T cells in HBSS buffer without Ca^{2+} and Mg^{2+} ions. Some SHG signal is also visible from the plasma membrane of the cells. The rightmost image is the overlap of TPEF and SHG images showing that apart from intracellular organelles, the SHG signal is also visible from the plasma membrane of the cells. Laser power = ~25 mW. Scale bar = 20 µm.

No co-localization studies were performed with any of the dyes synthesized by Dr. Igor Boczarow.

Staining in LN-18 cells

In LN-18 cells too, **IG-D** (10 µM) stained the intracellular organelles like in HEK 293T cells (Figure 42). In LN-18 cells, on increasing the laser power up to 55 mW, no SHG was visible from the plasma membrane or from anywhere else in the cells. Although the SHG signal for **IG-D** from HEK 293T cells was dim but no signal is visible in LN-18 cells.

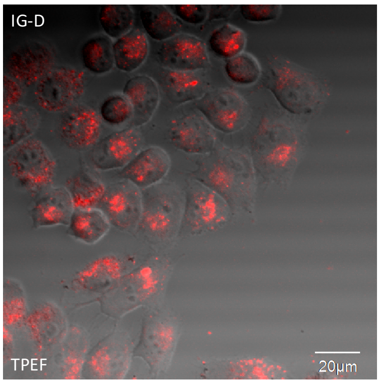

Figure 42: IG-D (10 µM) staining the intracellular organelles of LN-18 cells in HBSS buffer without Ca^{2+} and Mg^{2+} ions. Laser power = ~55 mW. Scale bar = 20 µm.

Staining in rat hippocampal neurons

The **IG-D** dye entered rat hippocampal neurons and stained the intracellular organelles (Figure 43). Apart from TPEF, a bright SHG signal was also visible from inside the cells suggesting that the dye stained the intracellular organelles non-centrosymmetrically. Despite increasing the laser power, no SHG signal was visible from the plasma membrane of the neurons unlike in HEK 293T cells. The imaging was performed in HBSS buffer without Ca^{2+} and Mg^{2+} ions to minimize endocytosis.

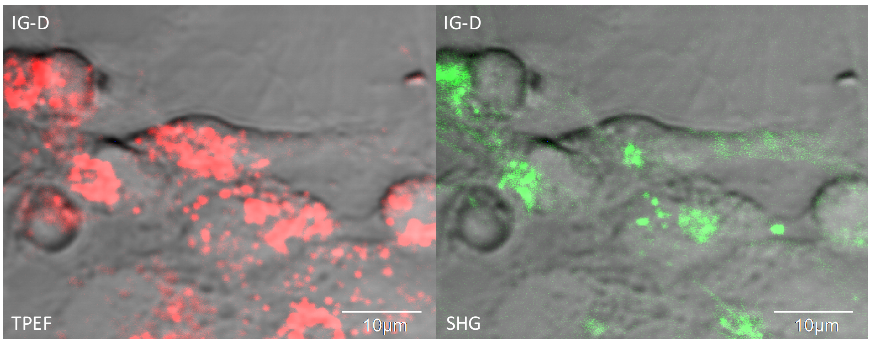

Figure 43: IG-D (10 µM) staining the interior of rat hippocampal neurons in HBSS buffer without Ca^{2+} and Mg^{2+} ions. Laser power = ~20 mW, Scale bar = 10 µm.

The above results show that replacing the charged moieties with hydrophilic non-charged groups did not improve plasma membrane localization.

Pyropheophorbide (PPa) -based dyes

I studied the localization of pyropheophorbide-*a* (PPa) based dyes (Figure 44), which are discussed in detail in Chapter 2, in HEK 293T cells, LN-18 cells, and rat hippocampal neurons. Sun *et al.* reported that pyropheophorbide-*a* methyl ester stains Golgi body, endoplasmic reticulum, mitochondria and lysosomes of NCI-h446 (epithelial cells derived from human lung cancer cell line) cells.[61] Pyropheophorbide-*a* methyl ester is not an amphiphilic molecule and hence is expected to stain the intracellular organelles; however, the TEG-substituted pyropheophorbides exhibit amphiphilic character and hence were expected to localize at the plasma membrane of the cells.

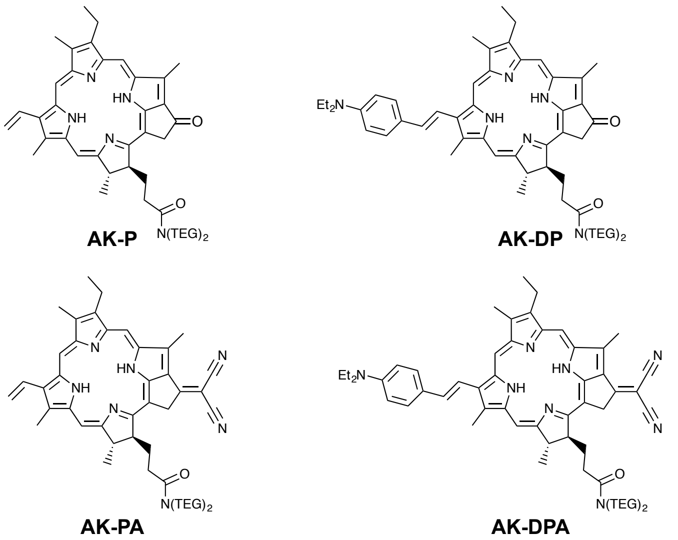

AK-P **AK-DP**

AK-PA **AK-DPA**

Figure 44: Molecular structures of bis-TEG amide attached pyropheophorbides.

Staining in HEK 293T cells

Staining of pyropheophorbides (Figure 45) was performed in HBSS buffers with and without Ca^{2+} and Mg^{2+} ions. In both the buffers, all four pyropheophorbide-based dyes entered the cells without localizing at the plasma membrane. Additionally, no SHG signal was detected from intracellular organelles (Figure 45).

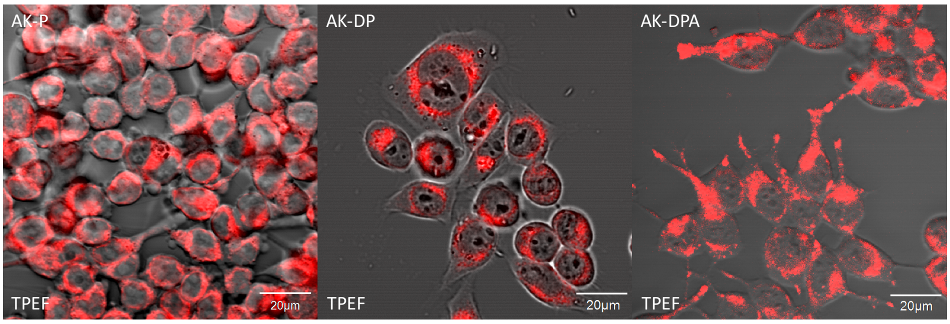

Figure 45: **AK-P** (at 800 nm), **AK-DP** (at 800 nm), and **AK-DPA** (at 870 nm) at a concentration of 10 µM each staining the intracellular organelles of HEK 293T cells. Scale bar = 20 µm.

When co-localization experiments were performed using **RH123** (mitochondria bound dye) and **Hoechst33342** (nucleus bound dye), it was found that all the pyropheophorbide-based dyes stained the intracellular organelles but it was not clear if it stained mitochondria or not (Figure 46). In the co-localization images, the areas where red is visible are the areas where pyropheophorbide dyes are stained, while the areas with yellow color are mitochondria. Since **RH123** is also detected by the far-red filter due to overlap of its fluorescence spectrum with the spectra of the pyropheophorbides, it cannot be deduced whether the pyropheophorbide dyes stain the mitochondria or not.

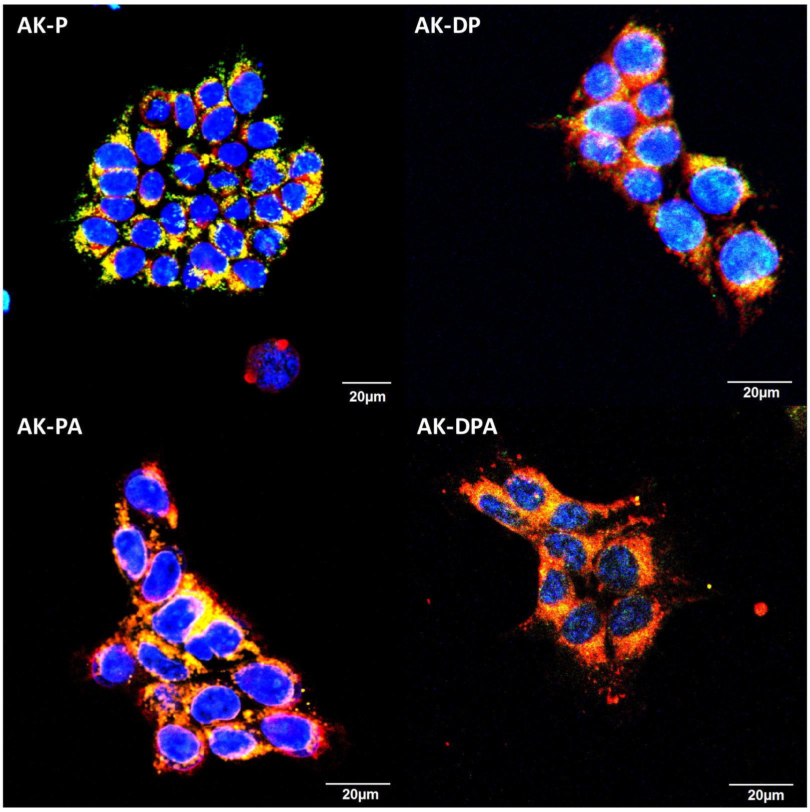

Figure 46: Co-localization of **AK-P**, **AK-DP**, **AK-PA**, and **AK-DPA** with **RH123** and **Hoechst33342** dyes. Blue color is from nucleus stained with only **Hoechst33342** dyes, while the red color is from intracelullar organelles stained with the pyropheophorbides. The yellow color is from the mitochondria stained with **RH123** and maybe also the pyropheophorbides. The pyrophrophorbides and **RH123** are excited from 800 nm to 840 nm respectively, while **Hoechst33342** is excited at 720 nm. Scale bar = 20 μm.

Staining in LN-18 cells

All the pyropheophorbide-based dyes (each 5 μM) stained the intracellular organelles of LN-18 cells with no SHG signal (Figure 47).

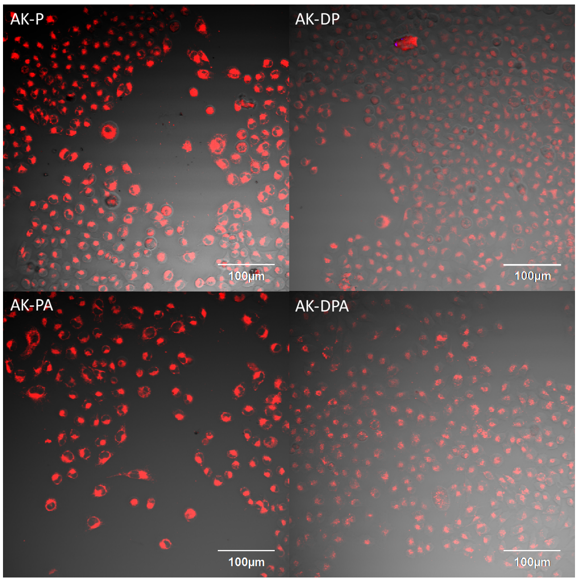

Figure 47: AK-P, **AK-DP**, **AK-PA**, and **AK-DPA** staining the intracellular organelles of LN-18 cells. The staining was performed in HBSS without Ca^{2+} and Mg^{2+} ions. $\lambda_{ext} = 840$ nm. Scale bar = 100 µm.

Staining in rat hippocampal neurons

In rat hippocampal neurons too, **AK-DPA** stained the intracellular organelles (Figure 48). Staining was performed in HBSS buffers with and without Ca^{2+} and Mg^{2+} ions, and no difference was observed between both buffers. The dye molecules seem to localize at the dendritic spines of the neurons giving TPEF signal but no SHG signal. Due to the limited availability of neurons, only **AK-DPA** was tested.

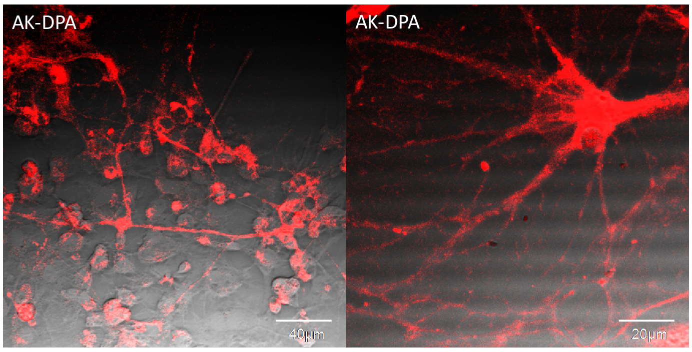

Figure 48: AK-DPA incubated with rat hippocampal neurons in HBSS buffers with and without Ca^{2+} and Mg^{2+} ions. The left image shows neurons in HBSS without Ca^{2+} and Mg^{2+} ions, while the right image shows neurons in HBSS with Ca^{2+} and Mg^{2+} ions. In both the cases, the dyes entered the soma of the neurons; however, signals are also observed from branched dendrites and axons. Scale bar = 40 µm (left image), 20 µm (right image).

Cell-based studies described here indicate that the TEG groups in the pyropheophorbides did not alter their cell localization properties. Since these dyes do not localize at the plasma membranes of live neurons, they are unsuitable to be used as voltage-sensitive dyes.

3.30 Conclusion and outlook

Table 1 summarizes the cellular localization study of charged and non-charged porphyrin-based dyes synthesized in the Anderson group in HEK 293T, LN-18, and rat hippocampal neurons.

Table 1: Summary of cellular localization study of the porphyrin-based dyes synthesized in the Anderson group in different cells.

Dye	HEK 293T	LN-18	Neurons	SHG signal
JR1 *(monocationic)*	Intracellular	*Not used*	*Not used*	No signal
JR1-plus *(dicationic)*	Intracellular	Intracellular	Intracellular + dendrites and axons	Yes (from intracellular organelles)
JR1-minus *(zwitterionic)*	Intracellular	Intracellular	Intracellular	Yes (from intracellular organelles)
HLA-1 *(dicationic)*	Plasma membrane	Plasma membrane	Plasma membrane	Yes
HLA-2 *(dicationic)*	Plasma membrane	Plasma membrane	Plasma membrane	Yes
HLA-3 *(zwitterionic)*	Intracellular	Intracellular	Intracellular + dendrites and axons	Yes (dim)
JDW-M *(neutral)*	Nucleus and Intracellular	*Not used*	*Not used*	No signal
JDW-D *(neutral)*	Nucleus and Intracellular	Nucleus and Intracellular	*Not used*	No signal
IG-M *(neutral)*	Intracellular	*Not used*	*Not used*	No signal
IG-D *(neutral)*	Intracellular and plasma membrane	Intracellular	Intracellular	Yes (dim)
PPa-based dyes *(neutral)*	Intracellular	Intracellular	Intracellular + dendrites and axons	No signal

Based on the above results, it can be concluded that porphyrin and pyropheophorbide –based non-charged dyes are not good candidates as electrochromic voltage-sensitive dyes because these dyes do not localize at the plasma membrane of live cells. Barsu *et al*. reported that non-charged dyes bearing six PEG groups do not localize at the plasma membrane of CHO cells and stain only the intracellular organelles.[62] Despite being amphiphilic, the non-charged dyes fail to localize at the membrane. The water-soluble glycol chains are amphiphilic themselves since they dissolve in both aqueous and organic solvents. Attaching dicationic or tricationic groups in pyropheophorbide-based dyes[63] could be useful to increase their amphiphilicity for effective plasma membrane localization. Porphyrin-based dyes, **JDW-M** and **JDW-D** functionalized with four hexaethylene glycol (HEG) chains crossed the nucleus membrane of the cells to stain the nucleus along with other intracellular organelles. Although the nucleus staining was not consistently reproducible, these results are useful to design future molecular rotors which can consistently stain the nucleus of the cells. Such dyes will be useful to study the viscosity of nucleus of the cells and study the relative change of viscosity of the nucleus and the cytosol. Such studies have not been performed due to lack of fluorescent molecular rotors, which can stain both the nucleus and the cytosol of live cells homogenously.

Charged dicationic porphyrin-based dyes functionalized with TEG-substituted aryl groups (**HLA1** and **HLA2**) localize at the plasma membrane of cells and are further studied for voltage-sensitivity in HEK 293T cells in Chapter 4. Perhaps, the increased overall hydrophilicity, enhanced by the presence of TEG groups is assisting in anchoring the dye in the plasma membrane bilayer. **JR1-plus** localizes at the plasma membrane of dendritic branches of neurons but enters into the soma as well, unlike **HLA1** and **HLA2**. The presence of TEG-substituted aryl groups decreases the SHG efficiency of these dyes in comparison to **JR1-plus**, apart from contributing towards the skewed orientation of the dye in lipid bilayer thus reducing its SHG efficiency even more. Digital enhancement was required to increase the SNR of the images of cells stained with **HLA1** and **HLA2**. Increasing the density of positive charges on **JR1-plus** may potentially increase its amphiphilicity (or overall hydrophilicity) to prevent it from entering the cells without decreasing the SHG efficacy. Nonetheless, I studied the voltage-sensitive efficacy of **HLA1** and **HLA2** in live cells through the patch-clamp system that I designed as discussed in the next chapter (Chapter 4). Although the dyes, **JR1-plus** and **JR1-minus** are taken up by the cells, they give bright structural SHG signals from intracellular organelles.

Two major concerns with porphyrin-based dyes are,

(1) The large size of porphyrins decreases their overall number density in the plasma membrane in comparison to small dyes, such as **FM4-64** and **di-4-ANEPPS**. The overall SHG intensity of a chromophore is directly dependent on the square of the number density (discussed in Chapter 1); hence, the SHG signal from porphyrin-based dyes is weak due to their low population in the plasma membrane.

(2) The large size of porphyrins increases their probability to disrupt the packing of the lipid bilayer as compared to small dyes thus affecting inherent properties of the plasma membrane.

However, due to their adjustable π-conjugated system, feasibility of various chemical modifications and high value of β_{zzz}, porphyrin-based dyes are promising candidates as SHG-based voltage-sensitive dyes. Although the above-studied amphiphilic dyes are not suitable to be used as electrochromic voltage-sensitive dyes, they can be further investigated for imaging various cellular organelles through SHG imaging, photochemical internalization based drug delivery,[32,34] two-photon PDT,[57,64,65] and studying nucleus and cellular viscosity.[53,54,56] In the next chapter, I describe the patch-clamp system that I designed and installed in the multiphoton microscope to test the voltage sensitivity of **HLA1**, **HLA2**, and **HLA2.Cu** dyes.

3.40 References

1 D. A. Dombeck, L. Sacconi, M. Blanchard-Desce and W. W. Webb, *J. Neurophysiol.*, 2005, **94**, 3628–3636.

2 J. E. Reeve, A. D. Corbett, I. Boczarow, W. Kaluza, W. Barford, H. Bayley, T. Wilson and H. L. Anderson, *Angew. Chem. Int. Ed.*, 2013, **52**, 9044–9048.

3 A. C. Millard, L. Jin, A. Lewis and L. M. Loew, *Opt. Lett.*, 2003, **28**, 1221–1223.

4 S. Preuss and W. Stein, *PLoS One*, 2013, **8**, e75678.

5 R. S. Ries, H. Choi, R. Blunck, F. Bezanilla and J. R. Heath, *J. Phys. Chem. B*, 2004, **108**, 16040–16049.

6 A. Hassner, D. Birnbaum and L. M. Loew, *J. Org. Chem.*, 1984, **49**, 2546–2551.

7 L. M. Loew, in *Membrane Potential Imaging in the Nervous System and Heart*, eds. M. Canepari, D. Zecevic and O. Bernus, Springer, 2015.

8 B. Kuhn and P. Fromherz, *J. Phys. Chem. B*, 2003, **107**, 7903–7913.

9 A. C. Millard, L. Jin, M. Wei, J. P. Wuskell, A. Lewis and L. M. Loew, *Biophys. J.*, 2004, **86**, 1169–1176.

10 D. S. Peterka, H. Takahashi and R. Yuste, *Neuron*, 2011, **69**, 9–21.

11 G. M. Cooper and R. E. Hausman, *The Cell: A Molecular Approach 2nd Edition*, Sinauer Associates, Inc., 2007.

12 J. E. Reeve, H. A. Collins, K. De Mey, M. M. Kohl, K. J. Thorley, O. Paulsen, K. Clays and H. L. Anderson, *J. Am. Chem. Soc.*, 2009, **131**, 2758–2759.

13 A. C. Diserens, N. De Tribolet, A. Martin-Achard, A. C. Gaide, J. F. Schnegg and S. Carrel, *Acta Neuropathol.*, 1981, **53**, 21–28.

14 J. E. Reeve, DPhil Thesis, University of Oxford, 2012.

15 I. López-Duarte, P. Chairatana, Y. Wu, J. Pérez-Moreno, P. M. Bennett, J. E. Reeve, I. Boczarow, W. Kaluza, N. A. Hosny, S. D. Stranks, R. J. Nicholas, K. Clays, M. K. Kuimova and H. L. Anderson, *Org. Biomol. Chem.*, 2015, **13**, 3792–3802.

16 L.-G. Wu, E. Hamid, W. Shin and H.-C. Chiang, *Annu. Rev. Physiol*, 2014, **76**, 301–331.

17 X.-S. Wu, B. D. McNeil, J. Xu, J. Fan, L. Xue, E. Melicoff, R. Adachi, L. Bai and L.-G. Wu, *Nat. Neurosci.*, 2009, **12**, 1003–1010.

18 J. C. Hay, *EMBO Rep*, 2007, **8**, 236–240.

19 U. Goyal and C. Blackstone, *Biochim. Biophys. Acta - Mol. Cell Res.*, 2013, **1833**, 2492–2498.

20 A. G. Manford, C. J. Stefan, H. L. Yuan, J. A. MacGurn and S. D. Emr, *Dev. Cell*, 2012, **23**, 1129–1140.

21 M. Oropesa-Ávila, Y. Andrade-Talavera, J. Garrido-Maraver, M. D. Cordero, M. de la Mata, D. Cotán, M. V Paz, A. D. Pavón, E. Alcocer-Gómez, I. de Lavera, R. Lema, A. P. Zaderenko, A. Rodríguez-Moreno and J. A. Sánchez-Alcázar, *Cell Death Dis.*, 2014, **5**, e1369.

22 J. a Subirana and M. Soler-Lopez, *Annu. Rev. Biophys. Biomol. Struct.*, 2003, **32**, 27–45.

23 C. A. Vandenberg, *Physiol. Sci.*, 1987, **84**, 2560–2564.

24 T. Kubota, Y. Shindo, K. Tokuno, H. Komatsu, H. Ogawa, S. Kudo, Y. Kitamura, K. Suzuki and K. Oka, *Biochim. Biophys. Acta - Mol. Cell Res.*, 2005, **1744**, 19–28.

25 D. L. Armstrong, C. Erxleben and J. A. White, *Calcium in Living Cells*, 2010, **99**, 183–197.

26 D. Wang, S. Grillner and P. Wallén, *J. Physiol.*, 2013, **591**.

27 A. Francois, A. Pizzoccaro, S. Laffray and E. Bourinet, *T-type calcium channels in pain neuronal circuits*, Springer-Verlag, 2014.

28 K. Malínská, A. Jelínková and J. Petrášek, *Methods Mol. Biol.*, 2014, **1209**, 1–11.

29 M. A. Gaffield and W. J. Betz, *Nat. Protoc.*, 2006, **1**, 2916–2921.

30 W. J. Betz, F. Mao and C. B. Smith, *Curr. Opin. Neurobiol.*, 1996, **6**, 365–371.

31 S. Bolte, C. Talbot, Y. Boutte, O. Catrice, N. D. Read and B. Satiat-Jeunemaitre, *J. Microsc.*, 2004, **214**, 159–173.

32 J. T. W. Wang, F. Giuntini, I. M. Eggleston, S. G. Bown and A. J. MacRobert, *J. Control. Release*, 2012, **157**, 305–313.

33 K. Berg, P. K. Selbo, A. Weyergang, A. Dietze, L. Prasmickaite, A. Bonsted, B. Engesaeter, E. Angell-Petersen, T. Warloe, N. Frandsen and A. Høgset, *J. Microsc.*, 2005, **218**, 133–147.

34 R. Dondi, E. Yaghini, K. M. Tewari, L. Wang, F. Giuntini, M. Loizidou, A. J. MacRobert and I. M. Eggleston, *Org. Biomol. Chem.*, 2016, **14**, 11488–11501.

35 C. Bechara and S. Sagan, *FEBS Lett.*, 2013, **587**, 1693–1702.

36 M. Gouterman, *J. Mol. Spectrosc.*, 1961, **6**, 138–163.

37 M. Nuriya, S. Fukushima, A. Momotake, T. Shinotsuka, M. Yasui and T. Arai, *Nat. Commun.*, 2016, **7**.

38 J. E. Reeve, A. D. Corbett, I. Boczarow, T. Wilson, H. Bayley and H. L. Anderson, *Biophys. J.*, 2012, **103**, 907–917.

39 D. W. Fawcett, in *The cell*, Saunders Philadelphia, 2nd Edn., 1981, p. 311.

40 S.-H. Shim, C. Xia, G. Zhong, H. P. Babcock, J. C. Vaughan, B. Huang, X. Wang, C. Xu, G.-Q. Bi and X. Zhuang, *Proc. Natl. Acad. Sci. U. S. A.*, 2012, **109**, 13978–13983.

41 M. Collot, R. Kreder, A. L. Tatarets, L. D. Patsenker, Y. Mely and A. S. Klymchenko, *Chem. Commun.*, 2015, **51**, 17136–17139.

42 D. R. Hochbaum, Y. Zhao, S. L. Farhi, N. Klapoetke, C. A. Werley, V. Kapoor, P. Zou, J. M. Kralj, D. Maclaurin, N. Smedemark-Margulies, J. L. Saulnier, G. L. Boulting, C. Straub, Y. K. Cho, M. Melkonian, G. K.-S. Wong, D. J. Harrison, V. N. Murthy, B. L. Sabatini, E. S. Boyden, R. E. Campbell and A. E. Cohen, *Nat. Methods*, 2014, **11**, 825–833.

43 P. Zou, Y. Zhao, A. D. Douglass, D. R. Hochbaum, D. Brinks, C. A. Werley, D. J. Harrison, R. E. Campbell and A. E. Cohen, *Nat. Commun.*, 2014, **5**.

44 W.-L. Zhou, Y. Ping, J. P. Wuskell, L. M. Loew and S. D. Antic, *J. Neurosci. Methods*, 2007, **164**, 225–239.

45 J. D. Wilkinson, DPhil Thesis, University of Oxford, 2014.

46 I. Boczarow, DPhil Thesis, University of Oxford, 2014.

47 E. Annoni, M. Pizzotti, R. Ugo, S. Quici, T. Morotti, M. Bruschi and P. Mussini, *Eur. J. Inorg. Chem.*, 2005, **2005**, 3857–3874.

48 T. Morotti, M. Pizzotti, R. Ugo, S. Quici, M. Bruschi, P. Mussini and S. Righetto, *Eur. J. Inorg. Chem.*, 2006, **2006**, 1743–1757.

49 I. Lopez-Duarte, J. E. Reeve, J. Perez-Moreno, I. Boczarow, G. Depotter, J. Fleischhauer, K. Clays and H. L. Anderson, *Chem. Sci.*, 2013, **4**, 2024–2027.

50 M. Pawlicki, H. A. Collins, R. G. Denning and H. L. Anderson, *Angew. Chem. Int. Ed.*, 2009, **48**, 3244–3266.

51 M. G. Kuzyk, *Opt. Lett.*, 2000, **25**, 1183–1185.

52 D. Li, T. J. Marks and M. A. Ratner, *J. Phys. Chem.*, 1992, **96**, 4325–4336.

53 M. K. Kuimova, S. W. Botchway, A. W. Parker, M. Balaz, H. A. Collins, H. L. Anderson, K. Suhling and P. R. Ogilby, *Nat. Chem.*, 2009, **1**, 69–73.

54 A. Vyšniauskas, D. Ding, M. Qurashi, I. Boczarow, M. Balaz, H. L. Anderson and M. K. Kuimova, *Chem. - Eur. J.*, 2017, **23**, 11001–11010.

55 I. López-Duarte, T. T. Vu, M. A. Izquierdo, J. A. Bull and M. K. Kuimova, *Chem. Commun.*, 2014, **50**, 5282–5284.

56 A. Vyšniauskas, M. Balaz, H. L. Anderson and M. K. Kuimova, *Phys. Chem. Chem. Phys.*, 2015, **17**, 7548–7554.

57 M. K. Kuimova, H. A. Collins, M. Balaz, E. Dahlstedt, J. A. Levitt, N. Sergent, K. Suhling, M. Drobizhev, N. S. Makarov, A. Rebane, H. L. Anderson and D. Phillips, *Org. Biomol. Chem.*, 2009, **7**, 889–896.

58 M. R. Dent, I. Lopez-Duarte, C. J. Dickson, P. Chairatana, H. L. Anderson, I. R. Gould, D. Wylie, A. Vysniauskas, N. J. Brooks and M. K. Kuimova, *Chem. Commun.*, 2016, **52**, 13269–13272.

59 P. S. Sherin, I. Lopez-Duarte, M. R. Dent, M. Kubankova, A. Vysniauskas, J. A. Bull, E. S. Reshetnikova, A. S. Klymchenko, Y. P. Tsentalovich and M. K. Kuimova, *Chem. Sci.*, 2017, **8**, 3523–3528.

60 L. E. Shimolina, M. A. Izquierdo, I. López-Duarte, J. A. Bull, M. V Shirmanova, L. G. Klapshina, E. V Zagaynova and M. K. Kuimova, *Sci. Rep.*, 2017, **7**, 41097.

61 X. Sun and W. N. Leung, *Photochem. Photobiol.*, 2002, **75**, 644–651.

62 C. Barsu, R. Cheaib, S. Chambert, Y. Queneau, O. Maury, D. Cottet, H. Wege, J. Douady, Y. Bretonniere and C. Andraud, *Org. Biomol. Chem.*, 2010, **8**, 142–150.

63 H. Taima, N. Yoshioka and H. Inoue, *Org. Biomol. Chem.*, 2009, **7**, 1176–1183.

64 M. Khurana, H. A. Collins, A. Karotki, H. L. Anderson, D. T. Cramb and B. C. Wilson, *Photochem. Photobiol.*, 2007, **83**, 1441–1448.

65 I. Stamati, M. K. Kuimova, M. Lion, G. Yahioglu, D. Phillips and M. P. Deonarain, *Photochem. Photobiol. Sci.*, 2010, **9**, 1033–1041.

Chapter 4

Testing the Voltage Sensitivity of Organic Dyes

Summary: *Precise testing and optimization of a voltage-sensitive dye in a lipid bilayer or a cell can be performed by applying controllable electric field from the outside and measuring optical response of the dye. Several bilayer-based setups have been demonstrated in the past to test voltage-sensitivity of optical dyes; however, all the setups are unique towards a voltage-sensitive mechanism. In this chapter, I discuss my attempt to design a lipid-based hemispherical lipid bilayer setup to test voltage sensitivity of optical dyes. Following that I describe a patch-clamp–based setup that I designed and installed in the multiphoton microscope to test the fluorescence and SHG –based voltage sensitivity of organic dyes. The patch-clamp setup was successful in measuring voltage-sensitivity of commercial dyes* ***FM4-64*** *and* ***di-4-ANEPPS*** *in HEK 293T cells. On testing a porphyrin-based dye* ***HLA1****, I found that the dye required high laser power to give notable signal-to-noise ratio because of which its voltage sensitivity could not be tested.*

4.0 Introduction

Voltage-sensitive organic dyes offer significant advantages over patch-clamp–based techniques to study the membrane potential of neurons, as discussed in Chapter 1. However, the voltage sensing efficacy of new organic dyes must be thoroughly tested before they are used. Whole-cell–based patch-clamp remains one of the primary techniques to test the voltage sensitivity and temporal resolution of optical organic dyes in live cells.[1–7] To test the voltage sensitivity of organic dyes in live cells, the input parameters such as precise change in membrane voltage and the time for which the voltage is applied (so that the dyes can sense them) must be controllable, which is possible by whole-cell patch-clamp technique. However, the complexities of patch-clamp–based techniques in live cells, such as high maintenance (of both cells and patch-clamp system), and requirement of advanced experimental skills led to development of alternate techniques to study the voltage sensitivity of optical organic dyes. Several lipid bilayer-based techniques such as droplet-on-hydrated-support bilayers (DHB),[8–11] hemispherical lipid bilayers (HLB),[12–14] planar lipid bilayers (PLB),[15,16] droplet interface bilayers (DIB),[10,17] and giant unilamellar vesicles (GUVs)[18] have been developed over the years as non-cellular model systems to test the voltage sensitivity of organic dyes. These techniques are easier to set-up compared to cell-based patch-clamp system. All the above-mentioned bilayer-based techniques work by the same principle: a known changing potential difference is applied across the lipid bilayer containing the organic dye to give an optical readout (in terms of change in fluorescence or SHG signal). The optical readout is the measure of the voltage sensitivity of the dyes, which can be mapped against the applied potential difference to determine the sensitivity and time resolution of the dye.

Lipid bilayer setups are excellent models to study structures of cellular membranes although they have various limitations. In artificial bilayers, each of the components of the cell membrane can be designed and studied in isolation; however, it is a challenge to design a bilayer setup that exactly mimics the cell membrane and is responsive to changes in all the environment factors, such as temperature, pH, stress, and lipid-order.[10] Voltage sensitivity data acquired from lipid bilayer setups are not always reproducible in cells. The bilayer setups are primarily composed of synthetic lipids; however, the plasma membranes of cells are composed of membrane proteins, glycoconjugates, and ion channels along with lipid bilayer, collectively acting as a more complex system.[19] All these transmembrane organelles interfere with the orientation and solubility of the dye, and also affect the dye response to electric field and so the dyes do not always behave alike in lipid model systems and live cells.[20–22] Here, I briefly discuss various bilayer set ups that have been used in the Anderson group in attempts to test the voltage sensitivity of organic dyes.

Droplet-on-hydrated-support bilayers (DHBs)

Wallace and coworkers designed a highly stable DHB system that forms bilayers at the contact point between a lipid monolayer-coated water droplet and a planar lipid–coated hydrogel immersed in an immiscible lipid-oil solution (Figure 1).[8,23] This system can be used for simultaneous electrical recording and total internal reflection fluorescence (TIRF) imaging.

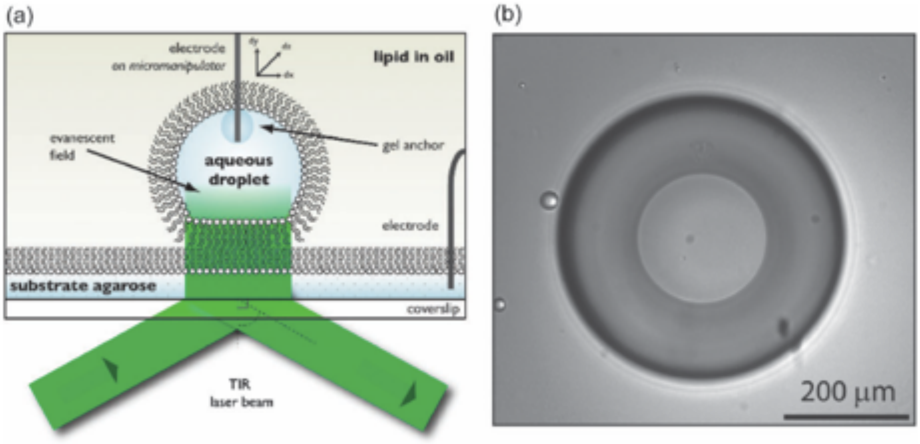

Figure 1: A droplet-on-hydrated-support bilayers (DHB) system. (a) Scheme of a DHB system suitable for simultaneous TIRF imaging and electrical recording. The bilayer forms at the contact point between the monolayer droplet and the lipid-coated surface. (b) Image of a DHB system on an inverted microscope showing the bilayer contact area (on an inverted microscope). Image adapted with permission from *Mol. BioSys*t., 2008, 4, 1191–1208 and J. Am. Chem. Soc., 2007, 129, 16042–16047. Copyright 2007 American Chemical Society.

Dr. James Wilkinson from Anderson group used the above system to test the voltage sensitivity of a photo-induced electron transfer (PeT)-based dye (Figure 2).

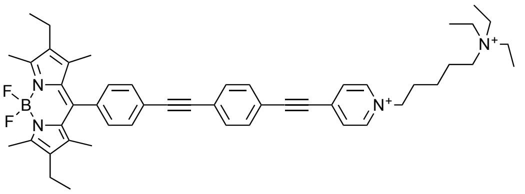

Figure 2: PeT-based dye synthesized in the Anderson group.

Anderson and coworkers observed bright fluorescence of the PeT dye from the bilayer; however, they did not see any change in fluorescence on applying a voltage of ±100 mV. The reason for no response to change of voltage remains unclear. Wallace and coworkers reported that this system works for measuring the voltage sensitivity of the electrochromic dye di-8-ANEPPS.[11] However, this system cannot be useful for SHG-based dyes because SHG travels in the forward direction of the excitation light and hence it requires a two-way system (i.e. the objective and condenser must be placed on opposite sides of the bilayer), but in the DHB system the light source and the detector are on the same side. Consequently, although versatile, DHB systems are not useful for measuring the voltage sensitivity of SHG-based dyes.

Droplet interface bilayers (DIBs)

Over the years, Bayley and coworkers have developed various types of droplet interface bilayer systems with versatile properties and applications.[17,24,25] Droplet interface bilayers (DIBs) are formed when two aqueous droplets coated with lipid monolayers in an oil/lipid mixture are brought together to form a bilayer of biomolecular thickness at the interface. Asymmetric DIBs formed by the lipid-in approach (Figure 3 B) are of particular interest because they can mimic the asymmetric lipid composition of cells as the inner and outer leaflets of most cells are different.[17,26] DIBs offer significant advantages, such as an electric field can be easily applied to asymmetric DIBs, they are stable for up to two weeks, and the droplets can be separated and reformed easily. Due to their asymmetric nature, these bilayer systems can be useful for SHG imaging.

Dr. James Reeve from the Anderson group used this system unsuccessfully to test the voltage sensitivity of the **JR1** dye. Due to several reasons (all of them not discussed here), no SHG signal was detected from the dyes embedded in the bilayer of the DIB system. It was concluded that DIBs are unsuitable for multiphoton imaging, as the high laser power required for nonlinear optical imaging drill holes in the membrane of the bilayer. The energy of the laser power was enough to make the droplets forming the bilayer to fuse into one another thus making this system unsuitable to the voltage sensitivity of nonlinear optical dyes. Moreover, the difference in refractive indices between the oil and water phases cause undesirable lensing effect.

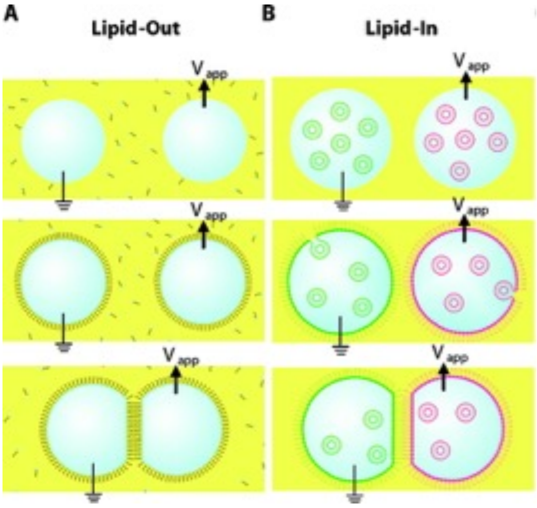

Figure 3: Construction of DIBs using the lipid-out and lipid-in approaches. (A) In the lipid-out approach, lipids are mixed in an oil bath to form a monolayer around water droplets, and when two water droplets are brought in contact, the monolayers exclude oil to form a lipid bilayer at the interface. (B) In the lipid-in approach, two water droplets containing different compositions of lipid mixtures (green and red) are brought together to form an asymmetric bilayer at the phase boundary. Image adapted with permission from J. Am. Chem. Soc., 2008, 130, 5878. Copyright 2008 American Chemical Society.

Hemispherical lipid bilayers (HLBs)

Over the years, HLBs have been used several times to test the voltage sensitivity of potentiometric dyes.[13,14,27] This system was adopted by Anderson and coworkers to test the voltage sensitivity of **JR1** successfully (Figure 4).[12]

To form an HLB, the tip of a silanized microscale glass electrode is coated with oil-lipid mixture and the electrode is backfilled with an aqueous buffer. The coated electrode is submerged in the same aqueous buffer bath under the microscope and a partial positive pressure is applied from the backside of the electrode to blow out a bubble of bilayer in the bath, which attains the bilayer thickness over time. To apply an electric field, the glass electrode is fitted with a Hamilton glass syringe (10 μL), which is connected to a square wave generator amplifier. To complete the electrical circuit, a reference electrode already connected to the same amplifier is dipped in the aqueous buffer bath. The dye is mixed in the bath so that it orients in the bilayer non-centrosymmetrically. The imaging is performed simultaneously to applying the electric field to test the voltage-sensitivity of the dye (Figure 4).

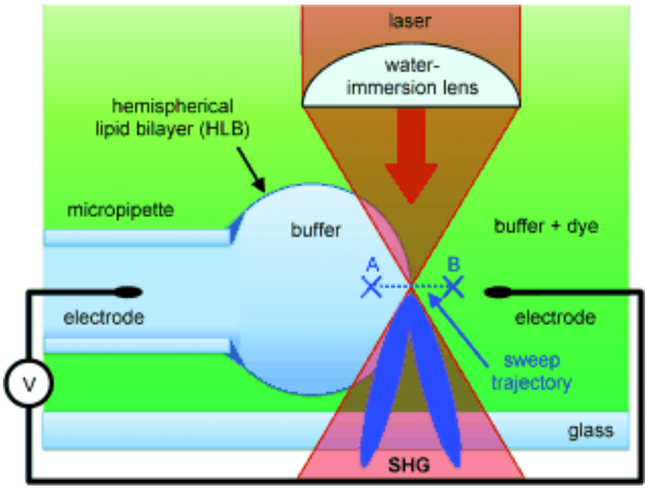

Figure 4: Schematic of the HLB system designed by Dr. James Reeve *et al.*[12] The dye preincubated in the buffer binds non–centrosymmetrically at the external leaflet of the bilayer, which is placed right in between the lens and the objective. Imaging is performed repeatedly at the focal point A-B to monitor the change of SHG signal while simultaneously applying the electric field. The diameter of the hemispherical droplet is around 300 µm. Image adapted with permission from *Angew. Chem. Int. Ed.*, 2013, **52**, 9044–9048. Copyright 2013 The Authors. Published by Wiley-VCH Verlag GmbH & Co. KGaA.

Anderson and cowrokers designed the HLB-based system in a custom made multiphoton microscope in the laboratory of Prof. Tony Wilson at the Department of Engineering, University of Oxford, (Figure 5)[12]. Setting up the HLB system in the microscope was not trivial and several challenges were encountered. As shown in Figure 5, the bilayer was extruded from the pipette fitted in a Hamilton syringe. The syringe was held by a laboratory clamp, which makes the positioning and sub-microscale manipulation of the electrode under the lens very difficult. Since the imaging must be performed in the dark, the experimenter cannot stand near the microscope to manipulate the position of the electrode while performing imaging. Also, due to laser safety reasons, the microscope should be blacked out from the experimenter while in use. Most importantly, the bilayer formed from this system was not very stable and the imaging had to be performed within few seconds of the formation of the bilayer.

Despite the above-mentioned challenges, Anderson and coworkers designed and used this system to compare the voltage sensitivity of **JR1** with commercial dyes, **FM4-64**, **di-4-ANEPPS**, and **RH123** (Figure 16, Chapter 1).[12]

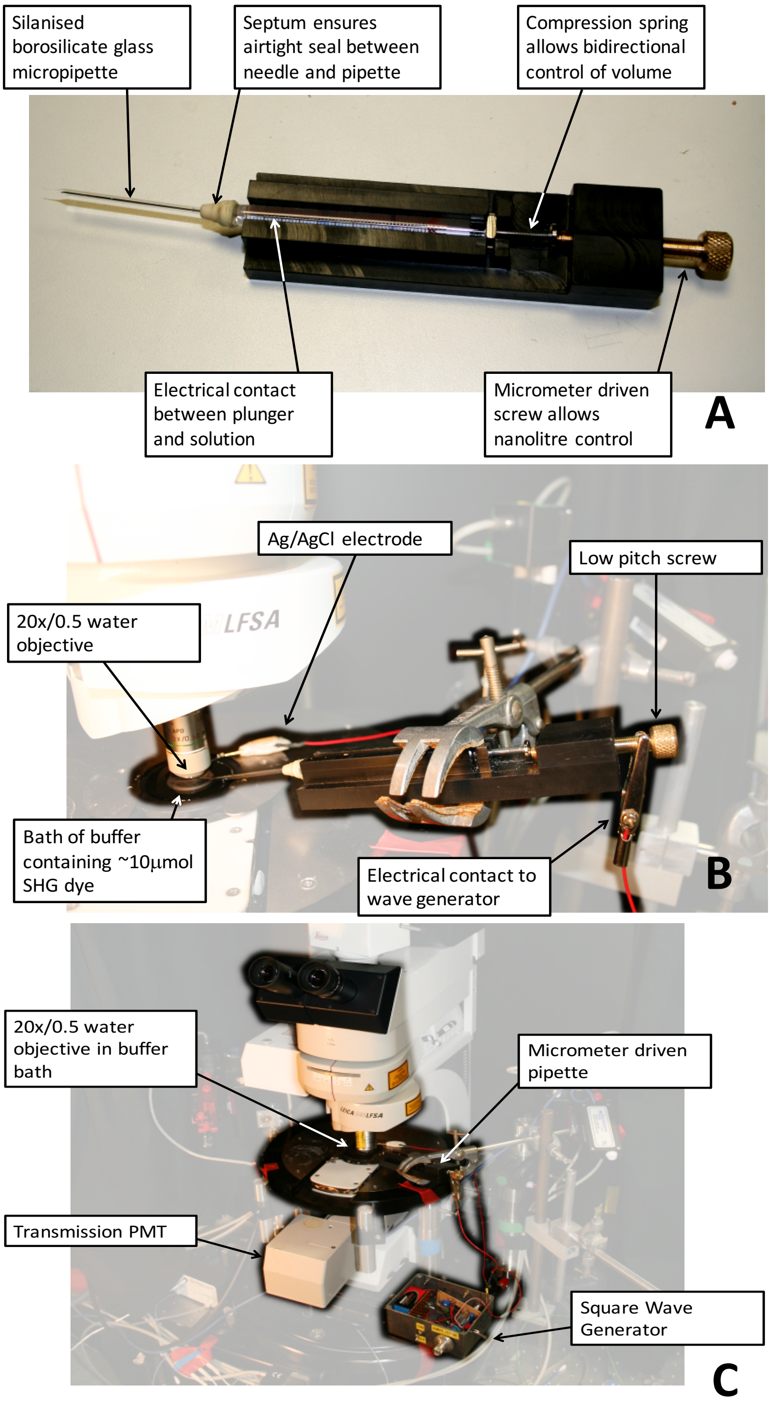

Figure 5: (A) Hamilton glass syringe fitted with a silanised micro-electrode (filled with buffer and its tip coated with lipid-oil mixture) and a screw for applying pressure. (B) The syringe system is electrically connected with a clip and positioned under the microscope with the pipette tip submerged in the buffer bath. (C) Picture of the whole HLB system installed within the custom-made microscope. A custom-built square-wave generator, an amplifier and digitizer are connected to the syringe. Image acquired from Anderson group computer server with permission from Prof. Harry L. Anderson.

4.10 Results and discussion

4.11 Hemispherical lipid bilayers (HLBs)

To test the voltage sensitivity of the porphyrin-based dyes (including **HLA1**), I embarked on reproducing the HLBs in our commercial multiphoton microscope. The setup of our microscope is significantly different from the one used previously by Anderson and coworkers in the Department of Engineering, University of Oxford.[12] The microscope is enclosed in a black metallic box, which serves the dual role of being a Faraday cage (to shield the microscope detectors and the electrical system from external electric and magnetic fields) as well as a mandatory safety box to keep the intense laser light from escaping the intended light path (Figure 6). Such an enclosed system does not allow any space for mounting a clamped Hamilton syringe connected to a square-wave generator as in Figure 5 to form HLBs. Instead, I used commercial PatchStar micromanipulators from Scientifica to mount a pipette holder, which is connected to a pre-amplifier further connected to an Axon Multiclamp 700B amplifier. The micromanipulator provides sub-micrometer scale movement in three degrees of freedom (x, y, and z) ensuring greater precision for positioning and manipulating the pipette under the microscope than the custom made metallic-clamp system used by Dr. James Reeve in the Anderson group. The pipette holder was connected to a plastic syringe through a silicone tube to apply pressure to extrude the HLB. The stepwise procedure that I followed in an attempt to form stable HLBs is:

(1) **Pipette preparation**: I pulled the pipettes with long tapering (using a Narishige PC-10 vertical pipette puller) and carefully broke their tips so that their diameter is approx. 100 μm.

(2) **Silanization of the pipettes**: The pipettes were cleaned by sequential incubation in 1:1 mixture of HCl and MeOH and conc. H_2SO_4 for 30 minutes each. The cleaned pipettes were silanized by incubation in 2% solution of TMS-Cl in toluene for 2 h as described by Cras *et al.*[28] The sequential incubation in HCl and MeOH mixture and H_2SO_4 is more effective in cleaning the glass surfaces than other standard procedures, such as piranha acid or hydrogen peroxide according to Cras *et al.*[28]

(3) **Forming HLBs:** A silanized pipette was backfilled with phosphate buffer (50 mM KCl, 50 mM K_2HPO_4, 50 mM KH_2PO_4, pH = 7.0) and then its tip was layered with an oil-lipid mixture (prepared by mixing dodecane with 30 mM DPhPC lipid and 5 mM oxidized cholesterol). The pipette was then submerged in the buffer bath to position it

under the objective at the focal point. Positive pressure was applied using the syringe to extrude HLB.

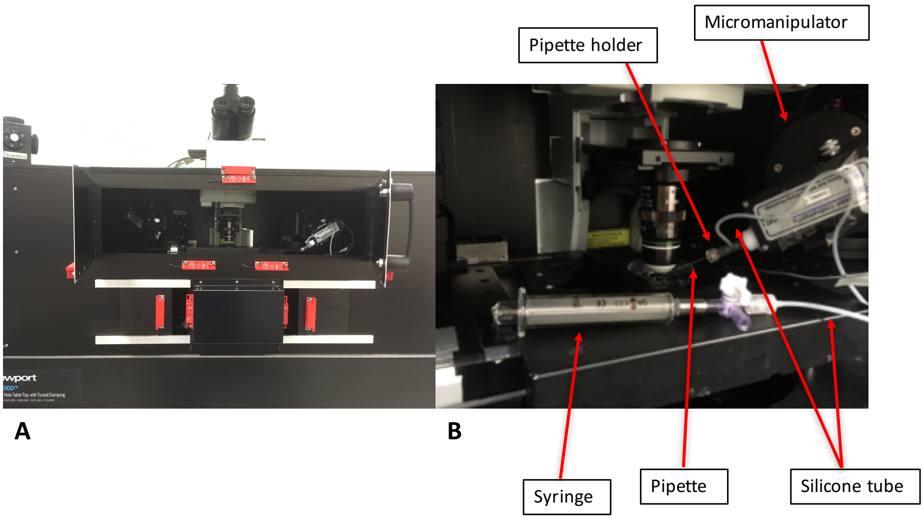

Figure 6: Microscope setup. (A) Microscope setup inside the black metallic box, which acts as both Faraday cage and the shield to block trespassing laser light. (B) Picture of the setup prepared by me to form HLBs and for live-cell patch-clamping too.

On applying positive pressure, only short lived (1–2 s) HLBs were formed. Despite multiple attempts, formation of a stable HLB bilayer with lifetime of more than 30 s was not achieved. Change of solvent in the oil-lipid mixture from dodecane to squalene (higher viscosity) or using a different lipid, DOPC did not help either. Despite using several silanized pipettes of different diameters I was unsuccessful to form stable HLBs. One of the reasons for the short lifetime of the HLBs might be that I was applying the pressure using a syringe to extrude the bilayer. Since the tip of the pipette is around 100 μm, the volume of the bilayer formed is in the order of nanoliters. Extruding such a small volume of liquid through the pipette manually is not trivial. Therefore, I shifted to using a syringe pump to apply pressure at a rate as slow as 1 μL/h. However, the only difference the use of the pump made was that the short-lived HLB were extruded slower than in the manual case. One of the major differences of the HLB extruding system I was using than the system used by Reeve and coworkers is that the distance between the point of pressure applied and the pipette tip is lengthier in the current system resulting in higher inaccuracies. Additionally, Reeve was controlling the liquid volume throughout as he was applying pressure to a Hamilton syringe filled with buffer while I was controlling both air and liquid volumes. I was applying pressure using a syringe connected to tube filled with air, which is connected to the pipette holder holding the buffer filled pipette. Due to differences in the expandability of air and aqueous buffer, the pressure applied through the syringe does not necessarily translate as it is to the water, and the elastic tube too expand and contract on application of pressure resulting into inaccuracies.

After numerous unsuccessful attempts, I moved on to design a whole-cell patch-clamp system in our microscope setup.

4.12 Whole-cell patch-clamp

Whole-cell patch-clamp is a versatile technique to measure the membrane potential of excitable cells, such as neurons and heart cells.[29] In whole-cell patch-clamp, a known voltage or current is applied to a cell and the responsive current or voltage is measured. Whole-cell patch-clamp is preferred over artificial lipid bilayer systems for numerous reasons. Firstly, whole-cell patch-clamp employs real live cells instead of synthetic lipid bilayers. No other method can be more reliable than directly testing the dyes in live cells. Secondly, when a known potential difference is applied, the resultant current can be directly compared with the optical read out. Any artifacts in the voltage sensitivity of the dye can be directly addressed by comparison with the current. Thirdly, when coupled with optical fluorescence and SHG-based microscopy, this method provides overall information about the interaction of the dye with the cells. The effect of various factors, such as time of plasma membrane localization, effect of cellular organelles and cell trafficking system on the dye, photostability of the dye, effect of the dye on the intrinsic membrane potential of the cells can be studied simultaneously. Fourthly and most importantly, although patch-clamp requires exceptional experimental skills, it is widely used by scientists and so it has been optimized over the years, and well defined protocols are available in literature.

The process of formation of a whole-cell patch-clamp configuration is described in Figure 7. In a whole-cell method, a glass microelectrode filled with an intracellular buffer is attached to the cell membrane such that there is a tight seal between them. The seal is popularly known as ‘giga-seal’ because it has an electrical resistance in the order of gigaohms and prevents leakage of any current flowing between the cell membrane and the glass electrode. The formation of the giga-seal (explained in Figure 7) and whole-cell mode cannot be viewed with optical microscopes because of the resolution limitations resulting from the light diffraction limit. The process is monitored electrically with the help of an amplifier, which is connected to a digitizer to send and receive signals from the computer. The electrical measurement process of the three-step–based whole-cell formation is further described in Figure 8.

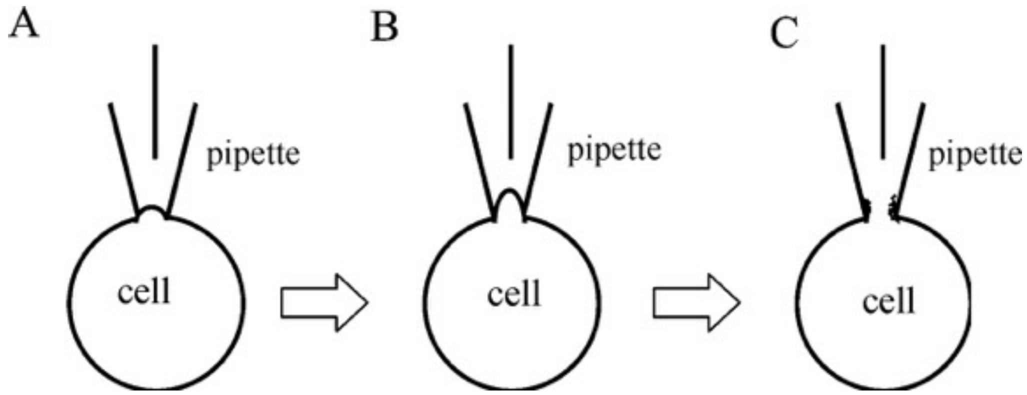

Figure 7: Steps to perform whole-cell patch-clamp.[30] (A) An intracellular solution filled glass pipette of tip resistance around 3–7 MΩ is gently pressed against the cell membrane without piercing through the membrane. (B) After making contact with the cell membrane, a mild suction is applied to aspirate a membrane patch in the glass pipette to form a seal of resistance in the order of 1–10 GΩ, popularly known as giga-seal. (C) After forming the giga-seal, a further suction is applied to break into the cell without loosing the giga-seal to form the whole-cell mode. Image adapted from *Adv. Physiol. Educ.*, 2008, 32, 209–211 (permission not required). Copyright 2008 American Physiological Society.

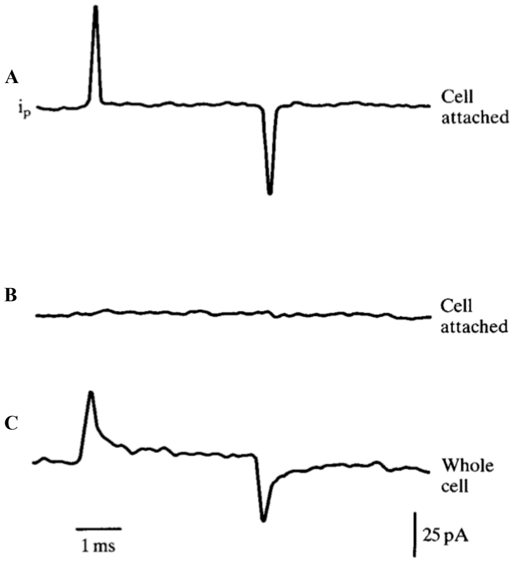

Figure 8: Electrical sequence of changes during the formation of a whole-cell mode. (A) When the giga-seal is formed, a transient current flows due to the intrinsic capacitance of the pipette. (B) The capacitance is adjusted by injecting an extra current through the pipette with the help of the amplifier. (C) After rupturing the cell membrane, when the whole-cell mode is achieved, a transient current is passed through the cell due to the capacitive nature of the cellular membrane. Image adapted with permission from *Microelectrode Techniques- The Plymouth Workshop Handbook, 2nd Edition, Edited by David Ogden, 1994,* published by *The Company of Biologists Lmited.* Copyright 1987 The Company of Biologists Limited.

Figure 9 represents the electrical circuit schematic of a cell in a whole-cell mode. The pipette with resistance R_s, is connected in series to the cell, which has a resistance R_c and a capacitance C_m. Since the cell has a dual nature of acting as a resistor and a capacitor, we can assume that the resistive and capacitive parts are connected in parallel and so they have the same potential difference across them. V_p is the required command potential difference that is applied to the cell through the amplifier; however, due to the presence of a series resistance R_s (due to the resistance of the pipette and electrode) there is a voltage drop across the membrane. The value of the drop is, $i_p R_s$, where $i_p$is the current flowing through the pipette towards the cell. This voltage drop must be compensated by subtracting from the command potential, V_p

with the help of the patch-clamp amplifier to get the real cell potential, $V_c = V_p - i_p R_s$.[29] The pipette current, i_p divides into two components to flow through the resistive cell R_c (in the order of giga-ohm) as i_m (=V_c/R_c) and capacitive cell C_m as i_c (= $C_m.\, dV_c/dt$). The potential difference across the cell at any time *t*, can be expressed as:

$$V_c(t) = V_c(\infty) + \{V_c(0) - V_c(\infty)\}\, e^{-t/\tau}$$

where $V_c(t)$ is the potential difference at time *t*, $V_c(0)$ is at time 0, $V_c(\infty)$ is at ∞ time (after a long time), and τ is the time constant. The value of τ is, $C * \frac{R_s R_c}{R_c + R_s} = C * R_s$ because $R_c \gg R_s$.

Since, $R_c \gg R_s$, minimal current flows through the R_c, and so we can assume that C_m and R_s in series with each other form an RC circuit during the whole-cell mode. In the case of a sudden change in V_p (Figure 9b), the current flows through the capacitive cell C_m. In the beginning of the step of V_p (when a sudden step change in command potential is applied from the amplifier), since V_c (0) is steady, the current flowing into the cell to discharge the capacitor is i_p(0) = V_p/R_s (Figure 9b). The pipette current exponentially declines to steady level and thus the V_c too reaches a steady state.[29] The schematic in Figure 9 is of an ideal whole cell mode but practically, there are other factors like current leakage, pipette capacitance etc., which also contribute to the overall circuit. Taking all those factors into account will make the full circuit more complicated and mathematically complex to understand, and so I have discussed a simple circuit for better understanding.

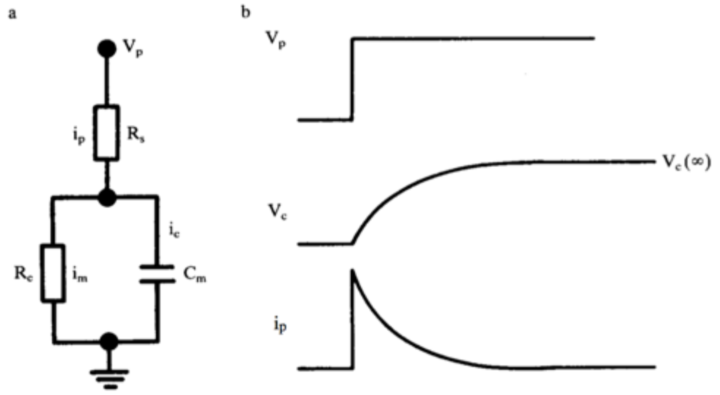

Figure 9: (a) Equivalent electrical circuit of a cell in whole-cell mode. The pipette current $\boldsymbol{i_p}$ that flows from the series resistance $\boldsymbol{R_s}$ between the cell and the pipette is divided into two currents: $\boldsymbol{i_m}$, which flows through the cell resistance $\boldsymbol{R_c}$, and $\boldsymbol{i_c}$, which flows through the cell capacitance $\boldsymbol{C_m}$. The pipette current $\boldsymbol{i_p}$ produces an error in voltage equal to $\boldsymbol{i_p R_c = V_p - V_c}$. (b) Changes in $\boldsymbol{V_c}$ and $\boldsymbol{i_p}$ following a voltage step of $\boldsymbol{V_p}$. Image adapted with permission from *Microelectrode Techniques- The Plymouth Workshop Handbook, 2nd Edition, Edited by David Ogden, 1994,* published by *The Company of Biologists Lmited.* Copyright 1987 The Company of Biologists Limited.

4.12.1 The patch-clamp system

While setting up the patch-clamp system in conjugation with the microscope, I encountered various challenges, which are inherent in setting up a new patch-clamp system.

The setup for patch-clamp of live cells is significantly different from the setup developed during HLB-based experiments. Numerous factors such as the dimensions of the glass bottom dishes (sample holder), the type of cell (sample), pipette tip shape and resistance, micromanipulators to position and manipulate the pipettes, extracellular and intracellular solutions, Faraday caging to protect from external electrical and magnetic noise, and tight tubing to apply required suction to form giga-seal must be optimized to perform a successful patch-clamp experiment. Apart from these factors, the amplifier (Multiclamp 700B from Molecular Devices), the digitizer (Digidata 1550 from Molecular Devices), and the microscope optics must be calibrated; however, these three factors cause least of the troubles because the optimized instruments are available commercially.

The objectives (lens) and their arrangement in the microscope played important roles in optimizing some of the above-mentioned parameters, such as dimensions of the sample holder and positioning of the micromanipulators. Here, I briefly discuss the schematic of the whole patch-clamp system (Figure 10) that I set-up.

The water immersion focusing objective (lens) of the microscope has a working distance of 2 mm and theoretically allows an approach angle of up to 34° for a pipette to be positioned under it; however, I used angles up to 30° to have ample space for pipette movement (Figure 10). Patch-clamp experiments are relatively easier to perform on inverted microscopes because of presence of ample space for patching (because the focusing objective and the detectors are placed at the bottom) which is not the case in our upright multiphoton microscope. Custom-made poly-D-lysine coated glass bottom dishes (total diameter = 50 mm) with a height of less than 9 mm were designed to allow enough space for movement of pipettes. The glass diameter of 30 mm (Figure 10) of the dish provided enough glass-bottom space for plating cells so that various single cells could be patched in the same dish allowing several experiments to be performed from the same dish.

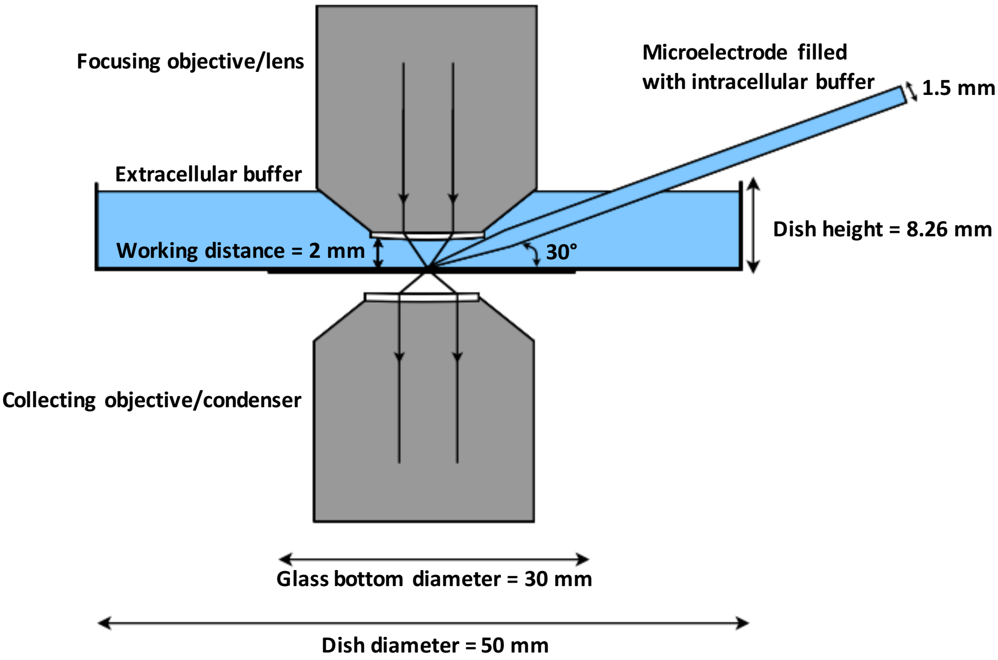

Figure 10: Scheme of patch-clampsystem installed in the upright microscope. The water immersion focusing objective (lens, *N.A.* = 1.05, working diatance = 2 mm) allows a pipette of tip diameter = ~2 μm at 30° angle to be positioned under it. The poly-D-lysine coated custom-made dish (total diameter = 50 mm, glass bottom diameter = 30 mm) from MatTek® has height of 8.26 mm to allow extra space for movement of the pipette. The outer diameter of the pipette is 1.5 mm, which is 75% of the lens working distance and hence it was tapered in the end to allow space for movement under the lens. The light focused on the sample by the water immersion objective is collected by the air-based objective (*N.A.* = 0.9). Image is not to scale.

Cell type: The type of the cell plays a crucial role in patch clamping experiments. Although patch-clamping is mostly performed on dendritic neurons,[31–33] other cell types such as *Xenopus oocytes*,[34] cardiomyocytes,[35,36] and HEK 293T cells[37–39] are widely used for various purposes.

Xenopus Oocytes are one of the easiest cells to patch because of their relatively large size (~ 0.5–1 mm), which make them visible with the naked eye. However, they have follicle and vitelline layers covering the plasma membrane[40] that need to be removed, which is not a trivial task, and the cells frequently get damaged during this process.[29] Single electrode voltage-clamp of large oocytes is not possible because they produce large voltage-error. Due to the large size of the oocytes, large currents are produced in the order of μA. Since the series resistance is in the order of MΩ, the error (defined as $i_p R_s$ in Figure 9) can mount up to several volts, which will make the whole-cell recording redundant (because cell membranes have potential difference in the order of mV). Generally, voltage-clamp experiments of oocytes are performed using a two-electrode voltage clamp, where one electrode is used for imparting the command voltage to the cell and the other electrode is used for measuring the voltage across the cell.[41] For this reason, single electrode whole-cell patch-clamp is performed on only one single cell in the case of smaller cells (e.g. neurons, HEK 293T etc.) and never on a cluster of cells. Moreover, the oocytes are filled with yolk, which do not allow imaging of the full structure of the cell.

Initially, I started working with HEK 293T cells because they are robust and are easier to patch because of their globular shape (allowing sufficient space to be patched with pipettes inclined at 30° angle). HEK 293T cells were procured and cultured per the protocol mentioned in Chapter 3.

Neonatal cardiomyocytes are difficult to patch because they are relatively flat and keep beating thus making formation of giga-seal very difficult. I did not attempt to patch cardiomyocytes because they contract, which leads to damage of the giga-seal. I studied localization of a different dye in neonatal myocytes, which is discussed in Chapter 5.

After gaining experience in patch clamping HEK 293T cells, I worked with primary rat hippocampal neurons *in vitro* and rat brain slices *ex vivo*. The details of working with neurons are discussed in Chapter 5 with a different dye.

Pipettes: Glass pipettes (Harvard Instruments) were pulled using a Narishige PC-10 pipette puller. The outer diameter of the pipettes is 1.5 mm, which is 75% of the lens working distance (2 mm). So, pipettes with larger tapering are pulled to allow space under the lens for movement (Figure 10). The pipette tip resistance is around 3–7 MΩ (for diameter = ~2 μm). The pipettes should be pulled fresh on the day of experiment as pulled pipettes accumulate dust particles on their tips, which hinders giga-seal formation with the cell membrane. The pipettes are fitted in the pipette holder and are connected to a pre-amplifier head-stage (CV-7B, Axon Instruments). The pre-amplifier is fitted on the micromanipulators (PatchStar from Scientifica) for high precision positioning and movement of the pipettes.

Cellular solutions: Extracellular (EC) and intracellular (IC) buffer solutions of similar osmolarities were prepared. Osmolarity balance between EC and IC is important to prevent the cells from exploding (if the IC solution is of greater osmolarity than the EC solution) or imploding (if the EC solution is of greater osmolarity than the IC solution). The compositions of the EC and IC solutions are well documented and various compositions have been used depending on the type of cell and experiment.[7,32,34,39,42,43] The composition of the EC used here is NaCl (130 mM), KCl (2.5 mM), HEPES (10 mM), glucose (10 mM), $CaCl_2$ (2 mM), $MgCl_2$ (1.3 mM) at pH = 7.4 (adjusted with NaOH) and osmolarity = 304 mOsm. The composition of IC is KCl (10 mM), NaCl (5 mM), EGTA (2 mM), K-gluconate (115 mM), HEPES (10 mM) at pH = 7.3 (adjusted with KOH) and osmolarity = 292 mOsm. The solutions were filtered with a 0.2 μm pore size syringe filter prior to use to remove any dust particles or impurity for effective giga-seal formation.

Faraday caging: Faraday caging is required to shield the patch-clamp recording from external electrical and magnetic noise. Since the current measured in the patch-clamp setup is in the order of pA, it is very sensitive to external electromagnetic radiations. In our case, the Faraday cage acted as a shield too to block the intense laser light if it escapes the light path (Figure 6). The shield also blocks any external light from contaminating the fluorescence and SHG light generated by the dye.

Tubing: The suction necessary to form the giga-seal and to rupture the cell membrane to go into whole-cell mode was applied using a glass syringe connected to an airtight silicone tube (Figure 6). Non-expandable airtight glass syringes allow more precision for pressure control than plastic syringes.

After setting up the system in the microscope, I used two commercial voltage sensitive dyes, **FM4-64** and **di-4-ANEPPS** to test the efficacy of the system.

4.13 Testing the voltage sensitivity of FM4-64 and di-4-ANEPPS

FM4-64, a dicationic dye (Figure 11), has been shown to be voltage sensitive by both the SHG and TPEF techniques.[4,12,39] Here, I tested voltage sensitivity of **FM4-64** in HEK 293T cells both extracellularly and intracellularly. The imaging was performed at a wavelength of 840 nm for two major reasons. First, the light penetrates deepest in any tissue at a wavelength range of 800–870 nm.[44] At shorter wavelengths, the high-energy light (at lower wavelengths) can cause photo damage and at longer wavelengths, it is absorbed by water. Second, since I am primarily working on SHG-based voltage sensitivity of porphyrins and other porphyrinoids, light of wavelength of 840 nm leads to generation of maximum signal because β_{zzz} of porphyrins is highest around the wavelength of 840 nm due to resonance enhancement.[45,46] Since **FM4-64** and **di-4-ANEPPS** are commercially available voltage-sensitive dyes, the motivation behind testing their voltage sensitivity is to test the working of patch-clamp system and gain experience on it.

4.13.1 FM4-64

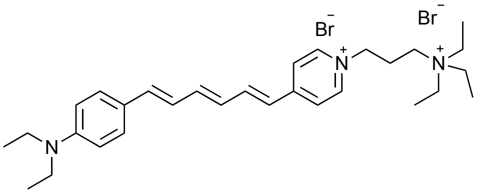

Figure 11: Chemical structure of **FM4-64**.

FM4-64 was incubated with HEK 293T cells (~70% confluent) in EC buffer. After 5 min of incubation, cells were placed under the microscope, a single cell was located, the giga-seal was formed with a pipette, and then whole-cell mode was achieved by applying suction. After obtaining the whole-cell mode, the cell was finely focused using the laser to achieve a plane that provides the brightest TPEF and SHG signals. Caution is necessary while focusing on the cell, as using intense laser power to find the plane of the brightest signal might photobleach the dye and cause damage to the cell (this step often results in losing the giga-seal, failing the entire experiment). A resting potential of −70 mV was applied to the cell following which a square-wave potential difference of 100 mV was applied at various time points, and changes in TPEF and SHG signals were recorded for several cells. I performed experiments at different dye concentrations, 10 μM, 25 μM, and 70 μM.

FM4-64 at 10 μM concentration

Initially, I incubated HEK 293T cells with 10 μM of dye and applied square-wave potential difference of 100 mV for 2 s intervals to capture images at every 0.2 s. Changes in TPEF and SHG intensities at three distinct areas of a cells were explored by frame-scan (raster-based) of the whole cell (Figure 12). Three regions of the same cell were monitored to check if the dye works uniformly in all the regions of a cell.

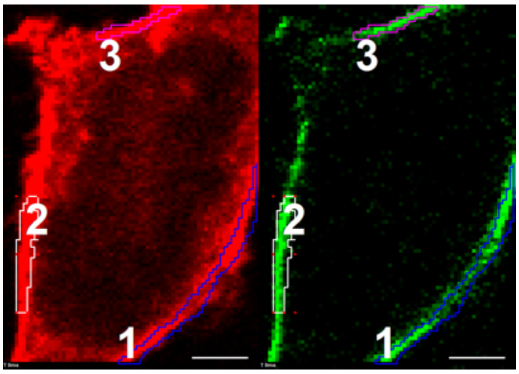

Figure 12: TPEF (red) and SHG (green) images of HEK 293T cells under application of a square-wave potential difference of 100 mV with a 2 s interval. Change in TPEF and SHG intensities were studied at three different parts of the plasma membrane cell, 1, 2, and 3. Wavelength = 840 nm, laser power = 1.8 mW, pixel dwell time = 10 μs/pixel. Scale bar = 5 μm.

The measured changes in TPEF and SHG intensities with respect to change in applied potential difference for all three regions are displayed in Figure 13. It was found that the dyes behave differently in the different regions. Region 1 displayed better change in voltage sensitivity in contrast to regions 2 and 3. On the other hand, region 2 underwent considerable photobleaching compared to regions 1 and 3. TPEF signal for region 2 in Figure 12 was corrected for photobleaching, while SHG was not (Figure 13). Region 2 did not show significant SHG-based voltage sensitivity. The signal to noise ratio for both TPEF and SHG of region 3 was very poor (Figure 13).

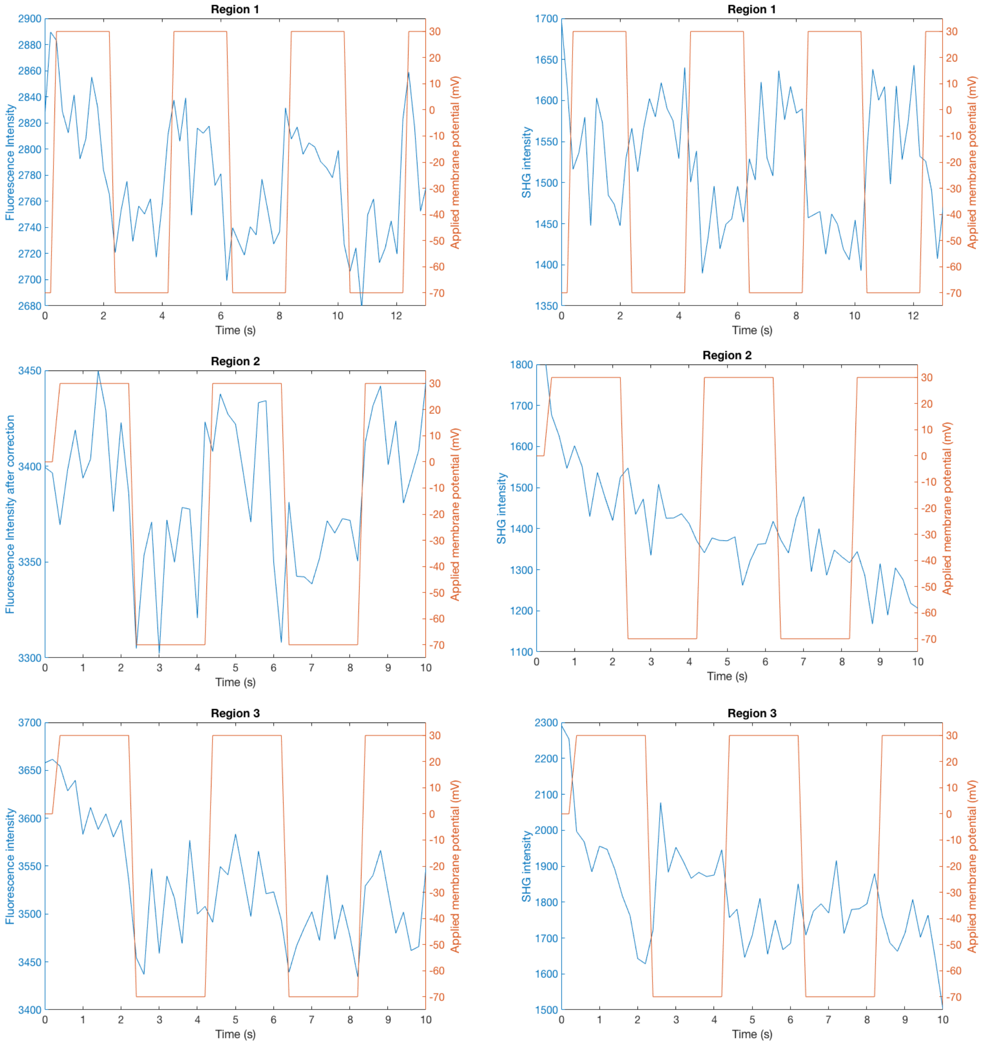

Figure 13: Change of TPEF (left column) and SHG intensities (right column) with respect to 100 mV (–70 mV to +30 mV) of applied potential difference. In region 1, the TPEF and SHG intensities change according to the change in potential difference. In region 2, photobleaching was observed unlike in region 1. The fluorescence spectrum was corrected for photobleaching but the SHG spectrum not , as the signal to noise ratio was too poor to give any meaningful change in the signal. In region 3, no substantial photobleacing was observed; however, the signal to noise ratio for both TPEF and SHG was poor. No averaging performed and the traces represent single trial imaging.

Since the laser power was applied for several seconds, photobleaching was evident; however, the reasons for different behavior of the dye in different parts of the plasma membrane of the same cell are not properly understood. The differences could be resulting from the difference in the number density of the dye molecules in the three parts. The poor signal to noise ratio could be attributed to the low dye concentration of 10 µM. Previous studies showing better voltage sensitivity of **FM4-64** in neurons were obtained using much higher dye concentrations (from 50 µM to 500 µM) and laser powers (up to 10 mW) at line scanning mode or at frame scanning mode of smaller field of view.[3,39,47] However, since photobleaching is already observed at 10 µM, a higher dye concentration and laser power will certainly cause greater photobleaching (which is toxic to cells). In my experience, a laser power of more than 2 mW breaks the giga-seal at a full frame scanning mode with a pixel dwell time of 10 µs/pixel.

The experiment was repeated by varying the scanning parameters. The concentration and laser power were maintained at 10 µM and 1.5 mW respectively, but the imaging time was reduced to 26 ms/image and the potential difference of 100 mV was applied every 520 ms for better signal to noise ratio. To further improve signal to noise ratio, the signals were measured 5 times and averaged (Figure 14). By this method, the maximum TPEF-based voltage sensitivity was found to be around 3.5% while SHG-based sensitivity was found to be approx. 4%.

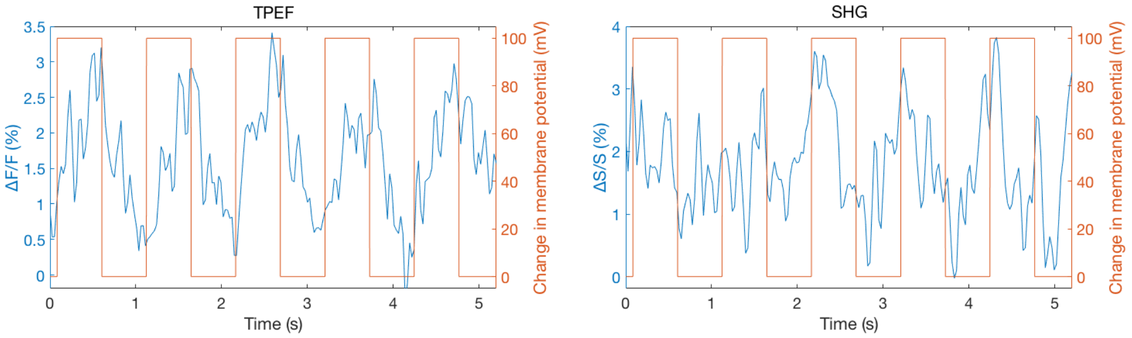

Figure 14: Change in TPEF and SHG intensities of **FM4-64** (10 µM) in HEK 293T cell on application of a square-wave potential difference of 100 mV. The fluorescence change is from 0–3.5%, while the SHG change is from 0–4 %. The signals are averaged over five trails. The photobleaching was corrected by curve fitting application in MATLAB and the lines were smoothed using smoothing spline function in MATLAB.

FM4-64 at 25 µM concentration

I increased the dye concentration to 25 µM and restudied the voltage sensitivity **of FM4-64**. The voltage steps were applied at every 130 ms instead of 2 s and images were taken at low scanning time of every 26 ms/image at a pixel dwell time of 0.5 µs/pixel. Low image scanning time (= high scanning rate) decreases the overall signal to noise ratio but more data can be acquired before substantial photobleaching take place. The image of the full plasma membrane of the cell was analyzed (Figures 15 and 16).

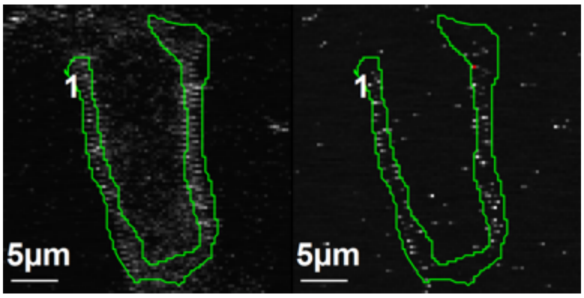

Figure 15: TPEF (left) and SHG (right) images of the **FM-64** (25 µM) acquired at very high scanning rate. Change in TPEF and SHG intensities were studied around the plasma membrane marked green color curve. Wavelength = 840 nm, laser power = 1.5 mW. Scale bar = 5 µm.

Despite recording signals at high scanning rate, significant photobleaching was observed over a time range of 14 s. Due to high image scanning rate, the signal to noise ratio was poor (Figure 16) resulting in no significant change in SHG intensity for a change in 100 mV potential difference.

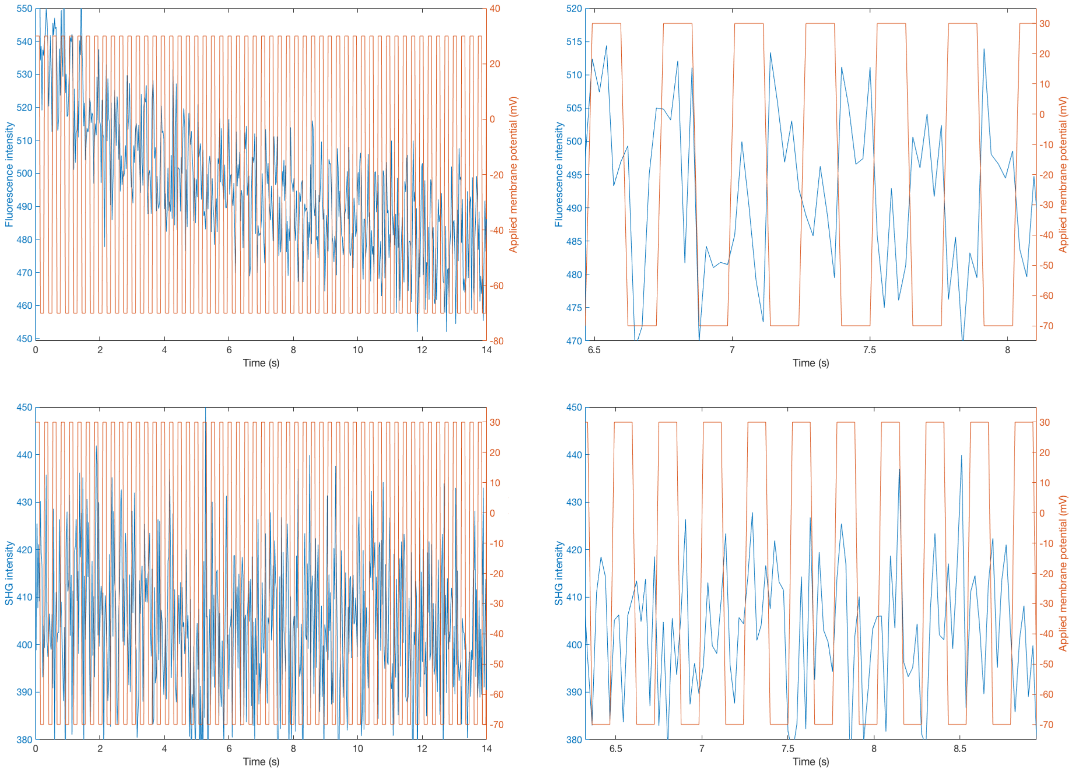

Figure 16: Change of fluorescence (top row) and SHG intensities (bottom row) of **FM4-64** in HEK 293T cell with respect to applied potential difference of 100 mV. Over a time of 14 s, the dyes photobleach, which is seen as the exponential decrease of the TPEF signal (top left image). The top right image shows how the TPEF intensity changes while applying 100 mV (–70 mV to +30 mV) potential difference. No significant change in SHG signal was observed due to poor signal to noise ratio. No averaging was performed and the traces represent a single trial imaging.

It must be appreciated that the TPEF and SHG traces shown here are taken on a single trial without performing any averaging. It is a common practice to report the change of voltage sensitivity of dyes by TPEF or SHG by averaging over 5 to 50 trials to improve the signal to noise ratio as I performed in Figure 14.[4,12,39,47,48] Although, such a practice of averaging gives high signal to noise ratio but during the process, crucial information can be lost. An ideal voltage sensitive dye should be able to give high signal to noise ratio in a single trial. One of the major disadvantages of averaging is that the accurate data cannot be interpreted and the optimization gets complex because the dye undergoes photobleaching over time due to high concentration and intense laser power.[49] Despite its shortcomings, averaging of signals gives information about the quality of the temporal resolution, about the behavior of the dye in the cells over certain time frame, and the change in membrane potential.

FM4-64 at 70 μM concentration

I performed a line scan (probe of a linear section of cell) at the imaging time of 2.1 ms/line on a cell incubated with 70 μM of **FM4-64** using 1.5 mW laser power (Figure 17). A potential difference of 100 mV was applied every 210 ms. No averaging of signals was performed. As per literature, a line scan at higher concentrations (> 50 μM) yields better signal to noise ratio for SHG-based voltage sensitivity of **FM4-64**.[4,39] As expected, the signal to noise ratio was improved drastically on increasing the dye concentration and performing imaging at line-scanning mode. At line-scanning mode, the photobleaching is not as significant as during frame-scanning mode.

On performing line-scan imaging, the TPEF-based voltage sensitivity was found to be only 4% but SHG-based voltage sensitivity was found to be approx. 10% even without averaging the signals (Figure 17). This is significant increase from the SHG-based sensitivity of 4% observed at 10 μM after the lines were averaged 5 times (Figure 14). Line-scanning mode was not applied at lower concentrations because as observed in Figures 12 and 13, there could be differences in voltage sensitivity at different areas due to non-uniform localization of the dyes. Due to the differences in dye localization, it is not trivial to find a line where significant voltage sensitivity of the dye could be recorded and so frame-scanning mode is preferred at lower concentrations although, susceptible to photobleaching. Although at higher concentrations too, the localization of the dye is not uniform, the probability presence of more dyes per unit volume is higher and hence the probability of recording signals with high signal to noise ratio is more.

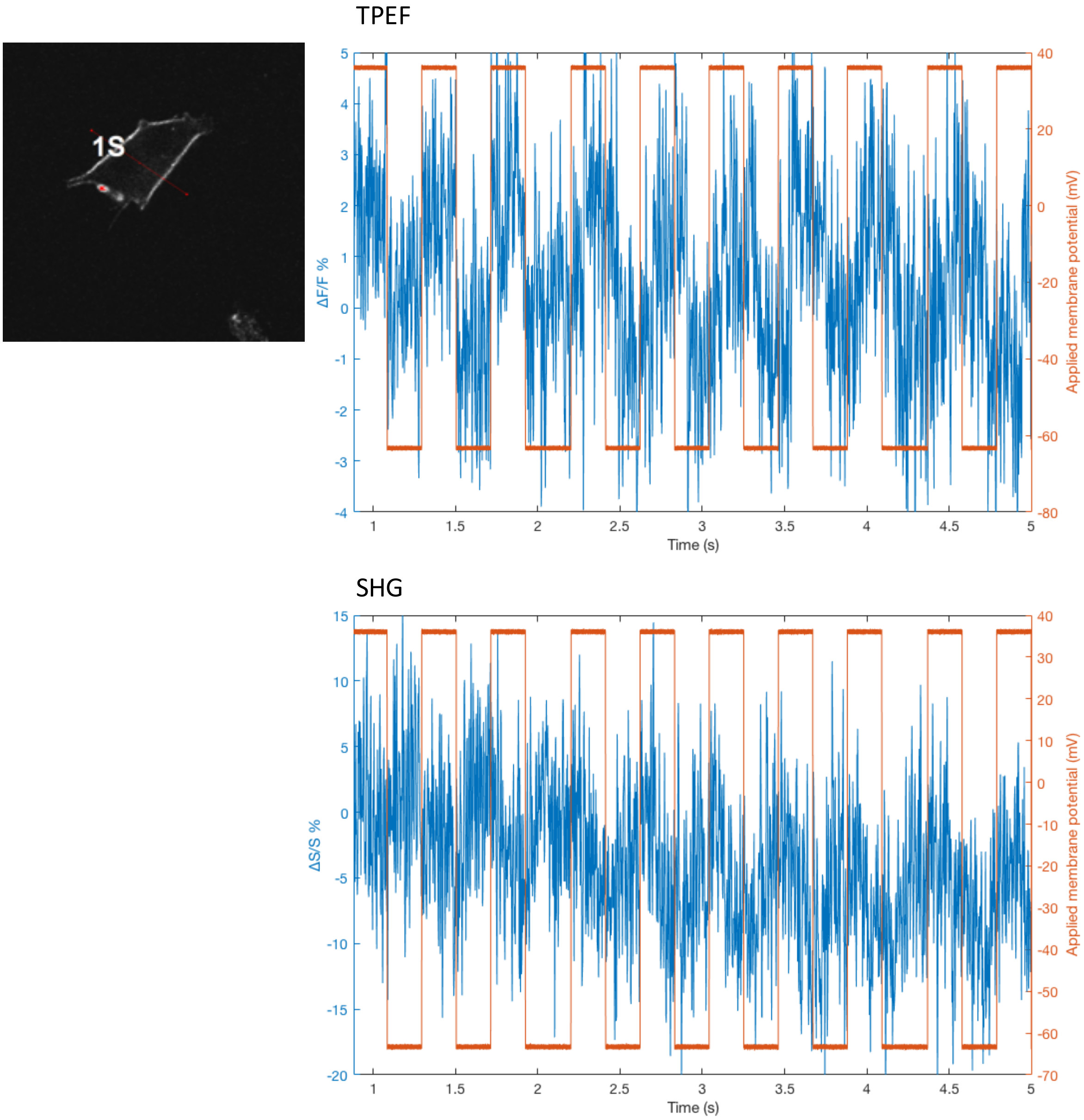

Figure 17: Reference image of HEK 293T incubated with 70 µM of **FM4-64** scanned at line scanning (2.1 ms per line) mode. Change in TPEF (top) and SHG intensities (bottom) of **FM4-64** (70 µM) on application of 100 mV of potential difference across the cell membrane. Line scanning at a time of 2.1 ms/line gave better signal to noise ratio than frame scanning (26 ms/frame). The change in TPEF intensity is up tp 4% on application of 100 mV (–70 mV to +30 mV) of potential difference. In SHG, the change was up to 10%. Traces are not averaged and taken on a single trial.

I also tested the voltage sensitivity of **FM4-64** for small increments (20 mV) in voltage. A potential difference of 20 mV steps were applied from −70 mV to 10 mV; however, the dye did not display any notable change in the TPEF and SHG intensities. The signal was mostly covered with noise even after averaging the signal over five trials (Figure 18).

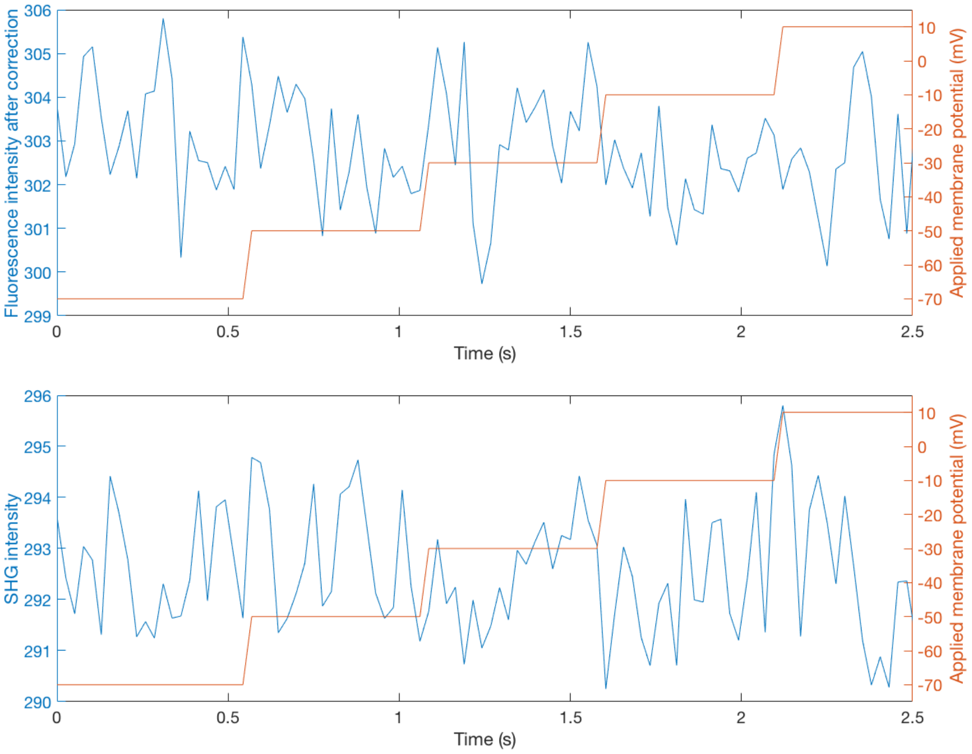

Figure 18: Trace of TPEF (top) and SHG (bottom) intensities on application of 20 mV increments of potential difference from −70 mV to 10 mV. No substantial change in the intensities were observed on changing the applied potential difference. Traces are averaged over five trials.

4.13.2 Di-4-ANEPPS

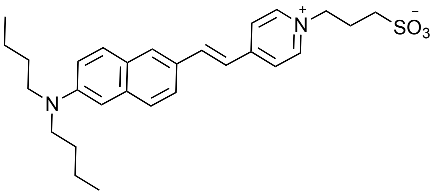

Figure 19: Chemical structure of **di-4-ANEPPS**.

Di-4-ANEPPS is an another electrochromic voltage-sensitive dye (Figure 19), which gives both TPEF and SHG responses.[27,42,50–52] Millard *et al.* reported that the voltage-sensitivity of **di-4-ANEPPS** can be as high as 18% and 30% at 850 nm and 910 nm at a dye concentration of ~3 µM, when averaged over more than 10 images; however, no information regarding the laser power was reported.[27,42] Reeve *et al.* reported that the voltage sensitivity of **di-4-ANEPPS** in a HLB is 3–4%, when illuminated with 90 mW laser light at a concentration of 5 µM and averaged over four times.[12] There have been inconsistencies in the voltage-sensitivity values reported across the literature owing to different experimental procedures. In my experience, **di-4-ANEPPS** did not show significant SHG-based voltage sensitivity, when illuminated with a laser light of power up to 2 mW perhaps due to low signal to noise ratio. The signal to noise ratio was low due to low image scanning time (26 ms/image at 0.5 µs/pixel). To increase the signal to noise ratio, I increased the image scanning time but no significant change in SHG signals were seen on application 100 mV of potential difference.

Following several unsuccessful attempts, I changed the delivery method from bath delivery to intracellular delivery. I delivered 10 µM of **di-4-ANEPPS** intracellularly by forming a giga-seal. Although there was no change in SHG signal due to poor signal to noise ratio, the TPEF-based voltage sensitivity was found to be around 2–3% on a single trial without averaging (Figures 20 and 21). In a hope to increase the signal to noise ratio, experiments were also performed by increasing the laser power and dye concentration (up to 100 µM) but no substantial difference from these results were observed.

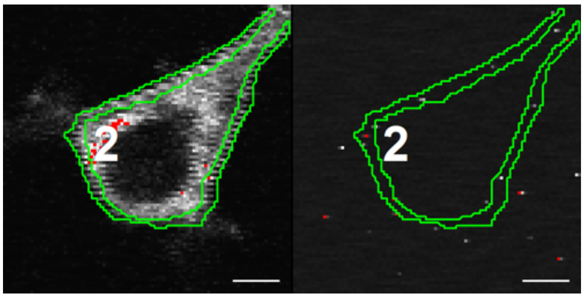

Figure 20: TPEF (left) and SHG (right) images of HEK 293T incubated with 10 µM of **di-4-ANEPPS**. In the TPEF image, the dyes can be seen from inside the cells. No sigificant SHG signal is seen due to low laser power and low image scanning time (26 ms/image at 0.5 µs/pixel). Change in TPEF and SHG intensities were studied around the plasma membrane region make green color curve. Wavelength = 840 nm, laser power = 1.5 mW; scale bar = 5 µm.

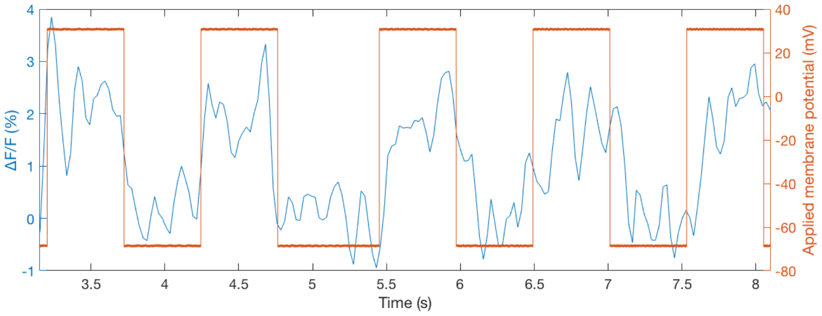

Figure 21: Voltage sensitivity of **di-4-ANEPPS** (10 µM) by TPEF on application of square-wave potential difference of 100 mV (–70 mV to +30 mV) of 130 ms interval. The trace represents a single trial without averaging. The signal from 3 s is shown because the signals before 3 s were found to be of poor signal to noise ratio.

The voltage sensitivity values of **FM4-64** and **di-4-ANEPPS** measured here significantly vary from the literature reported values, which themselves show a high level of inconsistency. The inconsistencies in the voltage sensitivity, temporal resolution, and photostability of the dyes can be attributed to various factors. I used HEK 293T cells, while the voltage sensitivities of these dyes are reported in HLBs, neurons, and neuroblastoma cells. Size of the cell, orientation of the dye in the plasma membrane, laser power, wavelength of light used, dye concentration, and quality of giga–seal formed can largely affect the voltage measuring efficiency of an electrochromic dye. One of the major disadvantages of styryl–based dyes (such as **FM4-64** and **di-4-ANEPPS**) is that these dyes can photoisomerize around the C=C bonds, which can cause spectral shifts beyond the electrochromic responses of these dyes.[53,54] Porphyrin-based dyes are not affected by photoisomerism because no cis-trans conformations are possible in the porphyrin-based dyes synthesized in the Anderson group. Moreover, for TPEF-based sensitivity, the microscope configuration also plays a significant role apart from the inherent characteristics of the dye and the cell as discussed in Chapter 1. Despite variations in the voltage sensitivities of the organic dyes, the overall motive of testing **FM4-64** and **di-4-ANEPPS**, which was to test and gain experience in the patch-clamp setup, is served.

4.13.3 HLA-1

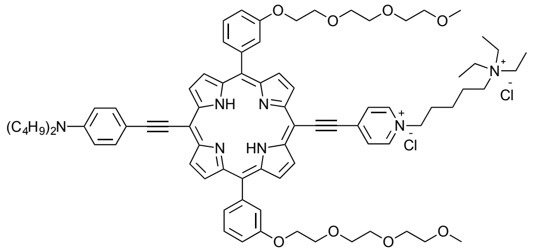

Figure 22: Chemical structure of **HLA-1**.

After testing the efficacy of patch-clamp system in conjugation with the multiphoton microscope, I attempted to test the voltage sensitivity of **HLA-1** (Figure 22) because this dye localized in the plasma membrane of live mammalian cells (Chapter 3). The SHG-based signal to noise ratio of **HLA-1** (30 µM) was poor even at a laser power of 5 mW because of which frame-scanning of the cell was not possible and so the cells were imaged in line-scanning mode (λ = 870 nm; image scanning time = 2.9 ms/line at 20 µs/pixel). An advantage of line-scanning mode over frame scanning mode is that the laser power could be increased up to tens of milliwatts without causing significant photobleaching or photodamage. While forming whole-cell mode, a perfect giga-seal was not obtained at high dye concentrations (~30 µM) due to unknown reasons. Similar effects were observed by Dr. James Reeve and coworkers when they attempted to form giga-seal to deliver **JR1-plus** in rat brain slices by intracellular injection.[45,55] Since a perfect giga-seal was not obtained, the command voltage applied did not necessarily translate into membrane voltage and so the recording was poor. To compensate for the poor giga-seal, the laser power was increased up to 15 mW and then up to 90 mW. At 90 mW, changes in TPEF and SHG signals were seen (Figure 23) but the cell died within few seconds due to significant photodamage.

Despite changing several parameters like laser scanning modes and times, dye concentration, and dye loading methods, no voltage sensitivity was detected. I tested **HLA2.Cu** dye (with quenched fluorescence as discussed in Chapter 3) up to 100 µM concentrations but such high concentration led to precipitation of the dyes and a perfect giga-seal was not achieved. Moreover, the signal to noise ratio of **HLA2.Cu** is poorer than **HLA-1** or **HLA-2**. No significant change in SHG intensity was seen (data not shown).

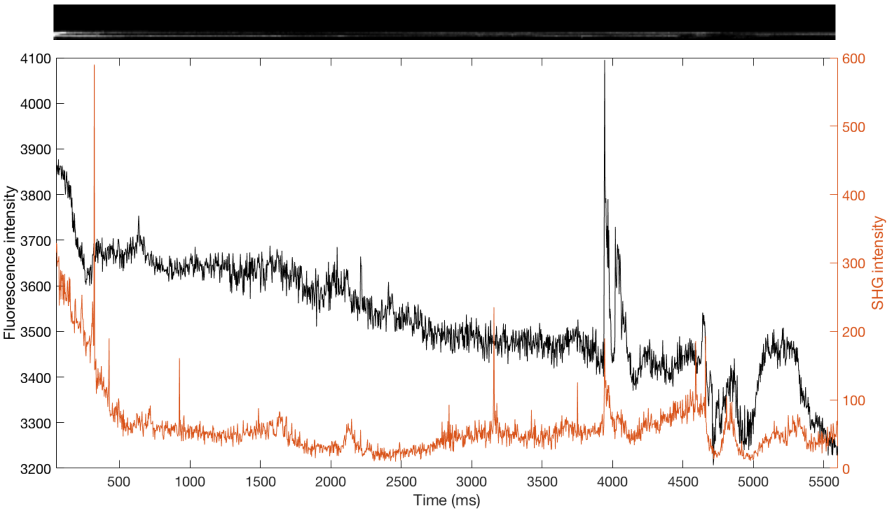

Figure 23: SHG line–scanning image of **HLA-1** overlaid with the traces of change in fluorescence and SHG intensities. A square–wave potential difference of 200 mV was applied across the plasma membrane of a HEK 293T cell. Traces show that the locations of change in fluorescence and SHG intensites are the same but they do not correlate with the applied voltage waveform.

The poor performance of **HLA-1** and **HLA2.Cu** could be attributed to several factors. Apart from β_{zzz} (β_{zzz} is the characteristic of SHG efficiency of a high as discussed in Chapters 1 and 2), the overall SHG efficiency is also dependent on the square of the number density of the dyes. As already discussed in Chapter 3, porphyrin-based dyes being bigger in size than **FM4-64** or **di-4-ANEPPS**, most likely have a lower number density in the plasma membrane thus affecting the overall SHG efficiency. Moreover, the β_{zzz} of **HLA-1** is similar to the value of **FM4-64** and significantly lower than **JR1-plus** and **JR1**.[55] The low β_{zzz} of **HLA-1** when combined with low number density further reduces the SHG efficiency. Additionally, the hydrophilic groups of **HLA-1** might affect the orientation of the dye in the plasma membrane as its amphiphilic axis is not collinear with the dipolar axis, which might affect the SHG response. This is because for a dye to give maximal SHG signal, its dipolar axis must be parallel to the direction of laser polarization which is attained when the dipolar axis of the dye is collinear with its amphiphilic axis.

4.20 Conclusion

In this chapter, I outlined various lipid–based model systems adopted by researchers to study optical probes by different microscopy techniques. I described my unsuccessful attempts to form stable hemispherical lipid bilayers under the multiphoton microscope. I designed a patch-clamp system in the multiphoton microscope with lens working distance of 2 mm and demonstrated its working by testing two commercial voltage–sensitive probes, **FM4-64** and **di-4-ANEPPS**. The patch-clamp system worked successfully and I could form giga-seals and carry recordings from live cells in whole-cell patch-clamp mode. The voltage sensitivity of **FM4-64** was tested at different concentrations in both frame–scan and line–scanning modes with different image acquiring rates and voltage step protocols. **FM4-64** showed good voltage sensitivity at higher concentrations and when the signals were averaged in agreement with the literature. However, the quantitative agreement of sensitivity with literature was not attained because experimental conditions. **Di-4-ANEPPS** being a zwitterionic dye was mostly internalized by cells when delivered extracellularly and its voltage sensitivity was found to be significant only for two–photon excited fluorescence when delivered intracellularly. Testing of these dyes helped to optimize image scanning and voltage change protocols to attain high voltage sensitivity for both TEPF and SHG with minimal photobleaching. The voltage sensitivity of **HLA-1** could not be studied due to poor SHG-based signal to noise ratio at low laser power.

A porphyrin–based dye that localizes in the plasma membrane of live cells and whose dipolar axis is collinear with its amphiphilic axis might give better signal to noise ratio than **HLA-1**. In the next chapter, I discuss a new porphyrin–based dye that I designed and synthesized that satisfies the above–mentioned criteria.

4.30 References

1 E. W. Miller, J. Y. Lin, E. P. Frady, P. A. Steinbach, W. B. Kristan and R. Y. Tsien, *Proc. Natl. Acad. Sci.*, 2012, **109**, 2114–2119.

2 C. R. Woodford, E. P. Frady, R. S. Smith, B. Morey, G. Canzi, S. F. Palida, R. C. Araneda, W. B. Kristan, C. P. Kubiak, E. W. Miller and R. Y. Tsien, *J. Am. Chem. Soc.*, 2015, **137**, 1817–1824.

3 J. Jiang, K. B. Eisenthal and R. Yuste, *Biophys. J.*, 2007, **93**, L26–L28.

4 D. A. Dombeck, L. Sacconi, M. Blanchard-Desce and W. W. Webb, *J. Neurophysiol.*, 2005, **94**, 3628–3636.

5 D. A. Dombeck, M. Blanchard-Desce and W. W. Webb, *J. Neurosci.*, 2004, **24**, 999–1003.

6 P. Zou, Y. Zhao, A. D. Douglass, D. R. Hochbaum, D. Brinks, C. A. Werley, D. J. Harrison, R. E. Campbell and A. E. Cohen, *Nat. Commun.*, 2014, **5**.

7 D. R. Hochbaum, Y. Zhao, S. L. Farhi, N. Klapoetke, C. A. Werley, V. Kapoor, P. Zou, J. M. Kralj, D. Maclaurin, N. Smedemark-Margulies, J. L. Saulnier, G. L. Boulting, C. Straub, Y. K. Cho, M. Melkonian, G. K.-S. Wong, D. J. Harrison, V. N. Murthy, B. L. Sabatini, E. S. Boyden, R. E. Campbell and A. E. Cohen, *Nat. Methods*, 2014, **11**, 825–833.

8 A. J. Heron, J. R. Thompson, A. E. Mason and M. I. Wallace, *J. Am. Chem. Soc.*, 2007, **129**, 16042–16047.

9 J. R. Thompson, A. J. Heron, Y. Santoso and M. I. Wallace, *Nano Lett.*, 2007, **7**, 3875–3878.

10 S. Leptihn, O. K. Castell, B. Cronin, E.-H. Lee, L. C. M. Gross, D. P. Marshall, J. R. Thompson, M. Holden and M. I. Wallace, *Nat. Protoc.*, 2013, **8**, 1048–1057.

11 M. I. Wallace, S. Leptihn and J. R. Thompson, *World Intellect. Prop. Organ.*, 2011.

12 J. E. Reeve, A. D. Corbett, I. Boczarow, W. Kaluza, W. Barford, H. Bayley, T. Wilson and H. L. Anderson, *Angew. Chem. Int. Ed.*, 2013, **52**, 9044–9048.

13 A. Matiukas, B. G. Mitrea, M. Qin, A. M. Pertsov, A. G. Shvedko, M. D. Warren, A. V. Zaitsev, J. P. Wuskell, M. de Wei, J. Watras and L. M. Loew, *Hear. Rhythm*, 2007, **4**, 1441–1451.

14 L. M. Loew and L. L. Simpson, *Biophys. J.*, 1981, **34**, 353–365.

15 V. S. Sokolov, A. N. Gavrilchik, A. O. Kulagina, I. N. Meshkov, P. Pohl and Y. G. Gorbunova, *J. Photochem. Photobiol. B Biol.*, 2016, **161**, 162–169.

16 A. Wiese, J. O. Reiners, K. Brandenburg, K. Kawahara, U. Zähringer and U. Seydel, *Biophys. J.*, 1996, **70**, 321–329.

17 W. L. Hwang, M. Chen, B. Cronin, M. A. Holden and H. Bayley, *J. Am. Chem. Soc.*, 2008, **130**, 5878–5879.

18 M. D. Collins and S. E. Gordon, *J. Vis. Exp.*, 2013, e50227.

19 G. M. Cooper and R. E. Hausman, *The Cell: A Molecular Approach 2nd Edition*, Sinauer Associates, Inc., 2007.

20 M. Canepari, D. Zecevic and O. Bernus, *Membrane potential imaging in the nervous system and heart*, Springer, 2015.

21 G. Vereb, J. Szöllosi, J. Matkó, P. Nagy, T. Farkas, L. Vigh, L. Mátyus, T. A. Waldmann and S. Damjanovich, *Proc. Natl. Acad. Sci.*, 2003, **100**, 8053–8058.

22 F. M. Goñi, *Biochim. Biophys. Acta - Biomembr.*, 2014, **1838**, 1467–1476.

23 H. Bayley, B. Cronin, A. Heron, M. A. Holden, W. L. Hwang, R. Syeda, J. Thompson and M. Wallace, *Mol. Biosyst.*, 2008, **4**, 1191–1208.

24 G. Maglia, A. J. Heron, W. L. Hwang, M. A. Holden, E. Mikhailova, Q. Li, S. Cheley and H. Bayley, *Nat. Nanotechnol.*, 2009, **4**, 437–440.

25 M. A. Holden, D. Needham and H. Bayley, *J. Am. Chem. Soc.*, 2007, **129**, 8650–8655.
26 P. F. Devaux and R. Morris, *Traffic*, 2004, **5**, 241–246.
27 A. C. Millard, L. Jin, M. Wei, J. P. Wuskell, A. Lewis and L. M. Loew, *Biophys. J.*, 2004, **86**, 1169–1176.
28 J. J. Cras, C. A. Rowe-Taitt, D. A. Nivens and F. S. Ligler, *Biosens. Bioelectron.*, 1999, **14**, 683–688.
29 D. Ogden and P. Stanfield, *Microelectrode Techniques - The Plymouth Workshop Handbook*, The Company of Biologists Limited, Cambridge, 2nd edn., 1994.
30 C. Li, *Adv. Physiol. Educ.*, 2008, **32**, 209–211.
31 A. Molleman, *Patch Clamping: An Introductory Guide to Patch Clamp Electrophysiology. 2003*, John Wiley & Sons, Ltd, 2003.
32 S. B. Kodandaramaiah, G. T. Franzesi, B. Y. Chow, E. S. Boyden and C. R. Forest, *Nat. Methods*, 2012, **9**, 585–587.
33 N. Osorio and P. Delmas, *Nat. Protoc.*, 2010, **6**, 15–27.
34 C. McClenaghan, M. Schewe, P. Aryal, E. P. Carpenter, T. Baukrowitz and S. J. Tucker, *J. Gen. Physiol.*, 2016, **147**, 497–505.
35 J. Ma, L. Guo, S. J. Fiene, B. D. Anson, J. A. Thomson, T. J. Kamp, K. L. Kolaja, B. J. Swanson and C. T. January, *Am. J. Physiol. Heart Circ. Physiol.*, 2011, **301**, H2006–H2017.
36 D. Ossola, M. Y. Amarouch, P. Behr, J. Vörös, H. Abriel and T. Zambelli, *Nano Lett.*, 2015, **15**, 1743–1750.
37 B. He and D. M. Soderlund, *Neurosci. Lett.*, 2010, **469**, 268–272.
38 M. A. Gandini, A. Sandoval and R. Felix, *Cold Spring Harb. Protoc.*, 2014, **2014**, 396–401.
39 P. Theer, W. Denk, M. Sheves, A. Lewis and P. B. Detwiler, *Biophys. J.*, 2011, **100**, 232–242.
40 J. N. Dumont and A. R. Brummett, *J. Morphol.*, 1978, **155**, 73–97.
41 B. Guan, X. Chen and H. Zhang, *Methods Mol. Biol.*, 2013, **998**, 79–89.
42 A. C. Millard, L. Jin, A. Lewis and L. M. Loew, *Opt. Lett.*, 2003, **28**, 1221–1223.
43 Y. L. Huang, A. S. Walker and E. W. Miller, *J. Am. Chem. Soc.*, 2015, **137**, 10767–10776.
44 K. R. Byrnes, R. W. Waynant, I. K. Ilev, X. Wu, L. Barna, K. Smith, R. Heckert, H. Gerst and J. J. Anders, *Lasers Surg. Med.*, 2005, **36**, 171–185.
45 J. E. Reeve, H. A. Collins, K. De Mey, M. M. Kohl, K. J. Thorley, O. Paulsen, K. Clays and H. L. Anderson, *J. Am. Chem. Soc.*, 2009, **131**, 2758–2759.
46 I. Lopez-Duarte, J. E. Reeve, J. Perez-Moreno, I. Boczarow, G. Depotter, J. Fleischhauer, K. Clays and H. L. Anderson, *Chem. Sci.*, 2013, **4**, 2024–2027.
47 M. Nuriya, J. Jiang, B. Nemet, K. B. Eisenthal and R. Yuste, *Proc. Natl. Acad. Sci.*, 2005, **103**, 786–790.
48 J. Jiang and R. Yuste, *Microsc. Microanal.*, 2008, **14**, 526–531.
49 L. Sacconi, D. A. Dombeck and W. W. Webb, *Proc. Natl. Acad. Sci.*, 2006, **103**, 3124–3129.
50 P. J. Campagnola and L. M. Loew, *Nat. Biotechnol.*, 2003, **21**, 1356–1360.
51 V. Montana, D. L. Farkas and L. M. Loew, *Biochemistry*, 1989, **28**, 4536–4539.
52 S. Preuss and W. Stein, *PLoS One*, 2013, **8**, e75678.
53 G. Hübener, A. Lambacher and P. Fromherz, *J. Phys. Chem. B*, 2003, **107**, 7896–7902.
54 B. Kuhn and P. Fromherz, *J. Phys. Chem. B*, 2003, **107**, 7903–7913.
55 J. E. Reeve, DPhil Thesis, University of Oxford, 2012.

Chapter 5

Plasma Membrane bound and Voltage-Sensitive Tricationic Porphyrin-based Dye

Summary: *Although donor-acceptor–based porphyrin dyes exhibit high SHG efficiency and SHG-based voltage sensitivity, they cannot be used to measure membrane potential of cells. This is because the existing porphyrin dyes do not localize at the plasma membrane of cells to give SHG at low laser power. Despite possessing dicationic amino and zwitter ionic amino-sulfonate groups like commercial plasma membrane bound dyes, **FM4-64** and **di-4-ANEPPS**, the porphyrin-based dyes are easily taken up by the cells. **HLA-1**, a dicationic porphyrin-based dye functionalized with arylated-TEG groups at the meso-positions localize at the plasma membrane of live cells but require high laser power to give notable SHG. I postulate that **HLA-1** localized at the plasma membrane of cells unlike dicationic and zwitter-ionic porphyrin-based dyes because there is a balance between the hydrophobicity and hydrophilicity of **HLA-1**. Based on this data, I designed and synthesized a tricationic porphyrin-based dye, **AK-1** that I discuss in this chapter. I perform various cellular-based studies to study the cellular localization of the dye. The studies that I performed are:*

1. *The dye, **AK-1** localized at the plasma membrane of four different kind of mammalian cells, HEK 293T cells, U-87 MG cells, HeLa cells, and rat hippocampal neurons to give SHG at low laser power.*
2. *The dye gave significantly higher SHG and fluorescence than **HLA-1** at similar imaging conditions.*
3. *Multimodal fluorescence and SHG –based imaging was performed using **AK-1** with cellular organelles bound dyes **RH123** and Lysotracker yellow HEK-123. The efficacy of **AK-1** was compared to **FM4-64**.*
4. ***AK-1** was delivered to mice brain slices ex vivo through three different delivery methods, such as bath delivery, intracellular delivery, and pressure injection delivery. No SHG was detected from the brain slices through bath delivery and intracellular delivery; however, considerable SHG was seen from pressure injection delivery. Due to extensive background signal, a single neuron in the slices could not be isolated for patch-clamp experiments.*
5. *The dye resisted in formation of perfect giga-seals by patch-clamp method in HEK 293T cells and rat hippocampal neurons and hence its voltage sensitivity could not be studied by patch-clamp technique.*
6. *I studied the voltage sensitivity of **AK-1** in contracting neonatal myocytes and found that the dye give good response ($\Delta S/S$=60%) to the change in membrane potential. Further controlled study is required for optimization of the spatial and temporal resolution of the dye.*

7. *I also studied the localization of* ***AK-1*** *in gram-negative bacteria, E. coli and found that the dye was easily taken up by the E. coli cells in contrast to neutral porphyrin-based dye* ***JDW-M****. Moreover, I studied the dye localization in giant unilamellar vesicles (GUVs) and found that it does not stain the bilayer of GUVs. I found that none of the porphyrin-based dyes localize at the lipid bilayer of GUVs but commercial dye* **FM4-64** *stains the bilayer of GUVs and give good SHG signals.*
8. *I propose optogenetics-based techniques to test voltage sensitivity of* ***AK-1.*** *I also propose structure of a new voltage-sensitive dye,* ***AK-2*** *that should not resist formation of giga-seals by patch-clamp technique. The initial DFT calculations that I performed on the* ***AK-2*** *show it should exhibit good photophysical properties.*

Overall, this chapter unlocks doors for various future studies to investigate the interactions of porphyrin-based dyes with different kinds of cells and cellular organelles.

5.00 Introduction

An electrochromic voltage-sensitive dye must localize in the plasma membrane of live cells to successfully measure the membrane potential. Although, the donor-acceptor porphyrin-based dyes possess high voltage-sensitivity,[1] so far, they have not been used in live cells because they do not localize in the plasma membrane. The dicationic porphyrin-based dye, **JR1-plus** has been reported to stain the plasma membrane of live cells to give SHG signals[2] but the localization lasts for less than a minute as the dye is rapidly internalized by the cell trafficking system. As concluded in Chapters 3 and 4, dicationic TEG-substituted aryl-based porphyrin dye, **HLA-1** does localize in the plasma membrane of HEK 293T cells and rat hippocampal neurons; however, it exhibits poor signal to noise ratio. Although the signal to noise ratio could be improved by increasing the concentration of the dye, it hinders patch-clamp experiments possibly due to precipitation of the dye molecules. The non-collinearity of the amphiphilic axis and the dipolar axis of **HLA-1**, is one of the possible reasons for such poor signal to noise ratio.

I suggested that a porphyrin-based dye that localizes in the plasma membrane and whose amphiphilic and dipolar axis are collinear will give high signal to noise ratio and hence, will be a successful SHG-based voltage-sensitive dye. In this Chapter, I discuss the design and synthesis of such dye. Following, I describe plasma membrane localization studies in live cells including rat hippocampal neurons and mice brain slices. I demonstrate fluorescence and SHG –based multimodal imaging with the new dye. I show that the new dye is capable of sensing voltage change in rat neonatal myocytes. Apart from the porphyrin-based dyes, I also propose the structural design, possible synthetic route, and DFT calculation of a non-porphyrin–based dye, which might possess high SHG efficacy as a voltage-sensitive dye.

5.10 Materials and Methods

5.11 Synthesis and characterization

All the commercial reagents and solvents were procured from Sigma Aldrich unless specified. The chloroform, dimethylformamide, pyridine, tetrahydrofuran, and dimethylsulfoxide were procured from Fisher Scientific, and dichloromethane was procured from Honeywell Riedel-de-Haën. Deuterated solvents were procured from Aldrich. The SX-1 resins for size exclusion chromatography was procured from Bio-Beads® and the Dowex® chloride anion exchange resins were procured from Sigma Aldrich. The Geduran® Si 60 silica gel was used for flash column chromatography. Benchtop centrifuge from Eppendorf was used to wash the final compound **AK-1** with solvents during its purification.

The chemical reactions were performed under inert atmosphere (Ar gas) unless otherwise stated. NMR spectra were acquired on 400 MHz (Bruker AVIIIHD 400) and 500 MHz (Bruker AVII 500, Bruker AVIIIHD 500) spectrometers. Chemical shifts are reported in ppm relative to trimethylsilane (TMS) as internal standard. MALDI-ToF (Waters MALDI micro) spectrometer was used for mass analysis.

5.12 Absorption and fluorescence experiments

The UV-Vis (Perkin Elmer Lambda 20) and fluorescence (Edinburgh Instruments, Spectrofluorometer FS5) measurements were performed in DMF at 25 ºC.

Determination of molar absorption coefficient

For all the compounds, the absorption spectra were measured at three to four different concentrations to measure the molar absorption coefficient, ε. The same protocol as mentioned in Chapter 2 is used here.

Determination of quantum yield

The protocol used for pyropheophorbides as mentioned in Chapter 2 is used to measure the fluorescence quantum yields of the compounds discussed in this chapter. Pyropheophorbide-a methyl ester is used as the reference compound. The fluorescence of the final compound, **AK-1** was measured from 600 nm to 1400 nm to measure the quantum yield. Both the **AK-1** and reference compounds were excited at 500 nm at identical conditions.

5.13 Cell culture experiments

HEK 293T, U-87 MG, and HeLa cells

The HEK 293T, U-87 MG, and HeLa cells were cultured and passaged using the same procedure mentioned for HEK 293T cells in Chapter 3. The cells were plated on custom designed poly-D-lysine coated 50 mm glass bottom dishes from MatTek®. The dyes were imaged in Hank's balanced Salt solution (HBSS) buffer with Ca^{2+} and Mg^{2+} ions. For multimodal imaging experiments, **FM4-64** was procured from Biotium under the tradename SynaptoRed C2. **LysoTracker™ Yellow HCK-123** and rhodamine 123 (**RH123**) were procured from ThermoFisher Scientific.

Cultured rat hippocampal neurons

The rat hippocampal neurons were cultured using the exactly same procedure as mentioned in Chapter 3. The cultured neurons were a kind gift from Prof. Nigel Emptage, Department of Pharmacology, University of Oxford. The neurons were plated on six 50 mm dishes for the imaging experiments.

Mice brain slices

The mice brain slices were a kind gift from Dr. Michael Kohl, Department of Physiology Anatomy and Genetics (DPAG), University of Oxford. A few slices were also kindly provided by the laboratory of Dr. Ed Mann, DPAG, University of Oxford. Dr. Kohl provided the perfusion setup to be installed in the multiphoton microscope for performing the experiments on mice slices.

Postnatal day (P) 14-21 C57BL/6 mice of both sexes were anaesthetised by isoflurane inhalation. The animals were decapitated in accordance with British Home Office regulations. The brain was removed swiftly and stored in ice-cold (0–4 ºC) artificial cerebrospinal fluid (NaCl 126 mM, KCl 3 mM, NaH_2PO_4 1.25 mM, $MgSO_4$ 2 mM, $CaCl_2$ 2 mM, $NaHCO_3$ 26 mM, and glucose 10 mM; pH 7.2–7.4; osmolarity 285–300 mOsm L^{-1}) for approx. 10 min (aCSF). aCSF was continuously bubbled with carbogen gas (95% O_2 and 5% CO_2) for at least 30 min before use. A thin section of dorsal surface was cut with a scapel after separating the hemispheres. The dorsal part of the hemisphere was glued to a microtome pate for cyanoacrylate adhesive. Horizontal slices of entorhinal cortex (300–350 µm thick) were cut with a vibrotome (Leica VT 1000s) in aCSF.

For imaging experiments, the slices were stored in aCSF and bubbled continuously with carbogen using a perfusion setup. For bath delivery, the dye was dissolved in the aCSF, while for intracellular and pressure injection, the dye was dissolved in intracellular solution (prepared as mentioned in Chapter 4) using 0.1% DMSO.

Patch-clamp experiments

For patch-clamp experiments, the same materials and protocol were followed as described in Chapter 4. The amplifier (Multiclamp 700B) and the digitizer (Digidata 1550) were procured from Molecular devices. The pipettes (Harvard Instruments) with 3–7 MΩ resistance were pulled using a Narishige PC-10 pipette puller. The pipettes are connected to pre-amplifier head-stage (CV-7B, Axon Instruments) and adjusted using PatchStar™ micromanipulators from Scientifica®. The cells were incubated in extracellular solution, whose formulation is NaCl (130 mM), KCl (2.5 mM), HEPES (10 mM), glucose (10 mM), $CaCl_2$ (2 mM), $MgCl_2$ (1.3 mM) at pH = 7.4 (adjusted with NaOH) and osmolarity = 304 mOsm. The composition of the intracellular solution filled inside the pipettes is KCl (10 mM), NaCl (5 mM), EGTA (2 mM), K-gluconate (115 mM), HEPES (10 mM) at pH = 7.3 (adjusted with KOH) and osmolarity = 292 mOsm.

Neonatal cardiomyocytes

The plated neonatal myocytes were kindly provided by Dr. Pawel Swietach, DPAG, University of Oxford. The neonatal myocytes were prepared and plated on four 35 mm glass bottom dishes coated with fibronectin.

Postnatal day (P) 1–2 Sprague-Dawley rat pups were sacrificed by neck dislocation followed by exsanguination in accordance with British Home Office regulations. The hearts were separated from the body and stored in ice-cold ADS solution (NaCl 106 mM, KCl 5.3 mM, HEPES 20 mM, glucose 5 mM, $MgSO_4.7H_2O$ 0.4 mM, NaH_2PO_4 0.8 mM; pH 7.4 at 37 ºC). The hearts were cleaned and transferred to a fresh ADS solution. The atria and the associated tissues were removed under the dissection microscope and then the ventricles and remaining hearts were minced finely. The minced pieces were incubated with enzyme mix (containing collagenase at 0.5 mg/mL and pancreatin at 1.25 mg/mL in ADS buffer) and stirred for 5 min at 37 ºC. The supernatant was discarded and 8 mL of enzyme mix was again mixed with minced heart pieces and stirred at 37 ºC for 20 min. The supernatant was collected and mixed with 3 mL of newborn calf serum (NCS) media. The mixture was centrifuged at 1250 rpm for 5 min and pellet was suspended in 3 mL of NCS media after discarding the supernatant. The cells in the NCS media were suspended in 10 mL of supplemented DMEM media (67% DMEM, 17.5% M-199, 10% Horse serum, 5% NCS serum, 1% glutamine, 0.1% penicillin) and incubated for two hours at 37 ºC in a 5% CO_2 incubator. After two h, the cells were pooled, centrifuged at 1250 rpm for 5 min and the pellet was suspended in supplemented DMEM media to appropriate cell density. The cells were plated on the fibronectin coated glass bottom dishes and incubated at 37ºC for 24 h in 5% CO_2 atmosphere. After 24 h (Day 2), the cells were washed with ADS buffer and incubated in supplemented DMEM media containing 0.5% NCS media. Same procedure was followed on Day 3 but the cells were incubated with supplemented DMEM media without any NCS serum.

E. coli

E. coli culture (5 mL) at an optical density of 2 was provided by Dr. Matthias Schiedel (Postdoctoral researcher in group of Dr. Stuart Conway, Department of Chemistry, University Oxford).

5.14 Giant unilamellar vesicles (GUVs)

I prepared cell-sized (10–20 µm) giant unilamellar vesicles by the gel-assisted swelling technique as per literature.[3,4] Briefly, an aqueous solution (200 µL) of polyvinyl alcohol (5 mg/mL) and sucrose (300 mM), was applied on plasma-cleaned glass cover-slips (22 X 22 mm) after which the excess solution was removed by tilting the cover-slip by touching its edge with a wipe. The cover-slip was then dried at 60 ºC for 1 h and then coated with a lipid (DOPC or DPhPC) solution (5 mg/mL in chloroform) using a needle. The lipids were desiccated for 30 min and rehydrated in a GUV growth buffer (200 mM sucrose, 100 mM KCl, 20 mM Tris.HCl; pH 7.5) for 30 min. The GUVs are transferred through a Gilson pipette to the GUV observation buffer (200 mM glucose, 100 mM KCl, 20 mM Tris.HCl; pH 7.5) in a glass bottom dish for imaging.

5.15 Imaging experiments

I performed all the imaging experiments in extracellular (EC) buffer containing NaCl (130 mM), KCl (2.5 mM), HEPES (10 mM), glucose (10 mM), $CaCl_2$ (2 mM), $MgCl_2$ (1.3 mM) at pH = 7.4 (adjusted with NaOH) and osmolarity = 304 mOsm. The imaging experiments for the brain slices were performed in aCSF solution. The microscope specifications are the same as described in Chapter 3. Briefly, the multiphoton microscope (FV1200MPE) from Olympus equipped with a MaiTai® eHP DeepSee™ femtosecond pulsed laser (70 fs pulse width, 80 MHz repetition rate, continuously tunable between 690–1040 nm) from Spectra-Physics. The light was focused using a 2 mm working distance 25X multiphoton objective (XLPLN25XWMP2). For TPEF, the reflected light was passed through a 750 nm short pass filter before being passed through a 540 nm long pass (LP) filter or a dichroic mirror separating the light to pass through green (495 nm–540 nm) and red (570 nm–625 nm) band pass filters and then was detected by PMT detectors (Hamamatsu R3896 for green and Hamamatsu IR sensitive PMT-R10699 for red). For SHG, the light in the transmitted direction was collected through a 0.9 NA air-based condenser and then passed through a band-pass filter (420±15 nm) before being detected through a PMT detector (Hamamatsu R3896). All the images were acquired in analog-integration mode unless otherwise specified. The images were processed using Olympus Fluoview software and Imaris x64 7.7 software.

For membrane potential imaging in neonatal myocytes, on Day 4, the cells were incubated with **AK-1** dye in the EC buffer and imaged under the microscope. For membrane potential experiments, a small region of interest (14 X 12 pixels) of the plasma membrane was chosen and scanned at a rate of 200 μs/pixel in photon-counting mode for monitoring change in SHG intensity. High laser power of 15 mW at 870 nm is chosen because the imaging is performed in photon-counting mode. In photon-counting mode, the signal to noise ratio for SHG signals is high but the overall intensity is reduced significantly than analog-integration mode. The imaging experiment was performed at room temperature. Since neonatal myocytes contract (and hence generates action potential), the region of interest is not stationary. For monitoring the change in SHG intensity, a pixel was chosen and its oscillatory motion was tracked manually between two points. The change in SHG intensities at both the points were recorded and averaged to determine the change on intensity of the pixel in response to cell contraction.

5.20 Molecular Design

JR1-plus exhibit high SHG efficiency;[1,2] however, they do not localize in the plasma membrane of live cells despite possessing a dicationic group. Conventional styryl-based voltage-sensitive plasma membrane dyes such as **ASP**[5], **FM4-64**[6], and **di-4-ANEPPS**[7] are either monocationic or dicationic. The length of **ASP** dye is approximately 1.2 nm, while that of **FM4-64** is 2.1 nm (Figure 1). Because the length of **FM4-64** is almost twice the one of **ASP**, **FM4-64** has two cationic groups as compared to one cationic group for **ASP**. This means that for a dye to localize in the plasma membrane of cells, there must be a balance between its hydrophobicity and hydrophilicity. The length of **JR1-plus** is approximately 4.0 nm, which is almost twice the length of **FM4-64** but it is still dicationic. Hence, **JR1-plus** does not stain the plasma membrane of live cells. Interestingly, **HLA-1** with the same number of cationic groups as **JR1-plus**, localizes in the plasma membranes of live cells. Apart from dicationic groups, it possesses hydrophilic triethylene glycol (TEG) groups (Figure 1). The presence of the TEG groups provides an additional of hydrophilicity to the molecule thus, contributing towards its overall amphiphilicity. This means that **JR1-plus** does not localize in the plasma membrane of cells because its hydrophobicity and hydrophilicity are unbalanced. **HLA-1** gives poor SHG-based signal to noise ratio because it has low β_{zzz} as compared to **JR1-plus**,[8] and its amphiphilic and dipolar axes are not collinear.

A porphyrin-based dye with similar structure and β_{zzz} as **JR1-plus** but with an extra degree of hydrophilicity would stain the plasma membrane of cells and give high signal to noise ratio during imaging. I designed a new dye, **AK-1** (Figure 1) with enhanced amphiphilicity compared to **JR1-plus**. The new dye, **AK-1** has a similar donor-acceptor–based design, where a strong electron donating group, dibutyl aniline is connected to electron-deficient quaternarized pyridinium moiety via a conjugated free-base porphyrin. To keep the β_{zzz} value of the new dye in the range of **JR1-plus** and ensure collinearity between its amphiphilic and dipolar axes, I did not attach TEG-substituted aryl groups, which were used in **HLA-1**. However, to increase the overall amphiphilicity, I increase the number of cationic groups from two to three. The two cations in the **JR1-plus/HLA-1** are separated by a chain of five methylene groups but in the new dye, I separate any two cations by a chain of only three methylene groups. Reeve *et al.* could not form a giga-seal (high resistance seal during patch-clamp experiment as discussed in Chapter 4) while attempting to deliver **JR1-plus** in the mice brain slices, and this was attributed to the presence of greasy octyl chains attached to aniline nitrogen.[8] To reduce the greasiness, the electron-donor group in the new dye, **AK-1** is functionalized with butyl chains instead of octyl chains. It must be noted that reducing the chain length makes it difficult to work with the overall planar molecule because of decreased solubility in organic solvents.

Applying all the above-mentioned changes, I present a new tricationic porphyrin-based dye, **AK-1**. The length of the tricationic dye, **AK-1** is smaller than **JR1-plus** dye, thus, increasing its chances of localizing in the plasma membrane of cells.

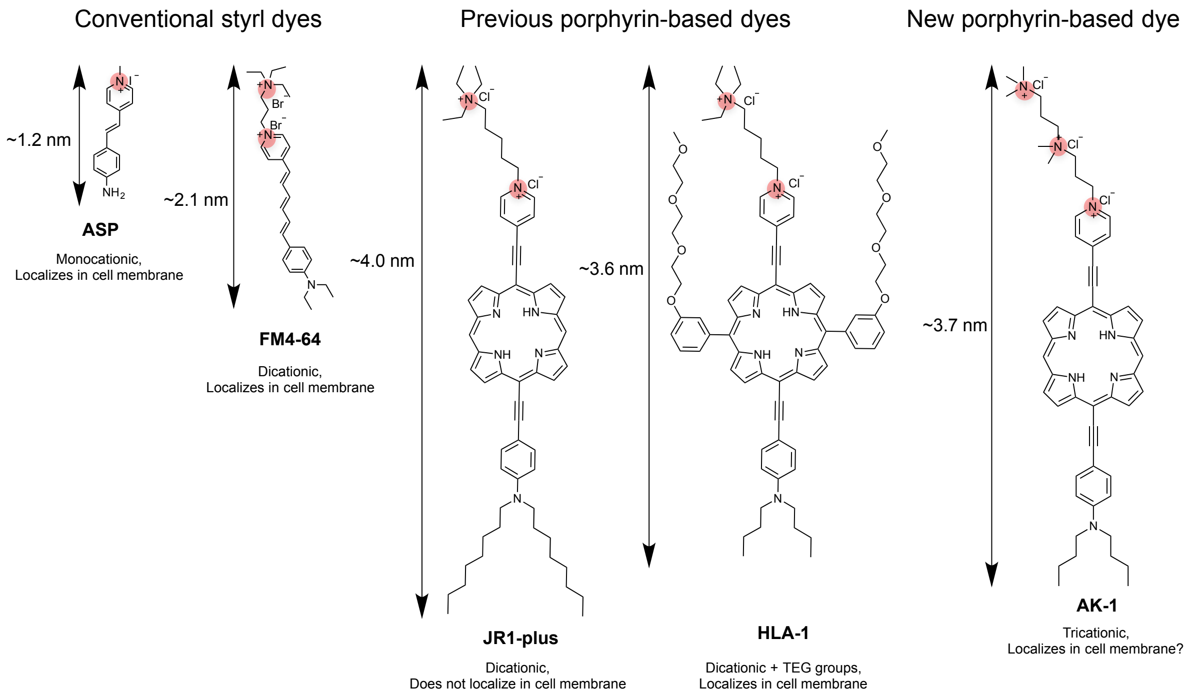

Figure 1: Comparison of the lengths of chemical structures and number of cationic groups of dyes with their abilities to localize in the plasma membrane of cells. **ASP**, one of the earliest plasma membrane voltage-sensitive dyes has a single cationic group with a length of approximately 1.2 nm. The length of **FM4-64** is twice the length of **ASP** but it has two cationic groups to be able to localize in the plasma membrane of cells. Porphyrin-based dye, **JR1-plus** being almost twice the size of **FM4-64** does not localize in the plasma membrane of live cells with two cationic groups. **HLA-1** with two cationic groups and two TEG groups, does localize in the plasma membrane of live cells due to enhanced amphiphilicity. **AK-1**, the new tricationic porphyrin-based dye has similar size to **HLA-1** but does not possess TEG-substituted aryl groups for increased SHG signal to noise ratio. The tricationic dye, **AK-1** with enhanced amphiphilicity compared to **JR1-plus** hopes to localize in the plasma membrane of live cells.

5.30 Results and Discussion

5.31 Synthesis

Retrosynthetic analysis

I considered two routes for the synthesis of **AK-1,** (X and Y Scheme 1). For either of the two routes, compound **2** is the starting porphyrin-containing synthon. Although, **2** is a novel compound, its structure is similar to the precursor of **JR1-plus**. The difference is that, in **2**, butyl chains are attached to the electron donating aniline instead of octyl chains.

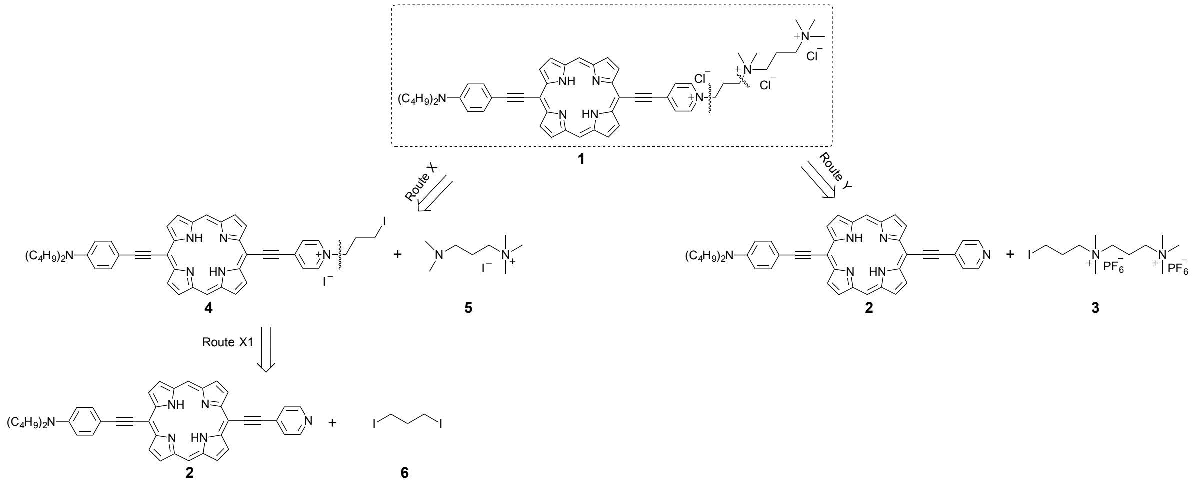

Scheme 1: Retrosynthetic analysis of **AK-1**. Route X is to first quaternarize **2** with diiodopropane to form **4** and then synthesizing **1**. Route Y is to directly quaternarize **2** to form **1** in a single step.

Synthesis of porphyrin 2

To synthesize **2**, I explored two different routes (Scheme 2). First route is to insert zinc metal into **8** and carry the reaction forward with metalated compound to remove zinc in the end. The advantage of this route is that zinc metalated porphyrins are relatively easier to work with than free-base porphyrins due to their enhanced solubility. In my experience, although the solubility was enhanced, the yields of intermediate reactions were low. The second route is to work on free-base porphyrin throughout. Free-base porphyrins are less soluble in organic solvents than zinc-metalated porphyrins but this synthetic route has two steps (insertion and deletion of zinc) less than zinc-metalated route. All compounds are characterized by NMR spectroscopy and mass spectrometry. Before following any of the two routes, compound **8** was synthesized from dipyromethane and trihexylsilane-propynal in presence of an oxidizing agent 2,3-dichloro-5,6-dicyano-*p*-benzoquinone (DDQ).[2]

First route: As shown in Scheme 2, zinc is inserted into **8** to synthesize **12**, which is then statistically mono-deprotected using tertabutylammoniumfluoride (TBAF) in the presence of ethanol stabilized chloroform and DCM to form **13**. Sonogashira coupling was performed on **13** to form donor-group decorated porphyrin **14**. Use of freshly recrystallized palladium catalyst and freshly distilled diisopropylamine increased the reaction yield compared to similar reactions performed previously to form **14**.[2,9] Compound **15** was formed by the full deprotection of **14** and then Sonogashira coupling was performed to form **16**. Zinc removal to form **2** did prove to be challenging despite of several attempts and the final compound could not be purified fully (^{1}H-NMR spectrum at Figure 26). Using trifluoroacetic acid (TFA) for zinc removal caused partial decomposition of porphyrin decreasing the yield to approx. 20%. Since **2** is synthesized in 10 steps, low yielding reactions required optimization.

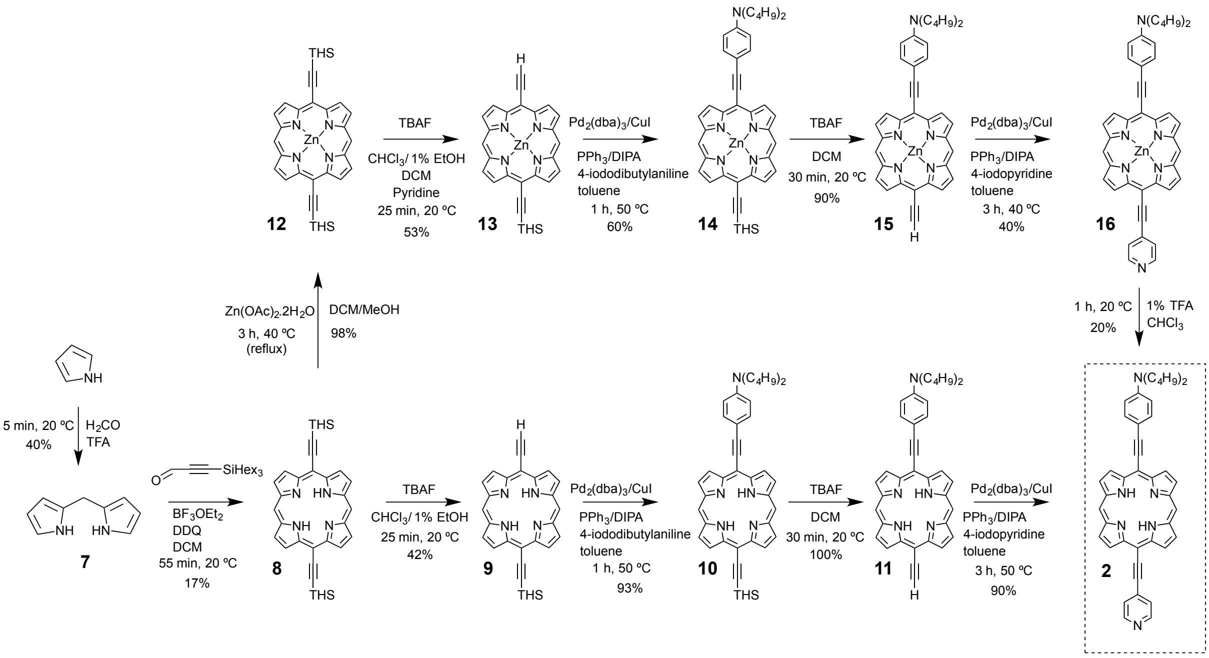

Scheme 2: Synthesis of porphyrin **2** through two different routes.

Second route: The biggest advantage of the second route is the lack of the low yielding zinc removal step. For statistical mono-deprotection to form **9**, instead of using a mixture of DCM and chloroform solvents, I used pure chloroform added with 1% dry ethanol to increase the reaction time (ethanol forms hydrogen bonding with TBAF) and hence control it to prevent full deprotection. On working with free-base porphyrin, the yields of Sonogashira coupling reactions increased significantly. It must be noted that freshly recrystallized palladium catalyst and freshly distilled diisopropylamine used in the Sonogashira coupling reactions were important for high yields. Using the free-base route, pure porphyrin **2** was isolated (^{1}H-NMR spectrum at Figure 27). The total yield of **2** starting from **8** using zinc metalated route is approximately 2.5%, while it is approximately 35% using free-base porphyrin route, thus, this route was selected for further upscale reactions.

Synthesis of hydrophilic head groups and porphyrin 1 (AK-1)

After synthesizing **2**, I embarked on synthesizing **1**. Attaching three cations groups has been the biggest challenge in the synthesis. Out of the two routes shown in Scheme 1, initially, I followed Route X, similarly to the literature-reported synthesis of multicationic compounds.[10] Compound **4** was synthesized by quaternarization of pyridine in **2**; however, synthesis of **1** from **4** exhibited significant challenges. The reaction was attempted by stirring the reagents in DMF at 80 ºC; however, despite several attempts, I was not able to form **1**. The reaction never proceeded and the starting material was recovered. At elevated temperatures, decomposition took place. After unsuccessful attempts of forming **1** from **4**, I pursued Route Y; i.e. single step quaternarization of pyridine in **2**.

To form **1** by Route Y, first, I synthesized the dicationic diamino moiety **20** according to the synthetic route shown in Scheme 3. Compound **17** was methylated to form **18** according to the literature procedure.[11] Compound **18** was reacted with diiodopropane to form the novel compound **19**. To enhance solubility in organic solvents, iodide anions of **19** were exchanged with hexafluorophosphate anions to form **20**.

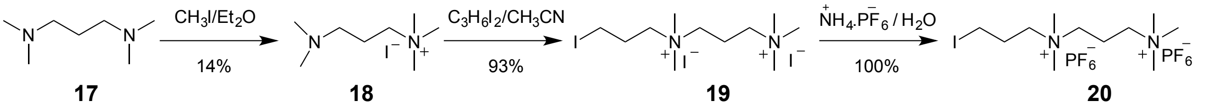

Scheme 3: Synthesis of hexafluorophosphate-based dicationic moiety and its intermediates.

I attempted to form **1** by quaternarization of pyridine in **2** with **20** in DMF because DMF has been widely used for similar reactions and it is a good solvent for dissolving of the starting materials;[2,9,10,12]. At temperatures below 90 ºC, no reaction took place and at elevated temperatures, the reagents decomposed (Scheme 4). Apart from DMF, I tested other solvents, such as 2-pentanone and 2-methoxyethanol but they were unsuccessful. Dr. Ismael Lopéz Duarte, a previous postdoctoral researcher in the Anderson group, successfully synthesized **JR1-plus** using 2-pentanone as the solvent at 85 ºC but it did not work to form tricationic **AK-1**. Since at elevated temperatures (>100 ºC), DMF decomposes in the presence of **2** and **20**, I changed the solvent to dimethylacetamide (DMA), which is more stable at higher temperatures (Scheme 4). The reaction proceeded in DMA at 115 ºC to form **21** (Scheme 4) successfully. The anions of **21** were exchanged to chloride anions using Dowex® 1X8 chloride resins to form **1 (AK-1)**.

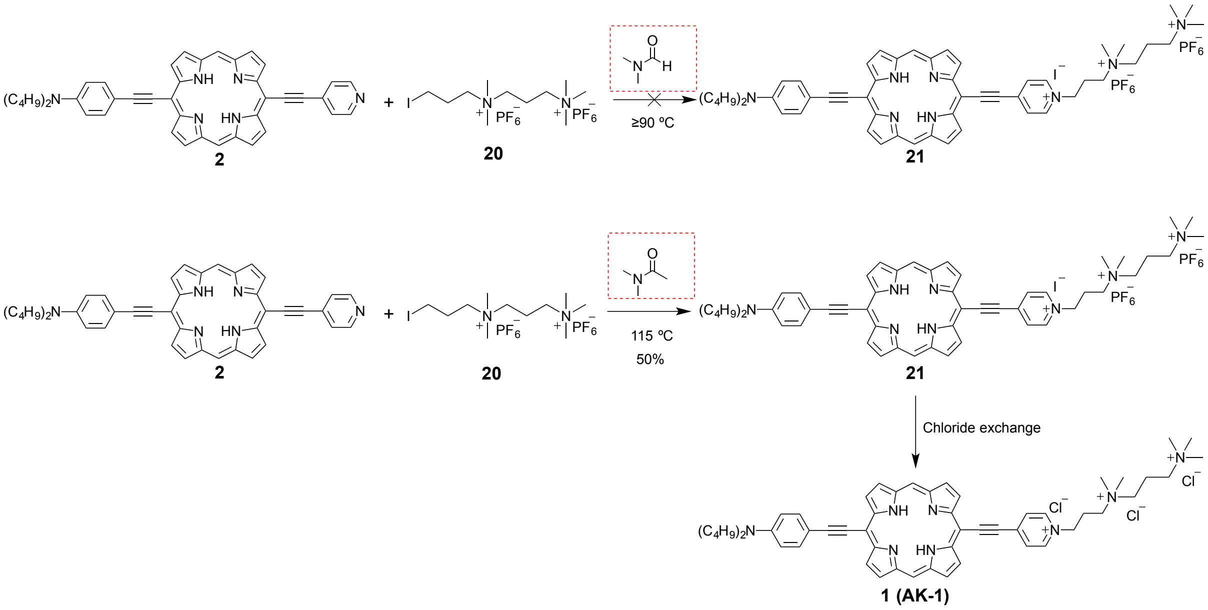

Scheme 4: Synthesis of **21** by quaternarization of pyridine in **2** with **20** in DMA (red box in bottom reaction) at 115 ºC. The same reaction did not take place in DMF (red box in top reaction). Compound **21** was converted to **1** by chloride anion exchange chromatography.

The NMR experiments of **1** were performed in d$_6$-DMSO. At room temperature, the water peak (because of DMSO and hygroscopic nature of the compound) is visible, hiding the peak of the charged alkyl groups. Prof. Timothy Claridge (Department of Chemistry, University of Oxford) successfully performed the ^{1}H-NMR at 50 ºC to move the water peak without moving the peaks of the compound (Figure 28). The chloride compound **1** was not particularly visible in MALDI mass spectrometry. However, at high laser power, a peak of **21** was visible in the sample of **1** (Figure 30) suggesting that there are traces of **21** in **1**.

5.32 Linear optical properties

The absorption and emission spectra of **AK-1** are similar to those of **JR1-plus** because there is no change in the π-conjugation of the whole molecule (Figure 2). The decrease in length of alkyl chains in the donor group from octyl to butyl and the increase of a cationic group did affect the molar absorption coefficients. Their emission spectra profiles are similar too. The absorption and emission spectra of **HLA-1** are slightly red shifted due to presence of TEG-substituted aryl groups but their shapes are similar to the spectra of **AK-1** and **JR1-plus**. It must be noted that the fluorescence spectra (acquired by exciting the molecules at their Soret bands) of all the three compounds are blue-shifted from the Q2 band. Despite taking measurements in different solvents, such as DMSO, mixture of acetic acid and DMSO, and mixture of tetrabutylammoniumhexafluorophosphate salt in DMF, I observed the similar blue-shifted spectra, which means that it is unlikely that the blue-shift is due to solvent impurity or aggregation. A similar kind of blue-shift is present in all the charged donor-porphyrin-acceptor compounds prepared in the Anderson group.[8]

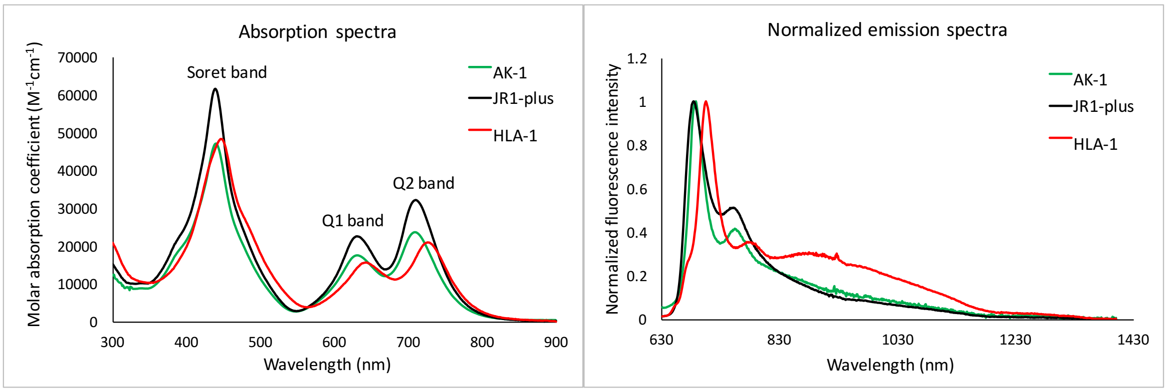

Figure 2: Comparison of absorption and emission spectra (in DMF at 25 ºC) of **AK-1**, **JR1-plus**, and **HLA-1**. Both the absorption and emission spectra of **AK-1** is similar to **JR1-plus** because both these molecules have the same conjugated π-system. The spectra of **HLA-1** is slightly red-shifted due to difference between π-conjugation because of presence of aryl groups.

The fluorescence quantum yield of **AK-1** is extremely low at a value of 0.0033 in DMF (measured through the spectrum recorded by exciting the compound at the Soret band). The fluorescence quantum yields of **JR1-plus** and **HLA-1** too are low at values of 0.0058 and 0.0011 respectively as measured by Dr. James Reeve and Dr. Jan Fleichhauer from the Anderson group.[8] Low quantum yields of these compounds mean that even a trace of fluorescent impurity could dominate the spectra of the compound. Low fluorescence quantum yield will be an advantage for SHG imaging due to low phototoxicity.

I measured the emission of the compounds at different wavelengths and found that the emission spectra changes around the Q1 band; data shown only for **AK-1** (Figure 3). The excitation and absorption spectra too do not overlap perfectly suggesting that there might be some impurity or different rotational conformations of the compound. However, the change in excitation and emission spectra is similar for all the compounds, which means that if there is an impurity then it is the same or similar impurity or they have same type of rotational conformations.

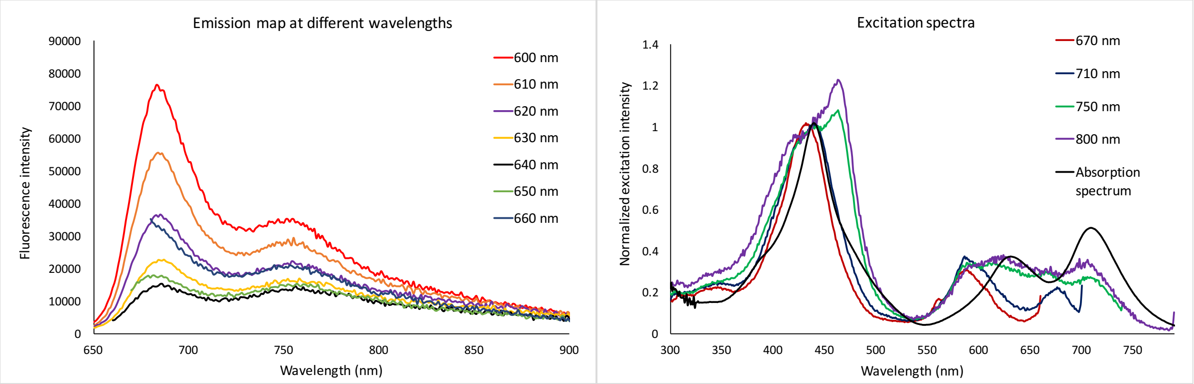

Figure 3: Emission and excitation spectra of **AK-1** at various wavelengths. In the emission spectra map, the spectra at 600 nm and 640 nm do not match. The excitation spectra do not overlap with the absorption spectra. The Q2 band of absorption spectra matches the Q2 band of excitation spectra when the compound was measured at 750 nm or 800 nm, while the Soret band matches when the measurement was done at 670 nm or 710 nm.

Since the **AK-1**, **JR1-plus**, and **HLA-1** are synthesized by three different scientists using different batches of reagents and synthetic routes, it is unlikely that all of them will have same impurity but the linear optical measurements indicate that they have same distribution of species. ^{1}H-NMR spectra of **AK-1** (Figures 28 and 29), **JR1-plus**,[2,8] and **HLA-1**[8] suggest non-aggregated compounds without visible impurity; and since the fluorescence quantum yield of **AK-1** is extremely low, it can be assumed that it is pure enough for cell-based imaging experiments.

5.33 Imaging in live mammalian cells

I performed imaging using **AK-1** *in vitro* in five different types of mammalian cells, HEK 293T cells, U-87 MG cells, HeLa cells, primary rat neonatal myocytes, and primary rat hippocampal neurons. HEK 293T (human embryonic kidney) and HeLa (cervical cancer cells derived from a cancer patient, Henrietta Lacks in 1951) cells were chosen because these cells are robust cell lines and are easy to handle. U-87 MG (Uppsala 87 Malignant Glioma) cells are human neuronal glioblastoma cells and were chosen to test if the dye behaves uniformly across various cell lines. Primary neonatal myocytes and hippocampal neurons were chosen because the final goal of the voltage-sensitive dye, **AK-1** is to test membrane potential in these types of cells.

The dye localized in the plasma membrane of all these types of cells and give bright fluorescence and SHG signals along with some internalization to give intracellular fluorescence. These experiments confirmed that a balance between hydrophobicity and hydrophilicity of organic dyes (as discussed at the beginning of this Chapter) is required to achieve plasma membrane localization. I observed that the **AK-1** concentration should be around 20 μM to give good SHG signal at less than 2–5 mW laser power. Less laser power is important to avoid phototoxicity and photodamage. The cells give SHG signal from the plasma membrane even after two hours of incubation. The images shown in this chapter are taken after 5–10 min (unless specified) of incubation in HBSS buffer at room conditions. It is worth noting that the images are not digitally enhanced unless otherwise specified.

5.33.1 HEK 293T cells

In HEK 293T cells, 5 μM concentration of dye gave good SHG signal at laser powers higher than 40 mW (causing photobleaching), while 20 μM of dye gave good SHG signal at a laser power of 3 mW (Figure 4). This result shows that to get significant SHG signal at low laser powers, a concentration of 20 μM is required. The SHG from the cells with 20 μM of dyes is visible only from the periphery of the cluster of cells and not from the plasma membrane of individual cells possibly because the dye molecules from any two cells touching each other are in centrosymmetric arrangements.

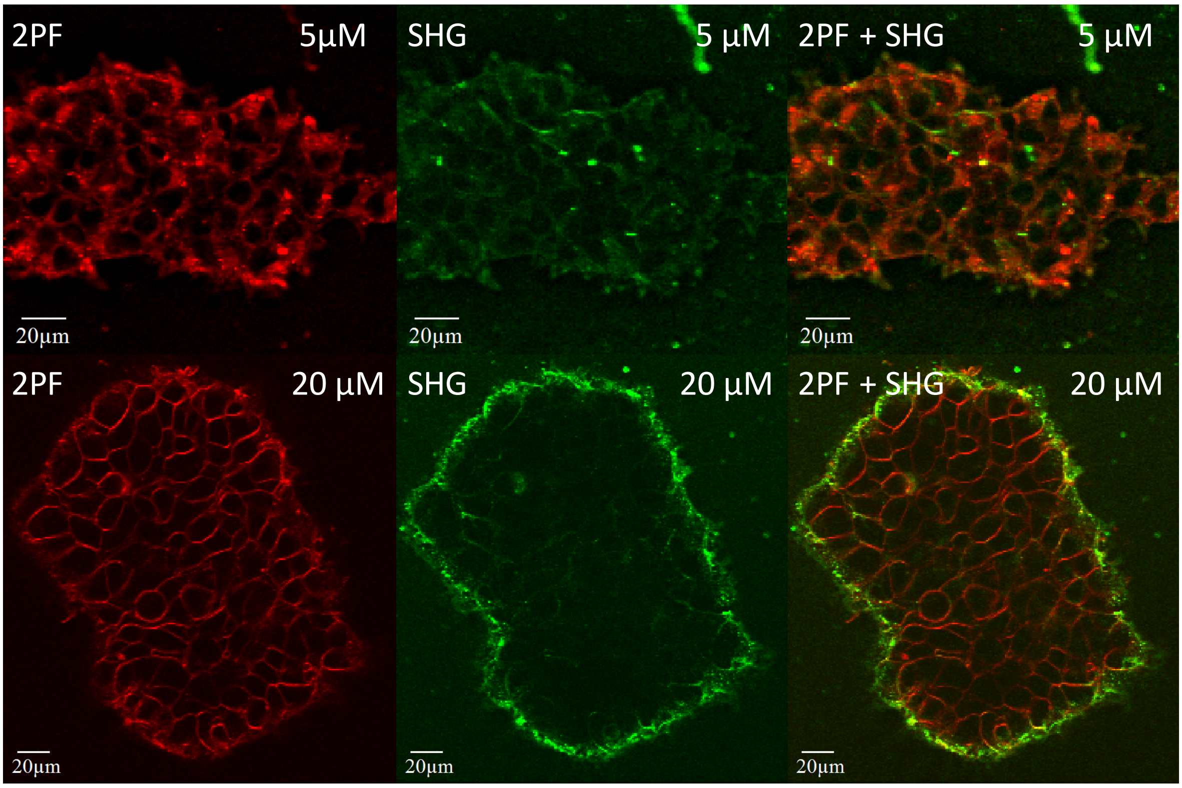

Figure 4: Two-photon fluorescence (2PF) and second harmonic generation (SHG) signals from HEK 293T cells incubated with 5 μM and 20 μM concentrations of **AK-1**. At 5 μM, the SHG signal (digitally enhanced) is visible at around 40 mW of laser power while at 20 μM, the SHG signal (no digital enhancement) is visible at as low as 3 mW laser power. The SHG from the cells with 20 μM of dyes is visible only from the periphery of the cluster of cells possibly because the dye molecules are in centrosymmetric arrangements. λ_{ext} = 870 nm. Scale bar = 20 μm.

I compared **AK-1** and **HLA-1** in HEK 293T cells under identical conditions (same laser power, pixel dwell time, and dye concentration) and found that **AK-1** gives better SHG and TPEF signals than **HLA-1** further confirming that **HLA-1** possibly orients in a skewed arranged in the plasma membrane to give low SHG signal (Figure 5). Apart from skewed orientation, the TEG-substituted aryl groups of **HLA-1** could be affecting the uptake of the dyes due to their interaction with the hydrophilic tails of the lipid bilayer (Figure 5). This consolidates the fact the rod-like structure of **AK-1** is more efficient for localization in amphiphilic cell membrane than **HLA-1** (Figure 5).

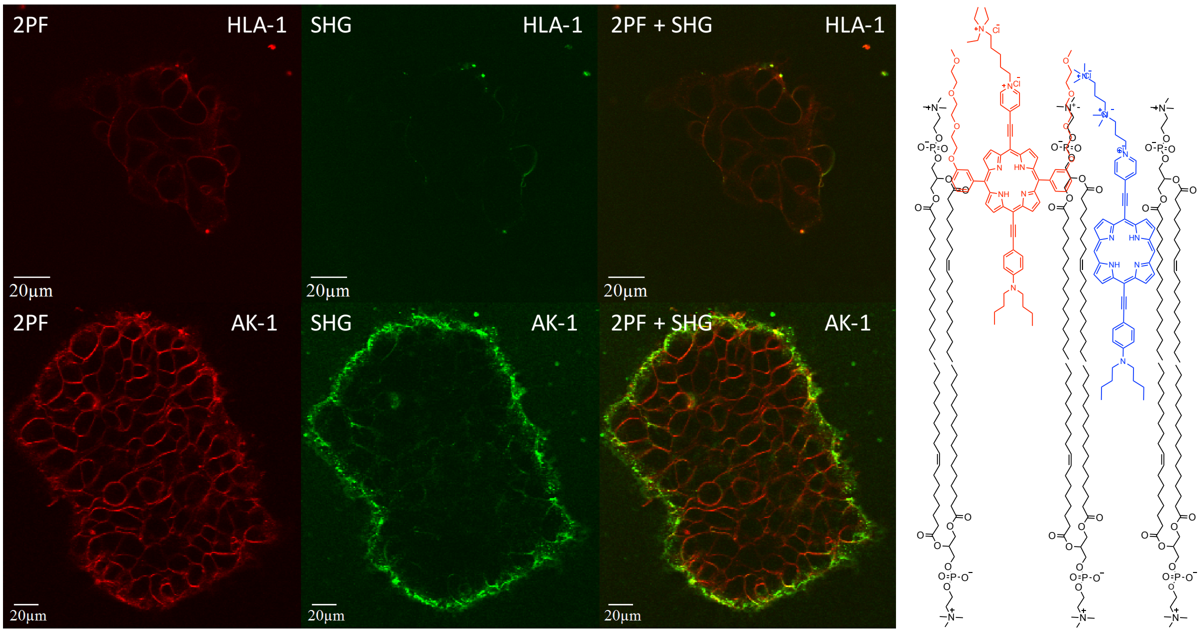

Figure 5: Imaging of **HLA-1** and **AK-1** in HEK 293T cells under identical conditions. **AK-1** gave substantially better SHG signal than **HLA-1**, which could be due to skewed orientation of **HLA-1** dye in plasma membrane. **HLA-1** gives less fluorescence than **AK-1** suggesting that the cellular uptake of the dyes might be different. λ_{ext} = 870 nm, laser power = 3 mW, scale bar = 20 µm. Depiction of uptake of **HLA-1** (red) and **AK-1** (blue) by the lipid bilayer (not simulated using molecular dynamics).

5.33.2 U-87 MG cells and HeLa cells

In U-87 MG cells and HeLa cells too, **AK-1** (10 µM) gave considerable SHG signal at high laser powers of more than ≥10 mW (Figure 6) like in HEK 293T cells. To get a clear view, the signals were digital enhancement (Figure 7). High laser powers (≥10 mW) from a femtosecond pulsed laser causes significant photodamage to the cells after 2–3 min of illumination and so to get clear signals, I increased the concentration of the dye.

I captured clear fluorescence and SHG images at low laser power without any digital enhancement by increasing the dye concentration to 25 µM in U-87 MG cells (Figure 8). No imaging was done in HeLa cells at higher concentrations.

The concentration-based studies performed on HEK 293T cells, U-87 MG cells, and HeLa cells prove that to get an optimal SHG signal at low laser powers (<5 mW), the concentration of the dye should be at least 20 µM. After performing the concentration-based studies, I studied the effect of the dyes on cells during continuous exposure to the laser.

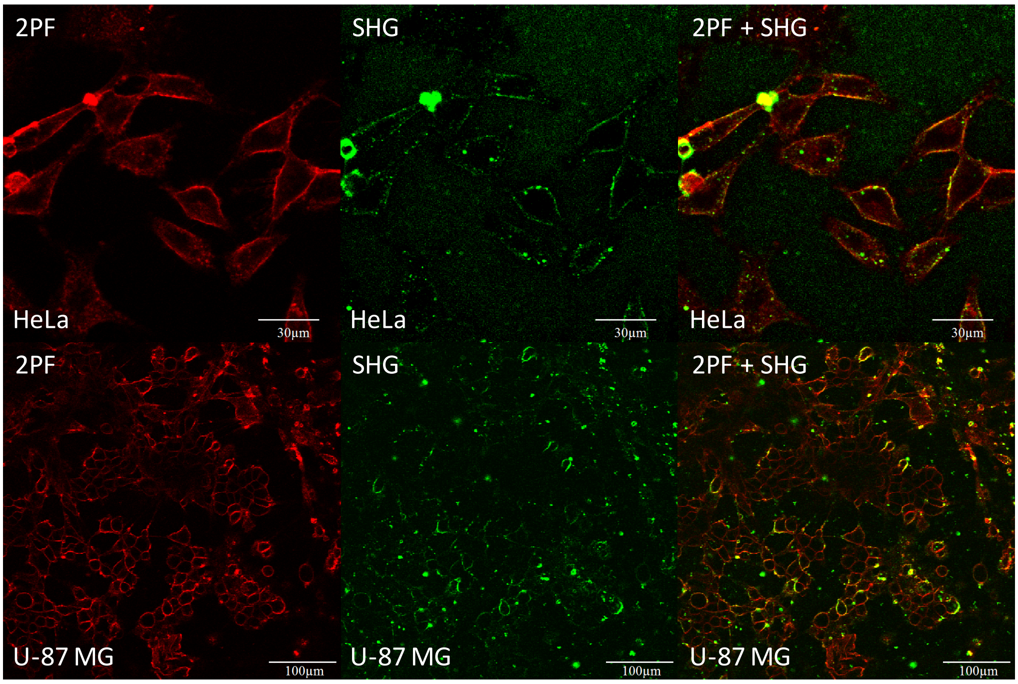

Figure 6: HeLa cells and U-87 MG cells incubated with 10 μM of **AK-1** at more than 10 mW laser powers. The images are digitally enhanced for clear 2PF and SHG signals. $\lambda_{ext} = 870$ nm, scale bar = 30 μm (HeLa cells), 100 μm (U-87 MG cells).

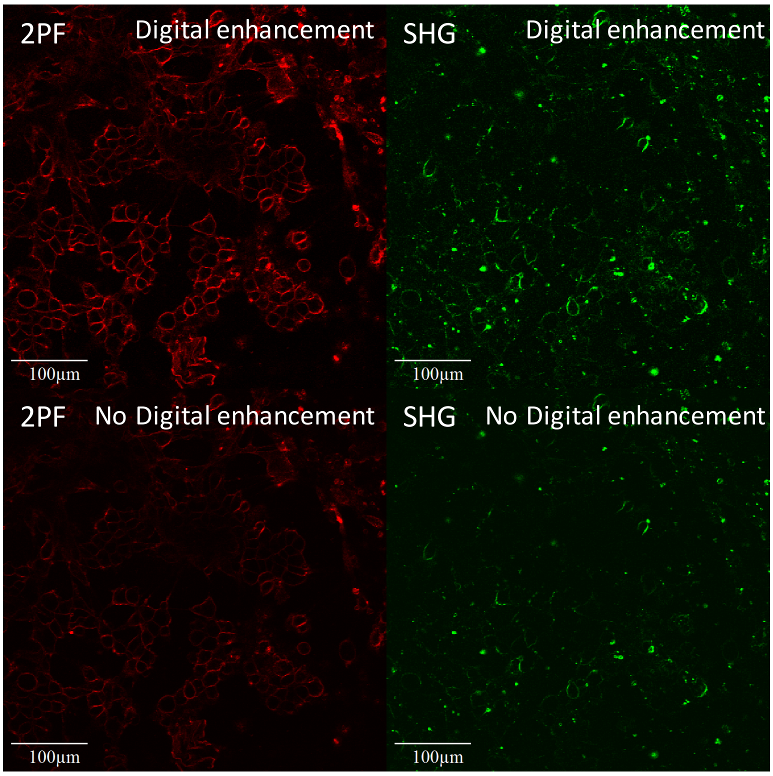

Figure 7: Digitally enhanced and non-enhanced images of U-87 MG cells incubated with 10 μM of **AK-1**. Even at more than 10 mW of laser power, digital enhancement is required to acquire clear fluorescence and SHG signals. $\lambda_{ext} = 870$ nm, scale bar = 100 μm.

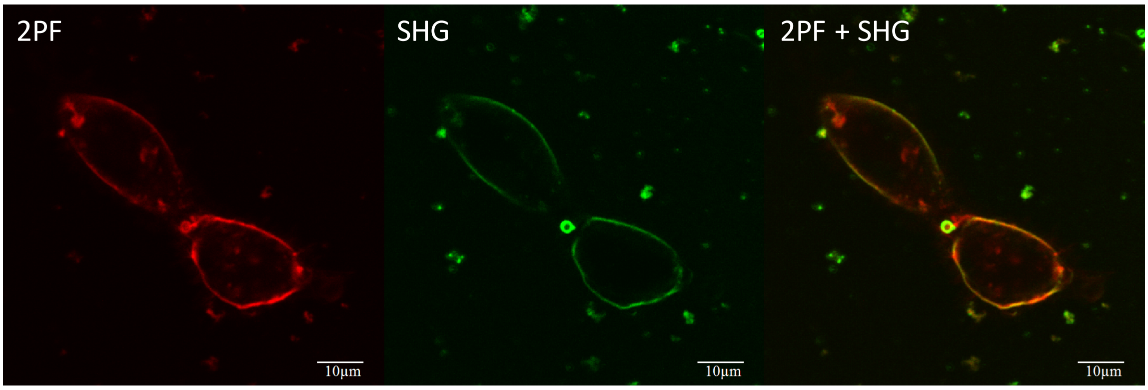

Figure 8: U87-MG cells incubated with 25 μM of **AK-1**. Significant amount of SHG visible at around 5 mW of laser power without any digital enhancement. λ_{ext} = 870 nm, scale bar = 10 μm.

After illuminating the cells with 5 mW laser power for 15 min continuously, the morphology of the cells started to change due to phototoxicity and photodamage. In the process, the fluorescence and SHG signals from the plasma membrane are found to be gradually enhanced (Figure 9). The reasons for the increase of fluorescence and SHG signals can be two-fold. As observed for **JR1-plus** in Chapter 3 and for previously reported dyes,[13] when mammalian cells becomes unhealthy, the dyes internalized by the cells are flushed out by organelles (*via* exocytosis) and dye molecules get localized in the plasma membrane. Hence, the total number of dyes in the plasma membrane increase to give stronger fluorescence and SHG signals. Another reason could be that when cells become unhealthy, the organization of lipids in membrane changes substantially leading to death/removal of transmembrane organelles allowing more dye molecules to compartmentalize in the plasma membrane to give brighter signals. It is not clear whether the cells here are dying only due to a necrosis-based event (photodamage and phototoxicity) or apoptosis, or combination of both. I observed similar behavior in all the cells I used to study **AK-1** dye. Previously, various kinds of fluorescence-based probes have been designed to study cellular apoptosis, which work due to a shift in the fluorescence spectra on trigger of apoptosis-based events in the cells.[14–16] In this case, it is unlikely that the fluorescence spectrum of **AK-1** is changing because fluorescence filter used in the microscope detects all the light above 540 nm. Since **AK-1** emits light above 630 nm, it is not possible to measure the electrochromic effect of the dye by two-photon excited fluorescence.

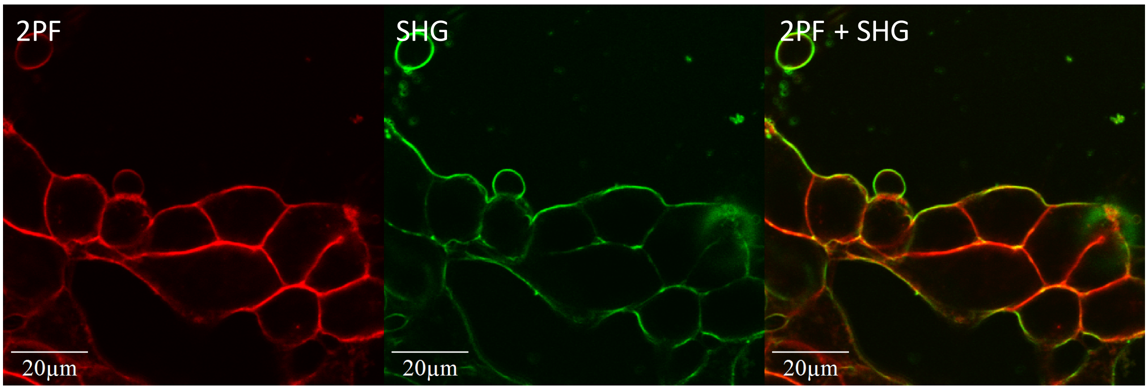

Figure 9: Bright fluorescence and SHG signals from U-87 MG cells after illumination with ~5 mW laser power for around 15 min. λ_{ext} = 870 nm, Dye concentration = 25 μM, scale bar = 20 μm.

5.33.3 Cultured rat hippocampal neurons

After successfully studying the plasma membrane localization of **AK-1** at various concentrations at low laser power in immortal cells, I tested the localization of the dyes in cultured primary rat hippocampal neurons since the dye is primarily designed to test the membrane potential of neurons. The dye localized in the plasma membrane of the neurons to give fluorescence and SHG signals at laser power of less than 1 mW (Figure 10); however, the concentration of the dye was increased to 40 μM. I increased the dye concentration so that I could image cells with high signal to noise ratio for longer times at the least possible laser power to avoid photodamage.

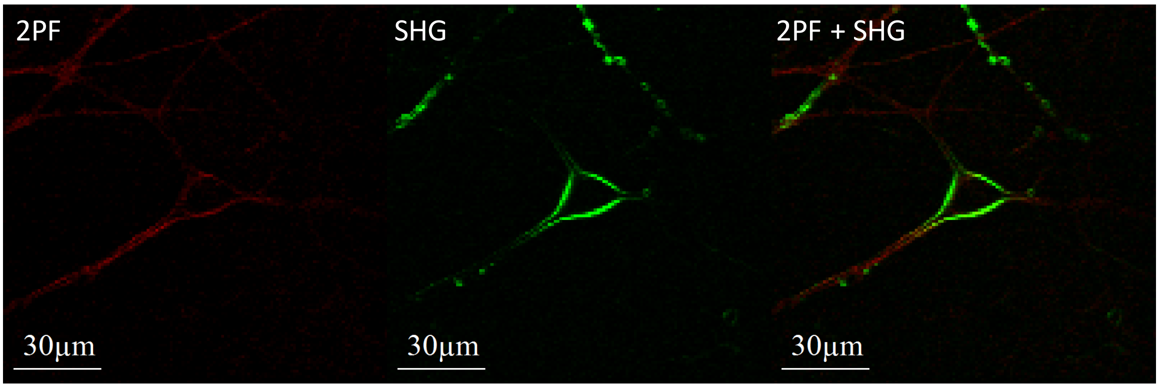

Figure 10: Fluorescence and SHG signal from plasma membrane of cultured hippocampal neurons. Both fluorescence and SHG signals can be seen from the soma as well as axons and dendrites of the neurons. λ_{ext} = 870 nm, Laser power = <1mW, scale bar = 30 μm.

5.33.4 Mice brain slices

Measuring membrane potential of neurons in thick brain slices (>250 μm) is of interest because in slices, the neurons remain intact with their inherent properties. Conventionally, the patch-clamp technique is widely used to measure membrane potential in thick slices; however, it allows measurement of only a few neurons out of millions. Nonlinear voltage-sensitive optical dyes that can measure voltage sensitivity deep inside thick slices will elucidate unknown information about the neuronal circuitry. Only a few voltage-sensitive dyes have been shown to measure action potential in thick brain slices.[6,17,18] Due to nonlinear characteristics and good plasma membrane localization efficiency of **AK-1,** I tested its localization *ex vivo* in mice brain slices applying three different delivery techniques, bath delivery, intracellular delivery through a pipette, and pressure injection into the slice *via* pipette. Slices can tolerate more laser power than *in vitro* cell cultures because in slices, the neuronal cells are located deep inside and protected by robust tissue and blood vessels. Here, I used various laser powers up to 10 mW without visible photodamage or phototoxicity.

Bath delivery

Initially, 8 μM of dye was delivered by dissolving the dye in perfusion chamber of the slices using 0.1% DMSO; however, no substantial signal was observed at this low concentration. The concentration was increased to 25 μM and the slices were reimaged for florescence and SHG signals. Fluorescence signals were visible for the plasma membrane of the soma of neurons as well as from dendrites and axons; however, no SHG was visible for the plasma membrane of the soma. Significant SHG signal was seen from small lumps which could be blood vessels or part of the tissue in the slices (Figure 11). The reason for lack of SHG could be that the dyes did not orient non-centrosymmetrically in the plasma membrane. As a control, localization of commercial dye, **FM4-64** was studied using bath delivery. Surprisingly, **FM4-64** stained everything in the slice including blood vessels, water bubbles, and the whole tissue making it almost impossible for the neurons to be distinguished (Figure 12). Despite repeated attempts, no change in the results was observed for both **FM4-64** and **AK-1**.

Although **AK-1** selectively stains the plasma membrane of the neurons by bath delivery unlike **FM4-64**, lack of SHG signals makes it unsuitable to be used as a SHG-based voltage-sensitive dye meant for bath delivery application. The background fluorescence observed in the case of **FM4-64** could be removed by washing the slices with fresh buffer as reported previously for styryl dyes.[19,20] Dombeck *et al* reported the voltage sensitivity of **FM4-64** in slices;[6,17] however, they delivered the dye only through pressure injection or intracellular delivery. My personal communication with Dr. Daniel Dombeck, who is the lead author of the paper, revealed that they never managed to get SHG from the plasma membrane of neurons in slices by bath delivery.

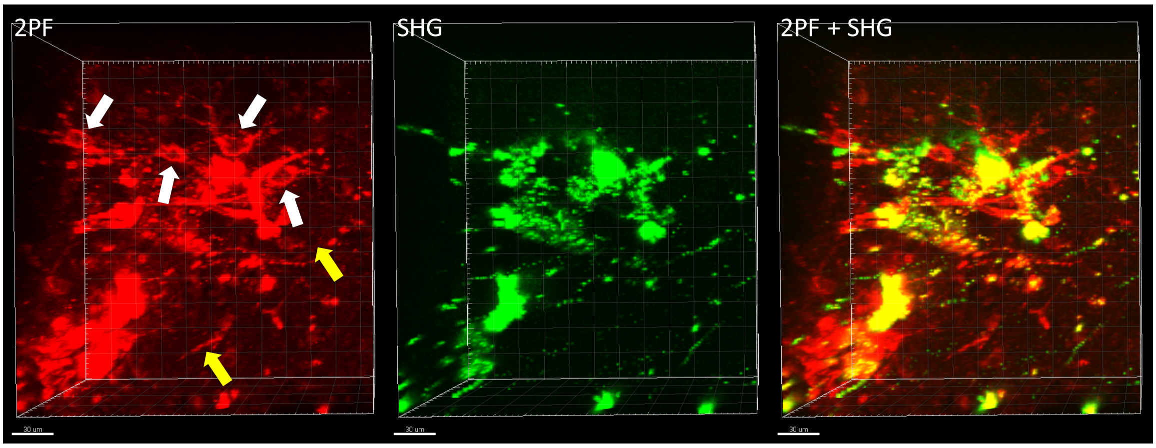

Figure 11: 3D images of brain slices incubated with **AK-1** by bath delivery. The dyes stained the plasma membrane of neurons as seen in 2PF image (marked with white arrows). Some fluorescence was also visible from the dendrites and axons (marked with yellow arrows). No SHG was visible from the plasma membrane of the soma of neurons; however, SHG was visible from dendrites and axons. Substantial SHG was visible from small lumps what could be blood vessels. λ_{ext} = 870 nm, scale bar = 30 µm.

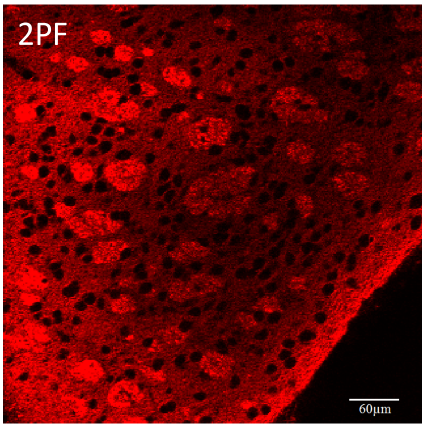

Figure 12: Fluorescence signal of **FM4-64** from the mice brain slices. The dye stained everything in the slices making the detection of neurons extremely difficult. λ_{ext} = 960 nm, scale bar = 60 µm.

Intracellular delivery

I delivered 25 µM of **AK-1** in neurons in the brain slices intracellularly by forming a seal. The dye emitted fluorescence from both plasma membrane and intracellular area but no significant SHG signal was visible (Figures 13 and 14). The reason for lack of SHG could be that the dye molecules flip-flopped or while forming the seal, the dye molecules which excreted out of the pipette due to positive pressure stained the extracellular leaflet of the plasma membrane to cancel the overall non-centrosymmetric effect. When I delivered **FM4-64** (50 µM) in a neuron intracellularly by forming a seal; surprisingly, the neuron was not visible due to background fluorescence from the dye molecules that left the pipette while forming the giga-seal (Figure 13). Previously, to get SHG from the plasma membrane of neuron in slices by intracellular delivery of **FM4-64** at 200 μM concentration, Dombeck *et al* used Advasep (see Appendix for structure) in the extracellular medium. Advasep acts as a scavenger for **FM-64** and so it removed any dye that escaped through the pipette while forming the seal to stain the blood vessels and extracellular leaflet of the plasma membrane.[6,21] Using Advasep for porphyrin-based dyes is not possible because it is specifically designed for FM-based dyes,[21] and designing a new scavenger molecule for **AK-1** is beyond the scope of this thesis.

The results show that **AK-1** has more affinity towards neurons than blood vessels and extracellular organelles in slices compared to **FM4-64**; however, due to lack of a scavenger molecule it cannot be delivered intracellularly to get strong SHG signal from the plasma membrane.

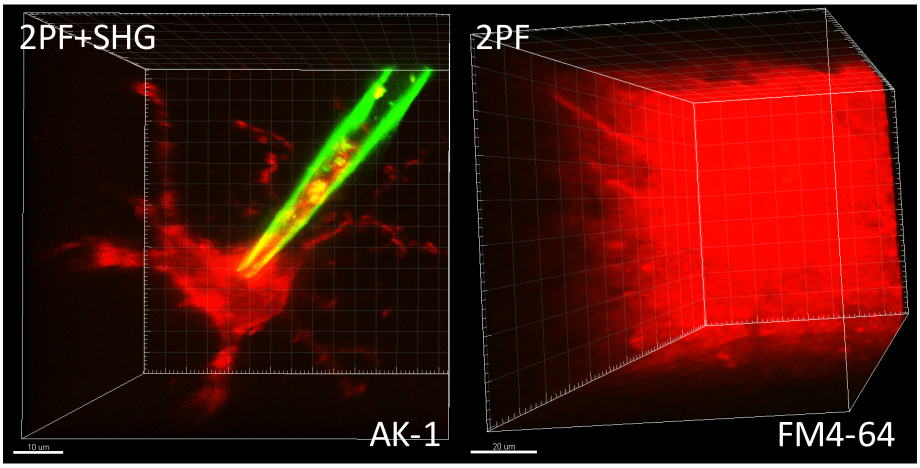

Figure 13: 3D images of intracellular delivery of **AK-1** (25 μM) and **FM4-64** (50 μM) in neurons located deep inside mice brain slices. **AK-1** stains the plasma membrane of the soma along with dendrites and axons to give fluorescence signal (red). 2PF signal from intracellular area is also visible, while lots of SHG signal (green) is visible from the pipette. **FM4-64** stains everything in the slice making visualization of a neuron impossible due to background fluorescence. λ_{ext} = 870 nm (**AK-1**), 960 nm (**FM4-64**), scale bar =10 μm (**AK-1**), 20 μm (**FM4-64**).

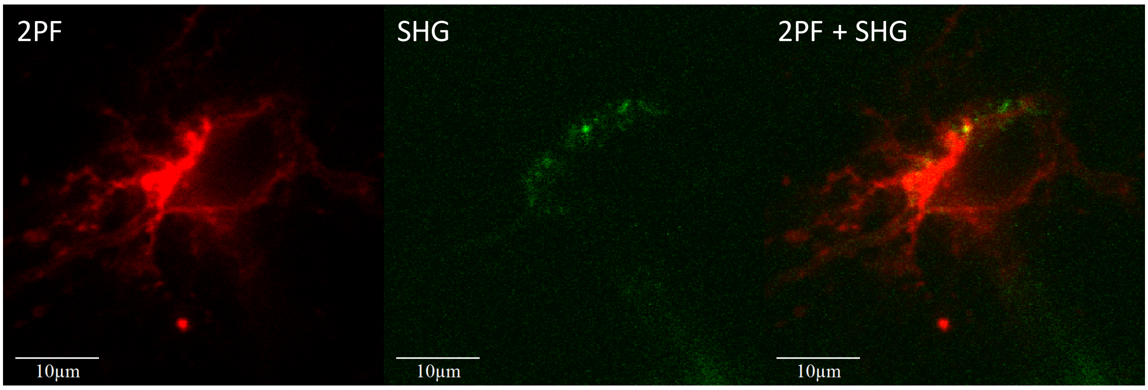

Figure 14: 2D cross-section of a neuron located deep inside a mice brain slice stained with **AK-1** (50 μM) intracellularly. Bright 2PF can be seen from the plasma membrane of the soma and dendrites and axons with very dim SHG (image digitally enhanced for SHG clarity) from just the soma. λ_{ext} = 870 nm, scale bar =10 μm.

Pressure injection

I injected the dye in the slices through a pipette to stain the neurons extracellularly. An advantage of pressure injection over intracellular delivery is that the dyes are not meant to stain the intracellular leaflet of the plasma membrane and hence, there is no cancellation of the non-centrosymmetric effect if any dye molecules excrete out of the pipette. As expected, SHG signal was visible from the plasma membrane of neurons in slices.

Intracellular injection was performed at two different concentrations of 25 μM and 100 μM (Figure 15). At 25 μM, the images had to be digitally enhanced for clarity because in slices, the light travelling to and from the sample gets scattered and hence not all the light is detected by the microscope. The concentration had to be increased up to 100 μM to get good SHG signal without digital enhancement; however, at such a high concentration, the dye molecules stained the lipid-based bubbles, the tissue, and other biological structures in slices to give strong SHG signals. Hence, there were significant background SHG signals and so, it was very difficult to distinguish a stained neuron. Dombeck *et al.* used 500 μM of **FM4-64** to label neurons in slices to get SHG by pressure injection, which is five times more than the concentration required for **AK-1**; however, they did not get background fluorescence or SHG because they used Advasep as a scavenger.[6] Dr. Dombeck mentioned in our correspondence that he lost SHG of **FM4-64** from neurons very quickly maybe due to flip-flop of dyes or because of presence of Advasep. In the case of **AK-1**, the SHG is not lost so soon but due to the presence of background signal, it was very difficult to find a neuron suitable to patch. Because the dye is injected using a pipette, the slices had to be pierced up to depths of more than 50–100 μm, which moves the relative locations of the neurons, making it even more difficult to locate a healthy and stained neuron to patch. Despite several attempts, I was unsuccessful in locating a healthy neuron and patch it to test the voltage sensitivity of **AK-1**.

In my experiments, without Advasep, **FM4-64** stained everything in slices when delivered through pressure injection. The image was similar to the image of **FM4-64** in Figure 13 and hence, not shown here.

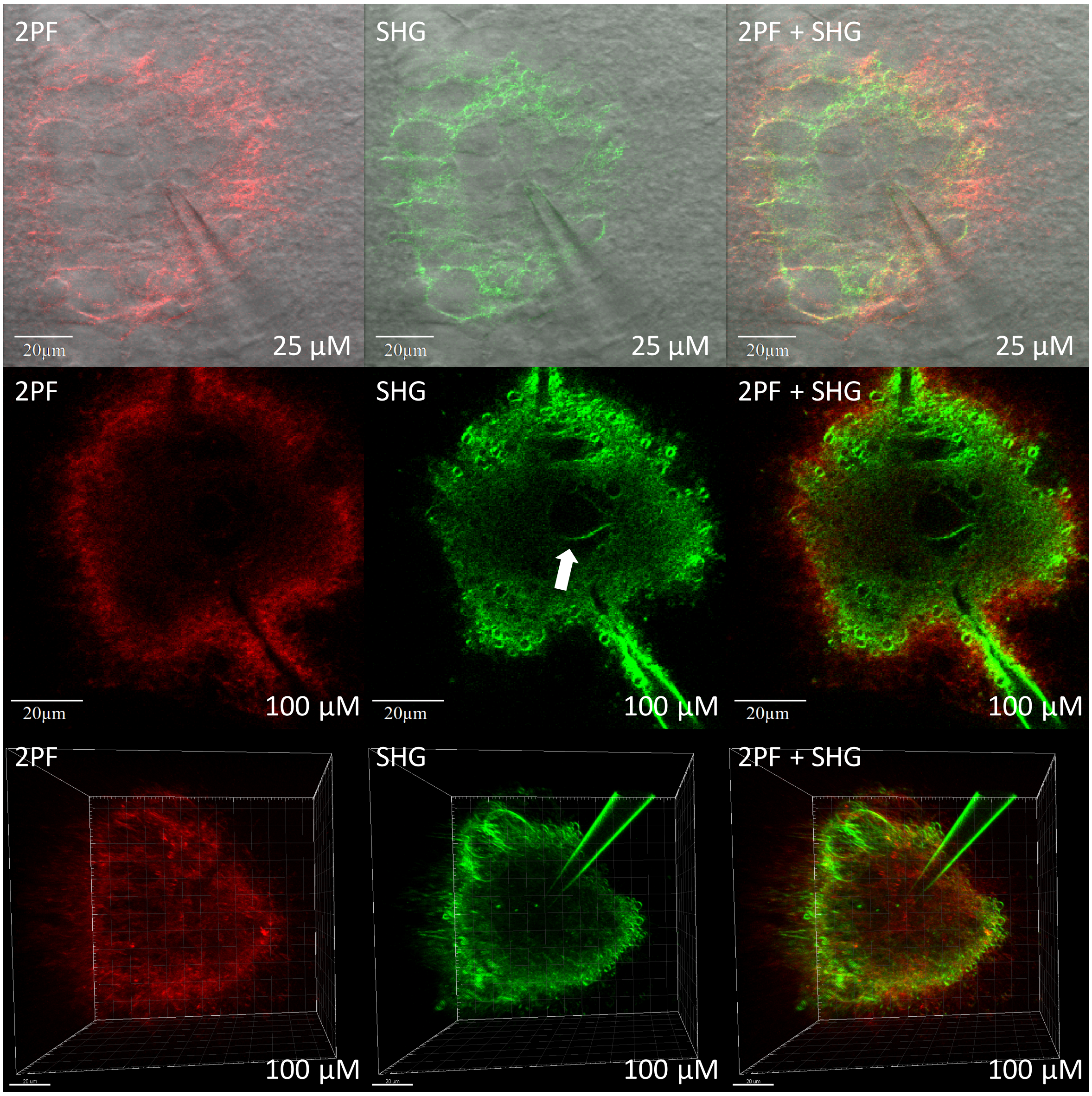

Figure 15: **AK-1** injected into the slices through a pipette to give 2PF (red) and SHG (green) signals from the plasma membrane. In the top row (2D cross-section), clear 2PF and SHG signals of **AK-1** (25 μM) are visible from the plasma membrane of the soma of the neurons; however, for clarity the images are the overlaid on the transmission images and had to be digitally enhanced. When the concentration was increased to 100 μM (middle and last rows), apart from a single neuron (pointed by a white arrow in the middle image), SHG is visible from lipid-based bubbles and extracellular organelles (2D cross-section). The 2PF signal from the neuron is dimmer than the SHG due to low quantum yield. It is very difficult to locate a neuron in the 3D images of the area stained with 100 μM of **AK-1** (third row). The images shown in the second row and third rows are from the same sample. The images in the third row are inverted upside down in the 3D image processing software, Imaris for better clarity. $\lambda_{ext} = 870$ nm, scale bar = 20 μm.

5.34 Multimodal imaging

After testing the plasma membrane localization of **AK-1** in various types of cells, I investigated its efficiency for multimodal imaging. Second harmonic generation (SHG) and two-photon excited fluorescence (TPEF) –based multimodal imaging has the potential to simultaneously image different cellular organelles labelled with different dyes. The fluorescence spectra of most commercial dyes designed for targeting different cellular organelles overlap, creating overlap among the fluorescence signals from various cellular organelles.[22–24] For effective multimodal imaging of SHG and TPEF simultaneously, either the SHG-based dye must not emit any fluorescence (have negligible quantum yield)[24] or the emission spectra of the dye must not overlap with the spectra of the TPEF-based dyes. SHG and TPEF –based multimodal imaging is mostly restricted to the samples where part of the sample itself gives a SHG signal, for example sarcomeres in cardiomyocytes, thus requiring only a single dye to be used for fluorescence.[25] **Ap3** (Chapter 1, Figure 15), an azo dye with negligible fluorescence quantum yield has been recently shown to be used for SHG and TPEF –based multimodal imaging.[24] No far-red or NIR plasma membrane bound dye has been reported, that could generate high SHG signal and be useful for multimodal imaging at the same time. The far-red to NIR –based emission spectrum of **AK-1** makes it suitable for TPEF and SHG –based multimodal imaging.

I performed multimodal imaging of **AK-1** (detected by SHG) in conjugation with other green and yellow dyes in photon-counting mode, to ensure better signal to noise ratio. I used **RH123**, the mitochondria bound dye as the green dye and LysoTracker™ Yellow HCK-123 (see Appendix for structure) as the yellow dye (Figure 16). For comparison, I used **FM4-64**, a widely-used plasma membrane bound dye. Apart from generating SHG signals, **FM4-64** also gave bright fluoresce signals from intracellular area in the red channel (575 nm–630 nm). The fluorescence signal from **FM4-64** actively interfered with signals generated from the yellow dye. Significant overlapping signals could be seen from the merged images of SHG and two-photon fluorescence. On the contrary, **AK-1** did not interfere with signals of the yellow dye in the red channel. The use of **AK-1** allowed simultaneous imaging of isolated multimodal signals from different cellular structures (Figure 16). It must be noted that the sizes of the cells in a cluster do not necessarily remain same throughout imaging due to biological events and so there are discrepancy in the sizes by approximately 2 μm.

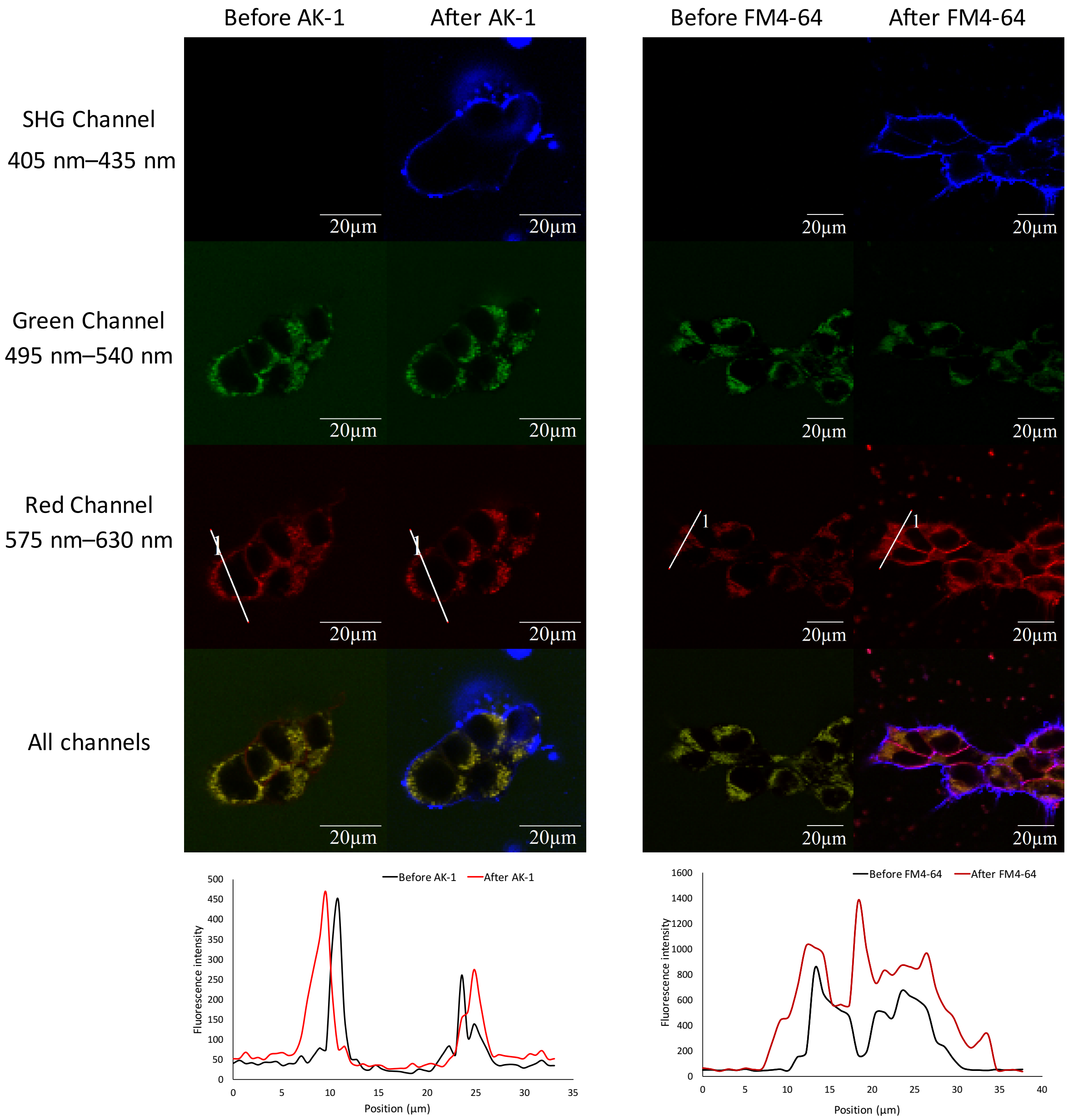

Figure 16: Images of HEK 293T cells incubated with **RH123** (20 µM) and **LysoTracker™ Yellow HCK-123** (3 µM). Images were taken by photon counting before and after addition of **AK-1** or **FM4-64**. The sizes of the cells expanded by ~2 µm when the cells were irradiated with the laser light second time after addition of **AK-1** or **FM4-64**. The SHG channels show clear images SHG from the plasma membrane of the cells generated after addition of **AK-1** and **FM4-64**. In the green channels, no significant change in the signals was observed after addition of either **AK-1** or **FM4-64**. In the red channel, there was no change in the fluorescence signal after addition of **AK-1** as shown in the intensity profile of the area depicted by the line drawn across a cell. After addition of **FM4-64**, there was a significant increase in the fluorescence signal from the intracellular area and the plasma membrane. Merged images of all the channels show substantial difference in the fluorescence signals from the intracellular area before and after addition of **FM4-64**, while the difference in the signal generated from the intracellular area before and after addition of **AK-1** is negligible. $\lambda_{ext} = 870$ nm, scale bar = 20 µm.

The azo dye reported by Nuriya *et al.* has negligible quantum yield, so it can be used for multimodal imaging in far-red channels (> 630 nm),[24] which is not possible for **AK-1**, since the fluorescence of **AK-1** starts from 630 nm. The β_{zzz} value (measure of SHG efficacy) of the azo dye is not reported; however, its SHG intensity is found to be lower than **FM4-64** at similar conditions by Nuriya *et al.*, thus suggesting that its β_{zzz} must be lower than the one of **FM4-64**. The value of β_{zzz} of donor-acceptor–based porphyrin dye is two to three times higher than **FM4-64** at wavelengths of 800 nm and 840 nm,[2,9,26] suggesting donor-acceptor porphyrin-based dye is a stronger SHG-based dye than the azo dye. The red-shifted absorption and emission spectra of **AK-1** makes it advantageous for deep tissue imaging with less photodamage.

Since **AK-1** emits fluorescence at wavelengths greater than 630 nm, it can also be used for dual color two-photon fluorescence-based imaging with conventional green and yellow dyes. Due to lack of specific filters in the microscope, I was not able to perform dual color imaging as discussed in Chapter 3 in case of pyropheophorbide dyes. Conventionally, dual color imaging in two-photon microscopy is achieved by cutting off the wavelengths at which the spectra of the dyes overlap.[27–29] Such a crude method of cutting off the overlapping spectra comes with disadvantages. First, it is not always possible to cut off the complete overlapping spectra because often the tails of the spectra overlap. Second, specific cutoff optical filters need to be installed in the microscope based on the dye used but it is not always feasible to install a different filter for every other dye. With the use of conventional green and far-red cutoff filters, **AK-1** could be used for dual color imaging.

5.35 Recording voltage sensitivity of dyes

5.35.1 Whole-cell patch clamping

Since, the whole-cell patch clamping of mice brain slices did not work, I pursued patch-clamping of HEK 293T cells and cultured rat hippocampal neurons stained with **AK-1**. I incubated the HEK 293T cells with 25 μM of **AK-1** to get bright SHG signal at less than 2 mW laser power and attempted to patch the cells. Despite several attempts, I was unsuccessful in forming a giga-seal. When I attempted to patch a cell not incubated with **AK-1**, I could form giga-seals and go into whole-cell mode every time. This experiment showed that the dye was preventing the formation of giga-seals. After many unsuccessful attempts, I shifted to working on cultured rat hippocampal neurons. In neurons too, I was not able to form giga-seal after several attempts. In neurons, I could form perfect giga-seals on cells not stained with **AK-1**. When cells stained with 25 μM of **AK-1** are used, the seal resistance was always approximately 90 MΩ. When I decreased the concentration of **AK-1** to 5 μM, I could form seals with resistances of up to 300–400 MΩ. I attempted to record voltage sensitivity with 300–400 MΩ seal but did not see any significant change in intensity of SHG signal. This is because whenever the seal resistances are below 1 GΩ, then there are leaks in the applied voltages and hence, proper whole-cell modes are not achieved making the recordings unreliable. The increase in seal resistance on decrease of the dye concentration further consolidates the fact that the dye molecules are preventing formation of giga-ohmic seals. The reason for non-formation of giga-seals in presence of porphyrin-based dyes remains unclear. Similar observation was made by Dr. James Reeve in case of **JR1-plus**.[8] He speculated that the greasiness of octyl chains in the electron donating group of **JR1-plus** prevents formation of giga-seals; however, **AK-1** is equipped with butyl chains. **Di-4-ANEPPS**, a commercial voltage-sensitive dye too has butyl chains but does not prevent formation of giga-seals. It must be noted that highly amphiphilic **AK-1** has high affinity towards glass surfaces and sticks to them. As observed in Figures 13 and 15, a film of **AK-1** dye molecules is formed on the inner surface of the glass pipette used for patch-clamping (green color SHG). This film might be preventing the formation of giga-ohmic seals with the cells. Such an intense film formation was not observed with **FM4-64** and **di-4-ANEPPS**.

5.35.2 Contracting neonatal cardiomyocytes

Since the **AK-1** dye was not allowing the cells to be patched, I tested its plasma membrane localization and membrane potential sensing efficiency in contracting neonatal myocytes. Contracting neonatal myocytes develop action potential on their own.[30,31]

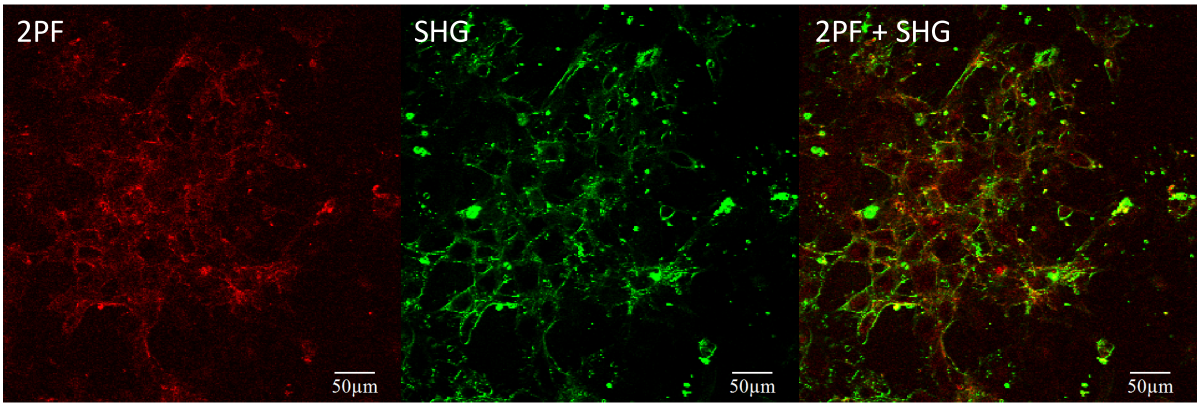

Figure 17: Neonatal myocytes incubated with 25 μM of **AK-1** and shone with 2 mW of laser power. Significant 2PF and SHG signals can be seen from the plasma membrane of the cells. λ_{ext} = 870 nm, laser power = 1.5 mW, scale bar = 50 μm.

Based on concentration-based experiments in immortal cells as discussed above, I incubated the myocytes with 25 μM concentration of dye to observe bright fluorescence and SHG signal from its plasma membrane (Figure 17). After testing plasma membrane localization, I tested the membrane potential sensing efficiency of the dye. Since the neonatal myocytes are in development stage, they undergo various biological changes dependent on temperature, pH, atmosphere, media, and hence an exact characterization of the change in membrane potential is not possible without patch-clamping experiments;[30,32] however, a change in SHG signal as the cells contract will show whether the dye can measure membrane potential of live cells.

I incubated **AK-1** (20 μM) with the neonatal cardiomyocytes and monitored a contracting small region of interest (Figure 18 A). Since the cell is contracting, a blinking pixel moves in an oscillatory motion (between points 1 and 2 as shown in Figure 18 B). The motion of the pixel is tracked manually and the change in its SHG intensity is studied (Figure 18 B–D). The timescales (400–600 ms) and the profiles of the spikes of the SHG signals in Figure 18 C, indicate that the dye is sensing the change in membrane potential. In neonatal myocytes, the timescale of one contraction is approx. 2 s, while the timescale of an action potential is around 200–600 ms.[33,34] The timescales of the spikes in Figure 18C, vary from 400 ms to 600 ms, which might be due to various reasons, such as application of high laser light (15 mW), effect of dye on the cellular dynamics, room temperature, HBSS buffer as the cellular media etc. The use of 15 mW of laser power at a pixel dwell time of 200 μs/pixel caused photobleaching (Figure 18C). The signals were corrected for photobleaching and the SHG-based voltage sensitivity was calculated by taking the values of lowest signals as baseline (Figure 18D). The maximum voltage sensitivity, $\Delta S/S$ reached up to value of 60%. The Anderson group has already shown in synthetic lipid bilayers (using 90 mW laser power) that donor-porphyrin-acceptor dyes are voltage-sensitive and the voltage sensitivity value can reach up to 50%/100 mV in hemispherical lipid bilayers.[1] Due to lack of a porphyrin-based dye, which localizes in the plasma membrane of live cells, until now the voltage sensitivity of porphyrin-based dyes has not been demonstrated in live cells. Here, I have shown that plasma membrane bound tricationic porphyrin-based dye, **AK-1** can sense the voltage changes in live cells. Since neonatal myocytes contract, studying their membrane potential by the patch-clamp technique is not trivial because often the giga-seal breaks due to movement of the plasma membrane. Patch-clamping experiments are performed in neonatal myocytes by adding drugs, such as blebbistatin, which inhibits contraction but do not alter its membrane potential.[35,36] However, since the cells are in developmental stages, such drugs can affect the inherent biological characteristics of the cells[37] and hence, voltage-sensitive probes are highly desirable for studying membrane potential of contracting myocytes.[33,38] SHG-based probe, **AK-1** will offer significant advantages over fluorescent-based probes to measure membrane potential of contracting myocytes, such as no background signal and low phototoxocity. Further experiments to optimize the voltage-sensitivity and temporal resolution of **AK-1** will require external electrical stimulation of the myocytes. Non patch-clamp–based electrical simulation techniques have been designed and widely used to electrically stimulate cardiac myocytes.[39–42] Such setups, where carbon or metallic electrodes are dipped in the extracellular solution and electrical pulses are applied by a stimulator offer an alternative to the patch-clamp method and hence can be used to optimize voltage sensitivity and temporal resolution of **AK-1**.

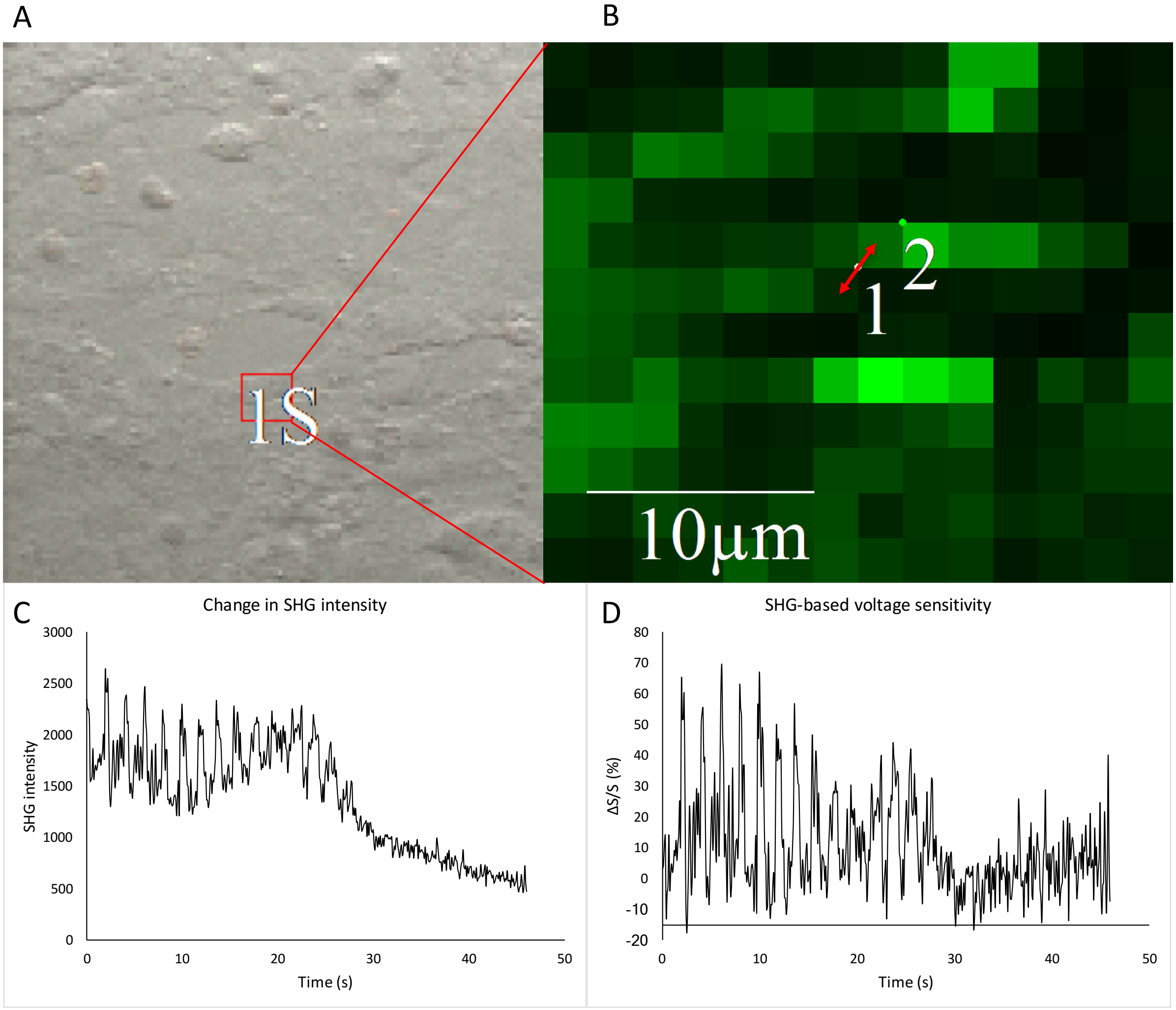

Figure 18: Change of SHG intensity on contracting neonatal myocytes. (A) The region of interest depicted by red box is chosen to monitor the change of SHG intensity (B) Enlarged image of the region of interest (14 X 12 pixels). Pixels 1 and 2, represent the same area of the plasma membrane. It oscillates between the positions 1 and 2 due to contraction of the cell. (C) Change in SHG intensity at the area which oscillates between pixels 1 and 2. Photobleaching of the dye can be seen as the intensity of SHG reduces. (D) Photobleaching corrected change in SHG-based voltage sensitivity. $\lambda_{ext} = 870$ nm; laser power = 15 mW at 200 μs/pixel.

5.36 Imaging in gram negative bacteria, *E. coli,* and giant unilamellar vesicles (GUVs)

5.36.1 Imaging in gram negative bacteria, *E. coli*

I used BL21(DE3) strain of gram negative bacteria, *E. coli* to test the localization of **AK-1**. The motivation behind imaging *E. coli* cells was to see whether **AK-1** is able to localize in the cell wall of the gram-negative bacteria. Since **AK-1** is made of porphyrin and cationic amino groups; for comparison, I also tested a different non-charged amphiphilic donor-acceptor–based porphyrin dye, **JDW-M** (Figure 19). The reason of choosing **JDW-M** and no other neutral porphyrin-based dyes is that **JDW-M** could cross the nuclear membrane of mammalian cells (as discussed in Chapter 3) and so I speculated that it might be able to cross the cell wall of gram negative bacteria.

Surprisingly, **AK-1** was found to cross the cell wall and clear fluorescence signals were observed from inside the cells (Figure 20). The bacteria cells died in few min. I did not study the dark toxicity and light toxicity of **AK-1** and hence, it remains unclear whether the dye itself is antibacterial or phototoxic.

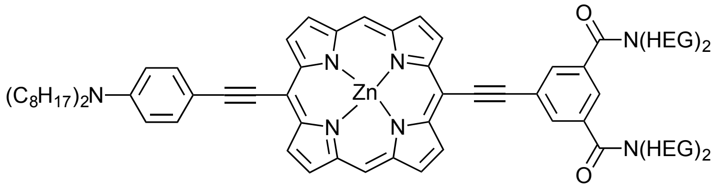

Figure 19: Chemical structure of **JDW-M** decorated with hexaethylene glycol (HEG) chains.

JDW-M did not stain either the cell wall or intracellular part of *E. coli.* On performing co-localization experiments of **AK-1** and **JDW-M**, SHG signals were visible from what could be the cell wall of the bacteria encircling fluorescence signals from intracellular area (Figure 20). The reason for SHG signal in co-localization experiment but not in individual dye experiments could be that when the bacteria died in presence of **AK-1**, then **JDW-M** was able to stain the bacteria but the cellular machinery of live bacteria did not allow staining of **JDW-M**. The co-localization experiment proves that the porphyrin structure of the dye is not viable enough to cross the cell wall of gram-negative bacteria. The difference between **AK-1** and **JDW-M** is the presence of cationic pyridinium and amino groups. Although **FM4-64** too contains cationic pyridinium and amino groups but has been known to stain the cell wall of *E. coli.*[43,44] This means that the cationic pyridinium groups are not sufficient to cross the cell wall of gram negative bacteria. Neither the porphyrin structure nor the amino cationic groups are independently able to cross the cell wall of *E. coli* but their combination can cross as observed for **AK-1**.

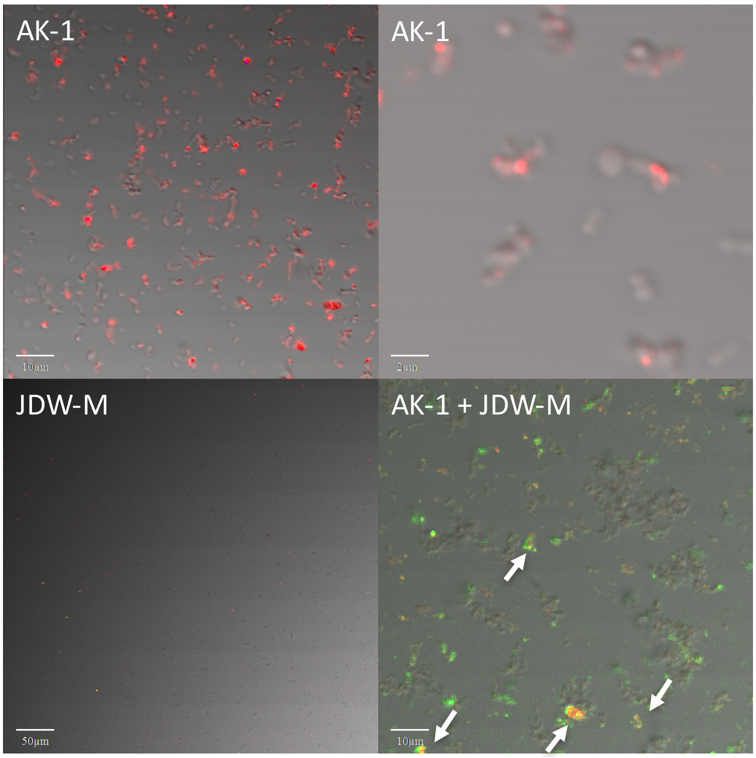

Figure 20: Nonlinear optical imaging of gram negative *E. coli* bacteria stained with **AK-1** and **JDW-M** dyes. Fluorescence signal seen from interior of *E. coli* stained with only **AK-1** (top left and top right). No fluorescence or SHG signal seen from bacteria stained with only **JDW-M** (bottom left). On co-localization of **AK-1** and **JDW-M**, green SHG signals could be seen encircling the red fluorescence signals coming from inside the bacteria (depicted by white arrows in the bottom right image). λ_{ext} = 870 nm, concentration of both **AK-1** and **JDW-M** = 5 μM. Scale bar = 10 μm & 2 μm (**AK-1**); 50 μm (**JDW-M**); 10 μm (**AK-1** + **JDW-M**).

Previously, cationic porphyrins have been reported as potential antimicrobial agents.[45–47] In general, small molecules find it difficult to cross the cell wall of gram negative bacteria. It has been recently reported by Hergenrother and coworkers in a *Nature* article that small molecules containing an amine group, are amphiphilic and rigid, and have low globularity are likely to cross the cell wall of gram negative bacteria to accumulate inside it.[48] Both **AK-1** and **JDW-M** tend to follow the rules as both of these molecules contain at least one amine group, are amphiphilic and have low globularity. The rigidity of these molecules is debatable due to presence of butyl and octyl chains. Nonetheless, only **AK-1** can cross the cell wall of the gram-negative bacteria and not **JDW-M**. This suggests that the cationic groups are playing important role/roles in for interaction with cell wall of gram negative bacteria. Further experiments will reveal more information about the interaction of these molecules with the cell wall of *E. coli* and could be useful in synthesizing new antimicrobial compounds.

5.36.2 Giant unilamellar vesicles (GUVs)

Since the cells could not be patched in presence of **AK-1** dye, I used cell-sized giant unilamellar vesicles (GUVs) to test the voltage sensitivity. GUVs are model lipid bilayers designed to mimic plasma membrane of live cells.[4,49,50] GUVs are used to study biological functions of membrane proteins, ion channels, lipid-order and lipid-disorder etc. Although GUVs have been widely used in fluorescence microscopy, stable patch-clamping of cell-sized GUVs has been a challenge for many years due to the following reasons. Often, when a giga-seal is formed by applying suction, the lipid membrane keeps aspirating inside the pipette and the GUVs rupture. Although patch-clamp technique has been around for decades, the events that take place at the molecular level during formation of a giga-seal and whole-cell mode are still unknown and so it has been a challenge to mimic the procedure in GUVs. Garten *et al.* recently reported an experimental procedure to form stable giga-seal and whole-GUV (similar to whole-cell) mode.[4] To prevent aspiration of lipids inside the glass pipette after formation of giga-seal, they incorporated beta-casein protein in the GUVs. The protein was found to block the lipid spreading inside the pipette and thus preventing GUVs from rupturing. They also treated the glass pipettes with Shipley S-1813, a novolac-based photoresist known to block diffusion of membranes.[51]

I formed stable cell-seized GUVs (using DOPC lipid) by gel assisted swelling technique as described in the literature.[4,50] After forming the GUVs, I incubated them with **AK-1** (50 µM) and imaged them under the multiphoton microscope. Surprisingly, the two-photon fluorescence signals were very dim and there were no SHG signals. I repeated the experiment by varying the concentration of **AK-1** but no SHG signals were seen (Figure 21). I also changed the concentration of lipids during GUV formation but was unsuccessful in getting any SHG signal. For comparison, I incubated the GUVs with **FM4-64** which gave bright fluorescence and SHG signals proving that the problem is neither in imaging method nor in the GUVs.

I stained the GUVs with pyropheophorbides too (from Chapter 2 and 3) but no SHG could be observed. The reason of testing the pyropheophorbides was to study the different TPEF and SHG –based transition dipole moments in 3D as in the lipid bilayer structure there will be no negative lensing effect (discussed in Chapter 2) because both intracellular and extracellular area are filled with similar refractive index buffer. The reasons for no SHG of the porphyrin-based dyes from the GUVs could be manifold. Firstly, since the fluorescence of **AK-1** is dim, the number density of the dyes in the lipid bilayer seem to be very low and since SHG is directly proportional to square of the number density, no SHG is seen. Since high concentration of up to 50 µM is used, another reason could be that the dye does not localize efficiently in the bilayer structure of the GUVs. Secondly, the dyes might undergo flip-flop in the GUVs to give no SHG. Flip-flop of dyes have been often observed in GUVs leading to fading of SHG.[52,53]

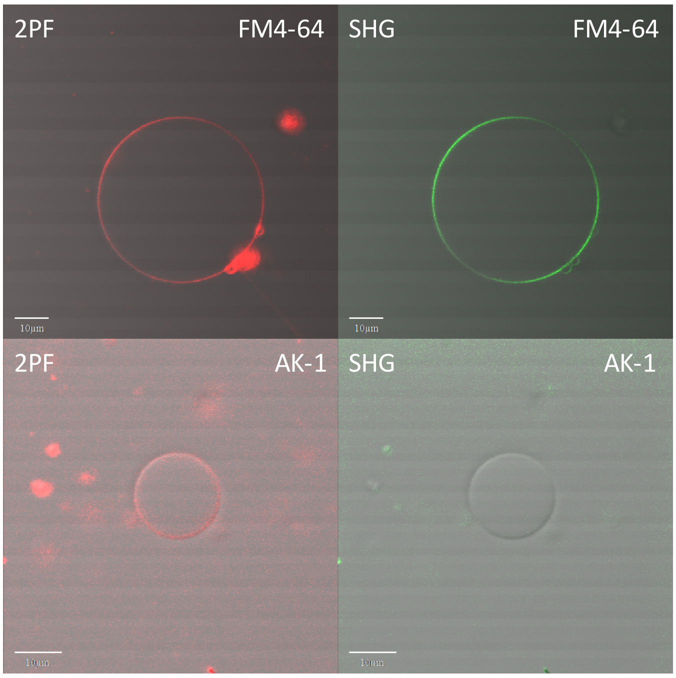

Figure 21: **FM4-64** and **AK-1** incubated in giant unilamellar vesicles (GUVs). Clear two-photon fluorescence and second harmonic generation signals are seen from GUVs stained with **FM4-64**. The fluorescence from GUVs stained with **AK-1** is dim and no SHG signal is seen. λ_{ext} = 850 nm (**FM4-64**), 870 nm (**AK-1**). Scale bar = 10 µm.

As no SHG signals were observed from GUVs, I did not pursue patch clamping to test the voltage sensitivity of the dyes.

5.40 Conclusion

I synthesized and characterized a new tricationic porphyrin-based dye, **AK-1**. To achieve higher yields, the experimental procedures for synthesizing the intermediates were modified from the procedures used in the literature[2]. This is the first example of an isolated and characterized tricationic porphyrin-based dye. The absorption and emission spectra of **AK-1** are similar to the spectra of other porphyrin-based dyes, **HLA-1** and **JR1-plus** due to similarity in their electronic conjugated structures.

I have shown that the tricationic porphyrin-based dye, **AK-1** can localize in the plasma membrane of various mammalian cells. Imaging was performed at various concentrations and it was found that concentration of 20 μM of the dye gives good SHG signal at less than 2 mW laser power. In mice brain slices, the dye showed better affinity for neurons than **FM4-64**, a widely-used voltage-sensitive dye. **AK-1** can be very useful for two-photon and SHG –based multimodal imaging. It is the first far-red to NIR shifted dye, which has been shown for multimodal imaging. If required, the fluorescence of **AK-1** can be completely quenched by inserting a metal like copper. The porphyrin-based dye **HLA2.Cu**, which similar structure to **HLA1** but inserted with copper metal gives no fluorescence signal but good SHG signal as discussed in Chapter 3 (Figures 21 and 22 of Chapter 3). The dye could be useful for deep multimodal imaging of tissues with minimal photobleaching and phototoxicity. The shifted spectrum of the dye also makes it suitable for dual color imaging in combination with conventional green and yellow dyes.

Since the voltage sensitivity of **AK-1** could not be studied by patch-clamp method, I propose use of an alternative optogenetics-based method, which is discussed in the 'Future work' section of this chapter. I have shown that **AK-1** is capable of measuring the voltage change in beating neonatal myocytes, although a more controlled system is required to compare its voltage sensitivity and temporal resolution with commercial voltage-sensitive dyes.

AK-1 crosses the cell wall of gram negative bacteria, *E. coli* to give fluorescence signals from the intracellular area. Control studies with another donor-acceptor–based amphiphilic porphyrin-based dye, **JDW-M** showed that the cationic ammonium groups in combination with the porphyrin structure are playing a significant role in cell wall crossing ability of **AK-1**. Co-localization study of **AK-1** and **JDW-M** gave both fluorescence and SHG images of *E. coli*. These dyes could be useful for studying the interaction between small molecules and the cell trafficking machinery of gram negative bacteria.

5.41 Future work

5.41.1 Optogenetics

Optogenetics can be used as an alternative technique to controllably excite neurons using light, to test voltage sensitivity of **AK-1**. Use of optogenetics and voltage-sensitive indicators simultaneously will ensure all-optical physiology, i.e. both electrical excitation and recording of membrane potential of neurons using light.[54,55] Various one-photon and two-photon –based light sensitive receptor proteins such as channelrhodopsin-2 (ChR2), C1V1$_{TT}$, ChIEF, ChETA$_{A}$ have been designed and used to excite neurons *in vitro, ex vivo*, and *in vivo*.[56–61] ChR2, the most widely used protein for optogenetics has been used in conjugation with other voltage-sensitive dyes (both organic and protein –based) to excite and record action potential from neurons.[54,62,63] One of the major concerns for the use of ChR2 for all-optical physiology has been the overlap of excitation spectra of ChR2 with emission spectra of voltage-sensitive dyes, which lead to the surplus unwanted stimulation of ChR2 from the fluorescence light that emitted from the voltage-sensitive dye. To avoid such a cross-talk between cell stimulation and imaging, far-red light emitting dyes have been designed.[62] Although **AK-1** has far-red to near-infrared (NIR) fluorescence, ChR2 cannot be used because the wavelength of SHG signal (435 nm for excitation at 870 nm) that dye produces will directly overlap with the excitation spectrum of ChR2 (λ_{max} = 470 nm) thus risking significant surplus unwanted stimulation. C1V1$_{TT}$, a two-photon–based photoreceptor with excitation maxima at 545 nm[60] could be used to excite cells labelled with **AK-1**. C1V1$_{TT}$ absorb light below 450 nm but the absorption efficiency is low (<10%). Without performing experiments, it could not be predicted how much cross-talk will take place between **AK-1** and C1V1$_{TT}$ from the SHG signal. According to previous studies, overlap of excitation spectrum of optogenetic protein and emission spectrum of voltage indicator at boundary wavelengths have not resulted in significant cross-talk thus suggesting that C1V1$_{TT}$ could possibly be used for measuring SHG-based voltage sensitivity of **AK-1**.[62] Until now, the use of SHG for all-optical physiology has not been demonstrated. SHG-based all-optical physiology tool will be able to record membrane potentials from many cells simultaneously with high spatial and temporal resolution, and minimal photodamage and phototoxicity. Time constraints and lack of optogenetics-based setup prevented me from performing these experiments myself during my DPhil studies.

5.41.2 New perylene-based dye

Although **AK-1** has shown very good plasma membrane localization efficiency in live cells, it prevents the cells from being patched to test its voltage sensitivity. Use of optogenetics setup as described above will be an optimal way to test the voltage sensitivity of porphyrin-based molecule **AK-1** in live cells. Porphyrin-based molecules show high two-photon absorption cross-section and high SHG efficiency because of their extended π-conjugated structure.[2,9,64,65] Here, I present the design, synthetic route, and DFT calculations of a new highly-conjugated and amphiphilic perylene-based molecule, **AK-2** (Figure 22), which might be able to give high fluorescence and SHG –based voltage sensitivity in live cells without inducing greasiness. Perylene-based dyes have been widely used in various applications, such as electrophotography, solar cells, paints, and light emitting diodes due to their high absorption coefficient.[66]

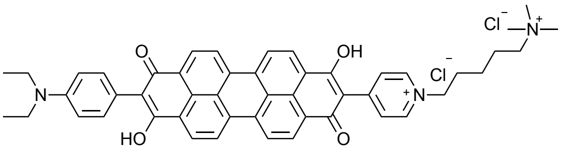

Figure 22: Chemical structure of new amphiphilic donor-acceptor–based perylene molecule, **AK-2**.

Possible synthetic route

Compounds **24** and **26** can be synthesized by the high temperature-based similar routes (Scheme 5) as suggested by Awad *et al.*[67] The dimerization of **24** and **26** could be possible by the route suggested by Buffet *et al.* (Scheme 6),[66] to form **29** followed by quaternarization to form **30**. It must be noted that the highly planar molecule, napthalic anhydride **22** does not easily solubilize in most of the organic solvents and the reactions are performed at high temperatures by melting it.

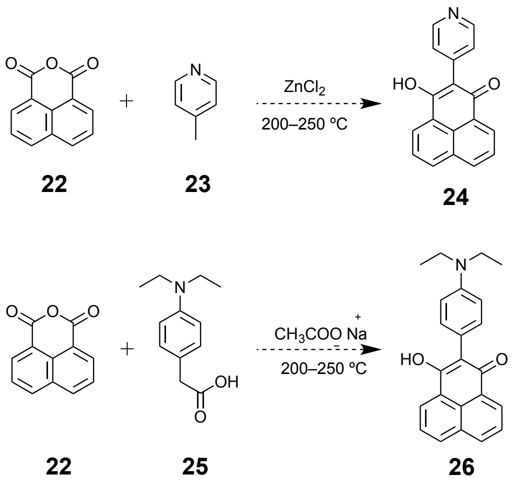

Scheme 5: Synthesis of **24** and **26** as reported by Awad *et al.*[67] Proposed synthesis of **28**.

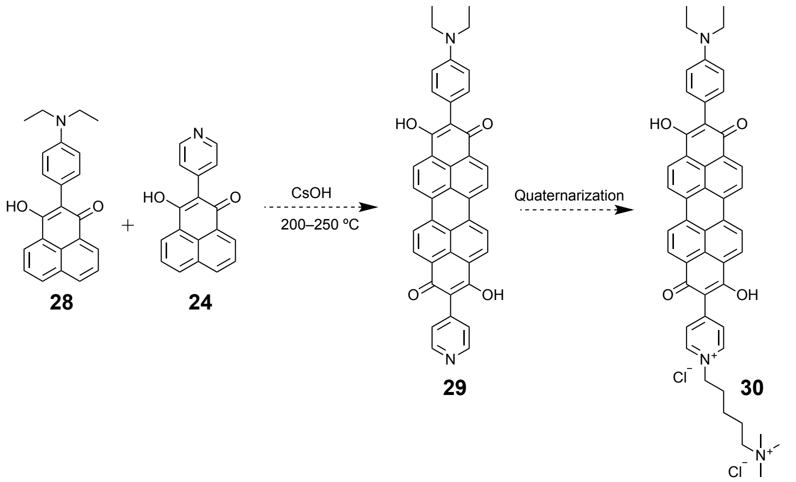

Scheme 6: Synthetic route to synthesize **29** by dimerization of **28** and **24**.

The structure of the new proposed dye, **AK-2** is similar to highly voltage-sensitive dye, **ANINNE-6 plus** (Figure 23).[68–70] These kind of rigid dyes do not undergo photoisomerism (photoisomerism causes variations in reported membrane potential values) because cis-trans isomerism is not possible and hence are more reliable than conventional styryl-based dyes, such as **FM4-64** and **di-4-ANEPPS**.[69] Moreover, the structural similarity of **AK-2** with **ANINNE-6 plus** raises hopes that it might allow the cells to be patch clamped to test its voltage sensitivity.

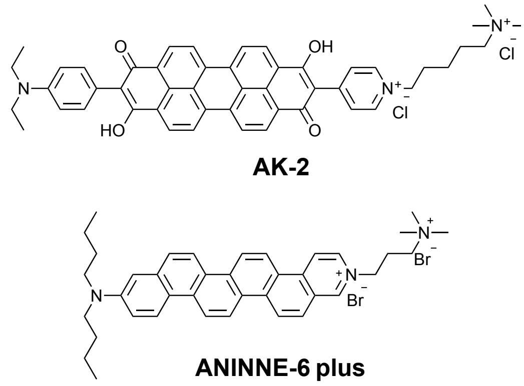

Figure 23: Chemical structures of commercial voltage-sensitive dye, **ANINNE-6 plus** and the new perylene-based dye **AK-2**.

DFT computational analysis of AK-2

I performed DFT analysis on the donor-acceptor–based perylene-based compounds to geometrically optimize the structure and observe its frontier molecular orbitals (HOMO and LUMO) in water solvated state. The DFT was performed at B3LYP/6-31G(d) level of theory. The torsional angle between the electron-donor and the backbone perylene molecule at the lowest transition state of **AK-2** is calculated to be 46° (Figure 24). A rotational scan around the

C–C bond was performed to calculate the energy barrier; maximum energy barrier was calculated to be less than 5 kcal/mol (Figure 24). Such a small energy barrier can be easily crossed at room temperature.

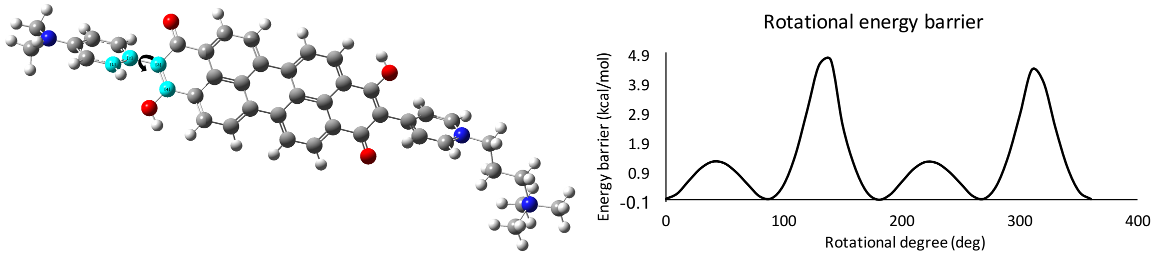

Figure 24: Geometrically optimized structure of **AK-2**. The torsional angle formed by the four carbon atoms (cyan blue) is 46º. Rotational scan around the C–C bond (black curvy arrow) was performed to calculate energy barrier. Maximum energy barrier across the 360º scan of the C–C bond is calculated to be less than 5 kcal/mol.

The calculation of frontier molecular orbitals (HOMO and LUMO) show that the pyridinium is not taking part in electronic conjugation, which means that the perylene backbone is itself highly electron deficient to complete the push-pull system (Figure 25). The electron-deficiency of the perylene molecule can be directly compared with the porphyrin molecule because the pyridinium group in the donor-acceptor–based porphyrin molecules too have been shown to not taking part in the electron conjugation.[9] At physiological conditions (pH = 7.4 at 25 ºC), the hydroxyl groups of **AK-2** might get deprotonated, and so I optimized its structure in deprotonated form in ground state and found that deprotonation does not cause significant changes in localizations of the HOMO and LUMO (Figure 25).

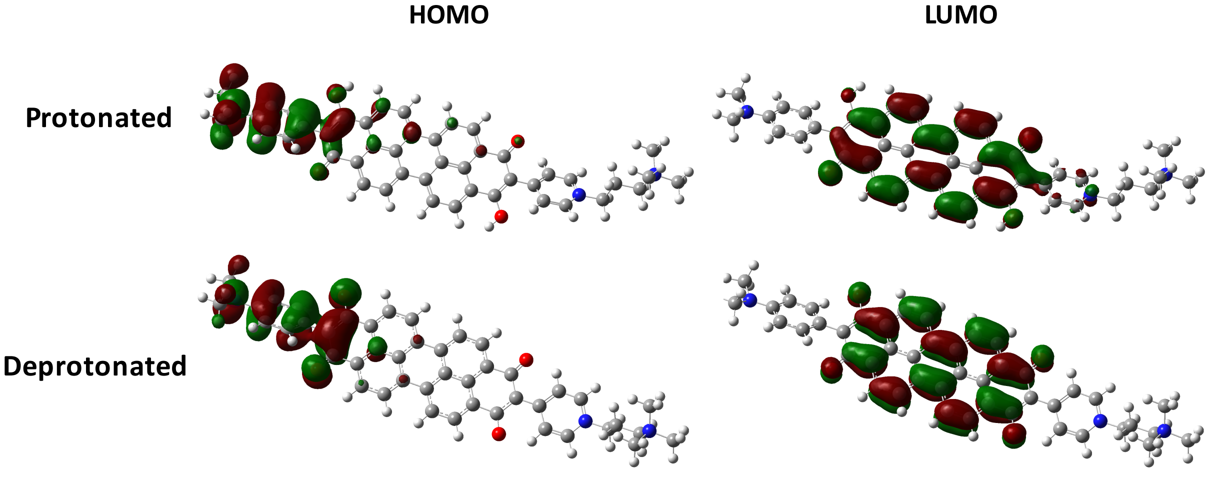

Figure 25: Localization of calculated HOMO and LUMO on geometrically optimized structure of **AK-2** in protonated and deprotonated forms. For simplicity of calculation, the ethyl chains in the donor group is replaced with methyl groups. HOMOs of the molecules are strongly localized over the aniline-based donor group. The LUMOs of the molecules are localized over the perylene backbone; the pyridinium group is not taking part in the electronic conjugation.

Perylene-based molecules already have red-shift absorption spectrum,[66] and the attachment of a strong electron-donor group will further shift the spectrum towards far-red. Such a molecule will possess similar photophysical properties as porphyrin-based molecules thus making it a good candidate for voltage-sensitive dyes.

5.50 Experimental synthetic procedures

Trihexylsilyl acetylene[71]

$$(C_6H_{13})_3Si-\equiv-H$$

Chlorotrihexylsilane (15.2 mL, 41.6 mmol) was added dropwise under Ar to a stirred solution of ethynylmagnesium bromide (0.50 M in THF, 100 mL, 50.0 mmol). The reaction mixture was heated at reflux for 1 h before HCl (aq.) (10%, 80 mL) was added. The organic layer was washed with water (80 mL) and dried over Na_2SO_4. The product was dried at a reduced pressure of 0.4 mbar for 30 min to yield a yellow oil. **Yield**: 10.0 g, 77.9%. **^{1}H NMR** (400 MHz, $CDCl_3$) δ/ppm: 2.35 (s, 1 H, ≡C*H*), 1.41–1.22 (m, 24 H, CH_2), 0.89–0.83 (m, 9 H, C*H*), 0.63–0.56 (m, 6 H, C*H*). **^{13}C NMR** (100 MHz, $CDCl_3$) δ/ppm: 94.1, 88.5, 33.3, 31.6, 23.9, 22.7, 14.3, 13.2. ***m/z* (ESI$^-$)** 307.3 ($C_{20}H_{40}Si$, M requires 308.3).

Trihexylsilyl propynal[2]

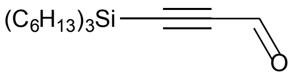

This reaction was performed according to literature procedure.[2] *n*-Butyl lithium (11.2 mL, 2.5 M solution in hexane) was added dropwise to a stirred solution of trihexylsilyl acetylene (6.6 g, 21.3 mmol), in dry THF (18 mL) at 0 °C. The mixture was stirred for 15 min at 0 ºC and then another 15 min at RT. The reaction mixture was transferred via cannula to a stirred solution of DMF (5 mL, mmol) in dry THF (18 mL) and stirred for 2 h at −80 ºC. The reaction mixture was quenched with HCl (10% v/v, 50 mL), washed with H_2O and extracted with Et_2O. The solution was dried over Na_2SO_4 and concentrated to give yellow oil. **Yield:** 6.71 g, 93.5%. **^{1}H NMR** (400 MHz, $CDCl_3$) δ/ppm: 9.17 (s, 1 H, C*H*O), 1.45–1.20 (m, 24 H, 2-5 hexyl-*H*), 0.89 (t, 9 H, $^3J = 6.7$ Hz, 6 hexyl-*H*), 0.68 (m, 6 H, 1-hexyl-*H*). **^{13}C NMR** (100 MHz, $CDCl_3$) δ/ppm: 175.9, 103.6, 102.5, 33.1, 31.5, 23.8, 22.7, 14.2, 12.6.

Dipyromethane 7[72]

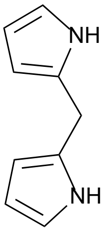

Formaldehyde (33% w/w solution in water, 10.8 mL, 120 mmol) was added to pyrrole (200 mL, 2.88 mol) and the solution degassed by repeated evacuation and stirring under Ar at RT. Trifluoroacetic acid (1.08 mL, 14.1 mmol) was added by syringe under vigorous stirring and in the Ar atmosphere. The reaction proceeded for 5 min before CH_2Cl_2 (200 mL) was added, followed immediately by Na_2CO_3 (aq., sat., 200 mL). The organic layer was washed with Na_2CO_3 (aq.) (sat., 2 × 200 mL) and water (2 × 200 mL), then dried over Na_2SO_4. The solvent and then excess pyrrole were evaporated under reduced pressure. Distillation of the oily residue in a Kugelrohr apparatus (180 ºC, 0.6 mbar) yielded the product **7** as a white solid. The product solidifies in the collecting vial into a robust stone difficult to remove. The convenient way to collect it is by washing with CH_2Cl_2. **Yield:** 6.9 g, 40%. **^{1}H NMR** (400 MHz, $CDCl_3$) δ/ppm: 7.76 (br s, 2 H, N*H*), 6.64 (m, 2 H, pyrrole α- *H*), 6.16 (m, 2 H, pyrrole β- *H*), 6.04 (m, 2 H, pyrrole β- *H*), 3.96 (s, 2 H, C*H$_2$*). **^{13}C NMR** (100 MHz, $CDCl_3$) δ/ppm: 121.2, 117.4, 108.4, 106.5, 26.4.

4-iodo-*N*,*N*-dibutylaniline[73]

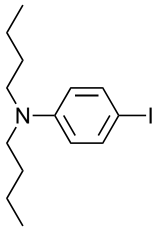

4-Iodoaniline (5.00 g, 22.8 mmol) was mixed with butyl iodide (10 mL, 88.0 mmol) with Na_2CO_3 (8.00 g) in DMF (13 mL). The mixture was degassed and then stirred under Ar for 18 h at 100 ºC. The crude mixture was diluted with toluene, washed with water. The crude reaction was again mixed with chloroform and washed with water (3 × 200 mL) and dried over Na_2SO_4. The solvent was evaporated and the crude material was purified by column chromatography on silica (9:1 40–60 °C petrol ether:CH_2Cl_2). **Yield:** 7.6 g, 100%. **^{1}H NMR** (400 MHz, $CDCl_3$) δ/ppm: 7.41 (d, 2 H, $^3J = 9.09$ Hz, Ar-H), 6.41 (d, 2 H, $^3J = 9.17$ Hz, Ar-H), 3.22 (t, 4 H, $^3J = 7.53$ Hz), 1.53 (m, 4 H), 1.33 (m, 4H), 0.94 (t, 6 H, $^3J = 7.34$ Hz). **^{13}C NMR** (100 MHz, $CDCl_3$)

δ/ppm: 147.7, 137.7, 114.1, 100.1, 50.8, 29.3, 20.4, 14.1. ***m/z* (ESI+)** 332.0, 333.0 ($C_{14}H_{22}IN$, M+H requires 332.0, M+2H requires 333.0).

5,15-bis[(trihexylsilyl)ethynyl]porphyrin 8[2,74]

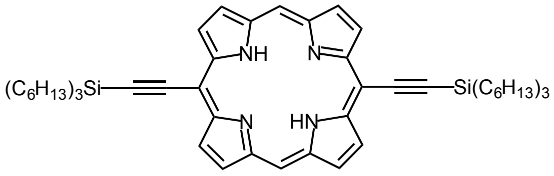

Porphyrin **8** was prepared according to an adapted literature procedure.[74] Dipyrromethane (1.55 g, 10.60 mmol) was dried *in vacuo* for 1 h before addition of dry CH_2Cl_2 (600 mL) and trihexylsilyl propynal (3.7 g, 11.00 mmol). The solution was freeze-pump-thaw-degassed and $BF_3.OEt_2$ (450 µL, 3.64 mmol) was added and the mixture was stirred at room temperature for 45 min in the dark. After this time, DDQ (3.43 g, 15.11 mmol) was added and the mixture was stirred under air for 10 min. The crude mixture was passed through a large silica plug (CH_2Cl_2) and further purified by flash chromatography on silica (4:1 40–60 °C petrol ether: CH_2Cl_2). Fractions were evaporated to give **8** as a purple oil. **Yield:** 1.65 g, 16.8%. **^{1}H NMR** (400 MHz, $CDCl_3$ with 1% C_5D_5N) δ/ppm: 10.09 (s, 2 H, meso-*H*), 9.67 (d, 4 H, ^3J = 4.5 Hz, β- *H*), 9.28 (d, 4 H, ^3J = 4.5 Hz, β- *H*), 1.86–1.74 (m, 12 H, hexyl-H), 1.64–1.54 (m, 12 H, hexyl-H), 1.50–1.35 (m, 24 H, hexyl-H), 1.10-1.02 (m, 12 H, hexyl-H), 0.93 (t, 18 H, ^3J = 7.06 Hz, hexyl-H).

5.51 Synthesis of porphyrin 2 with zinc metalation route (see Scheme 2)

Zinc-5,15-bis[(trihexylsilyl)ethynyl]porphyrin 12

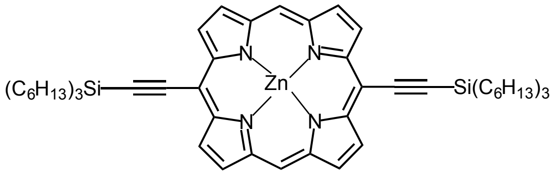

To a stirred solution of 10,20-bis-((trihexylsilyl)acetylene)-porphyrin **8** (450 mg, 0.48 mmol) in CH_2Cl_2 (180 mL) a solution of zinc acetate di-hydrate (1.7 g, 7.74 mmol) in MeOH (20 mL) was added. Reaction mixture was refluxed for 3 h. The solvent was then evaporated and obtained crude solid was purified by flash chromatography on silica (PET ether 40–60 °C : EtOAc : Py 10 : 1 : 1). **Yield:** 456 mg, 95%. **^{1}H NMR** (400 MHz, $CDCl_3$ with 1% C_5D_5N) δ/ppm: 9.83 (s, 2 H, meso-H), 9.61 (d, 4H, *J* = 4.4 Hz, β-H), 9.15 (d, 4H, *J* = 4.4 Hz, β- H), 1.93–1.82 (m, 12 H, hexyl-H), 1.70–1.60 (m, 12 H, hexyl-H), 1.56–1.40 (m, 24 H, hexyl-H), 1.16–1.07 (m, 12 H, hexyl-H), 0.97 (t, 18H, ^3J = 7.0 Hz, hexyl-H).

Zinc-5-ethynyl-15-[(trihexylsilyl)ethynyl]porphyrin 13

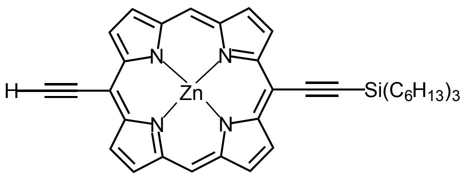

This porphyrin **13** was prepared according to a literature procedure.[2] Zinc-5,15-bis[(trihexylsilyl)ethynyl]porphyrin **12** (350 mg) was dissolved in mixture of $CHCl_3$ (8 mL), CH_2Cl_2 (8 mL), and pyridine (4 mL) and stirred at RT. The solution was put under Ar before *n*-Bu_4NF (0.36 mL, 1 M in THF,) was added. The reaction was carefully monitored by TLC (PET ether 40- 60 °C : EtOAc : Py, 10 : 1 : 1) - spotted every 10 min. When starting material and monodeprotected product appeared roughly equal in intensity, the reaction was quenched by pouring directly onto a silica plug in CH_2Cl_2. Crude reaction mixture was purified by flash chromatography on SiO_2 (PET ether 40–60 °C : EtOAc : Py 20 : 1 : 1 to 10 : 1 : 1 to 7.5 : 1 : 1). Fractions containing monodeprotected porphyrin product were evaporated to dryness to give **13** as a green glass. **Yield:** 131 mg, 53%. **^{1}H NMR** (400 MHz, $CDCl_3$ with 1% C_5D_5N) δ/ppm: 9.95 (s, 2H, meso-H), 9.68 (d, 2H, ^3J = 4.3 Hz, β-H), 9.63 (d, 2H, ^3J = 4.3 Hz, β-H), 9.18 (m, 4H, β-H), 4.17 (s, 1H, acetylene-H), 1.92–1.82 (m, 6H, hexyl-H), 1.69–1.59 (m, 6H, hexyl-H), 1.55–1.39 (m, 12H, hexyl-H), 1.15–1.05 (m, 6H, hexyl-H), 0.97 (t, 9 H, ^3J = 7.0 Hz, hexyl-H).

Zinc- *N*,*N*-dibutyl-4-({15-[(trihexylsilyl)ethynyl]porphyrin-5-yl}ethynyl)aniline 14

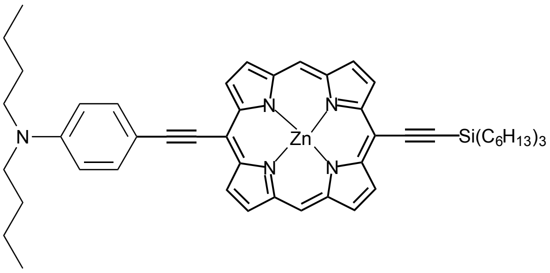

This porphyrin **14** was prepared according to an adapted literature procedure.[2] Zinc-5-ethynyl-15-[(trihexylsilyl)ethynyl]porphyrin, **13**, (131 mg, 0.186 mmol), $Pd_2(dba)_3$ (16 mg, 0.018 mmol), PPh_3 (18 mg, 0.068 mmol), and CuI (3.5 mg, 0.018 mmol) were transferred and dried in a Schlenk tube in vacuo for 1 h. DIPA (6 mL) and THF (6 mL) were added and the reaction mixture thoroughly freeze-pump-thaw degassed (3 cycles). 4-iodo-*N*,*N*-dibutylaniline (600 mg, 1.81 mmol) was added to the reaction mixture and the mixture was stirred at 50 °C for 1 h under Ar. Progress of the reaction was monitored by TLC (PET ether 40–60 °C : EtOAc : Py 10 : 1 : 1). Upon completion, the mixture was passed through a silica plug (PET ether 40–60 °C : EtOAc 3 : 1), concentrated and purified by flash chromatography on SiO_2 (PET ether 40–60 °C : CH_2Cl_2: Py 20 : 1 : 1 to 10 : 1 : 1 to pure CH_2Cl_2). Product **14** was obtained as a green glass. **Yield:** 110 mg, 65%. **^{1}H NMR** (400 MHz, $CDCl_3$ with 1% C_5D_5N) δ/ppm: 10.02 (s, 2H, meso-H), 9.85 (d, 2H, ^3J = 4.3 Hz, β-H), 9.75 (d, 2H, ^3J = 4.1 Hz, β-H), 9.29 (m, 4H, β-H), 7.91 (d, 2H, ^3J = 8.8 Hz, aniline-H), 6.82 (d, 2H, ^3J = 8.8 Hz, aniline-H), 3.41 (m, 4H, butyl-H), 1.88–1.78 (m, 6H, hexyl-H), 1.75–1.36 (m, 28H, butyl-H, hexyl-H), 1.10–1.00 (m, 10H, butyl-H, hexyl-H), 0.95(m, 9H, hexyl-H). **^{13}C NMR** (100 MHz, $CDCl_3$) δ/ppm: 152.7, 151.8, 149.3, 149.2, 148.3, 145.8, 145.8, 135.9, 133.1, 132.2, 131.8, 131.4, 131.3, 122.8, 111.7, 107.5, 102.4, 99.0, 98.8, 98.2, 51.0, 33.5, 31.9, 29.6, 24.6, 22.9, 20.5, 14.4, 14.2, 14.2. ***m/z* (MALDI-ToF)**: 905.66, 906.60, 907.54 ($C_{56}H_{71}N_5SiZn$, M requires 905.48, M+H requires 906.48, M+2H requires 907.47.0).

Zinc- *N*,*N*-dibutyl-4-[(15-ethynylporphyrin-5-yl)ethynyl]aniline 15

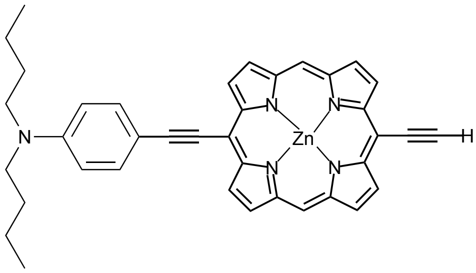

Intermediate porphyrin **14** was prepared according to literature procedure.[2] TBAF (1.0 M in THF, 0.715 mL, 0.715 mmol) was added to a solution of **14** (130 mg, 0.143 mmol) in a mixture of $CHCl_3$ (2 mL) and CH_2Cl_2 (3 mL) and stirred for 30 min at RT. The reaction mixture was passed through a silica plug (CH_2Cl_2) and evaporated to dryness to give **15**. **Yield:**100 mg, 100%. The crude product mixture contained trihexylsilane as byproduct. The crude product mixture was taken forward for Sonogashira coupling without any further purification because of high reactivity of the product. **^{1}H NMR** (400 MHz, $CDCl_3$ with 1% C_5D_5N) δ/ppm: 9.97 (s, 2H, meso-H), 9.85 (d, 2H, ^3J = 4.3 Hz, β-H), 9.73 (d, 2H, ^3J = 4.1 Hz, β-H), 9.27 (m, 4H, β-H), 7.92 (d, 2H, ^3J = 8.8 Hz, aniline-H), 6.81 (d, 2H, ^3J = 8.8 Hz, aniline-H), 4.16 (s, 1H, acetylene-H), 3.38 (m, 4H, butyl-H), 1.72–1.62 (m, 4H, butyl-H), 1.49–1.39 (m, 4H, butyl-H), 1.02 (t, 6H, ^3J = 7.3 Hz, butyl-H).

Zinc- *N*,*N*-dibutyl-4-({15-[(pyridin-4-yl)ethynyl]porphyrin-5-yl}ethynyl)aniline 16

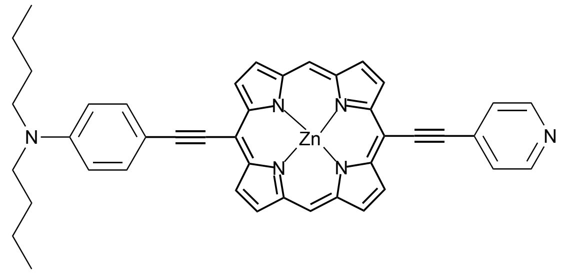

Porphyrin **16** was prepared according to literature procedure.[2] Zinc- *N*,*N*-dibutyl-4-[(15-ethynylporphyrin-5-yl)ethynyl]aniline **15** (100 mg, 0.16 mmol) was mixed with $Pd_2(dba)_3$ (13 mg, 10 μmol), PPh3 (15 mg, 57.1 μmol), CuI (4 mg, 21 μmol) and 4-iodopyridine (370 mg, 1.8 mmol) were dried *in vacuo* for 1 h before DIPA (6 mL) and THF (6 mL) were added and the mixture freeze-pump-thaw degassed. The mixture stirred at 40°C for 3 h under Ar. Upon completion, the mixture was passed through a silica plug (CH_2Cl_2) then purified by flash chromatography (CH_2Cl_2:THF 6:1 to 3:1) and the fractions were evaporated to dryness. The product mixture was recrystallized (MeOH layered over $CHCl_3$) to give **16** as a green solid. **Yield:** 72 mg, 64%. **^{1}H NMR** (400 MHz, $CDCl_3$ with 1% C_5D_5N) δ/ppm: 10.03 (s, 2H, meso-H), 9.84 (d, 2H, ^3J = 4.3 Hz, β-H), 9.76 (d, 2H, ^3J = 4.3 Hz, β-H), 9.33 (d, 2H, ^3J = 4.3 Hz, β-H), 9.29 (d, 2H, ^3J = 4.3 Hz, β-H), 8.78 (d, 2H, ^3J = 8.8 Hz, pyridine-H), 7.89 (m, 4H, pyridine-H, aniline-H), 6.81 (d, 2H, ^3J = 8.8 Hz, aniline-H), 3.41 (m, 4H, butyl-H), 1.74–1.64 (m, 4H, butyl-H), 1.49–1.39 (m, 4H, butyl-H), 1.03 (t, 6H, ^3J = 7.3 Hz, butyl-H). **^{13}C NMR** (100 MHz, $CDCl_3$) δ/ppm: 152.2, 151.6, 149.3, 149.2, 149.1, 136.0, 133.1, 132.5, 131.8, 131.5, 130.5, 125.2, 123.6, 123.3, 123.0, 122.8, 111.6, 109.6, 107.9, 50.9, 29.5, 20.5, 14.2. ***m/z* (MALDI-ToF)**: 700.20, 701.17, 702.15 ($C_{43}H_{36}N_6Zn$, M requires 700.23, M+H requires 701.23, M+2H requires 702.23).

***N*,*N*-dibutyl-4-({15-[(pyridin-4-yl)ethynyl]porphyrin-5-yl}ethynyl)aniline 2 (synthesized by zinc metalation route)**

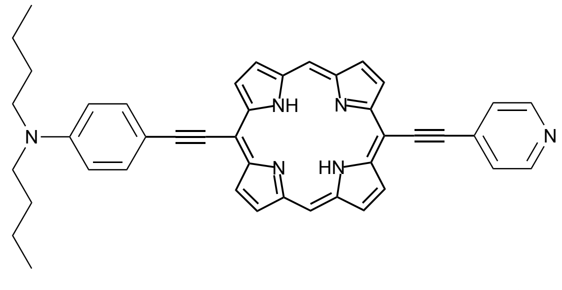

Porphyrin **2** was prepared according to literature procedure.[2] Zinc- *N*,*N*-dibutyl-4-({15-[(pyridin-4-yl)ethynyl]porphyrin-5-yl}ethynyl)aniline **16** (72 mg, 0.10 mmol) was dissolved in DCM (50 mL) mixed with 1% v/v trifluoro acetic acid and stirred at RT for 1 h. The stirring was stopped and the reaction mixture was washed with 50 mL of sat. Na_2CO_3 solution and three times with water. The crude mixture was dried over Na_2SO_4 and then purified by silica-based column chromatography (DCM:THF 5:1). The product was recrystallized to give **2** as a dark green solid. Please note that 15 mg of material was isolated as a pure material while 20 mg was impure after recrystallization. **Yield:** 15 mg, 23%. **^{1}H NMR** (400 MHz, $CDCl_3$) δ/ppm: 10.01 (s, 2H, meso-H), 9.72 (d, 2H, ^3J = 4.5 Hz, β-H), 9.61 (d, 2H, ^3J = 4.5 Hz, β-H), 9.26 (d, 2H, ^3J = 4.5 Hz, β-H), 9.24 (d, 2H, ^3J = 4.5 Hz, β-H), 8.76 (m, 2H, pyridine-H), 7.91 (d, 2H, ^3J = 8.6 Hz, aniline-H), 7.86 (m, 2H, pyridine-H), 6.83 (d, 2H, ^3J = 8.8 Hz, aniline-H), 3.43 (t, 4H, ^3J = 7.7 Hz, butyl-H), 1.77–1.67 (m, 4H, butyl-H), 1.51–1.41 (m, 4H, butyl-H), 1.05 (t, 6H, ^3J = 7.4 Hz, butyl-H), −2.44 (br s, 2H, -NH). ***m/z* (MALDI-ToF)**: 638.54, 639.54, 640.54 ($C_{43}H_{38}N_6$, M requires 638.32, M+H requires 639.32, M+2H requires 640.32).

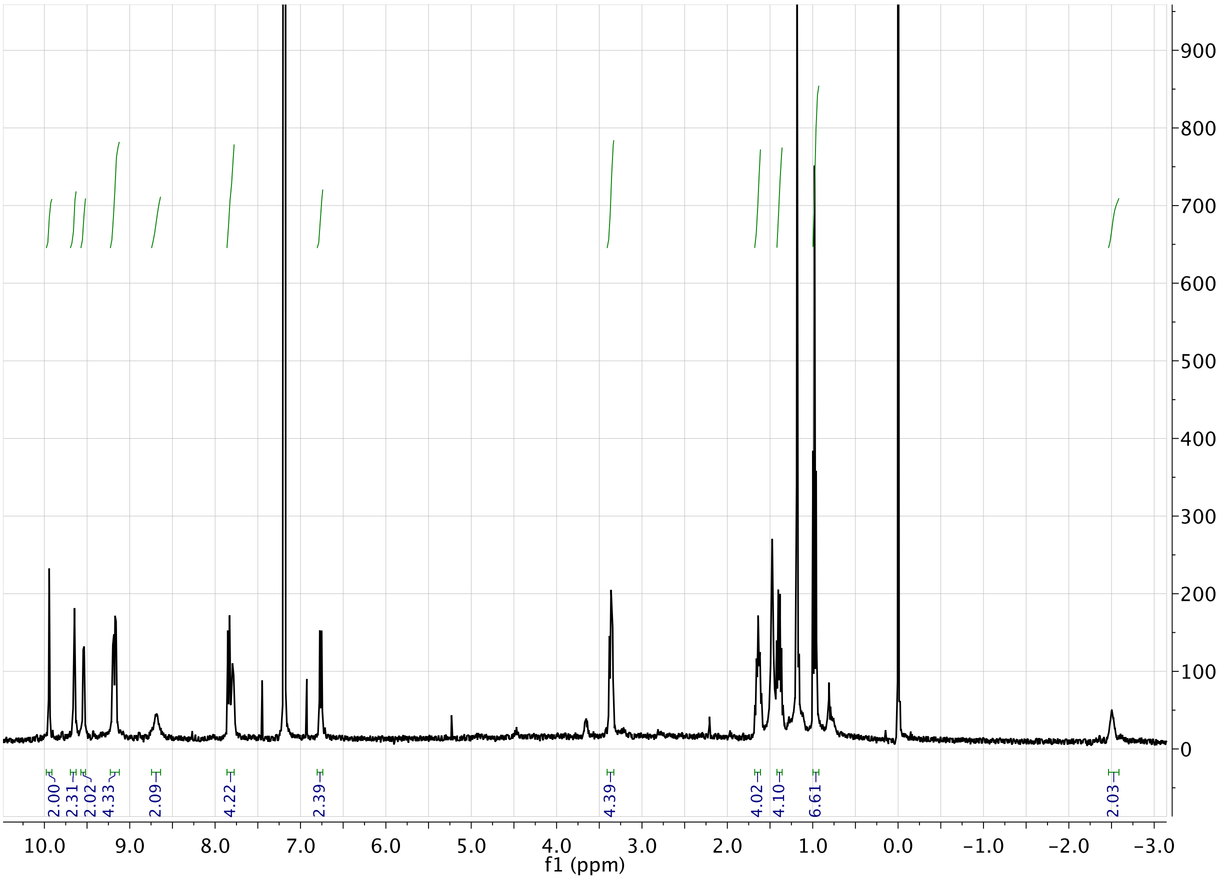

Figure 26: ^{1}H-NMR spectrum of **2** synthesized by zinc metalation route ($CDCl_3$,400 MHz, 25 °C).

5.52 Synthesis of porphyrin 2 with free-base porphyrin route (see Scheme 2)

5-ethynyl-15-[(trihexylsilyl)ethynyl]porphyrin 9

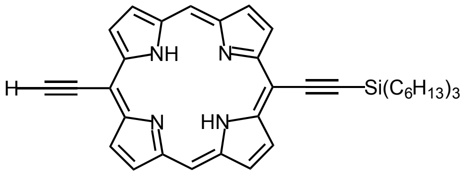

Porphyrin **9** was prepared according to literature procedure.[2] Amylene stabilized $CHCl_3$ was passed through alumina and then mixed with 1% of dry EtOH. Porphyrin **8** (500 mg, 0.54 mmol) was dissolved in the $CHCl_3$ (25 mL). The solution was put under Ar before *n*-Bu_4NF (0.54 mL, 1 M in THF,) was added. The reaction was carefully monitored by TLC (PET ether 40- 60 °C : EtOAc 10 : 1) - spotted every 10 min. When starting material and monodeprotected product appeared roughly equal in intensity, the reaction was quenched by pouring directly onto a silica plug in CH_2Cl_2. Crude reaction mixture was purified by flash chromatography on SiO_2 (PET ether 40–60 °C : EtOAc 20 : 1 : 1). Fractions containing monodeprotected porphyrin **9** were evaporated to dryness to give a purple glass. **Yield:** 145 mg, 42%. **^{1}H NMR** (400 MHz, $CDCl_3$) δ/ppm: 9.83 (s, 2H, meso-H), 9.57 (d, 2H, ^3J = 4.3 Hz, β-H), 9.52 (m, 2H, β-H), 9.13 (m, 4H, β-H), 4.21 (s, 1H, acetylene-H), 1.92–1.82 (m, 6H, hexyl-H), 1.70–1.60 (m, 6H, hexyl-H), 1.56–1.40 (m, 12H, hexyl-H), 1.16–1.06 (m, 6H, hexyl-H), 0.98 (t, 9 H, ^3J = 7.0 Hz, hexyl-H), −3.65 (br s, 2H, -NH).

N,*N*-dibutyl-4-({15-[(trihexylsilyl)ethynyl]porphyrin-5-yl}ethynyl)aniline 10

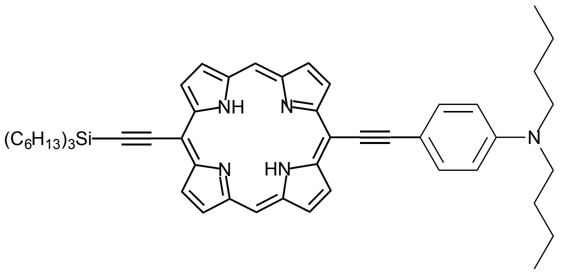

The porphyrin **10** was prepared according to an adapted literature procedure.[2] 5-ethynyl-15-[(trihexylsilyl)ethynyl]porphyrin **9**, (140 mg, 0.218 mmol), $Pd_2(dba)_3$ (22 mg, 0.021 mmol), PPh_3 (25 mg, 0.095 mmol), and CuI (5 mg, 0.026 mmol) were transferred and dried in a Schlenk tube in vacuo for 1 h. DIPA (8 mL) and toluene (8 mL) were added and the reaction mixture thoroughly freeze-pump-thaw degassed (3 cycles). 4-Iodo-*N*,*N*-dibutylaniline (721 mg, 2.18 mmol) was added to the reaction mixture and the mixture was stirred at 50 °C for 1 h under Ar. Progress of the reaction was monitored by TLC (PET ether 40–60 °C : EtOAc 10 : 1). Upon completion, the mixture was passed through a silica plug (CH_2Cl_2), concentrated and purified by flash chromatography on SiO_2 (PET ether 40–60 °C : CH_2Cl_2 20 : 1 : 1 to 10 : 1 : 1 to 5: 1 : 1). Porphyrin **10** was obtained as a green glass. **Yield:** 172 mg, 93%. **^{1}H NMR** (400 MHz, $CDCl_3$) δ/ppm: 9.91 (s, 2H, meso-H), 9.65 (m, 2H, β-H), 9.58 (d, 2H, ^3J = 4.3 Hz, β-H), 9.18 (m, 4H, β-H), 7.92 (d, 2H, ^3J = 8.6 Hz, aniline-H), 6.84 (d, 2H, ^3J = 8.6 Hz, aniline-H), 3.42 (t, 4H, ^3J = 7.8 Hz ,butyl-H), 1.90–1.80 (m, 6H, hexyl-H), 1.77–1.38 (m, 26H, butyl-H, hexyl-H), 1.13–1.03 (m, 12H, butyl-H, hexyl-H), 0.97 (t, 9H, ^3J = 6.8 Hz, hexyl-H), −2.83 (br s, 2H, -NH). ***m/z* (MALDI-ToF)**: 843.57, 844.56, 845.56 ($C_{56}H_{73}N_5Si$, M requires 843.56, M+H requires 844.56, M+2H requires 845.56).

N,N-dibutyl-4-[(15-ethynylporphyrin-5-yl)ethynyl]aniline 11

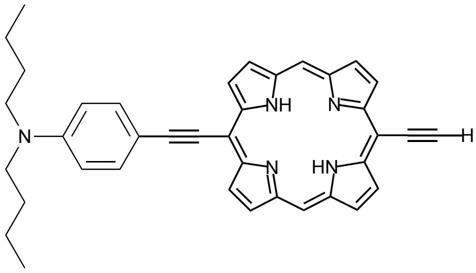

Intermediate porphyrin **11** was prepared as follows: TBAF (1.0 M in THF, 0.402 mL, 0.402 mmol) was added to a solution of **10** (170 mg, 0.201 mmol) in CH_2Cl_2 (30 mL) and stirred for 20 min at RT. The reaction mixture was passed through a silica plug (CH_2Cl_2) and evaporated to dryness to give **11**. **Yield:**112 mg, 100%. The crude product mixture contained trihexylsilane as byproduct. The crude product mixture was taken forward for Sonogashira coupling without any further purification because of high reactivity of the product. **^{1}H NMR** (400 MHz, $CDCl_3$) δ/ppm: 10.01 (s, 2H, meso-H), 9.72 (d, 2H, ^3J = 4.5 Hz, β-H), 9.63 (d, 2H, ^3J = 4.5 Hz, β-H), 9.25 (m, 4H, β-H), 7.91 (d, 2H, ^3J = 8.8 Hz, aniline-H), 6.83 (d, 2H, ^3J = 8.8 Hz, aniline-H), 4.20 (s, 1H, acetylene-H), 3.43 (m, 4H, butyl-H), 1.75–1.65 (m, 4H, butyl-H), 1.52–1.42 (m, 4H, butyl-H), 1.05 (t, 6H, ^3J = 7.4 Hz, butyl-H), −2.61 (br s, 2H, -NH).

N,*N*-dibutyl-4-({15-[(pyridin-4-yl)ethynyl]porphyrin-5-yl}ethynyl)aniline 2

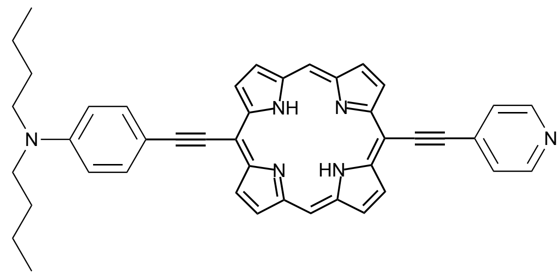

Porphyrin **2** was prepared according to literature procedure.[2] *N*,*N*-dibutyl-4-[(15-ethynylporphyrin-5-yl)ethynyl]aniline **11** (112 mg, 0.201 mmol) was mixed with $Pd_2(dba)_3$ (18 mg, 20.1 μmol), PPh_3 (21 mg, 80.0 μmol), CuI (4 mg, 21.0 μmol) and 4-iodopyridine (400 mg, 2.014 mmol) were dried *in vacuo* for 1 h before DIPA (9 mL) and toluene (9 mL) were added and the mixture freeze-pump-thaw degassed. The mixture stirred at 40°C for 3 h under Ar. Upon completion, the mixture was passed through a silica plug (CH_2Cl_2 with 5% MeOH) then purified by flash chromatography (CH_2Cl_2:THF 5:1 to 3:1) and the fractions were evaporated to dryness. The product mixture was recrystallized (MeOH layered over $CHCl_3$) to give **2** as a green solid. **Yield:** 115 mg, 90%. **^{1}H NMR** (400 MHz, $CDCl_3$) δ/ppm: 9.89 (s, 2H, meso-H), 9.66 (m, 2H, β-H), 9.52 (m, 2H, β-H), 9.16 (m, 4H, β-H), 8.84 (m, 2H, pyridine-H), 7.91 (d, 2H, ^3J = 8.8 Hz, aniline-H), 7.88 (m, 2H, pyridine-H), 6.84 (d, 2H, ^3J = 8.8 Hz, aniline-H), 3.44 (m, 4H, butyl-H), 1.77–1.67 (m, 4H, butyl-H), 1.53–1.43 (m, 4H, butyl-H), 1.05 (t, 6H, ^3J = 7.4 Hz, butyl-H), −2.61 (br s, 2H, -NH). ***m/z* (MALDI-ToF)**: 638.89, 639.84, 630.79 ($C_{43}H_{38}N_6$, M requires 638.31, M+H requires 639.31, M+2H requires 640.31). **UV-Vis** (DMF, 25 ºC) λ_{max} (log ε): 692 nm (4.36), 614 nm (4.41), 422 nm (4.89).

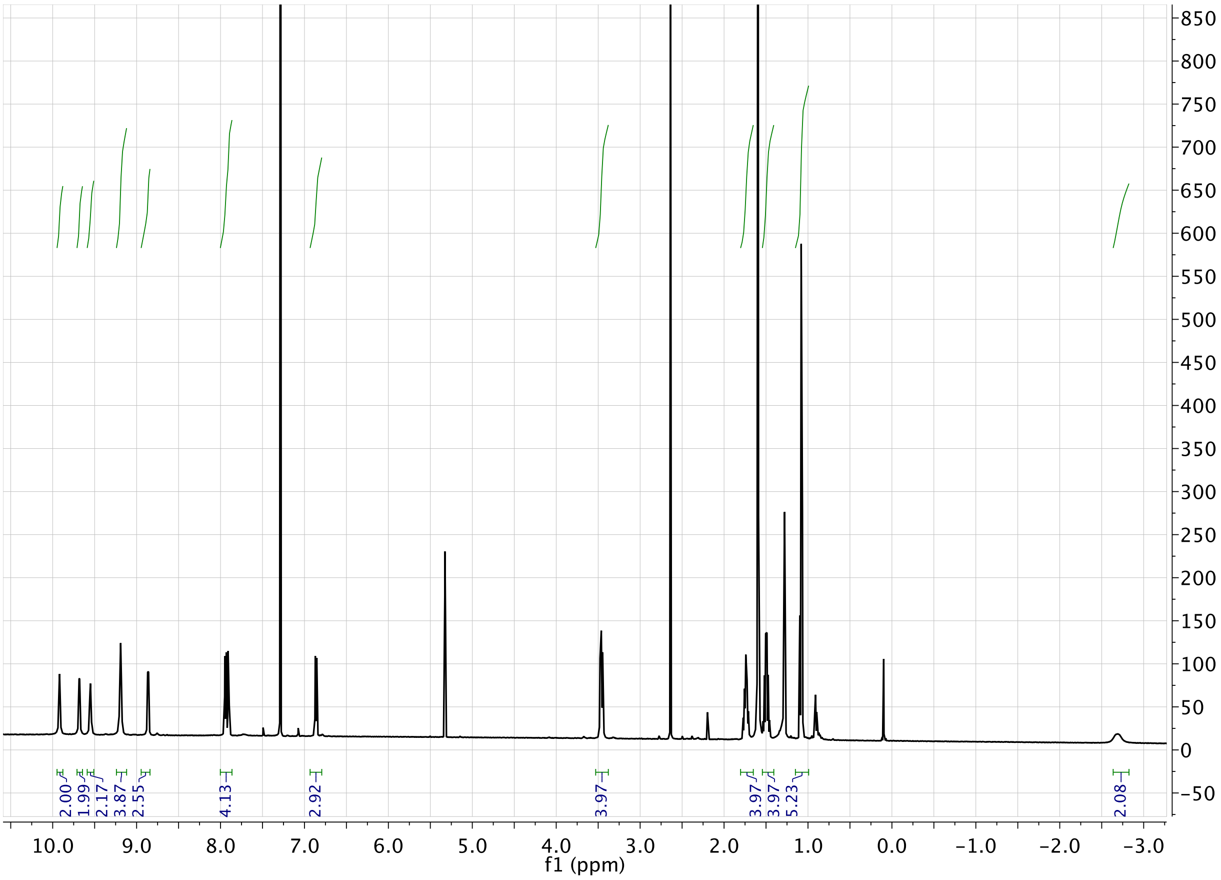

Figure 27: ^{1}H- NMR spectrum of **2** synthesized by free-base porphyrin route ($CDCl_3$,400 MHz, 25 ºC). The spectrum is cleaner than the spectrum of **2** synthesized by zinc metalated route as shown in Figure 26.

3-(Dimethylamino)-*N*,*N*,*N*-trimethylpropan-1-aminium iodide 18[11]

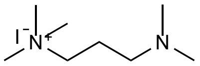

3-(Dimethylamino)-*N*,*N*,*N*-trimethylpropan-1-aminium iodide **18** was prepared according to literature procedure.[11] Briefly, *N*,*N*,*N*′,*N*′-tetramethyl-1,3-propanediamine **17** (5 g) was dissolved in diethyl ether (100 mL) and stirred. Methyl iodide (2.38 mL, 1 eq.) was added dropwise and the reaction mixture was stirred for 20 min until white precipitate formed. The white precipitate was washed with water (100 mL) three times and dried under high vacuum to yield **18** as a white amorphous powder. **Yield:** 1.45 g, 14%. **^{1}H NMR** (400 MHz, D_2O) δ/ppm: 3.31 (m, 2H), 3.12 (s, 9H), 2.41 (m, 2H), 2.21 (s, 6H), 1.96 (m, 2H). **^{13}C NMR** (100 MHz, D_2O) δ/ppm: 64.7, 54.6, 52.8, 43.6, 20.1. **m/z (ESI+)** 145.2, 146.2 ($C_8H_{21}N_2^+$ M^+ requires 145.2, $C_8H_{22}N_2^+$ $[M+H]^+$ requires 146.2).

N^1-(3-Iodopropyl)-*N*^{1},*N*^{1},*N*^{3},*N*^{3},*N*^{3}-pentamethylpropane-1,3-bis(aminium)-diiodide 19

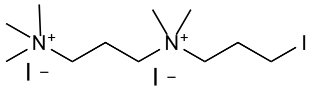

3-(Dimethylamino)-*N*,*N*,*N*-trimethylpropan-1-aminium iodide **18** (600 mg) was dissolved in acetonitrile (5 mL) and stirred followed by addition of 1,3-diiodpropane (2.7 mL, 10 eq.). The reaction mixture was refluxed for 24 h. The solvent was evaporated under reduced pressure to form yellow solid powder, which was washed with acetone to give white powder as **19**. **Yield:** 1.2 g, 93%. **^{1}H NMR** (400 MHz, D_2O) δ/ppm: 3.52 (m, 2H), 3.45 (m, 4H), 3.29 (t, 2H, ^3J = 6.4 Hz), 3.21 (s, 9H), 3.18 (s, 6H), 2.36 (m, 4H). **^{13}C NMR** (100 MHz, D_2O) δ/ppm: 62.3, 64.9, 60.0, 53.2, 51.0, 25.5, 17.0, -0.3. **m/z (ESI+)** 441.0 **(**$C_{11}H_{27}I_2N_2^+$ M^+ requires 441.0).

N^1-(3-Iodopropyl)-*N*^{1},*N*^{1},*N*^{3},*N*^{3},*N*^{3}-pentamethylpropane-1,3-bis(aminium)-di(hexafluorophosphate) 20

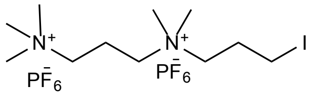

N^1-(3-Iodopropyl)-*N*^{1},*N*^{1},*N*^{3},*N*^{3},*N*^{3}-pentamethylpropane-1,3-bis(aminium)-diiodide **19** (1.00 g) was dissolved in water just below saturation concentration. Ammonium hexafluorophosphaste (3 eq.) solution in water was added dropwise and stirred at RT for 15 min to form precipitates. The precipitate was washed with water (100 mL) and dried under high vacuum to give product **20** as white solid. **^{1}H NMR** (400 MHz, d_6–DMSO) δ/ppm: 3.38 (m, 2H), 3.31 (m, 4H), 3.24 (t, 2H, ^3J = 6.8 Hz), 3.11 (s, 9H), 3.09 (s, 6H), 2.22 (m, 4H). **^{13}C NMR** (100 MHz, d_6–DMSO) δ/ppm: 63.9, 61.8, 59.6, 52.6, 50.6, 25.8, 16.8, 1.5. **m/z (ESI+)** 459.0, 460.0.0 **(**$C_{11}H_{27}F_6IPN_2^+$ M^+ requires 459.0, $C_{11}H_{28}F_6IPN_2^+$ $[M+H]^+$ requires 460.0).

4-[(15-{[4-(dibutylamino)phenyl]ethynyl}porphyrin-5-yl)ethynyl]-1-(3-{dimethyl[3-(trimethylazaniumyl)propyl]azaniumyl}propyl)pyridin-1-ium trichloride 1

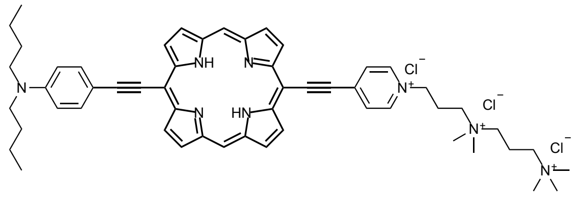

N,*N*-Dibutyl-4-({15-[(pyridin-4-yl)ethynyl]porphyrin-5-yl}ethynyl)aniline **2** (15 mg, 22.5 μmol) was mixed with *N*^{1}-(3-iodopropyl)-*N*^{1},*N*^{1},*N*^{3},*N*^{3},*N*^{3}-pentamethylpropane-1,3-diaminium-di(hexafluorophosphate) **20** (600 mg, 1 mmol, 45 eq.) and dried under high vacuum at 50 °C for 4 h. Dry dimethylacetamide (1.5 mL) was added to the mixture under presence of Ar gas and the reaction mixture was stirred at 115 °C for 6 h in inert atmosphere. TLC (20% THF in DCM) confirmed the consumption of starting material. Solvent was evaporated from crude mixture which was then purified by size column chromatography (SX-1 beads in DMF). The second band (product) obtained from the size column chromatography was passed through fresh Dowex 1X8 chloride form ion-exchange chromatography column. The reaction mixture was then sequentially washed with water (3 x 30 mL), MeOH (3 x 30 mL) and diethyl ether (1 x 30 mL). The process of ion-exchange and washing was repeated. In the end, the reaction mixture was again passed through size column chromatography (SX-1 beads in DMF). The solvent was evaporated under reduced pressure to yield the product **1** as green solid. **Yield:** 11 mg, 50%. **^{1}H NMR** (500 MHz, d$_6$–DMSO at 50 °C) δ/ppm: 10.46 (s, 2H, meso-H), 9.90 (d, 2H, ^3J = 4.5 Hz, β-H), 9.78 (d, 2H, ^3J = 4.5 Hz, β-H), 9.65 (d, 2H, ^3J = 4.5 Hz, β-H), 9.56 (d, 2H, ^3J = 4.5 Hz, β-H), 9.28 (d, 2H, ^3J = 6.1 Hz, pyridine-H), 9.00 (d, 2H, ^3J = 6.1 Hz, pyridine-H), 7.99 (d, 2H, ^3J = 8.4 Hz, aniline -H), 6.92 (d, 2H, ^3J = 8.4 Hz, aniline-H), 4.77 (t, 2H, ^3J = 4.4 Hz, a-H) 3.52 (m, 2H, c-H), 3.35 (t, 4H, ^3J = 7.6 Hz, butyl-H), 3.36 (m, 4H, d-H, f-H), 3.15 (m, 15 H, g-H, h-H), 2.64–2.54 (m, 2H, b-H), 2.28–2.18 (m, 2H, e-H), 1.68–1.58 (m, 4H, butyl-H), 1.49–1.39 (m, 4H, butyl-H), 1.01 (t, 6H, ^3J = 7.4 Hz, butyl-H). ***m/z* (MALDI-ToF)**: 1114.96, 1115.96, 1116.96, 1117.96 ($C_{54}H_{65}N_8F_{12}P_2$, M requires 1115.46, M+H requires 1116.46, M+2H requires 1117.46, M+3H requires 1118.46). **UV-Vis** (DMF, 25 ºC) $\lambda_{\max}$ (log ε): 709 nm (4.37), 631 nm (4.24), 440 nm (4.67). **Quantum yield** ϕ_f (DMF, 25 ºC): 0.0033.

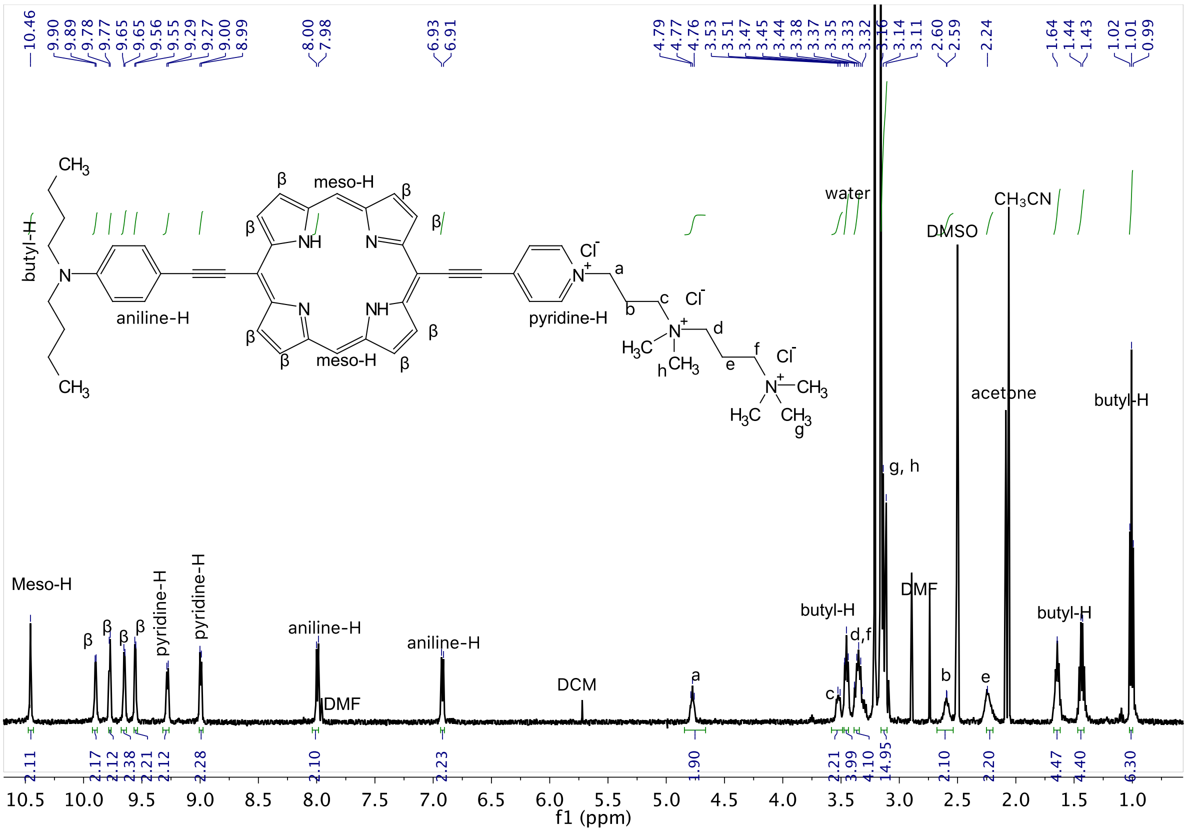

Figure 28: ^{1}H- NMR spectrum of **1 (AK-1)** (d$_6$-DMSO, 500 MHz, 50 ºC).

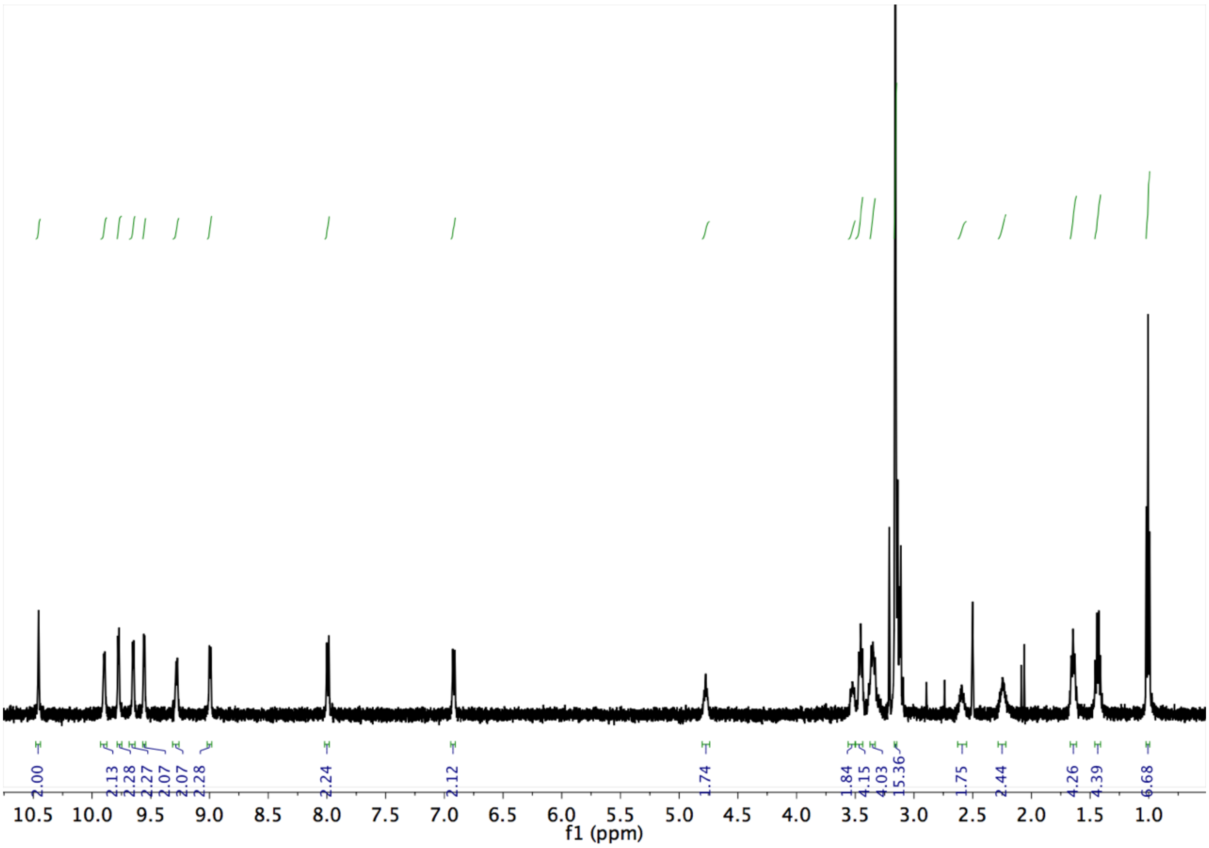

Figure 29: ^{1}H- NMR spectrum of **1 (AK-1)** (d$_6$-DMSO, 500 MHz, diffusion edited).

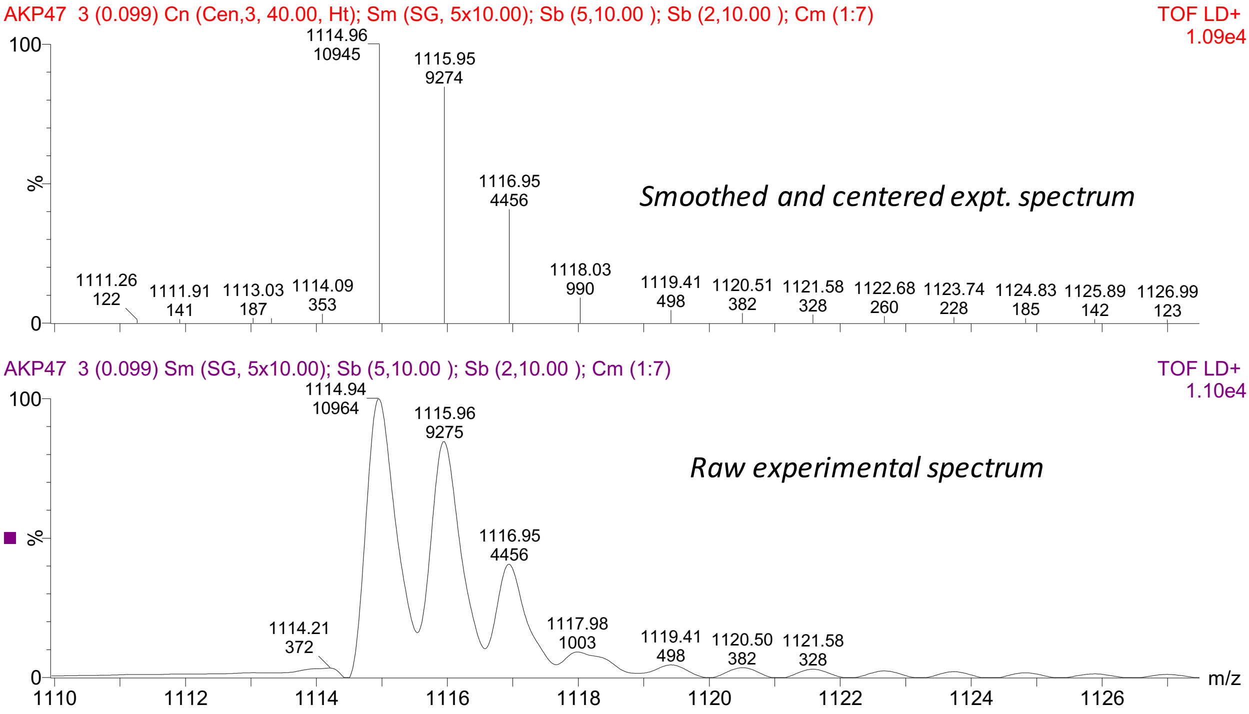

Figure 30: Isotopic mass spectra of **AK-1**.

5.60 References

1 J. E. Reeve, A. D. Corbett, I. Boczarow, W. Kaluza, W. Barford, H. Bayley, T. Wilson and H. L. Anderson, *Angew. Chem. Int. Ed.*, 2013, **52**, 9044–9048.

2 J. E. Reeve, H. A. Collins, K. De Mey, M. M. Kohl, K. J. Thorley, O. Paulsen, K. Clays and H. L. Anderson, *J. Am. Chem. Soc.*, 2009, **131**, 2758–2759.

3 A. Weinberger, F.-C. Tsai, G. H. Koenderink, T. F. Schmidt, R. Itri, W. Meier, T. Schmatko, A. Schröder and C. Marques, *Biophys. J.*, 2013, **105**, 154–164.

4 M. Garten, L. D. Mosgaard, T. Bornschlögl, S. Dieudonné, P. Bassereau and G. E. S. Toombes, *Proc. Natl. Acad. Sci.*, 2017, **114**, 328–333.

5 L. M. Loew, G. W. Bonneville and J. Surow, *Biochemistry*, 1978, **17**, 4065–4071.

6 D. A. Dombeck, L. Sacconi, M. Blanchard-Desce and W. W. Webb, *J. Neurophysiol.*, 2005, **94**, 3628–3636.

7 V. Montana, D. L. Farkas and L. M. Loew, *Biochemistry*, 1989, **28**, 4536–4539.

8 J. E. Reeve, DPhil Thesis, University of Oxford, 2012.

9 I. Lopez-Duarte, J. E. Reeve, J. Perez-Moreno, I. Boczarow, G. Depotter, J. Fleischhauer, K. Clays and H. L. Anderson, *Chem. Sci.*, 2013, **4**, 2024–2027.

10 I. López-Duarte, T. T. Vu, M. A. Izquierdo, J. A. Bull and M. K. Kuimova, *Chem. Commun.*, 2014, **50**, 5282–5284.

11 S. Yi, W. Leon, D. Vezenov and S. L. Regen, *ACS Macro Lett.*, 2016, **5**, 915–918.

12 I. López-Duarte, P. Chairatana, Y. Wu, J. Pérez-Moreno, P. M. Bennett, J. E. Reeve, I. Boczarow, W. Kaluza, N. A. Hosny, S. D. Stranks, R. J. Nicholas, K. Clays, M. K. Kuimova and H. L. Anderson, *Org. Biomol. Chem.*, 2015, **13**, 3792–3802.

13 M. Oropesa-Ávila, Y. Andrade-Talavera, J. Garrido-Maraver, M. D. Cordero, M. de la Mata, D. Cotán, M. V Paz, A. D. Pavón, E. Alcocer-Gómez, I. de Lavera, R. Lema, A. P. Zaderenko, A. Rodríguez-Moreno and J. A. Sánchez-Alcázar, *Cell Death Dis.*, 2014, **5**, e1369.

14 A. P. Demchenko, *Cytotechnology*, 2013, **65**, 157–172.

15 S. Grootjans, B. Hassannia, I. Delrue, V. Goossens, B. Wiernicki, Y. Dondelinger, M. J. M. Bertrand, D. V Krysko, M. Vuylsteke, P. Vandenabeele and T. Vanden Berghe, *Nat. Protoc.*, 2016, **11**, 1444–1454.

16 V. V. Shynkar, A. S. Klymchenko, C. Kunzelmann, G. Duportail, C. D. Muller, A. P. Demchenko, J. M. Freyssinet and Y. Mely, *J. Am. Chem. Soc.*, 2007, **129**, 2187–2193.

17 D. A. Dombeck, M. Blanchard-Desce and W. W. Webb, *J. Neurosci.*, 2004, **24**, 999–1003.

18 G. C. Carlson and D. A. Coulter, *Nat. Protoc.*, 2008, **3**, 249–255.

19 I. De Proost, I. Pintelon, I. Brouns, J. P. Timmermans and D. Adriaensen, *Cell Tissue Res.*, 2007, **329**, 421–431.

20 M. H. Mohajerani, A. W. Chan, M. Mohsenvand, J. LeDue, R. Liu, D. A. McVea, J. D. Boyd, Y. T. Wang, M. Reimers and T. H. Murphy, *Nat Neurosci*, 2013, **16**, 1426–1435.

21 A. R. Kay, A. Alfonso, S. Alford, H. T. Cline, A. M. Holgado, B. Sakmann, V. A. Snitsarev, T. P. Stricker, M. Takahashi and L.-G. G. Wu, *Neuron*, 1999, **24**, 809–817.

22 M. Drobizhev, N. S. Makarov, S. E. Tillo, T. E. Hughes and A. Rebane, *Nat. Methods*, 2011, **8**, 393–399.

23 F. Bestvater, E. Spiess, G. Stobrawa, M. Hacker, T. Feurer, T. Porwol, U. Berchner-Pfannschmidt, C. Wotzlaw and H. Acker, *J. Microsc.*, 2002, **208**, 108–115.

24 M. Nuriya, S. Fukushima, A. Momotake, T. Shinotsuka, M. Yasui and T. Arai, *Nat. Commun.*, 2016, **7**.

25 S. Awasthi, L. T. Izu, Z. Mao, Z. Jian, T. Landas, A. Lerner, R. Shimkunas, R. Woldeyesus, J. Bossuyt, B. Wood, Y. J. Chen, D. L. Matthews, D. K. Lieu, N. Chiamvimonvat, K. S. Lam, Y. Chen-Izu and J. W. Chan, *Circ. Res.*, 2016, **118**, e19–e28.
26 A. Khadria, Y. de Coene, P. Gawel, C. Roche, K. Clays and H. L. Anderson, *Org. Biomol. Chem.*, 2017, **15**, 947–956.
27 B. K. Agrawalla, H. W. Lee, W.-H. Phue, A. Raju, J.-J. Kim, H. M. Kim, N.-Y. Kang and Y.-T. Chang, *J. Am. Chem. Soc.*, 2017, **139**, 3480–3487.
28 X. Dong, J. H. Han, C. H. Heo, H. M. Kim, Z. Liu and B. R. Cho, *Anal. Chem.*, 2012, **84**, 8110–8113.
29 K. Rathore, C. S. Lim, Y. Lee and B. R. Cho, *Org. Biomol. Chem.*, 2014, **12**, 3406–3412.
30 H. Itoh, in *E-Cell System—Basic Concepts and Applications*, 2007, pp. 1–15.
31 T. Korhonen, S. L. Hänninen and P. Tavi, *Biophys. J.*, 2009, **96**, 1189–1209.
32 J. G. Jacot, H. Kita-Matsuo, K. A. Wei, H. S. V. Chen, J. H. Omens, M. Mercola and A. D. McCulloch, *Ann. N.Y. Acad. Sci.*, 2010, **1188**, 121–127.
33 T. J. Herron, P. Lee and J. Jalife, *Circ. Res.*, 2012, **110**, 609–623.
34 Q. Li, R. (Ruby) Ni, H. Hong, K. Y. Goh, M. Rossi, V. G. Fast and L. Zhou, *Sci. Rep.*, 2017, **7**, 1531.
35 M. Kovács, J. Tóth, C. Hetényi, A. Málnási-Csizmadia and J. R. Seller, *J. Biol. Chem.*, 2004, **279**, 35557–35563.
36 J. S. Allingham, R. Smith and I. Rayment, *Nat. Struct. Mol. Biol.*, 2005, **12**, 378–379.
37 Z. Liu, L. A. Van Grunsven, E. Van Rossen, B. Schroyen, J. P. Timmermans, A. Geerts and H. Reynaert, *Br. J. Pharmacol.*, 2010, **159**, 304–315.
38 A. Matiukas, B. G. Mitrea, M. Qin, A. M. Pertsov, A. G. Shvedko, M. D. Warren, A. V. Zaitsev, J. P. Wuskell, M. de Wei, J. Watras and L. M. Loew, *Hear. Rhythm*, 2007, **4**, 1441–1451.
39 N. Tandon, C. Cannizzaro, P. P.-H. G. Chao, R. Maidhof, A. Marsano, H. T. H. Au, M. Radisic and G. Vunjak-Novakovic, *Nat. Protoc.*, 2009, **4**, 155–173.
40 Y. Xia, J. B. McMillin, A. Lewis, M. Moore, W. G. Zhu, R. S. Williams and R. E. Kellems, *J. Biol. Chem.*, 2000, **275**, 1855–1863.
41 A. Brevet, E. Pinto, J. Peacock and F. E. Stockdale, *Science*, 1976, **193**, 1152–1154.
42 M. Radisic, H. Park, H. Shing, T. Consi, F. J. Schoen, R. Langer, L. E. Freed and G. Vunjak-Novakovic, *Proc. Natl. Acad. Sci. U. S. A.*, 2004, **101**, 18129–18134.
43 S. Lewenza, D. Vidal-Ingigliardi and A. P. Pugsley, *J. Bacteriol.*, 2006, **188**, 3516–3524.
44 I. Fishov and C. L. Woldringh, *Mol. Microbiol.*, 1999, **32**, 1166–1172.
45 C. S. Prasanth, S. C. Karunakaran, A. K. Paul, V. Kussovski, V. Mantareva, D. Ramaiah, L. Selvaraj, I. Angelov, L. Avramov, K. Nandakumar and N. Subhash, *Photochem. Photobiol.*, 2014, **90**, 628–640.
46 E. Reddi, M. Ceccon, G. Valduga, G. Jori, J. C. Bommer, F. Elisei, L. Latterini and U. Mazzucato, *Photochem. Photobiol.*, 2002, **75**, 462–470.
47 M. B. Spesia, D. Lazzeri, L. Pascual, M. Rovera and E. N. Durantini, *FEMS Immunol. Med. Microbiol.*, 2005, **44**, 289–295.
48 M. F. Richter, B. S. Drown, A. P. Riley, A. Garcia, T. Shirai, R. L. Svec and P. J. Hergenrother, *Nature*, 2017, **545**, 299–304.
49 T. Bhatia, P. Husen, J. Brewer, L. A. Bagatolli, P. L. Hansen, J. H. Ipsen and O. G. Mouritsen, *Biochim. Biophys. Acta - Biomembr.*, 2015, **1848**, 3175–3180.
50 A. Weinberger, F.-C. Tsai, G. H. H. Koenderink, T. F. F. Schmidt, R. Itri, W. Meier, T. Schmatko, A. Schröder and C. Marques, *Biophys. J.*, 2013, **105**, 154–164.

51 J. T. Groves, N. Ulman and S. G. Boxer, *Science*. 1997, **275**, 651–653.
52 J. E. Reeve, A. D. Corbett, I. Boczarow, T. Wilson, H. Bayley and H. L. Anderson, *Biophys. J.*, 2012, **103**, 907–917.
53 R. S. Ries, H. Choi, R. Blunck, F. Bezanilla and J. R. Heath, *J. Phys. Chem. B*, 2004, **108**, 16040–16049.
54 D. R. Hochbaum, Y. Zhao, S. L. Farhi, N. Klapoetke, C. A. Werley, V. Kapoor, P. Zou, J. M. Kralj, D. Maclaurin, N. Smedemark-Margulies, J. L. Saulnier, G. L. Boulting, C. Straub, Y. K. Cho, M. Melkonian, G. K.-S. Wong, D. J. Harrison, V. N. Murthy, B. L. Sabatini, E. S. Boyden, R. E. Campbell and A. E. Cohen, *Nat. Methods*, 2014, **11**, 825–833.
55 M. Scanziani and M. Hausser, *Nature*, 2009, **461**, 930–939.
56 A. M. Packer, D. S. Peterka, J. J. Hirtz, R. Prakash, K. Deisseroth and R. Yuste, *Nat. Methods*, 2012, **9**, 1202–1205.
57 F. Zhang, L.-P. Wang, E. S. Boyden and K. Deisseroth, *Nat. Methods*, 2006, **3**, 785–792.
58 E. S. Boyden, F. Zhang, E. Bamberg, G. Nagel and K. Deisseroth, *Nat. Neurosci.*, 2005, **8**, 1263–1268.
59 K. Deisseroth, G. Feng, A. K. Majewska, G. Miesenböck, A. Ting and M. J. Schnitzer, *J. Neurosci.*, 2006, **26**, 10380–10386.
60 J. Mattis, K. M. Tye, E. a Ferenczi, C. Ramakrishnan, D. J. O'Shea, R. Prakash, L. a Gunaydin, M. Hyun, L. E. Fenno, V. Gradinaru, O. Yizhar and K. Deisseroth, *Nat. Methods*, 2011, **9**, 159–172.
61 G. Nagel, T. Szellas, W. Huhn, S. Kateriya, N. Adeishvili, P. Berthold, D. Ollig, P. Hegemann and E. Bamberg, *Proc. Natl. Acad. Sci. U. S. A.*, 2003, **100**, 13940–13945.
62 Y. L. Huang, A. S. Walker and E. W. Miller, *J. Am. Chem. Soc.*, 2015, **137**, 10767–10776.
63 S. Willadt, M. Canepari, P. Yan, L. M. Loew and K. E. Vogt, *Front. Cell. Neurosci.*, 2014, **8**, 311–318.
64 M. Pawlicki, H. A. Collins, R. G. Denning and H. L. Anderson, *Angew. Chem. Int. Ed.*, 2009, **48**, 3244–3266.
65 J. D. Wilkinson, G. Wicks, A. Nowak-Krol, L. G. Lukasiewicz, C. J. Wilson, M. Drobizhev, A. Rebane, D. T. Gryko and H. L. Anderson, *J. Mater. Chem. C*, 2014, **2**, 6802–6809.
66 N. Buffet, É. Grelet and H. Bock, *Chem. - A Eur. J.*, 2010, **16**, 5549–5553.
67 W. I. Awad and A. O. Mohamad, *J. Org. Chem.*, 1960, **25**, 1872–1874.
68 P. Fromherz, G. Hübener, B. Kuhn and M. J. Hinner, *Eur. Biophys. J.*, 2008, **37**, 509–514.
69 B. Kuhn and P. Fromherz, *J. Phys. Chem. B*, 2003, **107**, 7903–7913.
70 S. Pagès, D. Côté and P. De Koninck, *Front. Cell. Neurosci.*, 2011, **5**, 20–30.
71 A. Krivokapic, DPhil Thesis, University of Oxford, 2002.
72 B. J. Littler, M. A. Miller, C. H. Hung, R. W. Wagner, D. F. O'Shea, P. D. Boyle and J. S. Lindsey, *J. Org. Chem.*, 1999, **64**, 1391–1396.
73 G. J. Mohr, F. Lehmann, U. W. Grummt and U. E. Spichiger-Keller, *Anal. Chim. Acta*, 1997, **344**, 215–225.
74 H. L. Anderson, *Tetrahedron Lett.*, 1992, **33**, 1101–1104.

Chapter 6

Two-Photon Microscopy of 3D Printed Tumor Spheroids

Summary: *Synthetic cellular spheroids that can mimic the spatial and physiological characteristics of the real 3D tumors will be useful for cancer-based studies, such as drug screening and understanding chemotaxis and progression of tumor. Existing spheroids do not mimic the spatial characteristics of real tumors and are not completely responsive to environmental changes. Dr. Mukherjee and coworkers developed Matrigel-based monocellular and multicellular spheroids of up to 1 mm in diameter through their new cell printing technology. In this chapter, I performed the two-photon microscopy of the spheroids (with expressed fluorescent proteins) over 7 days to study their spatial characteristics. The spheroids were composed of two different cell types, which are NIH3T3 fibroblast cells and OVCAR-5-based epithelial cancerous cells. The size of the spheroids made with only OVCAR-5 cells increased at a faster rate than the spheroids made with only NIH3T3 cells; while the multicellular spheroids made of both NIH3T3 and OVCAR-5 cells assumed a core-shell structure with the OVCAR-5 cells at the core and NIH3T3 cells at the periphery.*

6.00 Introduction

In the previous chapters, I have discussed the design, synthesis, and testing of plasma membrane bound porphyrin-based chromophores to be used as voltage-sensitive dyes by nonlinear optical microscopy. Most of the thesis deals with second harmonic generation; however, two-photon fluorescence, another nonlinear optical microscopy technique too has been found to be very useful in biological sciences. One of the biggest advantages of two-photon fluorescence microscopy is that it can be used to probe thick (up to few millimeters) biological tissues. In this chapter, I discuss the use of two-photon fluorescence microscopy to elucidate spatial properties of thick (≤1 mm) 3D tumor models.

6.01 3D cellular models

Cellular spheroids are emerging as new 3D *in vitro* model systems for various biological studies, such as understanding chemotaxis,[1] therapeutics screening,[2] understanding tumor-immune system interactions,[3] and several other biological processes.[4–8] Recently, 3D *in vitro* model systems have been shown to mimic embryogenesis[9] and parts of brain.[10,11] Although, 3D model systems have been used in various biological studies, they have found most use in cancer research.[4,12–16] Several types of 3D tumor models have been reported to study the behavior of various kinds of cancer. 3D tumor cellular models offer several advantages over 2D cell culture and *in vivo* animal –based model systems, such as

1. They are low cost compared to *in vivo* models and they can be used as high-throughput platforms.
2. They provide an ethical alternative to *in vivo* animal-based models.
3. 3D cellular models promote more interactions among the cells than 2D models, allowing the cells to retain their inherent properties.
4. Although the 3D model systems have not been shown to accurately mimic the *in vivo* model systems in whole, certain biological functions such as embryogenesis and angiogenesis have been mimicked.[9,17]
5. 3D cellular models offer the advantage of recreating each biological process or function in isolation.

Although the 3D tumor models reported so far offer several advantages, there are certain challenges associated with them. The tumor models synthesized by the current approaches are often non-reproducible in terms of size and shape, and they lack robust extracellular matrix.

Moreover, the size of most of the tumor models are less than 200 μm, while the size of a more representative model should be at least 400–500 μm to exhibit hypoxia at the core.[18,19]

Dr. Nobina Mukherjee, a postdoctoral researcher in the group of Prof. Hagan Bayley at the Chemistry Department of Oxford University, led a study to apply a new microfluidic-based approach to make Matrigel containing robust 3D tumor spheroids. Matrigel is a basement membrane extracellular matrix derived from Engelbreth-Holm-Swarm mouse tumors. It forms a 3D gel at 37 ºC and has been found to support cell morphogenesis, differentiation, and tumor growth.[20] Matrigel has been explored widely in cell biology and tissue engineering, because it resembles the matrix found in various tissues.[21] A printing technology has been developed in the Bayley group (Oxford Chemistry) to make cell-based 3D spheroidal models (Figure 1).[22–24] In this system, cells from a 2D immortalized cell culture are mixed with the Matrigel to form the bioink. This bioink is then used to develop 3D microtumors through the microfluidics-based system. The complete description of the printing technology is beyond the scope of this DPhil thesis.

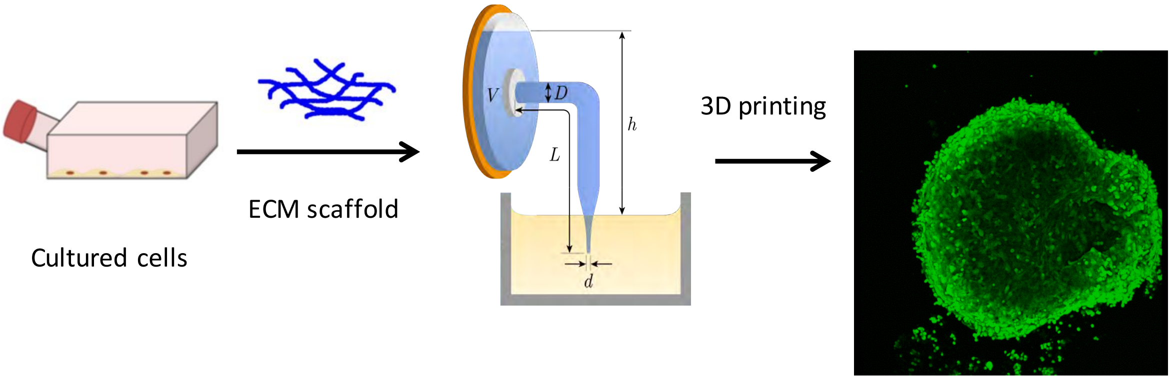

Figure 1: The cells are transfected with fluorescent proteins (e.g. GFP, RFP) and cultured. The cultured cells are embedded in an extracellular matrix scaffold, Matrigel and then printed into spheroids to the desired shape and size. In ambient cellular conditions, the spheroids behave as the tumor models. Image provided by Dr. Nobina Mukherjee.

The set-up offered several advantages over the conventional techniques, such as

1. It is low cost and can be used to develop spheroids in high throughput.
2. Spheroids are monodispersed with size variation of ≤5 %.
3. Spheroids of sizes of hundreds of microns in diameter can be obtained straight after printing without the necessity of 48 h – 1 week culture as required in the current existing approaches, such as the hanging drop method.[25,26]
4. The spheroids have a robust structural integrity maintained by gelled matrix of the Matrigel.

5. The spheroids are promising models for drug development. Preliminary studies with anticancer drug Paclitaxel showed that these spheroids are sensitive to differences in nanomolar drug concentrations.

Monodispersed spheroids of large sizes (400 μm – 800 μm) were developed to mimic nutrient and oxygen diffusion gradient, a key feature in solid tumor.

Dr. Mukherjee and coworkers developed both monocellular and multicellular models to study the efficacy of their system. They used various types of cells lines to make the models. In this chapter, I discuss two types of cell lines that they used to make the models. NIH3T3 fibroblast cells (pre-transfected with green fluorescence protein) were used as non-disease stromal cells and OVCAR-5 (pre-transfected with red fluorescence protein) epithelial cells were used as cancerous cells. The NIH3T3 stromal cells were used because they have been found to support tumor growth by playing a crucial role in the regulation of extracellular matrix required for epithelial tumor growth.[27–29] Co-culture of the stromal NIH3T3 and cancerous OVCAR-5 cells were made to mimic physiologically relevant tumor models. To study the spatial characteristics of the models, I imaged them using the multiphoton microscope, which offer several advantages as described below.

6.02 Optical microscopy

Optical microscopy is a versatile technique to study the spatial characteristics of biological systems.[30] With the advent of biocompatible fluorescent dyes and fluorescent proteins along with new commercially available imaging optical microscopes, the study of biological systems has become more accessible and increased exponentially.[31–42] The implications and benefits of laser-based fluorescence microscopy are unparalleled by any other technique. One-photon laser scanning microscopy (confocal microscope)[40,41,43] and two-photon microscopy[31,42,44] are two major optical imaging techniques used to study biological specimens. One-photon–based confocal microscopes normally employ visible light for excitation of fluorescent probes, while two-photon–based microscopes employ far-red to near infrared (NIR) light. Two-photon microscopy offers several advantages over one-photon–based confocal microscopy, which are,[31,32,42]

1. **Deep imaging**: Two-photon microscopy allows deeper imaging of biological tissues than one-photon microscopy. Although, conventional confocal microscopes employ higher energy light in the blue to red region, the light in this region get scattered more by biological tissues than the far-red to NIR light used by two-

photon microscopes.[45] One-photon–based confocal microscopes do not allow imaging of more than 100–150 μm in dense biological tissues, while two-photon microscopes have enabled high resolution imaging up to several millimeters.

2. **Less photodamage**: Two-photon microscopy causes less photo damage to live cells than one-photon microscopy. Since, two-photon microscopy employs longer wavelength light (usually >700 nm) than the one-photon microscopy (usually < 600 nm), it is less toxic to the tissues enabling long time imaging. However, in case of two-photon microscopy, the use of intense light might cause photodamage at the focal point during imaging.
3. **No out of focus signal**: Two-photon microscopy does not give out of focus photobleaching and background signal. Since, two-photon microscopy involves use of two photons simultaneously to excite the fluorescent probes, the probability of such an event is so low that it occurs only at the focal point and hence, no out of focus signal is generated. In one-photon microscopy, all the parts of the sample from which the photons travel gets illuminated.
4. **Clear signal**: Two-photon microscopy gives clearer signal than one-photon microscopy. One-photon–based confocal microscopes employ a pinhole to stop light coming from out of focus areas to reach the detectors. Such an approach normally results in decrease of overall fluorescence signals reaching the detector. Since, two-photon–based microscopes illuminate area only at the focal point, all the light illuminated by the sample is detected. Moreover, two-photon microscopy employs non-descanned detectors in which the light travels to the detector from the sample in the shortest possible path. In confocal microscopes, descanned detectors are used where light travels longer distance than in non-descanned detectors, which results in loss of fluorescence light before it reaches the detector. However, a disadvantage of two-photon microscopy is that generally the chromophores have low two-photon absorption cross-section which results in a low intensity signal.

Given the above-mentioned advantages of two-photon microscopy over one-photon microscopy, I imaged the 3D tumor models under the multiphoton microscope to study their spatial characteristics. The goal here was to image the models made of only fibroblast cells, only cancerous cells, and both fibroblast and cancerous cells, to study their time-based evolution. We hypothesize that since cancer cells (OVCAR-5 cells) multiply and grow faster than non-cancerous cells (NIH3T3 fibroblast cells), they consume nutrients at a faster rate, are soon deprived of oxygen and hence, are more likely to expand in size and create a hollow structure at the core. Multicellular models made of both fibroblast and cancerous cells should contain higher number of cancerous cells, as they outgrow fibroblasts after a few days.

6.10 Materials and methods

Dr. Mukherjee and coworkers developed spheroids of three different types,

1. Spheroids composing of only NIH3T3 fibroblast cells (transfected with green fluorescence protein, GFP).
2. Spheroids of only OVCAR-5 cancerous cells (transfected with red fluorescence protein, RFP).
3. Spheroids of both NIH3T3 (GFP) and OVCAR-5 (RFP) cells.

A complete description of development of the spheroids is not discussed here.

6.11 One-photon imaging (performed by Dr. Nobina Mukherjee)

One-photon confocal microscopy was performed on a Leica DFC7000T colour microscope camera (Leica Microsystems (UK) Ltd, UK) mounted on an inverted Leica DMi8 (Leica Microsystems) confocal laser-scanning microscope. The light was focused on the sample through a 20X HCX PL FLUOTAR focusing objective (NA = 0.5). The imaging was performed at room temperature. GFP was excited by 488 nm laser line while, RFP was excited by 540 nm laser line.

6.12 Two-photon imaging (performed by me)

General microscope specification: The imaging was performed under an upright multiphoton microscope (Olympus Fluoview FV1200MPE). The microscope is equipped with five PMT detectors (two in the reflected direction and three in the transmitted direction) and a 25X water immersion multiphoton lens objective (XLPLN25XWMP2 from Olympus) with 1.05 numerical aperture (NA) and working distance of 2 mm. The light source of the microscope is a Spectra-Physics MaiTai® eHP DeepSee™ femtosecond pulsed-laser (70 fs pulse width, 80 MHz repetition rate, continuously tunable between 690–1040 nm). The femtosecond pulsed-laser light was passed through a 690 nm long pass excitation filter and then focused through the focusing objective on the sample.

Spheroids made of NIH3T3 cells: The spheroids were imaged with light of wavelength 840 nm. Dynamic imaging with variable laser powers up to 30 mW was performed because the dense spheroids scatter light (pixel dwell time of 4 µs/pixel). 3D deep imaging was performed by taking images at every 5 µm in the vertical plane. Since the size of the spheroid range from 400 µm – 1 mm (bigger than full magnification of the lens), multiple area time lapse imaging was performed to take 3D images at various horizontal positions and then the images were stitched together using the Olympus Fluoview 4.2 software. The emitted light was collected by a PMT detector (Hamamatsu R3896) after passing through a green fluorescence filter (495–540 nm). The images were averaged by 5 Kalman frames.

Spheroids made of only OVCAR-5 cells: The spheroids were imaged with light of wavelength 780 nm. Dynamic imaging (changing laser power with variable laser powers up to 40 mW was performed to achieve deep imaging (pixel dwell time of 4 µs/pixel). In 3D, images were taken at every 12 µm section for all the samples on day 0 while, at 10 µm on day 2 and day 7. Multiple area time lapse imaging was performed in the same way as for spheroids made of NIH3T3 cells. The emitted light was collected by a PMT detector (Hamamatsu R3896) after passing through a red fluorescence filter (570–625 nm). The images were averaged by 3 Kalman frames.

Spheroids made of both OVCAR-5 and NIH3T3 cells: The imaging wavelength and conditions were similar to that of OVCAR-5 cells. In 3D, images were taken at every 10 µm section for all the samples. Green fluorescence light from GFP was collected in the transmitted direction through a 0.9 NA air-based condenser and then passed through a band-pass filter (490±20 nm) before being detected through a PMT detector (Hamamatsu R3896). Red fluorescence light from RFP collected in the reflected direction by a PMT detector (Hamamatsu R3896) after passing through a red fluorescence filter (570–625 nm). The images were averaged by 3 Kalman frames.

All the imaging was performed at room temperature and all the images were analyzed by FluoView 4.2 and Imaris x64 8.0.2 software.

6.20 Results and discussion

The three types of spheroids made of, only NIH3T3 cells (transfected with GFP), only OVCAR-5 cells (transfected with RFP), and both NIH3T3 (GFP) and OVCAR-5 (RFP) cells were imaged by both one-photon and two-photon microscopies. Here, I discuss one-photon imaging of the spheroids made of only NIH3T3 cells and two-photon imaging of all the types of spheroids.

6.21 Spheroids of NIH3T3 fibroblast cells

One-photon–based confocal imaging

Dr. Mukherjee imaged the spheroids composed of NIH3T3 cells transfected with green fluorescence protein (GFP) by one-photon–based confocal microscopy at three different time points, day 0, day 2, and day 7 to observe their evolution at physiological conditions over time. The days define the number of days since the spheroids are printed.

The one-photon–based confocal images of the spheroids fail to give the overall spatial information. The excitation maxima of GFP is around 490 nm and so it was excited by 488 nm laser line, which falls in the green region.[46] Deep imaging (>100 μm) cannot be achieved with this wavelength of light and it also causes photodamage of cells. The spheroids were developed in an ellipsoidal shape at a density of 10 million cells per mL (Day 0) and as the time progressed, the cell density of the spheroids increased due to cellular multiplication. Increased density hindered deep imaging due to light scattering. The thickness of the spheroid at day 0 was approx. 600 μm; however, imaging up to only 100 μm was possible (Figure 2). On day 2, the spheroids attained the spherical shape. Fluorescence was seen only from the periphery of the spheroid and no signal was detected from the center. On day 7, due to high cellular density (due to cell multiplication), only 50 μm of depth was achieved. To elucidate the overall spatial information, imaging up to at least half of the total diameter must be achieved so that the core is visualized. With such low depth imaging, it could not be concluded if there was cell death at the core of the spheroids due to hypoxia.

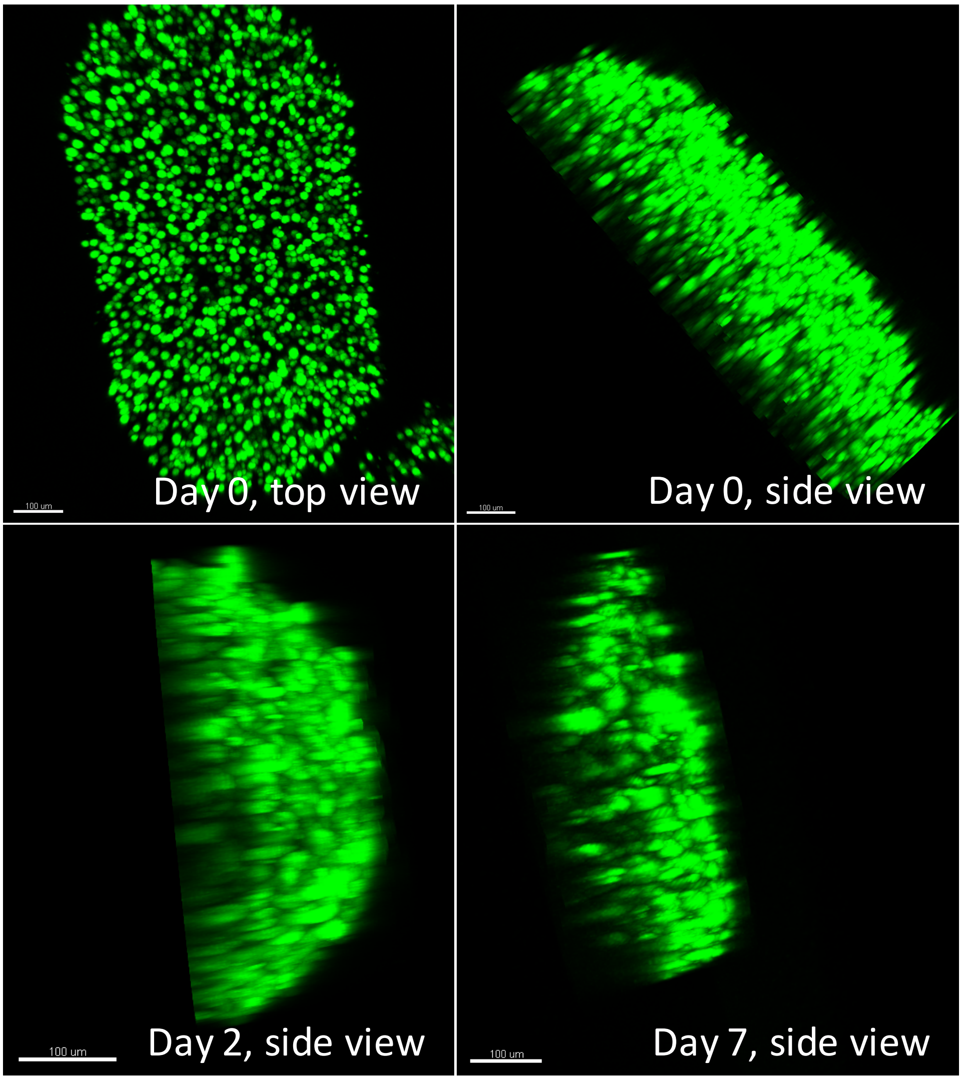

Figure 2: One-photon–based confocal images of spheroids composed of NIH3T3 cells (transfected with GFP) taken on day 0, day 2, and day 7. The thicknesses of the spheroids are approx. 600 µm; however, not more than 100 µm of depth could be imaged. As the time progresses (from day 0 to day 7), the cells multiply and the spheroids become denser thus making deep imaging difficult. At day 0, up to 100 µm of deep imaging was achievable, while at day 7, images only up to 50 µm depth were captured. Images were acquired by Dr. Nobina Mukherjee. Scale bar = 100 µm.

Two-photon imaging

As one-photon imaging was not able to give spatial information about the spheroids, I imaged them using two-photon microscopy. The two-photon absorption maxima of GFP lies at around 840 nm,[46] which is a blessing in disguise because in biological tissues, deepest imaging can be achieved with light of wavelength in the range of 800–870 nm.[47] The were irradiated with intense light of 840 nm using the femtosecond pulsed-laser spheroids at different days (day 0, day 2, and day 7).

Day 0

At day 0, up to 550 µm of deep imaging was achieved on spheroids of 600 µm in diameter (Figure 3). It can be seen in Figure 3 that cells are distributed homogeneously at the both periphery and core area.

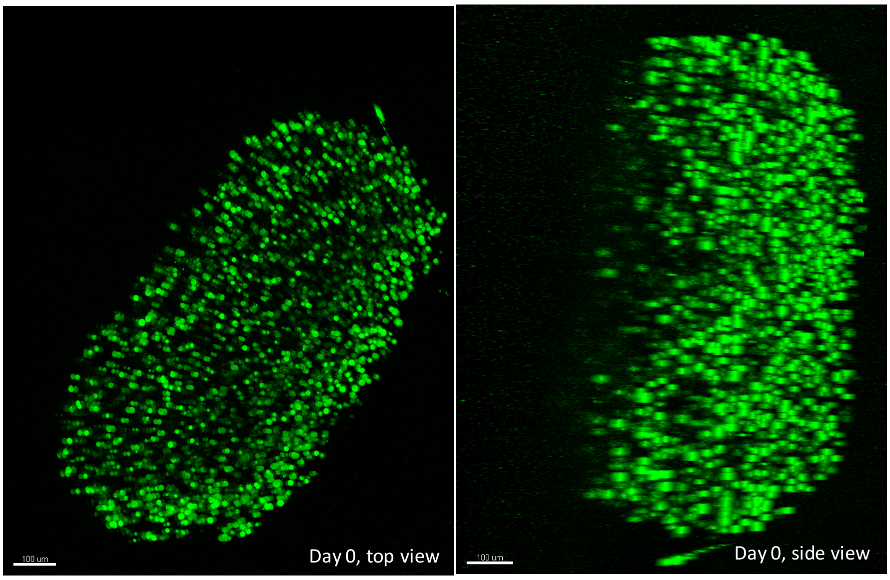

Figure 3: Two-photon images of spheroids on day 0 of top-view and side-view. Scale bar = 100 µm.

Day 2

On day 2, the spheroid attained a spherical shape. The total diameter of the spheroid was approx. 500 µm and imaging up to 400 µm deep was achieved (Figure 4 and Figure 5). The depth penetration was less than the imaging performed on day 0, because on day 2, the spheroid became denser. It was observed that there is more density of cells at the periphery than at the core area; however, the core area was not completely deprived of cells (Figure 6).

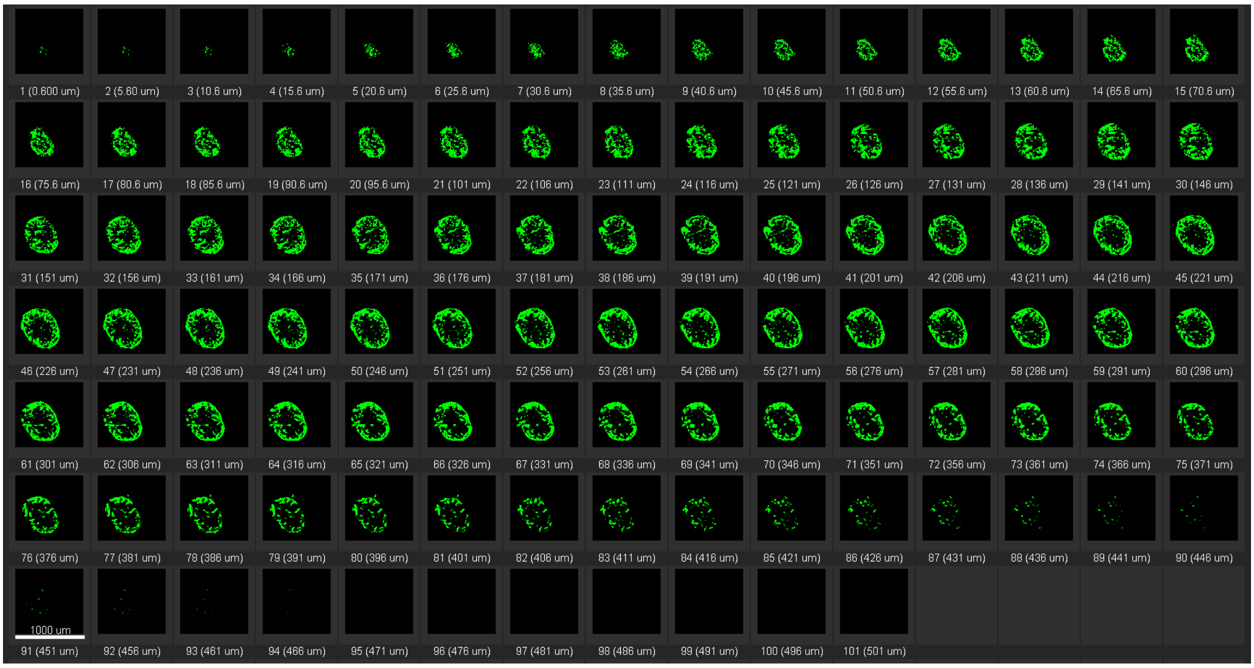

Figure 4: Images of spheroid sectioned at every 5 μm from the top. The images were attained up to depth of 400 μm. Scale bar = 1000 μm.

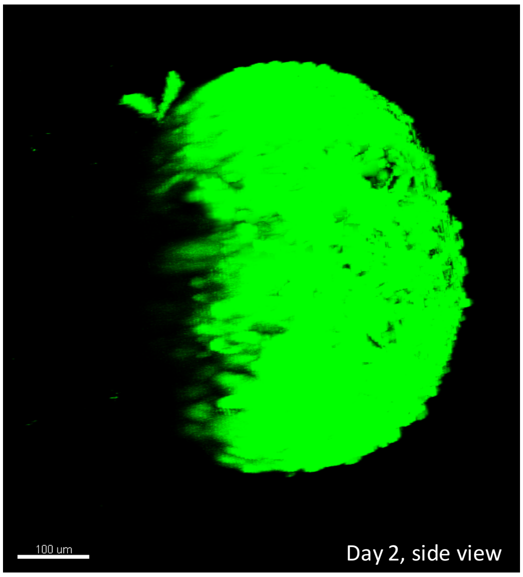

Figure 5: Side view image of the spheroid. Imaging up to depth of 400 μm was achieved. Scale bar = 100 μm.

Side view (Figure 5) and bottom view (Figure 6) images show that the cells are brighter at the periphery than at the core. This is because higher laser power was used to image the cells at the core which led to saturation of the signals coming from the periphery. The bottom view image of the spheroid was converted to voxels for clarity (Figure 6). Voxels are created in such a way that a collection of adjoining pixels are converted into one voxel without distorting the shape of the collection of pixels and the color intensity of all the voxels are normalized equally.

The normalization of intensity makes the visualization easy. The voxel-based image (right image, Figure 6) shows that there are few cells at the center than at the periphery.

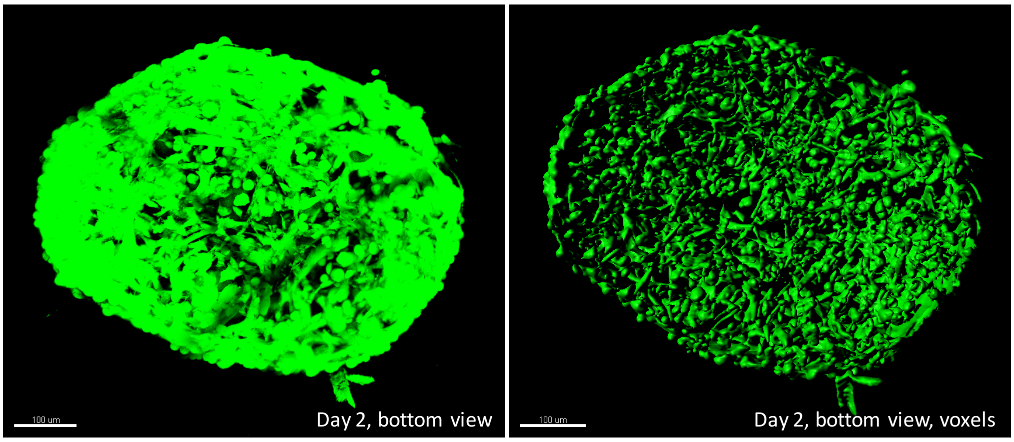

Figure 6: Bottom view of the spheroid on day 2. The left image is the pixel-based image acquired directly from the microscope, while the right image is the voxel-based image of the pixel image. By creating voxels, the intensities of all the cells are normalized. Scale bar = 100 µm.

Day 7

On day 7, up to 350 µm (spheroid diameter ≈ 600 µm) of deep imaging was achieved (Figure 7) in contrast to 50 µm as it was observed during one-photon imaging.

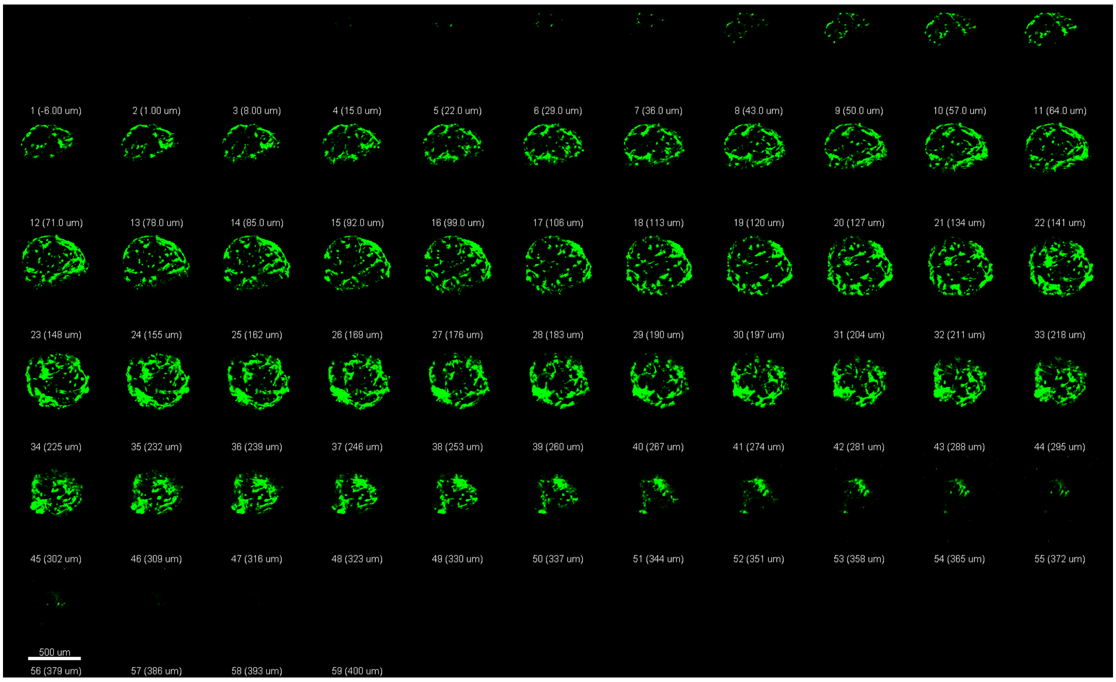

Figure 7: Images of spheroid sectioned at every 7 µm from the top. The images were attained up to depth of 350 µm. Scale bar = 500 µm.

In Figure 7, cells are visible at the center in all the sectional images apart from the periphery, which means that the spheroid is not completely hollow at the core. The bottom view (Figure 8) of the spheroid shows that there are certain void areas formed (marked with red arrows) around the spheroid due to nutrient gradient. Moreover, the fibroblast cells tend to form loop like structures with more affinity to thrive at the periphery.[48,49] Such voids were not observed in spheroids on day 2.

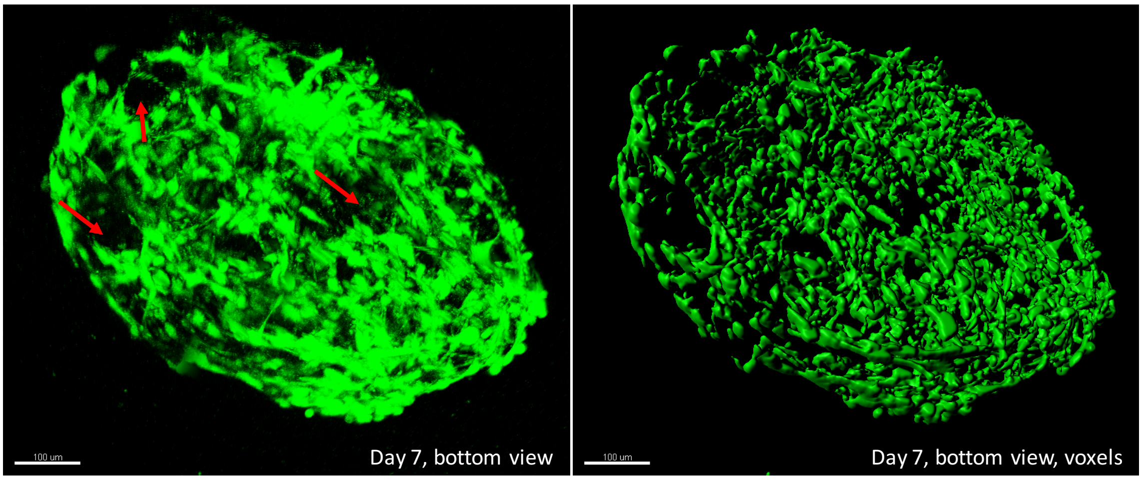

Figure 8: Bottom view pixel and voxel –based images of the spheroid on day 7. Scale bar = 100 µm.

The time-based imaging of the spheroid shows that the overall shape and size has changed. Moreover, the visibility of voids on day 7 shows that although the cells are multiplying there is uneven distribution of the nutrients leading to cell death at the areas where there is lack of nutrients. The two-photon microscopy clearly gave more information about the spatial features of the spheroids than one-photon microscopy. Figure 9 shows the side-by-side comparison of one-photon and two-photon images. It can be clearly seen that deeper imaging was possible with the two-photon microscopy than one-photon microscopy.

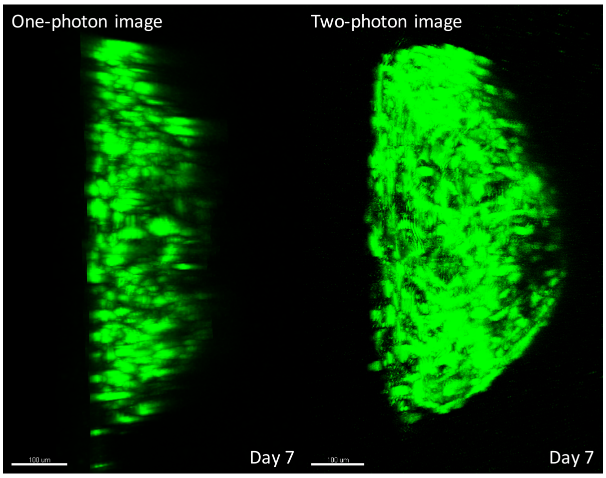

Figure 9: Comparison of one-photon and two-photon images of models printed with only 3T3NIH fibroblast cells on day 7. Deeper imaging was possible with two-photon microscopy than one-photon microscopy. Scale bar = 100 µm.

6.22 Spheroids of OVCAR-5 cancer cells

Spheroids composed of OVCAR-5 cancerous cells were printed at two different densities of 10 million cells per mL (diameter ≈ 550 µm) and 30 million cells per mL (diameter ≈ 850 µm). I imaged the spheroids by two-photon microscopy because one-photon microscopy was not helpful to give overall spatial information. The excitation wavelength was 780 nm because RFP has negligible two-photon absorption cross-section from 810 nm – 980 nm.[37] The pixel dwell time was 4 µs/pixel and the images were averaged by 3 Kalman frames. The laser power was varied as per depth to get high resolution images. As the time progressed, the sizes of the spheroids changed, they became denser, and hollow at the core. The characteristics of both the types of spheroids are similar. Only the denser spheroid (printed at 30 million cells per mL) is discussed hereafter.

Day 0

On day 0, up to 400 µm of deep imaging was achievable (Figure 10 and Figure 11). Due to scattering of light, not many cells were observed at the core.

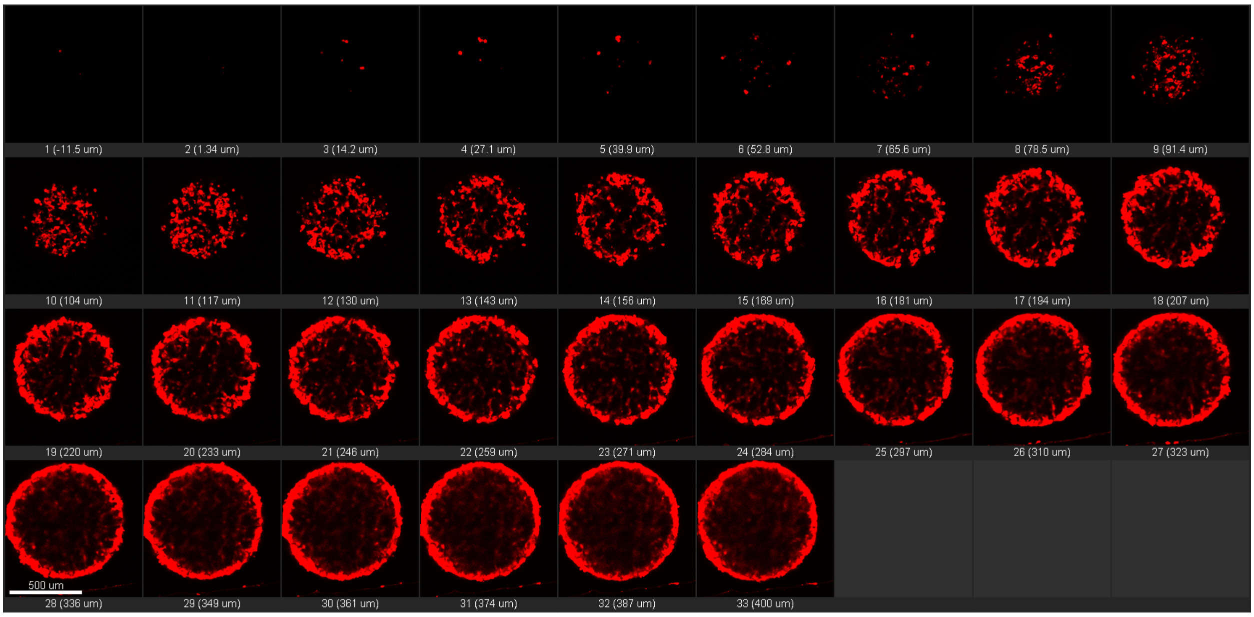

Figure 10: Spheroid made of OVCAR-5 cells at a density of 30 million cells per mL. Images of spheroid sectioned at every 12 µm from the top. Scale bar = 500 µm.

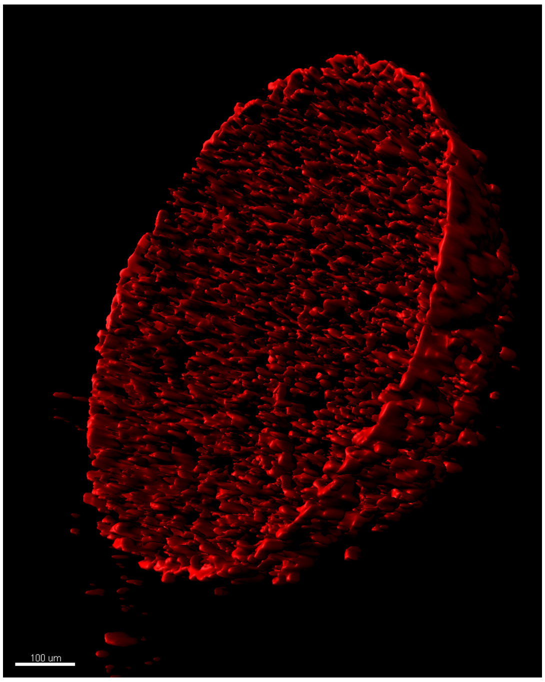

Figure 11: Volex version of the spheroid made of OVCAR-5 cells. Scale bar = 100 µm.

Day 2

On day 2, the depth imaging was more difficult as the spheroids became denser. The total diameter of the tumor was approx. 1070 µm (Figure 12). This shows that from day 0 to day 2, the cancer cells multiply at a faster rate than was observed for spheroids made of NIH3T3 fibroblast cells. Most of the cells were on the periphery (Figure 13). However, due to scattering of light, it could not be known if there are significant number of cells at the core.

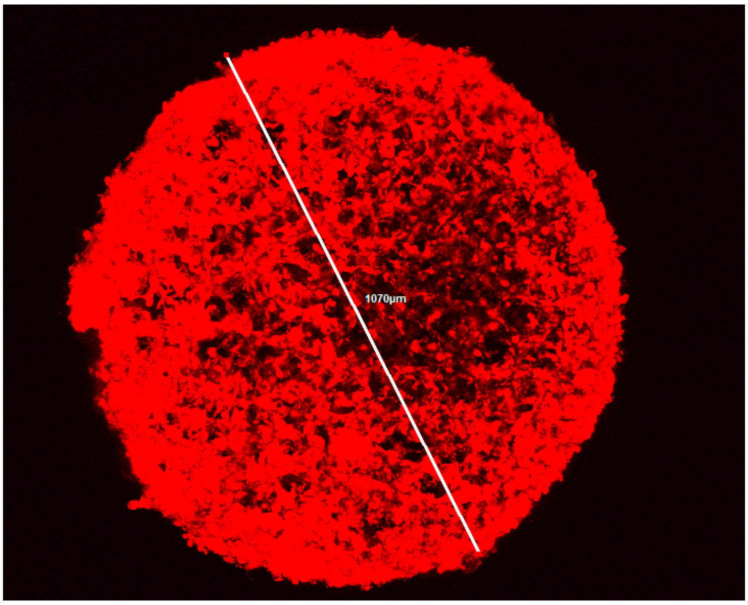

Figure 12: 2D projection of tumor on day 2. Total diameter is 1070 µm.

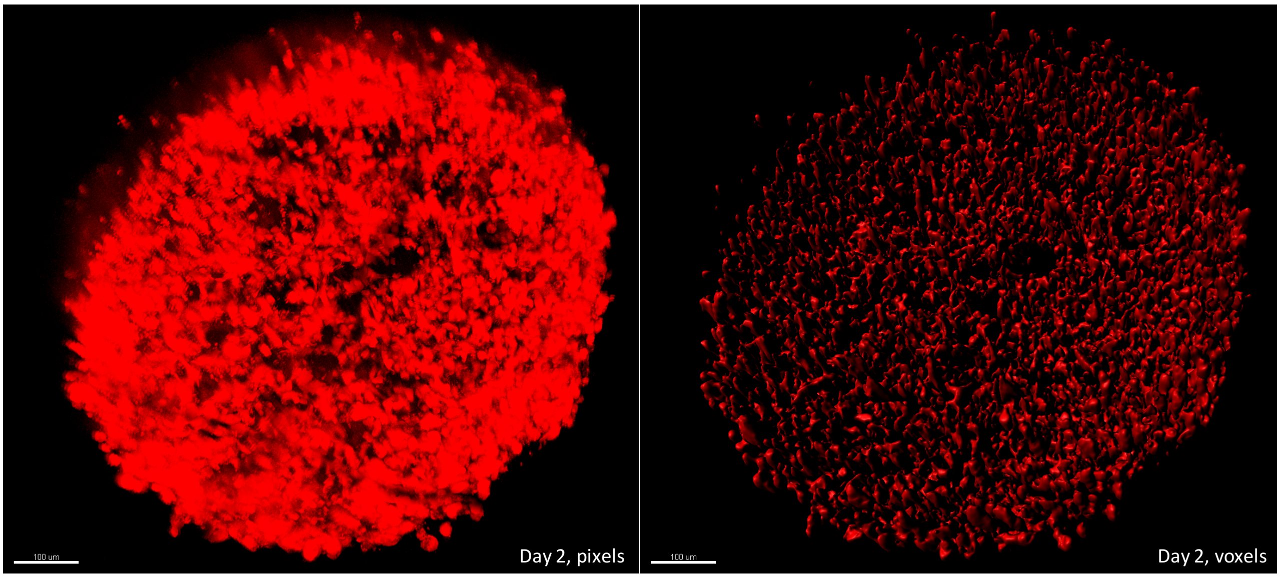

Figure 13: Bottom view pixel and voxel –based images of the OVCAR-5–based spheroid on day 2. Scale bar = 100 µm.

Day 7

On day 7, the tumor models attained various shapes. Some tumors broke out and the spherical shape was lost while others remained intact. The breakage happens during handling of the sample; sometimes they get attached to the tissue culture flask because of which they break while being taken out for imaging. High laser powers (>10 mW) were used at the deeper sections for imaging that led to saturation of the signals at the periphery. The voxel version of the tumor models on day 7 are shown as Figure 14. Due to high density, a comprehensive imaging of the core area was not achieved; however, the broken spheroid (left image, Figure 14) indicates that the core is mostly hollow.

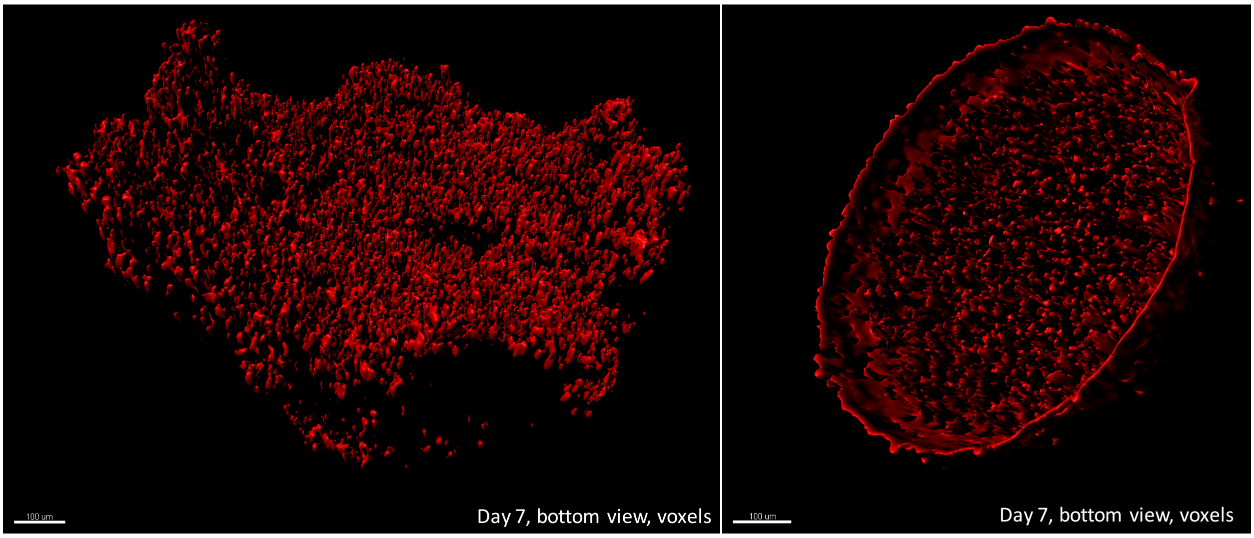

Figure 14: Voxel version of bottom view of the tumor models on day 7. Scale bar = 100 µm.

I colored the voxel image of the spherical shaped tumor model to cyan and merged it with the red colored pixel image for clarity at the core (Figure 15). Few cyan colored voxels could be seen at the center indicating that the spheroid is not completely hollow; however, the density of the cells at the center is lower than it was observed for spheroids composed of NIH3T3.

The time-based imaging of spheroids made of OVCAR-5 cancerous cells show that the tumor grow at the faster rate than the spheroid made of NIH3T3 fibroblast cells and are hollower at the core due to availability of limited oxygen.

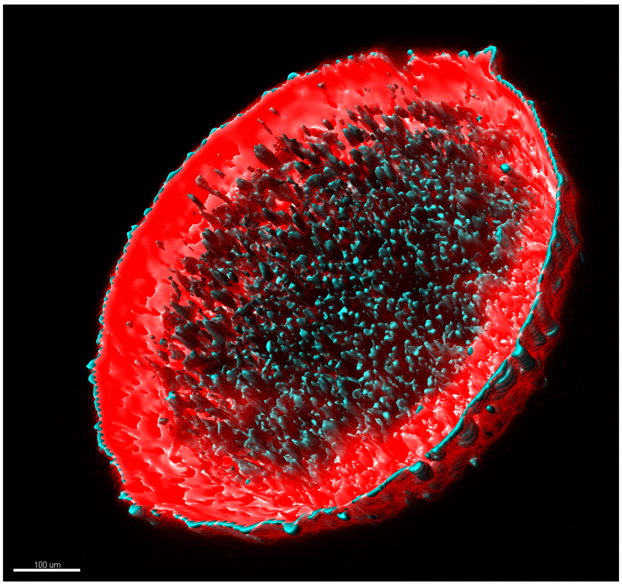

Figure 15: Cyan colored voxel version merged with red color pixel version of the spheroid. Scale bar = 100 µm.

6.23 Spheroids of both OVCAR-5 cancer cells and NIH3T3 fibroblast cells

Dr. Mukherjee also developed spheroids by mixing both OVCAR-5 and NIH3T3 cells because real tumors in the human body are composed of both cancerous and non-cancerous cells. I imaged the spheroids under the multiphoton microscope at three different days, day 0, day 2, and day 7. The excitation wavelength was 780 nm to excite both GFP and RFP.[37] The pixel dwell time was 4 µs/pixel and the images were averaged by 3 Kalman frames. The laser power was varied as per depth to get high resolution images.

Since, the emission spectra of both RFP and GFP overlap (Figure 16), and the spectrum of RFP spans from 540 nm to 750 nm, conventional fluorescence filter system of the multiphoton microscope was not useful to acquire separate signals of GFP and RFP. Since the green filter in the microscope (Figure 17, Chapter 1) takes light in the wavelength range of

495–540 nm, RFP signals were also detected through this filter. Pure GFP signals were acquired by passing the light through a special filter of wavelength range 470–510 nm in the transmitted direction. I collected RFP signals only from red filter (570–625 nm) in the reflected direction; however, GFP was also detected from the red filter because GFP emits light up to 650 nm. The pure GFP signals obtained from transmitted direction were subtracted from the signals obtained from the signals acquired in the reflected direction to obtain pure RFP signals. Using this approach, the emissions from GFP and RFP were segregated and later merged to have an overview of the spheroids.

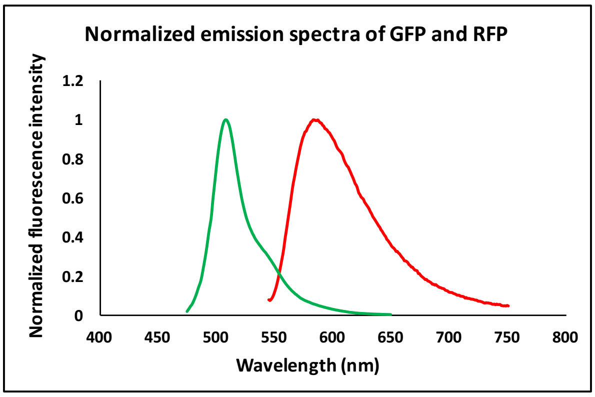

Figure 16: Fluorescence spectra of GFP (green) and RFP (red). Spectra acquired from ThermoFischer Scientific website.

Day 0

The cells in the spheroid were uniformly distributed on day 0 (Figure 17). Red color is emitted from the OVCAR-5 cells transfected with RFP, while green color is emitted from NIH3T3 cells transfected with GFP. The spheroid was composed with equal density of fibroblast and cancerous cells.

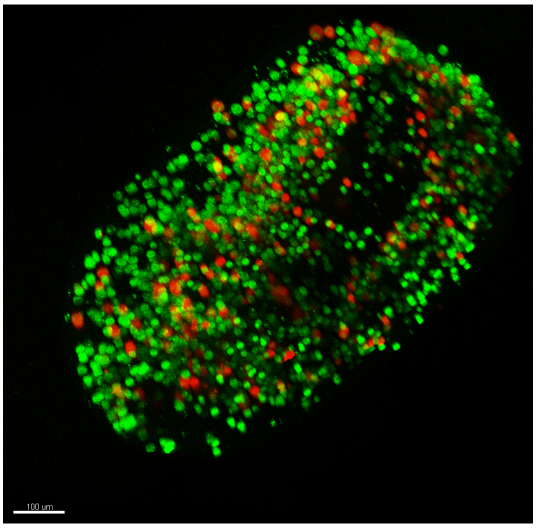

Figure 17: Spheroid composed of both OVCAR-5 and NIH3T3 cells imaged on day 0. Scale bar = 100 µm.

Day 2

On day 2, the model attained a spherical shape. The difference between the number of fibroblast cells and cancer cells reduced since day 0 due to faster multiplication rate of OVCAR-5 than fibroblast cells (Figure 18). The image of the full spheroid was not possible due to light scattering because of which imaging only up to the depth of 360 µm was possible. The model evolved into a core-shell structure, where core is made of the OVCAR-5 cells and the shell is made of fibroblast cells. Diameter of the spheroid was 720 µm.

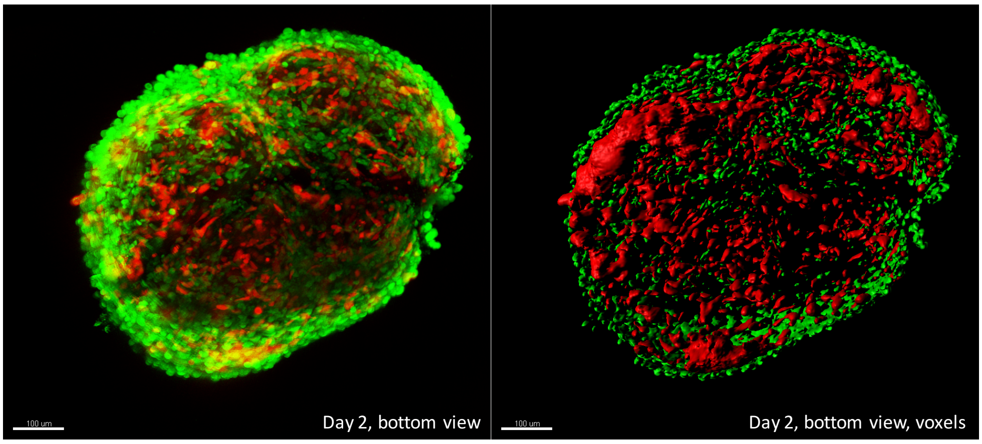

Figure 18: Bottom view of the spheroid on day 2. Scale bar = 100 µm.

Day 7

On day 7, a few multicellular spheroids broke (Figure 19) during handling just like those of only OVCAR-5 cancerous cells, while others remained intact (Figure 20). A full overview of the broken spheroid was achieved (Figure 19) but not of the intact spherical spheroid. Due to light scattering only a hollow structure was visible for the intact spheroid (Figure 20). The core-shell arrangement was also visible on day 7.

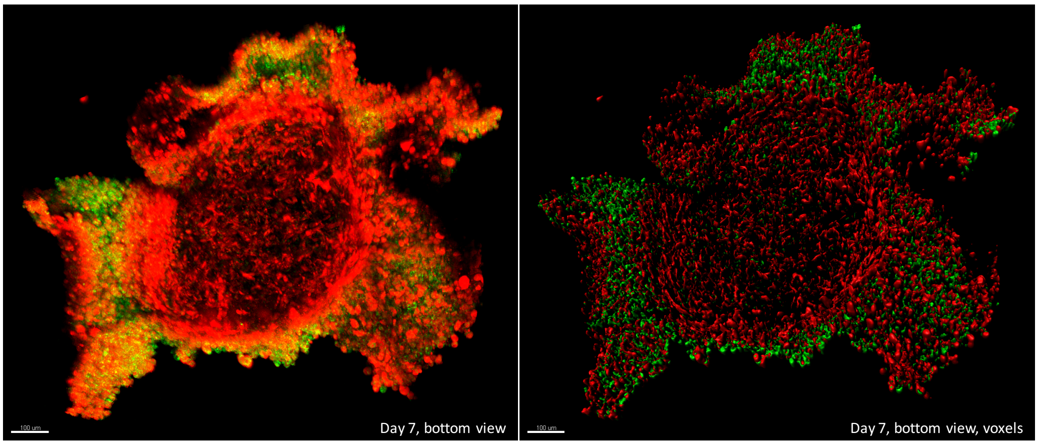

Figure 19: Bottom view of the pixel and voxel versions of the broke spheroid on day 2. Scale bar = 100 µm.

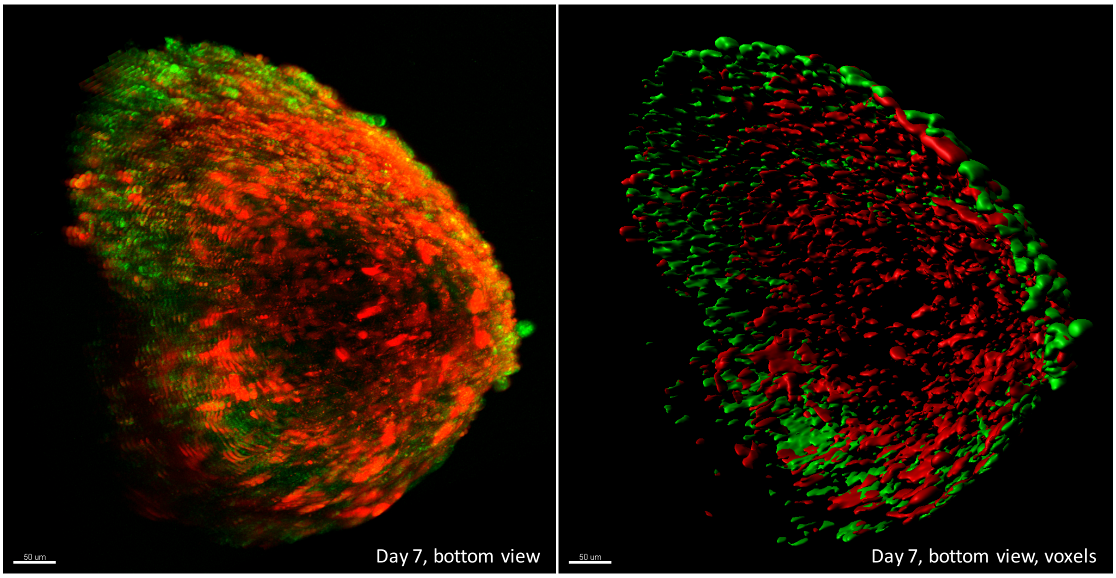

Figure 20: Bottom view of the spherical hollow shaped spheroid on day 2. Scale bar = 50 µm.

On day 7, the cancerous OVCAR-5 cells clearly outnumbered the NIH3T3 fibroblast cells (Figure 21). The fibroblast cells were mostly localized at the periphery while, most of the inner space of the model was taken over by the cancer cells. This is because the fast multiplying cancerous cells consumed most of the nutrients and oxygen, leaving very little or no nutrients for the fibroblasts. The fibroblast cells thrive only at the periphery due to abundance of oxygen.

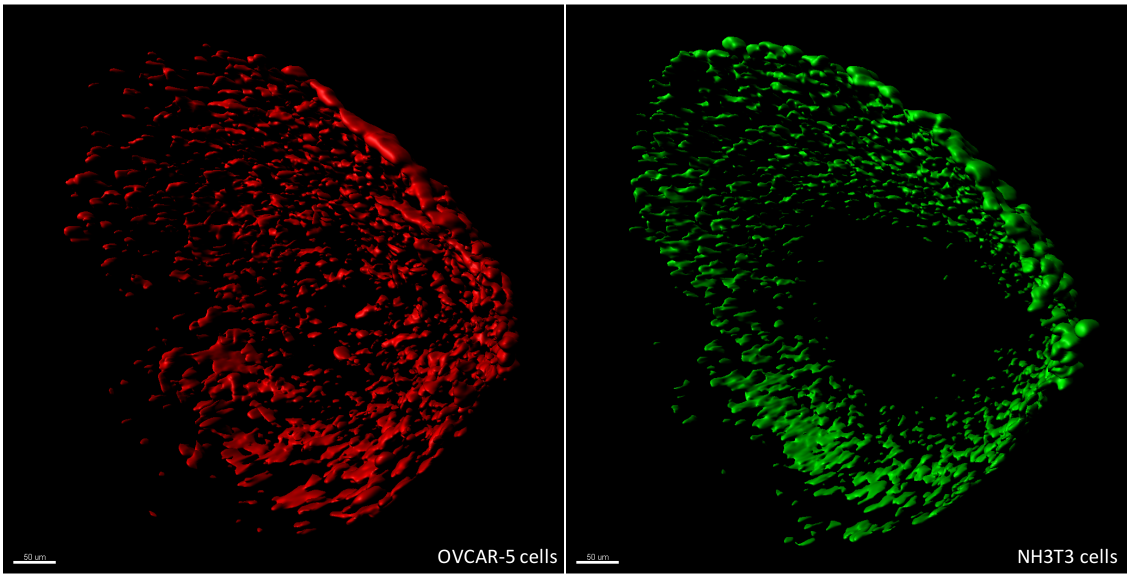

Figure 21: Bottom view of the spheroid on day 7. The OVCAR-5 cells are more in number than NIH3T3 fibroblast cells. The fibroblast cells are mostly localized in clusters at the periphery while the cancerous cells are thriving all over the spheroid except the core area due to hypoxia. Scale bar = 50 µm.

6.30 Conclusion

In this chapter, I have discussed the development and imaging of monocellular and multicellular 3D microtumors. The two-photon microscopy elucidated more information about the spatial characteristics of the cellular spheroids than one-photon microscopy. The 3D microtumors showed over 90% viability on day 0 and typical cellular behaviors, including migration and proliferation in culture after printing. The sizes of the spheroids made from only OVCAR-5-based epithelial cancerous cells increased at a faster rate than the spheroids made of only NIH3T3 fibroblast cells. For all the models, the density of the cells at the core was less than at the periphery due to hypoxia. The structural integrity of individual 3D microtumors were maintained over the course of one week, as observed with the time-based study (Figures 3–21). The extracellular matrix composition influences the survival, development, migration, proliferation, morphology, and function of embedded cells.[50,51] The local degradation of the Matrigel matrix allowed cellular reorganization and movement (Figures 8, 14, and 19). In the multicellular spheroid, the number of cancer cells clearly outnumbered the number of fibroblast cells after 7 days due to enhanced cell proliferation in cancer cells. The multicellular spheroid assumed a core-shell structure, through reorganization in the cellular niche, with OVCAR-5 cells at the core. It can be concluded that the printing approach provides a new route to achieve spatial arrangements of co-cultures and two-photon microscopy allows studying these biological processes. The engineered structures might be used as cost-effective tissue models to aid drug development, or might open new opportunities in regenerative medicine, e.g. in organ repair.

6.40 References

1 A. Vasaturo, S. Caserta, I. Russo, V. Preziosi, C. Ciacci and S. Guido, *PLoS One*, 2012, **7**, e52251.

2 M. Zanoni, F. Piccinini, C. Arienti, A. Zamagni, S. Santi, R. Polico, A. Bevilacqua and A. Tesei, *Sci. Rep.*, 2016, **6**, 19103.

3 C. Hirt, A. Papadimitropoulos, V. Mele, M. G. Muraro, C. Mengus, G. Iezzi, L. Terracciano, I. Martin and G. C. Spagnoli, *Adv. Drug Deliv. Rev.*, 2014, **79–80**, 145–154.

4 D. M. Lewis, M. R. Blatchley, K. M. Park and S. Gerecht, *Nat. Protoc.*, 2017, **12**, 1620–1638.

5 Q. Xie, J. Xie, J. Zhong, X. Cun, S. Lin, Y. Lin and X. Cai, *Cell Prolif.*, 2016, **49**, 236–245.

6 Y. Imamura, T. Mukohara, Y. Shimono, Y. Funakoshi, N. Chayahara, M. Toyoda, N. Kiyota, S. Takao, S. Kono, T. Nakatsura and H. Minami, *Oncol. Rep.*, 2015, **33**, 1837–1843.

7 D. R. Griffin, W. M. Weaver, P. O. Scumpia, D. Di Carlo and T. Segura, *Nat. Mater.*, 2015, **14**, 737–744.

8 D. Anton, H. Burckel, E. Josset and G. Noel, *Int. J. Mol. Sci.*, 2015, **16**, 5517–5527.

9 S. E. Harrison, B. Sozen, N. Christodoulou, C. Kyprianou and M. Zernicka-Goetz, *Science.*, 2017, **356**, eaal1810.

10 F. Birey, J. Andersen, C. D. Makinson, S. Islam, W. Wei, N. Huber, H. C. Fan, K. R. C. Metzler, G. Panagiotakos, N. Thom, N. A. O'Rourke, L. M. Steinmetz, J. A. Bernstein, J. Hallmayer, J. R. Huguenard and S. P. Paşca, *Nature*, 2017, **545**, 54–59.

11 G. Quadrato, T. Nguyen, E. Z. Macosko, J. L. Sherwood, S. Min Yang, D. R. Berger, N. Maria, J. Scholvin, M. Goldman, J. P. Kinney, E. S. Boyden, J. W. Lichtman, Z. M. Williams, S. A. McCarroll and P. Arlotta, *Nature*, 2017, **545**, 48–53.

12 A. Nyga, U. Cheema and M. Loizidou, *J. Cell Commun. Signal.*, 2011, **5**, 239–248.

13 K. P. M. Ricketts, U. Cheema, A. Nyga, A. Castoldi, C. Guazzoni, T. Magdeldin, M. Emberton, A. P. Gibson, G. J. Royle and M. Loizidou, *Small*, 2014, **10**, 3954–3961.

14 F. Leonard and B. Godin, *Methods Mol. Biol.*, 2016, **1406**, 239–251.

15 Z. F. Bielecka, K. Maliszewska-Olejniczak, I. J. Safir, C. Szczylik and A. M. Czarnecka, *Biol. Rev.*, 2017, **92**, 1505–1520.

16 M. Zanoni, F. Piccinini, C. Arienti, A. Zamagni, S. Santi, R. Polico, A. Bevilacqua and A. Tesei, *Sci. Rep.*, 2016, **6**, 19103.

17 N. Gupta, J. R. Liu, B. Patel, D. E. Solomon, B. Vaidya and V. Gupta, *Bioeng. Transl. Med.*, 2016, **1**, 63–81.

18 G. Mehta, A. Y. Hsiao, M. Ingram, G. D. Luker and S. Takayama, *Drug Deliv. Cancer Today's Challenges, Tomorrow's Dir.*, 2012, **164**, 192–204.

19 R. K. Jain, P. Au, J. Tam, D. G. Duda and D. Fukumura, *Nat. Biotechnol.*, 2005, **23**, 821–823.

20 H. K. Kleinman and G. R. Martin, *Semin. Cancer Biol.*, 2005, **15**, 378–386.

21 V. Trivedi, A. Doshi, G. K. Kurup, E. Ereifej, P. J. Vandevord and A. S. Basu, *Lab Chip*, 2010, **10**, 2433–2442.

22 A. K. Au, W. Huynh, L. F. Horowitz and A. Folch, *Angew. Chem. Int. Ed.*, 2016, **55**, 3862–3881.

23 G. Villar, A. D. Graham and H. Bayley, *Science.*, 2013, **340**, 48–52.

24 S. Ma, N. Mukherjee, E. Mikhailova and H. Bayley, *Adv. Biosyst.*, 2017, **1**, 1700075.

25 R. Foty, *J. Vis. Exp.*, 2011.

26 M. Shri, H. Agrawal, P. Rani, D. Singh and S. K. Onteru, *Sci. Rep.*, 2017, **7**, 1203.

27 J. Westermarck, A. Seth and V. M. Kähäri, *Oncogene*, 1997, **14**, 2651–2660.

28 M. Trojanowska, *Oncogene*, 2000, **19**, 6464–6471.

29 K. K. Kim, M. C. Kugler, P. J. Wolters, L. Robillard, M. G. Galvez, A. N. Brumwell, D. Sheppard and H. A. Chapman, *Proc. Natl. Acad. Sci.*, 2006, **103**, 13180–13185.

30 A. Diaspro, in *Confocal and Two-Photon Microscopy: Foundations, Applications and Advances*, ed. A. Diaspro, Wiley-VCH, 2001, p. 576.

31 F. Helmchen and W. Denk, *Nat. Methods*, 2006, **2**, 932–940.

32 P. G. Bush, D. L. Wokosin and A. C. Hall, *Front. Biosci.*, 2007, **12**, 2646–2657.

33 M. Albota, *Science.*, 1998, **281**, 1653–1656.

34 S. R. Marder, *Chem. Commun.*, 2006, 131–134.

35 C. R. Stoltzfus, L. M. Barnett, M. Drobizhev, G. Wicks, A. Mikhaylov, T. E. Hughes and A. Rebane, *Sci Rep*, 2015, **5**, 11968.

36 R. Heim, A. B. Cubitt and R. Y. Tsien, *Nature*, 1995, **373**, 663–664.

37 M. Drobizhev, N. S. Makarov, S. E. Tillo, T. E. Hughes and A. Rebane, *Nat. Methods*, 2011, **8**, 393–399.

38 M. Pawlicki, H. A. Collins, R. G. Denning and H. L. Anderson, *Angew. Chem. Int. Ed.*, 2009, **48**, 3244–3266.

39 F. Bestvater, E. Spiess, G. Stobrawa, M. Hacker, T. Feurer, T. Porwol, U. Berchner-Pfannschmidt, C. Wotzlaw and H. Acker, *J. Microsc.*, 2002, **208**, 108–115.

40 W. B. Amos, J. G. White and M. Fordham, *Appl. Opt.*, 1987, **26**, 3239–3243.

41 Minski, M., US Patent, 3013467, 1961.

42 W. Denk, J. H. Strickler and W. W. Webb, *Science.*, 1990, **248**, 73–76.

43 R. H. Webb, *Reports Prog. Phys.*, 1996, **59**, 427.

44 M. Göppert-Mayer, *Ann. Phys.*, 1931, **401**, 273–294.

45 W. Denk and K. Svoboda, *Neuron*, 1997, **18**, 351–357.

46 M. Drobizhev, N. S. Makarov, S. E. Tillo, T. E. Hughes and A. Rebane, *Nat. Methods*, 2011, **8**, 393–399.

47 K. R. Byrnes, R. W. Waynant, I. K. Ilev, X. Wu, L. Barna, K. Smith, R. Heckert, H. Gerst and J. J. Anders, *Lasers Surg. Med.*, 2005, **36**, 171–185.

48 A. D. Rape, W. Guo and Y. Wang, *Biomaterials*, 2011, **32**, 2043–2051.

49 K. K. Elineni and N. D. Gallant, *Biophys. J.*, 2011, **101**, 2903–2911.

50 J. Thiele, Y. Ma, S. M. C. Bruekers, S. Ma and W. T. S. Huck, *Adv. Mater.*, 2014, **26**, 125–148.

51 M. W. Tibbitt and K. S. Anseth, *Biotechnol. Bioeng.*, 2009, **103**, 655–663.

7.00 Appendix

Chemical structures of organic molecules mentioned in the thesis

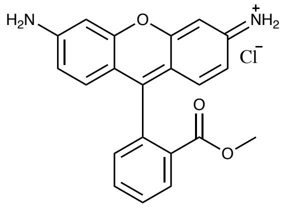

RH123

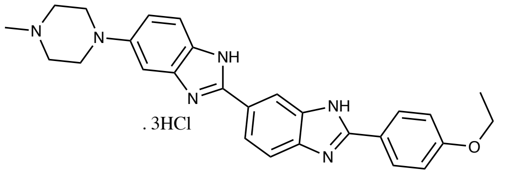

Hoechst33342

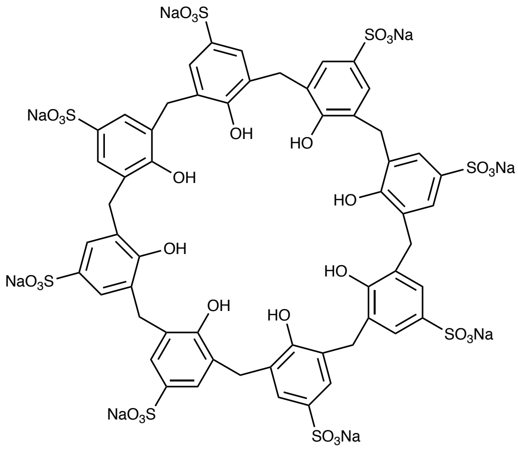

Advasep 7

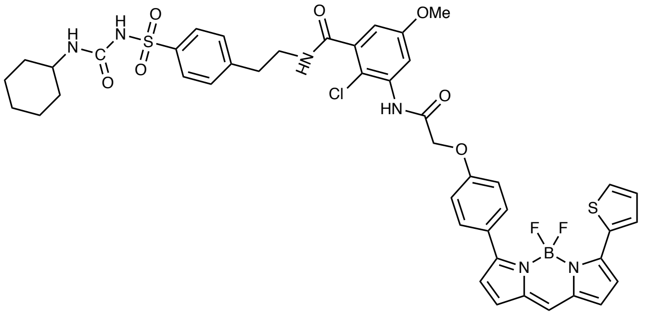

ER Tracker™ Red (BODIPY™ TR Glibenclamide)

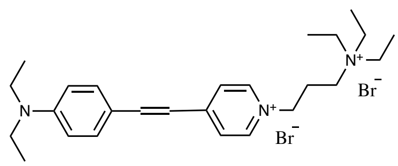

FM1-43

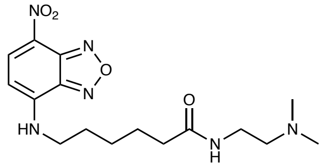

Lysotracker^{TM} Yellow HCK-123